ISSN: 2327-4352 Volume 5, Number 4, April 2017

Scientific Research Publishing

Journal of Applied Mathematics and Physics

ISSN: 2327-4352

www.scirp.org/journal/jamp

JOURNAL EDITORIAL BOARD

ISSN 2327-4352 (Print) ISSN 2327-4379 (Online)
http://www.scirp.org/journal/jamp

Editor-in-Chief

Prof. Wen-Xiu Ma University of South Florida, USA

Editorial Board (According to Alphabet)

Dr. Izhar Ahmad King Fahd University of Petroleum and Minerals, Saudi Arabia
Dr. S. Joseph Antony University of Leeds, UK
Prof. Roberto Oscar Aquilano Instituto de Física Rosario, Argentina
Prof. Ping-Hei Chen National Taiwan University, Chinese Taipei
Prof. Wanyang Dai Nanjing University, China
Dr. Steven B. Damelin The American Mathematical Society, USA
Prof. Beih El-Sayed El-Desouky Mansoura University, Egypt
Prof. Chaudry Masood Khalique North-West University, South Africa
Dr. Ki Young Kim Samsung Advanced Institute of Technology, South Korea
Prof. Xiang Li Beijing University of Chemical Technology, China
Prof. Xing Lü Beijing Jiaotong University, China
Dr. Jafar Fawzi Mansi Al Omari Al-Balqa' Applied University, Jordan
Prof. Rosa Pardo Complutense University of Madrid, Spain
Prof. Sanzheng Qiao McMaster University, Canada
Dr. Daniele Ritelli University of Bologna, Italy
Dr. Babak Daneshvar Rouyendegh Atilim University, Turkey
Prof. Morteza Seddighin Indiana University East, USA
Dr. Marco Spadini University of Florence, Italy
Prof. Hari Mohan Srivastava University of Victoria, Canada
Dr. Divine Tito Fongha Wanduku Keiser University, USA
Prof. Ping Wang Penn State University Schuylkill, USA
Prof. Xiaohui Yuan Huazhong University of Science and Technology, China

Scientific Research Publishing

Journal of Applied Mathematics and Physics, 2017, 5, 836-989
http://www.scirp.org/journal/jamp
ISSN Online: 2327-4379
ISSN Print: 2327-4352

Table of Contents

Volume 5 Number 4 April 2017

Archimedes' Principle Revisited

P. Mohazzabi.....836

The Exact Solution of the Space-Time Fractional Modified Kdv-Zakharov-Kuznetsov Equation

Q. Y. Jin, T. C. Xia, J. B. Wang.....844

Kinematic Relativity of Quantum Mechanics: Free Particle with Different Boundary Conditions

G. P. Kamuntavičius, G. Kamuntavičius.....853

Gravitation as Geometry or as Field

W. Petry.....862

Exact Time Domain Solutions of 1-D Transient Dynamic Piezoelectric Problems with Nonlinear Damper Boundary Conditions

N. M. Khutoryansky, V. Genis.....873

The Faraday Isolator, Detailed Balance and the Second Law

G. S. Levy.....889

Error Analysis and Variable Selection for Differential Private Learning Algorithm

W. L. Nie, C. Wang.....900

Energy Conservation and Gravitational Wavelength Effect of the Gravitational Propagation Delay Analysis

P. Kornreich.....912

Decay Rate for a Viscoelastic Equation with Strong Damping and Acoustic Boundary Conditions

Z. Y. Ma.....922

A Note on the Cosmological Constant in $f(R)$ Gravity

P. K. F. Kuhfittig.....933

Classical Fundamental Unique Solution for the Incompressible Navier-Stokes Equation in $\mathbb{R}^N$

W. S. Khedr.....939

Biomechanical Study of Vertebral Compression Fracture Using Finite Element Analysis

H. Takano, I. Yonezawa, M. Todo, M. H. Mazlan, T. Sato, K. Kaneko.....953

Journal of Applied Mathematics and Physics, 2017, 5, 836-989
http://www.scirp.org/journal/jamp
ISSN Online: 2327-4379
ISSN Print: 2327-4352

Exact Solution for Thermal Stagnation-Point Flow with Surface Curvature and External Vorticity Effects

R. M. C. So, E. W. S. Kam……...…966

Journal of Applied Mathematics and Physics (JAMP)
Journal Information

SUBSCRIPTIONS

The *Journal of Applied Mathematics and Physics* (Online at Scientific Research Publishing, www.SciRP.org) is published monthly by Scientific Research Publishing, Inc., USA.

Subscription rates:
Print: $39 per issue.
To subscribe, please contact Journals Subscriptions Department, E-mail: sub@scirp.org

SERVICES

Advertisements
Advertisement Sales Department, E-mail: service@scirp.org

Reprints (minimum quantity 100 copies)
Reprints Co-ordinator, Scientific Research Publishing, Inc., USA.
E-mail: sub@scirp.org

COPYRIGHT

Copyright and reuse rights for the front matter of the journal:
Copyright © 2017 by Scientific Research Publishing Inc.
This work is licensed under the Creative Commons Attribution International License (CC BY).
http://creativecommons.org/licenses/by/4.0/

Copyright for individual papers of the journal:
Copyright © 2017 by author(s) and Scientific Research Publishing Inc.

Reuse rights for individual papers:
Note: At SCIRP authors can choose between CC BY and CC BY-NC. Please consult each paper for its reuse rights.

Disclaimer of liability
Statements and opinions expressed in the articles and communications are those of the individual contributors and not the statements and opinion of Scientific Research Publishing, Inc. We assume no responsibility or liability for any damage or injury to persons or property arising out of the use of any materials, instructions, methods or ideas contained herein. We expressly disclaim any implied warranties of merchantability or fitness for a particular purpose. If expert assistance is required, the services of a competent professional person should be sought.

PRODUCTION INFORMATION

For manuscripts that have been accepted for publication, please contact:
E-mail: jamp@scirp.org

Scientific Research Publishing

Journal of Applied Mathematics and Physics, 2017, 5, 836-843
http://www.scirp.org/journal/jamp
ISSN Online: 2327-4379
ISSN Print: 2327-4352

Archimedes' Principle Revisited

Pirooz Mohazzabi

Department of Mathematics and Physics, University of Wisconsin-Parkside, Kenosha, WI, USA
Email: mohazzab@uwp.edu

How to cite this paper: Mohazzabi, P. (2017) Archimedes' Principle Revisited. *Journal of Applied Mathematics and Physics*, **5**, 836-843.
https://doi.org/10.4236/jamp.2017.54073

Received: February 28, 2017
Accepted: April 24, 2017
Published: April 27, 2017

Copyright © 2017 by author and Scientific Research Publishing Inc.
This work is licensed under the Creative Commons Attribution International License (CC BY 4.0).
http://creativecommons.org/licenses/by/4.0/

Open Access

Abstract

Based on Newton's third law of motion, we present a different but quite general analysis of Archimedes' principle. This analysis explains the reduction in apparent weight of a submerged object in all cases, regardless of its position in the fluid. We also study the case in which the object rests on the bottom of the container where the net hydrostatic force on it is downward, and explain where in this case the reduction in the apparent weight comes from.

Keywords

Archimedes' Principle, Buoyancy, Apparent Weight

1. Introduction

Although the law of buoyancy was discovered by Archimedes over 2200 years ago, even today from time to time new articles appear in the literature inspecting its various aspects. More specifically, in the last two decade or so, more than a dozen papers have been published in different journals, ranging from pedagogical points of view [1] [2] to scrutinizing the original statements made by Archimedes [3] [4].

Archimedes' principle is one of the most essential laws of physics and fluid mechanics. Basically the principle states an object immersed in a fluid is buoyed up by a force equal to the weight of the fluid that it displaces. This principle, which is perhaps the most fundamental law in hydrostatics, explains many natural phenomena from both qualitative and quantitative points of view. The principle of isostasy, for example, which states that Earth's crust is in floating equilibrium with the denser mantle below [5] [6], is simply based on Archimedes' principle.

One of the applications of Archimedes' principle is in measurement of density of an irregularly shaped object. The simplest method is to use a graduated cylinder filled with water to a certain level. The object is then slowly lowered into

the cylinder until it becomes completely submerged. The increase in the level of water inside the cylinder is simply equal to the volume of the object. This method, however, requires that the diameter of the cylinder be at least as large as the diameter of the object, which reduces the accuracy of the measurement. In addition, this method certainly cannot be used to measure the volume of a large object such as a boulder. The problem, however, can be resolved by taking advantage of Archimedes' principle. A container partially filled with water is placed on a scale and the reading of the scale is recorded. The object is then hung from a string above the water, and slowly lowered into it until it is completely submerged, but without touching the bottom of the container (if the object is less dense than water, it can be pushed under water). The reading of the scale will increase by the mass of the displaced water (assuming that the scale measures mass), from which the volume of the object can be determined [7]. Alternatively, the object can be hung above water from a scale. As the object is lowered into water, the reading of the scale decreases by an amount equal to the mass of the displaced water. Thus, a boulder hanging from a spring or dial scale can be lowered into a large volume of water, such as a pond or a lake, and from the change of the reading of the scale, its volume can be determined.

Even though Archimedes' principle is over 2200 years old and despite its importance in hydrostatics, there are still some questions about it that have not yet been fully answered in the literature. For instance, debates are still going on regarding the interpretation of the principle when an object rests on the bottom of a fluid-filled container, where it experiences a net downward force by the fluid. It is therefore the objective of this article to derive the principle from a different point of view and answer some of the questions associated with the principle that have not been settled in the literature.

2. Derivations of Archimedes' Principle

A rigorous derivation of Archimedes' principle involves the concept of virtual work. In this method, the buoyant force is set equal to the negative of the gradient of the potential energy during an infinitesimal virtual displacement of the submerged object [8] [9]. This approach applies to objects of any shape; however, it has the limitation that the object must be completely surrounded by the fluid and that it should not be in contact with the container.

Alternatively, there are two simpler derivations of the principle [8]. One is based on the plausible argument that if the principle were not true, the subvolume of a fluid displaced by an object would not be in equilibrium. More specifically, the net fluid force on an arbitrarily shaped object would be the same as that on an equal volume of the fluid which was in equilibrium before it was displaced by the object [10] [11] [12] [13]. Therefore, the buoyant force is equal to the weight of the fluid displaced. This argument applies to any object of any shape regardless of its position in the container.

The second approach is based on the variation of hydrostatic pressure P_f as a function of depth of the fluid,

$$P_f = D_f gy \tag{1}$$

where D_f is density of the fluid, y is the depth, and g is the acceleration due to gravity. In this approach, an object of simple geometry such as a rectangular or cylindrical block is considered and the net fluid force due to the difference of hydrostatic pressure at the top and the bottom of the block is calculated [14]. This approach is simple; however, the proof for arbitrarily shaped objects is more involved as stated above [15], and it works only for objects that are completely surrounded by fluid. For objects resting on the bottom of the container, there is no fluid pressure in the contact area and the proof fails.

We now present a different quite general, yet simple derivation of Archimedes' principle that is valid regardless of the position of the object in the fluid. In this approach, the object can be completely surrounded by the fluid, be in contact with the walls of the container, rest on the bottom of the container, or even float in the fluid with only a fraction of its volume submerged.

3. A Different Approach to Archimedes' Principle

Consider a fluid of density D_f and an object of arbitrary shape of mass m and volume V, denser than the fluid. The fluid is in a container of cross-sectional area A and has a height H before the object enters it, as shown in **Figure 1(a)**. The object is supported by a string and, at this time, the tension in the string is mg.

Because fluid forces on the side walls of the container cancel, before the object enters the fluid, the net force F exerted by the fluid on the container is only due to the hydrostatic pressure at the bottom of the container, which is given by

$$F = D_f gHA. \tag{2}$$

Now we lower the object down into the fluid until it is submerged as shown in **Figure 1(b)**. This causes the height of the fluid in the container to increase by δH, where δH is given by

$$\delta H = \frac{V}{A} \tag{3}$$

Therefore, the net fluid force on the bottom of the container increases by δF, which is given by

$$\delta F = D_f g\delta HA = D_f gV \tag{4}$$

which is exactly equal to the weight of the fluid displaced. Therefore, when the object enters the fluid, the level of the fluid increases and the container experiences an additional downward fluid force equal to the weight of the fluid displaced by the object. This downward force can easily be detected by placing the container on a scale [7]. But then according to Newton's third law of motion, the container (through the fluid) exerts an equal upward force on the submerged object.

Therefore, regardless of its position, a submerged object experiences an

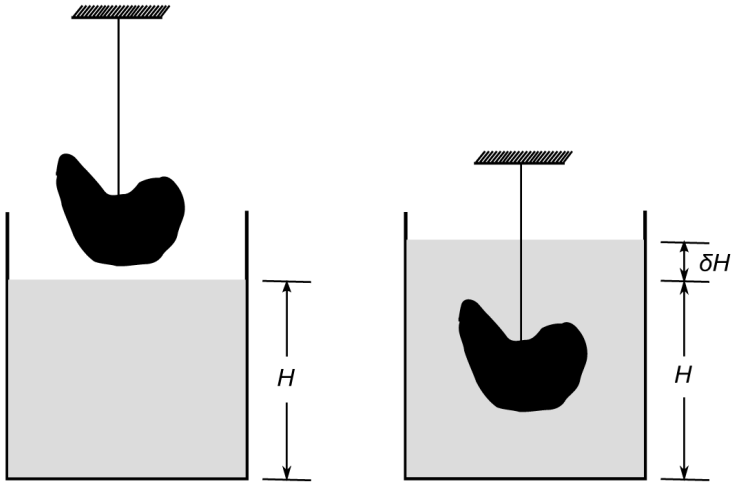

Figure 1. A fluid and an object of arbitrary shape which is denser than the fluid. (a) Before the object is lowered into the fluid, the height of the fluid is H; (b) When the object is lowered into the fluid, the height of the fluid increases by δH.

upward force from the container-fluid system which is equal to the weight of the fluid displaced, $D_f gV$. Consequently, the tension in the string in **Figure 1(b)** and the reading of the scale in **Figure 2(b)** (to be explained later) would each be given by

$$F = mg - D_f gV \tag{5}$$

which is exactly the apparent weight of the object.

Note that the above analysis remains valid regardless of the position of the object in the fluid. Thus the object can be completely surrounded by the fluid, rest on the bottom of the container with no fluid under it, touch the walls of the container, or even float in the fluid with only a fraction of it submerged. In the case of a floating object, however, the volume V in the above equations should be taken to be the sub-volume of the object that is submerged.

A question that normally comes up during discussions of Archimedes' principle is that when an object in the form of a rectangular block rests on the bottom of a container with no fluid under it, where does the upward buoyant force come from? In fact, in this case because of the fluid pressure on top of the block, the net hydrostatic force on it would be *downward*, resulting in the apparent weight of the block to be greater than its true weight. But this conclusion is in complete contradiction with all observations since even in this case the apparent weight of the block is less than its true weight by the weight of the fluid displaced.

To resolve this contradiction, one may argue that in reality when a submerged object rests on the bottom of the container, there is almost always some fluid between the surfaces that appear to be in contact unless the surfaces are specially prepared and treated to prevent fluid seepage. This is because for ordinary flat surfaces, the actual area of contact is always much smaller than the apparent contact area [16] [17]. In fact the real contact area can be less than the apparent

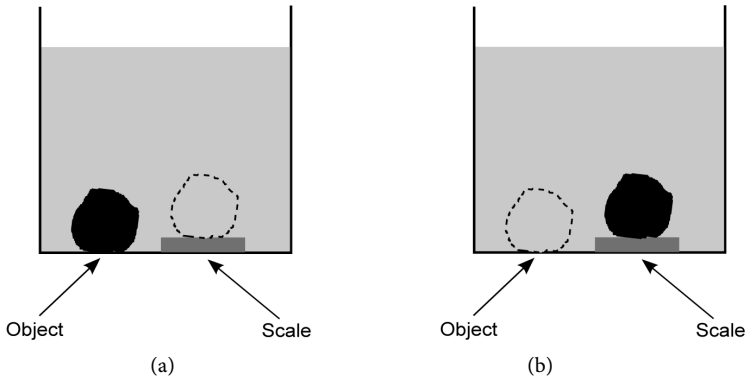

Figure 2. (a) An object denser than a fluid rests on the bottom of a container filled with the fluid. A weight scale is also located at the bottom of the container. The dashed region shows a volume of the fluid equal to the volume of the object; (b) The object has been moved to the top of the scale, displacing an equal volume of the fluid from that region.

macroscopic area by a factor of 10^4 [18]. However, if the surfaces are prepared properly to prevent fluid seepage between them, then obviously there is no fluid pressure there. Therefore, if a block rests on the bottom of the container with no fluid seepage between them, there would be no upward fluid force on the object and consequently there would be no buoyant force on it. Nonetheless, as explained below, experiments show that the even under these circumstances the apparent weight of the object is less than its true weight by the weight of the fluid displaced.

To resolve this apparent paradox, Jones and Gordon [19] designed an experiment to eliminate the upward fluid force on the bottom of a submerged object. They used an aluminum block resting on another aluminum block with highly flat contact surfaces. The surfaces were flat enough to prevent water from seeping between them but did not result in significant intermolecular forces between them [20]. They observed that the net fluid force on the object was in fact *downward*. Several years later, Bierman and Kincanon [3] re-examined this problem by using a submerged block in contact with the bottom of a container which had a hole in it, and studied the force needed to lift the block. Their experiment showed that this force increased linearly with the depth of the fluid, consistent with the laws of hydrostatics. Again, these experiments showed that the net fluid force on the object was indeed *downward*. Bierman and Kincanon concluded that in the statement of Archimedes' principle involving the buoyant force; it should be stressed that the submerged object must be surrounded by the fluid and not simply submerged.

What is missing in the interpretation of the experimental results of Jones and Gordon and of Bierman and Kincanon is that these experiments do not measure the apparent weight of the object. What they measure is the force needed to separate the object from the bottom of the container. This is similar to a suction cup sticking to a tabletop, where the net fluid (atmosphere) force on it is downward. The force needed to lift the suction cup straight up is much greater than the weight of the suction cup. To measure the weight of the suction cup, it must be

placed on a scale, regardless of whether air is driven out from under it or not.

One year later, Graf [4] argued that the reading of a scale located at the bottom of a container is the same when a submerged block is balanced on a thin pin and the pin bottom rests on the scale (where there is buoyant force) and when the block rests on the scale without any fluid seepage between them (where there is no buoyant force). He then concluded that when an object denser than a fluid is submerged in it, the apparent weight of the object is the same regardless of whether the submerged object rests on the bottom of the container or not. However, Graf did not explain where the upward force in the latter case comes from. In what follows, we address this issue and explain where in this case the reduction of the apparent weight comes from.

Consider an object of any shape of mass m and volume V resting at the bottom of a container filled with a fluid of density D_f, as shown in **Figure 2(a)**. A scale similar to that described by Graf [4] is also placed at the bottom of the container, and its tare function is used to zero its reading. The region enclosed by the dashed line contains a volume of the fluid that is equal to the volume of the object.

We now move the object and place it on the scale, as shown in **Figure 2(b)**. There may or may not be fluid seepage between the object and the scale, which is immaterial. As a result, the weight of the object mg is added to the scale but, at the same time, the weight of the fluid in the dashed region is removed from the top of the scale. Therefore, the reading of the scale S will be

$$S = mg - D_f gV \tag{6}$$

where the second term on the right hand side is the weight of the fluid in the dashed region. Consequently, the apparent weight of the object is less than its true weight by exactly the buoyant force on the object as if it was completely surrounded by the fluid. This analysis clearly shows where the reduction in the apparent weight in this case comes from; it comes from removal of a volume of fluid, equal to the volume of the object, from the region directly above the scale.

4. Discussion and Summary

In this article, we have looked at Archimedes' principle from a different, but quite general, perspective in the context of Newton's third law of motion. When an object enters a fluid in a container, the height of the fluid increases, resulting in a higher hydrostatic pressure and hence a higher downward force on the bottom of the container. Then according to Newton's third law, the container-fluid system exerts an equal upward force on the object resulting in the reduction of its apparent weight, regardless of the position of the object in the fluid. We have also shown where the reduction of the apparent weight of a submerged object comes from, when the object rests on the bottom of the container with no fluid seepage between them. The analysis presented here helps clarify why Archimedes' principle works the way it does, and why a submerged object appears to be lighter even when the net fluid force on it is downward.

Finally, we point out that Archimedes' principle does not consider surface tension. In fact, presence of surface tension results in violation of the principle [21]. Furthermore, Archimedes' principle breaks down in complex fluids [22].

Acknowledgements

I would like to thank Richard W. Karwatka for carefully reviewing the manuscript and making helpful suggestions.

References

[1] Loverude, M.E., Kautz, C.H. and Heron, P.R.L. (2003) Helping Students Develop an Understanding of Archimedes' Principle. I. Research on Student Understanding. *American Journal of Physics*, **71**, 1178-1187. https://doi.org/10.1119/1.1607335

[2] Heron, P.R.L., Loverude, M.E., Shaffer, P.S. and McDermott, L.C. (2003) Helping Students Develop an Understanding of Archimedes' Principle. II. Development of Research-Based Instructional Materials. *American Journal of Physics*, **71**, 1188-1195. https://doi.org/10.1119/1.1607337

[3] Bierman, J. and Kincanon, E. (2003) Reconsidering Archimedes' Principle. *The Physics Teacher*, **41**, 340-344. https://doi.org/10.1119/1.1607804

[4] Graf, E.H. (2004) Just What Did Archimedes Say about Buoyancy? *The Physics Teacher*, **42**, 296-299. https://doi.org/10.1119/1.1737965

[5] Wicander, R. and Monroe, J.S. (2006) Essentials of Geology. 4th Edition, Thomson Brooks/Cole, Belmont, 239.

[6] Monroe, J.S. and Wicander, R. (2012) The Changing Earth, Exploring Geology and Evolution. 6th Edition, Brooks/Cole CENGAGE Learning, Belmont, 253.

[7] Mohazzabi, P. and James, M.C. (2012) A Simple Apparatus for Demonstrating Fluid Forces and Newton's Third Law. *The Physics Teacher*, **50**, 537-539. https://doi.org/10.1119/1.4767486

[8] Vermillion, R.E. (1991) Derivations of Archimedes' Principle. *American Journal of Physics*, **59**, 761-762. https://doi.org/10.1119/1.16763

[9] Leroy, B. (1985) Archimedes Principle: A Simple Derivation. *European Journal of Physics*, **6**, 56-57. https://doi.org/10.1088/0143-0807/6/1/107

[10] Halliday, D., Resnick, R. and Walker, J. (2005) Fundamentals of Physics. 7th Edition, Wiley, New York, 367-368.

[11] Sears, F.W. and Zemansky, M.W. (1960) College Physics. 3rd Edition, Addison-Wesley, Reading, 244.

[12] Duncan, W.J., Thom, A.S. and Young, A.D. (1970) Mechanics of Fluids. 2nd Edition, American Elsevier Publishing Company, New York, 24-25.

[13] Walshaw, A.C. and Jobson, D.A. (1972) Mechanics of Fluids. 2nd Edition, Longman, London, 2.

[14] Murray, R.L. and Cobb, G.C. (1970) Physics, Concepts and Consequences. Prentice-Hall, Englewood Cliffs, 371.

[15] Granger, R.A. (1995) Fluid Mechanics. Dover, New York, 127-128.

[16] Lantz, M.A., O'Shea, S.J. and Welland, M.E. (1997) Atomic-Force-Microscope Study of Contact Area and Friction on NbSe2. *Physical Review B*, **55**, 10776-10785. https://doi.org/10.1103/PhysRevB.55.10776

[17] Lantz, M.A., O'Shea, S.J. and Welland, M.E. (1997) Simultaneous Force and Conduction Measurements in Atomic Force Microscopy. *Physical Review B*, **56**, 15345-

15352. https://doi.org/10.1103/PhysRevB.56.15345

[18] Krim, J. (2002) Friction at Macroscopic and Microscopic Length Scales. *American Journal of Physics*, **70**, 890-897. https://doi.org/10.1119/1.1484153

[19] Jones, G.E. and Gordon, W.P. (1979) Removing the Buoyant Force. *The Physics Teacher*, **17**, 59-60. https://doi.org/10.1119/1.2340127

[20] Ray, J.R. and Johnson, E. (1979) Removing the Buoyant Force, a Follow-Up. *The Physics Teacher*, **17**, 392-393. https://doi.org/10.1119/1.2340279

[21] Falkovich, G., Weinberg, A., Denissenko, P. and Lukaschuk, S. (2005) Floater Clustering in a Standing Wave. *Nature*, **435**, 1045-1046. https://doi.org/10.1038/4351045a

[22] Wilson, R.M. (2012) Archimedes's Principle Gets Updated. *Physics Today*, **65**, 15. https://doi.org/10.1063/pt.3.1701

Scientific Research Publishing

Submit or recommend next manuscript to SCIRP and we will provide best service for you:

Accepting pre-submission inquiries through Email, Facebook, LinkedIn, Twitter, etc.
A wide selection of journals (inclusive of 9 subjects, more than 200 journals)
Providing 24-hour high-quality service
User-friendly online submission system
Fair and swift peer-review system
Efficient typesetting and proofreading procedure
Display of the result of downloads and visits, as well as the number of cited articles
Maximum dissemination of your research work

Submit your manuscript at: http://papersubmission.scirp.org/
Or contact jamp@scirp.org

Journal of Applied Mathematics and Physics, 2017, 5, 844-852
http://www.scirp.org/journal/jamp
ISSN Online: 2327-4379
ISSN Print: 2327-4352

The Exact Solution of the Space-Time Fractional Modified Kdv-Zakharov-Kuznetsov Equation

Qiuyan Jin[1], Tiecheng Xia[1,2*], Jinbo Wang[2]

[1]Department of Mathematics, Shanghai University, Shanghai, China
[2]Science and Technology on Communication Security Laboratory, Chengdu, China
Email: qiuyanjin815@163.com, *xiatc@shu.edu.cn, doctor03@163.com

How to cite this paper: Jin, Q.Y., Xia, T.C. and Wang, J.B. (2017) The Exact Solution of the Space-Time Fractional Modified Kdv-Zakharov-Kuznetsov Equation. *Journal of Applied Mathematics and Physics*, **5**, 844-852.
https://doi.org/10.4236/jamp.2017.54074

Received: March 3, 2017
Accepted: April 25, 2017
Published: April 28, 2017

Copyright © 2017 by authors and Scientific Research Publishing Inc.
This work is licensed under the Creative Commons Attribution International License (CC BY 4.0).
http://creativecommons.org/licenses/by/4.0/
Open Access

Abstract

In this paper, we get many new analytical solutions of the space-time nonlinear fractional modified KDV-Zakharov Kuznetsov (mKDV-ZK) equation by means of a new approach namely method of undetermined coefficients based on a fractional complex transform. These solutions have physics meanings in natural sciences. This method can be used to other nonlinear fractional differential equations.

Keywords

Analytical Solutions, the Space-Time Fractional Modified KDV-ZK Equation,Nonlinear Fractional Differential Equation, Modified Riemann-Liouville Derivative

1. Introduction

Nonlinear fractional differential equations (NFDEs) are universal models of the classical differential equations of integer order. In recent years, the fractional order derivative and integral is becoming a hot spot of international research; it can more accurately describe the nonlinear phenomena in physics. Such as chemical kinematics, chemical physics and geochemistry, communication, physics, biology, engineering, mathematics, diffusion processes in porous media, in vibrations in a nonlinear string, power-law non-locality, and power-law long-term memory can use NFDEs as models to express these problem [1] [2] [3] [4] [5]. In the last few years, it has become an important issue and matter of interest for researchers about the study of analytical and numerical solutions of fractional differential equations (FDEs). There are a lot of effective methods which can be used to study soliton, such as the fractional functional sub-equation method [6], the fractional modified trial equation method [7], the first integral method

[8], the fractional functional variable method [9], the extended tanh-function method [10], the (G'/G)-expansion method [11] [12] and so on.

The present article aims to find out the modified KDV-Zakharov Kuznetsov [13] [14] [15] equation's exact solutions by using named method of undetermined coefficients. The following is the organization of this paper. Some basic definitions and mathematical preliminaries of the fractional calculus are introduced in the next section. Investigated method of undetermined coefficients applied to solve fractional differential equations based on a fractional complex transform is presented in Section 3. In Section 4, we apply method of undetermined coefficients to the space-time nonlinear fractional modified KDV-ZK equation. Finally, we give some conclusions.

2. Basic Definitions

Fractional calculus is a generalization of classical calculus. There are a lot of approaches developed over years to generalize the concept of fractional order derivative, such as, Riemann-Liouville, Grünwald-Letnikow, Caputo [16], Kolwankar-Gangal, Oldham and Spanier, Miller and Ross, Cresson have presented many methods, and Jumnarie put forward a modified Riemann-Liouville derivative [17] [18].

In the section, the some properties and definitions of the modified Riemann-Liouville derivative that will be applied in the sequel of the work were given.

The following is the modified Riemann-Liouville derivative defined by Jumarie [17] [18]

$$D_t^{\alpha} f(t) = \begin{cases} \dfrac{1}{\Gamma(-\alpha)} \displaystyle\int_0^t (t-\xi)^{-\alpha-1} \left[f(\xi) - f(0) \right] \mathrm{d}\xi, & \alpha < 0, \\ \dfrac{1}{\Gamma(1-\alpha)} \dfrac{\mathrm{d}}{\mathrm{d}t} \displaystyle\int_0^t (t-\xi)^{-\alpha} \left[f(\xi) - f(0) \right] \mathrm{d}\xi, & 0 < \alpha < 1, \\ \left(f^{(n)}(t) \right)^{(\alpha-n)}, & n \le \alpha \le n+1, \ n \ge 1. \end{cases} \tag{1}$$

Remark1. $f: R \to R, t \to f(t)$ denote a continuous but not necessarily differentiable function.

The probability calculus, fractional Laplace problems, and fractional variational calculus successfully applied Jumarie's modified Riemann-Liouville derivative. To summarize a few useful formulae by Jumarie's modified Riemann-Liouville derivative in [17] [18], we give some properties as follows

$$D_t^{\alpha} t^{\gamma} = \frac{\Gamma(\gamma+1)}{\Gamma(\gamma+1-\alpha)} t^{\gamma-\alpha}, \quad \gamma > 0, \tag{2}$$

$$D_t^{\alpha} \left(c f(t) \right) = c D_t^{\alpha} f(t), \quad c = \text{constant}, \tag{3}$$

$$D_t^{\alpha} f\left[g(t) \right] = f_g'\left[g(t) \right] D_t^{\alpha} g(t), \tag{4}$$

$$D_t^{\alpha} f\left[g(t) \right] = D_g^{\alpha} f\left[g(t) \right] (g')^{\alpha}, \tag{5}$$

$$D_t^\alpha \left[af(t) + bg(t) \right] = aD_t^\alpha f(t) + bD_t^\alpha g(t). \tag{6}$$

Remark 2. J. H. He *et al.* in [19] modified the chain rule given by Equation (5) to the formula

$$D_t^\alpha f\left[g(t) \right] = \sigma_t' f_g'\left[g(t) \right] D_t^\alpha g(t), \tag{7}$$

where σ_t' is called the sigma indexes (see [19]). Therefore, Equation (5) is modified to the forms

$$D_t^\alpha f\left[g(t) \right] = \sigma_t' D_g^\alpha f\left[g(t) \right] (g')^\alpha. \tag{8}$$

3. Method of Undetermined Coefficients

In the section, we introduce the generally steps of method of undetermined coefficients

Step 1: We set a nonlinear fractional order partial differential equation as follows

$$P\left(u, D_t^\alpha u, D_x^\beta u, D_t^\alpha D_t^\alpha u, D_t^\alpha D_x^\beta u, D_x^\beta D_x^\beta u, \cdots \right) = 0,\ 0 < \alpha, \beta < 1 \tag{9}$$

where u is an unknown function about x, t two independent variables, $D_t^\alpha u, D_x^\alpha u$ modified Riemann-Liouville derivative of u, and P is a polynomial of u and its partial fractional derivatives, in which includes the highest order derivatives and the nonlinear terms.

Step 2: By using the traveling wave transformation

$$\begin{aligned} &u(x,t) = U(\xi), \\ &\xi = \frac{kx^\beta}{\Gamma(\beta+1)} - \frac{ct^\alpha}{\Gamma(\alpha+1)}, \end{aligned} \tag{10}$$

where k and c are non zero arbitrary constants. And by using the chain rule

$$\begin{aligned} D_t^\alpha u &= \sigma_t' \frac{\mathrm{d}U}{\mathrm{d}\xi} D_t^\alpha \xi, \\ D_x^\alpha u &= \sigma_x' \frac{\mathrm{d}U}{\mathrm{d}\xi} D_x^\alpha \xi, \end{aligned} \tag{11}$$

where σ_t' and σ_x' are called the sigma index. The sigma index usually is determined by gamma function [20]. In general, we can take $\sigma_t' = \sigma_x' = l$, where l is a constant.

Substituting (10) along with (2) and (11) into (9), we can rewrite Equation (9) in the following nonlinear ordinary differential equation

$$Q\left(U, U', U'', U''', \cdots \right) = 0, \tag{12}$$

where the prime denotes the derivative with respect to ξ. For the convenience of calculation, we should obtain a new equation by integrating Equation (12) term by term one or more times.

Step 3: By the following form [21], assume that solution of the Equation (14) can be represented

$$U(\xi) = A\mathrm{sech}^m \xi, \tag{13}$$

where A is nonzero constant, m is obtained by balancing the highest order term and nonlinear term of Equation (9) or Equation (12).

Step 4: Substituting the constant A and m into Equation (14), we can obtain the solution of the fractional order Equation (9).

4. The (3 + 1) Dimensional Space-Time Fractional mKDV-ZK Equation

In this current sub-section, we apply method of undetermined coefficients to solve the (3 + 1) dimensional space-time fractional mKDV-ZK equation of the form,

$$D_t^{\alpha}u + \mathrm{d}u^2u_x + eu_{xxx} + fu_{xyy} + gu_{xzz} = 0, \quad t > 0,\ 0 < \alpha < 1, \tag{14}$$

where d, e, f and g are nonzero constants, α is a parameter describing the order of the fractional space-time-derivative. When $f = 0$, $g = 0$, d, $e \neq 0$, Equation (14) is called the fractional modified KDV equation

$$D_t^{\alpha}u + \mathrm{d}u^2u_x + eu_{xxx} = 0, \quad t > 0,\ 0 < \alpha < 1, \tag{15}$$

when $\alpha = 1$, Equation (14) is called the modified KDV-ZK equation

$$u_t + \mathrm{d}u^2u_x + eu_{xxx} + fu_{xyy} + gu_{xzz} = 0, \quad t > 0. \tag{16}$$

The modified KDV-ZK equation is applied in many physical areas. Existence of the solutions for this equation has been considered in several papers, see references in [22] [23]. Next, we will obtain the non-topological soliton and dark soliton solutions to Equation (14) by method of undetermined coefficients [24] [25].

Therefore, we use the following transformations,

$$u(x, y, z, t) = U(\xi), \quad \xi = kx + py + qz - \frac{\lambda t^{\alpha}}{\Gamma(1+\alpha)}, \tag{17}$$

Where k, p, q, λ are nonzero constants.

Substituting Equation (17) with Equation (2) and Equation (11) into Equation (14), we have

$$-\lambda U' + kdU^2U' + k^3eU''' + kfp^2U''' + kgq^2U''' = 0, \tag{18}$$

where $\text{“}U'\text{”} = \dfrac{\mathrm{d}U}{\mathrm{d}\xi}$. By once integrating and setting the constants of integration to zero, we obtain

$$-\lambda U + \frac{kd}{3}U^3 + k\left(ek^2 + fp^2 + gq^2\right)U'' = 0. \tag{19}$$

4.1. The Non-Topological Soliton Solution

To get the non-topological soliton solution of Equation (19), we can make the assumption,

$$U(\xi) = A\operatorname{sech}^m\xi, \tag{20}$$

where

$$\xi = kx + py + qz - \frac{\lambda t^{\alpha}}{\Gamma(1+\alpha)}, \tag{21}$$

where k, p, q, λ are nonzero constants coefficients. The m is unknown at this point and will be determined later. From the Equation (20)-(21), we obtain

$$\frac{\mathrm{d}U(\xi)}{\mathrm{d}\xi} = -Am\operatorname{sech}^{m+1}\xi \sinh\xi, \tag{22}$$

and

$$\begin{aligned}\frac{\mathrm{d}^2U(\xi)}{\mathrm{d}\xi^2} &= -Am(m+1)\operatorname{sech}^{m}\xi(-\operatorname{sech}\xi\tanh\xi)\sinh\xi + \left(-Am\operatorname{sech}^{m+1}\xi\cosh\xi\right)\\ &= Am(m+1)\operatorname{sech}^{m+2}\xi\sinh^2\xi - Am\operatorname{sech}^{m}\xi\\ &= Am(m+1)\operatorname{sech}^{m+2}\xi\left(\frac{1}{\operatorname{sec}h^2\xi}-1\right) - Am\operatorname{sech}^{m}\xi\\ &= Am^2\operatorname{sech}^{m}\xi - Am(m+1)\operatorname{sech}^{m+2}\xi,\end{aligned} \tag{23}$$

and

$$U^3(\xi) = A^3\operatorname{sech}^{3m}\xi. \tag{24}$$

Thus, substituting the ansatz (23)-(27) into Equation (21), yields to

$$\begin{aligned}&-\lambda A\operatorname{sech}^{m}\xi + \frac{kd}{3}A^3\operatorname{sech}^{3m}\xi\\ &+k\left(ek^2 + fp^2 + gq^2\right)\left(Am^2\operatorname{sech}^{m}\xi - Am(m+1)\operatorname{sech}^{m+2}\xi\right) = 0.\end{aligned} \tag{25}$$

Now, from Equation (25), equating the exponents $m+2$ and $3m$ leads to

$$m+2 = 3m, \tag{26}$$

so that

$$m = 1. \tag{27}$$

From Equation (25), setting the coefficients of $\operatorname{sech}^{m+2}\xi$ and $\operatorname{sech}^{3m}\xi$ terms to zero, we obtain

$$\frac{kd}{3}A^3 - Ak\left(ek^2 + fp^2 + gq^2\right)m(m+1) = 0, \tag{28}$$

by using Equation (27) and after some calculations, we have

$$A = \pm\sqrt{\frac{6\left(ek^2 + fp^2 + gq^2\right)}{d}}. \tag{29}$$

We find, from setting the coefficients of $\operatorname{sech}^{m}\xi$ terms in Equation (25) to zero

$$-\lambda A + Am^2k\left(ek^2 + fp^2 + gq^2\right) = 0, \tag{30}$$

also we get

$$\lambda = k\left(ek^2 + fp^2 + gq^2\right). \tag{31}$$

From Equation (29), it is important to note that

$$d\left(ek^2+fp^2+gq^2\right)>0. \tag{32}$$

Thus finally, the 1-soliton solution of Equation (14) is given by:

$$u_1(x,y,z,t)=\sqrt{\frac{6\left(ek^2+fp^2+gq^2\right)}{d}}\operatorname{sech}\left(kx+py+qz-\frac{d\left(ek^2+fp^2+gq^2\right)t^{\alpha}}{\Gamma(1+\alpha)}\right), \tag{33}$$

$$u_2(x,y,z,t)=-\sqrt{\frac{6\left(ek^2+fp^2+gq^2\right)}{d}}\operatorname{sech}\left(kx+py+qz-\frac{d\left(ek^2+fp^2+gq^2\right)t^{\alpha}}{\Gamma(1+\alpha)}\right). \tag{34}$$

4.2. The Dark Soliton Solution

In order to start off with the solution hypothesis, we use the solitary wave ansatz of the form

$$U(\xi)=A\tanh^m\xi, \tag{35}$$

and

$$\xi=kx+py+qz-\frac{\lambda t^{\alpha}}{\Gamma(1+\alpha)}, \tag{36}$$

where k, p, q, λ are the free parameters. Also the m is unknown at this point and will be determined later.

From Equations (35)-(36), we obtain

$$\frac{\mathrm{d}U(\xi)}{\mathrm{d}\xi}=Am\left(\tanh^{m-1}\xi-\tanh^{m+1}\xi\right) \tag{37}$$

and

$$\frac{\mathrm{d}^2U(\xi)}{\mathrm{d}\xi^2}=Am\left\{(m-1)\tanh^{m-2}\xi-2m\tanh^m\xi+(m+1)\tanh^{m+2}\xi\right\}, \tag{38}$$

and

$$U^3(\xi)=A^3\tanh^{3m}\xi. \tag{39}$$

Substituting Equations (35)-(39) into Equation (19), gives

$$\begin{aligned}&-\lambda A\tanh^m\xi+\frac{kd}{3}A^3\tanh^{3m}\xi\\&+Amk\left(ek^2+fp^2+gq^2\right)\left\{(m-1)\tanh^{m-2}\xi\right.\\&\left.-2m\tanh^m\xi+(m+1)\tanh^{m+2}\xi\right\}=0.\end{aligned} \tag{40}$$

Now, from Equation (40), equating the exponents of $\tanh^{3m}\xi$ and $\tanh^{m+2}\xi$ gives,

$$3m=m+2, \tag{41}$$

which yields

$$m=1. \tag{42}$$

Setting the coefficients of $\tanh^{3m}\xi$ and $\tanh^{m+2}\xi$ terms in Equation (40)

to zero, we have

$$\frac{kd}{3}A^3 + Akm(m+1)\left(ek^2 + fp^2 + gq^2\right) = 0, \tag{43}$$

then, we get

$$A = \pm\sqrt{-\frac{6\left(ek^2 + fp^2 + gq^2\right)}{d}}. \tag{44}$$

Again, from Equation (40) setting the coefficients of $\tanh^m \xi$ terms to zero,

$$-\lambda A - 2m^2 Ak\left(ek^2 + fp^2 + gq^2\right) = 0, \tag{45}$$

and from Equation (45) we have

$$\lambda = -2k\left(ek^2 + fp^2 + gq^2\right). \tag{46}$$

Equation (46) prompts the constraint

$$d\left(ek^2 + fp^2 + gq^2\right) < 0. \tag{47}$$

Thus finally, the dark soliton solution for the (3 + 1) dimensional space-time fractional mKDV-ZK equation is given by:

$$u_3(x,y,z,t) = \sqrt{-\frac{6\left(ek^2 + fp^2 + gq^2\right)}{d}}\tanh\left(kx + py + qz + \frac{2k\left(ek^2 + fp^2 + gq^2\right)}{\Gamma(1+\alpha)}\right), \tag{48}$$

$$u_4(x,y,z,t) = -\sqrt{-\frac{6\left(ek^2 + fp^2 + gq^2\right)}{d}}\tanh\left(kx + py + qz + \frac{2k\left(ek^2 + fp^2 + gq^2\right)}{\Gamma(1+\alpha)}\right). \tag{49}$$

5. Conclusion

In this article, we have got the new solutions for the (3 + 1) dimensional space-time fractional mKDV-ZK equation by using the method of undetermined coefficients. Up to now, we could not find that these solutions were reported in other papers. In order to solve many systems of nonlinear fractional partial differential equations in mathematical and physical sciences, such as, the space-time fractional mBBM equation, the time fractional mKDV equation, the nonlinear fractional Zoomeron equation and so on, we can use the method of undetermined coefficients recommended herein would be general to a certain extent.

Acknowledgements

This work is in part supported by the Natural Science Foundation of China (Grant Nos. 11271008, 61072147).

References

[1] Baskonus, H.M. and Bulut, H. (2015) On the Numerical Solutions of Some Fractional Ordinary Differential Equations by Fractional Adams-Bashforth-Moulton Method. *Open Mathematics*, **13**, 547-556. https://doi.org/10.1515/math-2015-0052

[2] Bulut, H., Belgacem, F.B.M. and Baskonus, H.M. (2015) Some New Analytical Solutions for the Nonlinear Time-Fractional KdV-Burgers-Kuramoto Equation. *Advances in Mathematics and Statistical Sciences*, 118-129.

[3] Baskonus, H.M., Mekkaoui, T., Hammouch, Z. and Bulut, H. (2015) Active Control of a Chaotic Fractional Order Economic System. *Entropy*, **17**, 5771-5783. https://doi.org/10.3390/e17085771

[4] Cao, J. and Xu, C. (2013) A High Order Schema for the Numerical Solution of the Fractional Ordinary Differential Equations. *Journal of Computational Physics*, **238**, 154-168.

[5] Hammouch, Z. and Mekkaoui, T. (2012) Travelling-Wave Solutions for Some Fractional Partial Differential Equation by Means of Generalized Trigonometry Functions. *International Journal of Applied Mathematical Research*, **1**, 206-212.

[6] Guo, S., Mei, L., Li, Y. and Sun, Y. (2012) The Improved Fractional Sub-Equation Method and Its Applications to the Space-Time Fractional Differential Equations in Fluid Mechanics. *Physics Letters A*, **376**, 407-411.

[7] Gurefe, Y., Sonmezoglu, A. and Misirli, E. (2011) Application of the Trial Equation Method for Solving Some Nonlinear Evolution Equations Arising in Mathematical Physics. *Pramana-Journal of Physics*, **77**, 1023-1029. https://doi.org/10.1007/s12043-011-0201-5

[8] Taghizadeh, N., Mirzazadeh, M. and Samiei Paghaleh, A. (2012) The First Integral Method to Nonlinear Partial Differential Equations. *Applications and Applied Mathematics: An International Journal*, **7**, 117-132.

[9] Sun, H.G., Zhang, Y., Chen, W. and Reeves, D.M. (2014) Use of a Variable-Index Fractional-Derivative Model to Capture Transient Dispersion in Heterogenerous Media. *Journal of Contaminant Hydrology*, **157**, 47-58.

[10] Fan, E.G. (2000) Extended Tanh-Function Method and Its Applications to Nonlinear Equations. *Physics Letters A*, **277**, 212-218.

[11] Wang, M., Li, X. and Zhang, J. (2008) The (G'/G)-Expansion Method and Travelling Wave Solutions of Nonlinear Evolution Equations in Mathematical Physics. *Physics Letters A*, **372**, 417-423.

[12] Zhang, J., Wei, X. and Lu, Y. (2008) A Generalized (G'/G)-Expansion Method and Its Applications Evolution Equations in Mathematical Physics. *Physics Letters A*, **372**, 3653-3658.

[13] Biswas, A. and Zerrad, E. (2010) Solitary Wave Solution of the Zakharov-Kuznetsov Equation in Plasmas with Power Law Onolinearity. *Nonlinear Analysis B*, **11**, 3272-3274.

[14] Biswas, A. and Zerrad, E. (2009) 1-Soliton Solution of the Zakharov-Kuznetsov Equation with Dual-Power Law Nonlinerity. *Communications in Nonlinear Science and Numerical Simulation*, **14**, 3574-3577.

[15] Ebadi, G., Mojaver, A., Milovic, D., Johnson, S. and Biswas, A. (2012) Solitons and Other Solutions to the Quantum Zakharov-Kuznetsov Equation. *Astrophysics and Space Science*, **341**, 507-513.

[16] Oldham, K.B. and Spaniner, J. (1974) The Fractional Calculus. Academic Press, New York.

[17] Jumarie, G. (2012) An Approach to Differential Geometry of Fractional Order via Modified Riemann-Liouville Derivative. *Acta Mathematica Sinica, English Series*, **28**, 1741. https://doi.org/10.1007/s10114-012-0507-3

[18] Jumarie, G. (2006) Modified Riemann-Liouville Derivative and Fractional Taylor Series of Nondifferentiable Functions Further Results. *Computers & Mathematics with Applications*, **51**, 1367.

[19] He, J.H., Elagan, S.K. and Li, Z.B. (2012) Geometrical Explanation of the Fractional Complex Transform and Derivative Chain Rule for Fractional Calculus. *Physics Le-*

tters A, **376**, 257.

[20] Ibrahim, R.W. (2012) Fractional Complex Transforms for Fractional Differential Equations. *Advances in Difference Equations*, **2012**, 192. https://doi.org/10.1186/1687-1847-2012-192

[21] Kilbas, A.A., Srivastava, H.M. and Trujillo, J.J. (2006) Theory and Application of Fractional Differential Equations. Elsevier, New York.

[22] Matebese, B.T., Adem, A.R., Khalique, C.M. and Biswas, A. (2011) Solutions to Zakharov-Kuznetsov Equation with Power Law Nonlinearity in (1+3)-Dimensions. *Physics of Wave Phenomena*, **19**, 148-154. https://doi.org/10.3103/S1541308X11020117

[23] Lslam, M.H., Khan, K., Ali Akbar, M. and Salam, M.A. (2014) Exact Traveling Wave Solutions of Modified Kdv-Zakharov-Kuznetsov Equation and Viscous Burger Equation. *Springer Plus*, **3**, 105. https://doi.org/10.1186/2193-1801-3-105

[24] Guner, O., Bekir, A., Moraru, L. and Biswas, A. (2015) Bright and Dark Soliton Solutions of the Generalized Zakharov-Kuznetsov-Benjamin-Bona-Mahoney Nonlinear Evolution Equation, Dark Soliton and Periodic Wave Solutions of Nonlinear Evolution Equations. *Proceedings of the Romanian Academy*, **16**, 422-429.

[25] Bakodah, H.O., Al Qarni, A.A., Banaja, M.A., Zhou, Q., Moshokoa, S.P. and Biswas, A. (2017) Bright and Dark Thirring Optical Solitons with Improved Adomian Decomposition Scheme. *Optik*, **130**, 1115-1123.

Scientific Research Publishing

Submit or recommend next manuscript to SCIRP and we will provide best service for you:

Accepting pre-submission inquiries through Email, Facebook, LinkedIn, Twitter, etc.
A wide selection of journals (inclusive of 9 subjects, more than 200 journals)
Providing 24-hour high-quality service
User-friendly online submission system
Fair and swift peer-review system
Efficient typesetting and proofreading procedure
Display of the result of downloads and visits, as well as the number of cited articles
Maximum dissemination of your research work

Submit your manuscript at: http://papersubmission.scirp.org/
Or contact jamp@scirp.org

Journal of Applied Mathematics and Physics, 2017, 5, 853-861
http://www.scirp.org/journal/jamp
ISSN Online: 2327-4379
ISSN Print: 2327-4352

Kinematic Relativity of Quantum Mechanics: Free Particle with Different Boundary Conditions

Gintautas P. Kamuntavičius [1], G. Kamuntavičius [2]

[1]Department of Physics, Vytautas Magnus University, Kaunas, Lithuania
[2]Christ's College, University of Cambridge, Cambridge, UK
Email: gintautas.kamuntavicius@vdu.lt

How to cite this paper: Kamuntavičius, G.P. and Kamuntavičius, G. (2017) Kinematic Relativity of Quantum Mechanics: Free Particle with Different Boundary Conditions. *Journal of Applied Mathematics and Physics*, **5**, 853-861.
https://doi.org/10.4236/jamp.2017.54075

Received: March 16, 2017
Accepted: April 27, 2017
Published: April 30, 2017

Copyright © 2017 by authors and Scientific Research Publishing Inc.
This work is licensed under the Creative Commons Attribution International License (CC BY 4.0).
http://creativecommons.org/licenses/by/4.0/

Open Access

Abstract

An investigation of origins of the quantum mechanical momentum operator has shown that it corresponds to the nonrelativistic momentum of classical special relativity theory rather than the relativistic one, as has been unconditionally believed in traditional relativistic quantum mechanics until now. Taking this correspondence into account, relativistic momentum and energy operators are defined. Schrödinger equations with relativistic kinematics are introduced and investigated for a free particle and a particle trapped in the deep potential well.

Keywords

Special Relativity, Quantum Mechanics, Relativistic Wave Equations, Solutions of Wave Equations: Bound States

1. Introduction

The known attempts to apply the ideas of special relativity theory (SRT) in quantum mechanics, formulated in the third decade of 20-th century and present in numerous textbooks, are based on using the quantum mechanical momentum operator $\hat{p} = -i\hbar\nabla$ in the nonrelativistic Schrödinger equation for the free particle with the Hamiltonian corresponding to the classical SRT expression for energy:

$$E = \sqrt{m^2c^4 + p^2c^2} = mc^2 + \frac{p^2}{2m} - \frac{p^4}{8m^3c^2} + \cdots \quad (1)$$

The first term of this expansion mc^2 is constant in an arbitrary reference frame, hence it can be considered as part of the potential, defined with an accuracy up to a constant. The second term in the right hand side looks like the

nonrelativistic kinetic energy, hence the third one is the first order correction.

The modified Schrödinger equation with relativistic kinematics becomes

$$i\hbar\frac{\partial}{\partial t}\Psi = \hat{E}\Psi. \tag{2}$$

The accepted treatment of operator present in left hand side $i\hbar\frac{\partial}{\partial t}$ is that it is associated with the total relativistic energy, *i.e.*

$$\hat{E} = i\hbar\frac{\partial}{\partial t}. \tag{3}$$

However, this Schrödinger equation with relativistic kinematics does not correspond to the requirement that the operator of relativistic equation has to be invariant in respect of Lorentz transformations. Two possible solutions of this problem are known. The first one gives the Klein-Gordon equation, following directly from square of total energy of free particle expression applying defined quantum mechanical operators $\hat{p}$ and $\hat{E}$:

$$\left(\Delta - \frac{\partial^2}{\partial(ct)^2}\right)\Psi = \left(\frac{mc}{\hbar}\right)^2\Psi. \tag{4}$$

Right hand side of this equation is invariant in any reference system, so the problem of Lorentz invariance is satisfied and the eigenfunctions of equation transform according to the irreducible representations of the Lorentz group.

The other method is introduced by Dirac. He postulated the possibility of quantum operator $\hat{E}$ linearization, *i.e.* presentation in form

$$\hat{E} = \beta_1\hat{p}_x + \beta_2\hat{p}_y + \beta_3\hat{p}_z + \beta_4, \tag{5}$$

where β_j is fourth order matrices. The conditions for these matrices follow from square of relativistic energy expression, present in operator form:

$$\hat{E}^2 = \hat{p}^2c^2 + m^2c^4. \tag{6}$$

Finally, the Dirac equation, satisfying invariance in respect of Lorentz transformations, is

$$i\hbar\frac{\partial}{\partial t}\Psi = \left(\beta_1\hat{p}_x + \beta_2\hat{p}_y + \beta_3\hat{p}_z + \beta_4\right)\Psi. \tag{7}$$

In this paper, we show the statements applied for these equations' construction are problematic and an alternative way is necessary. We challenge the existing ideas by defining quantum mechanical momentum and energy operators as corresponding to classical, rather than the relativistic momentum and energy correspondingly. The new definition of operators is then further inspected solving the well-known problems for a free particle and particle trapped in the deep potential well.

2. Main Points of Classical SRT and Quantization

For successful quantization, first the main equations of SRT have to be present

in terms of momenta instead of velocities. The Lorentz factor:

$$\gamma = \left(1-\left(v/c\right)^2\right)^{-1/2} = \left(1-\left(p_0/mc\right)^2\right)^{-1/2}, \tag{8}$$

hence the relativistic momentum $p = \gamma mv$, expressed in terms of nonrelativistic one $p_0 = mv$, is

$$p = p_0\left(1-\left(p_0/mc\right)^2\right)^{-1/2}. \tag{9}$$

This expression, essential for relativistic dynamics, defines relativistic momentum, approaching infinity at $p_0 \to mc$ and undefined for larger values of p_0, hence satisfying the condition $p_0 < mc$, following from the usual $v < c$.

The quantum operator $-i\hbar\nabla$ is without any dependence on speed of light, its eigenvalues are not restricted, hence it demonstrates the correspondence to p_0 rather than to the relativistic momentum p. Moreover, the origin of this operator is nonrelativistic, because it appears in quantum mechanics at least in three different ways, following directly from classical mechanics.

The first one, suggested by Dirac [1], applies Poisson brackets of Lagrangian dynamics for canonical coordinate and momentum, proportional to the imaginary constant. The postulation that corresponding operators of quantum dynamics have to satisfy the analogous condition

$$\left[x_i, \hat{p}_j\right] = i\hbar\delta_{ij} \tag{10}$$

gives

$$\hat{p}_j = -i\hbar\frac{\partial}{\partial x_j}. \tag{11}$$

The second way of introducing this operator follows from de Broglie wave [2] definition

$$\psi_p\left(x,t\right) = \left(2\pi\hbar\right)^{-1/2}\exp\left(-\frac{i}{\hbar}\left(\frac{p^2}{2m}t - px\right)\right). \tag{12}$$

The equation, whose solutions are these waves, is the Schrödinger equation for free nonrelativistic particle. This can be demonstrated by taking the time derivative

$$i\hbar\frac{\partial}{\partial t}\psi_p\left(x,t\right) = \frac{p^2}{2m}\psi_p\left(x,t\right) \tag{13}$$

and two coordinate derivatives

$$-\frac{\hbar^2}{2m}\frac{\partial^2}{\partial x^2}\psi_p\left(x,t\right) = \frac{p^2}{2m}\psi_p\left(x,t\right). \tag{14}$$

The right hand sides of both equations coincide, hence the de Broglie wave and arbitrary superpositions of these waves are solutions of the Schrödinger equation. Obviously, the conclusion follows that the operator $-i\hbar\partial/\partial x$ corresponds to the nonrelativistic momentum and $i\hbar\partial/\partial t$ is the quantum operator of nonrelativistic kinetic energy $p^2/2m$.

The third method of momentum operator definition follows from translations

in the space generator

$$\hat{P}(a)=\exp\left(a\frac{\mathrm{d}}{\mathrm{d}x}\right) \tag{15}$$

definition and momentum conservation law [1]. Action of this operator gives the translation of argument:

$$\hat{P}(a)\psi(x)=\psi(x+a). \tag{16}$$

Intrinsic Hamiltonian of a quantum system is invariant in respect of translations. As a result it gives the center of mass of the system momentum conservation, hence the momentum operator is proportional to the derivative of the corresponding variable. Again, this is the classical momentum.

Therefore, the consideration of origins of the quantum mechanical momentum operator leads to the conclusion that it cannot be associated with relativistic momentum $p=\gamma mv$, having characteristic dependence on speed of light and present in the classical relativity expression $E^2=c^2p^2+m^2c^4$. The relativistic momentum operator can be expressed in terms of the nonrelativistic one as

$$\begin{aligned}\hat{p}&=\hat{p}_0\left(1-\left(\hat{p}_0/mc\right)^2\right)^{-1/2}\\&=\hat{p}_0\sum_{k=0}^{\infty}\binom{2k}{k}\left(\frac{\hat{p}_0}{2mc}\right)^{2k},\end{aligned} \tag{17}$$

where $\binom{n}{k}=\frac{n!}{k!(n-k)!}$ is the binomial coefficient.

Now the relativistic momentum operator obtains the necessary dependence on c. Both operators have the same system of eigenfunctions but different corresponding sets of eigenvalues, expressible in the same way, as operators.

The relativistic energy of particle, moving in a laboratory reference frame with constant velocity v, equals

$$E=\gamma mc^2=mc^2\left(1-\frac{2T_0}{mc^2}\right)^{-1/2}. \tag{18}$$

Here again one has the characteristic for SRT energy dependence on velocity. At $T_0=mv^2/2$ approaching $mc^2/2$, the energy takes infinite value, hence it is defined only for smaller, allowed by SRT, values of nonrelativistic kinetic energy. The corresponding quantum mechanical operator is

$$\hat{E}=mc^2\sum_{k=0}^{\infty}\binom{2k}{k}\left(\frac{\hat{T}_0}{2mc^2}\right)^{k}, \tag{19}$$

where

$$\hat{T}_0=-\frac{\hbar^2}{2m}\Delta \tag{20}$$

is the nonrelativistic kinetic energy operator. The above consideration and conclusions concerning the relativistic momentum are valid for the eigenvalues and eigenfunctions of the relativistic energy operator.

The relativistic kinetic energy operator $\hat{T}$ can be expressed in terms of the

nonrelativistic one as

$$\hat{T} = \hat{E} - mc^2 = mc^2 \sum_{k=1}^{\infty} \binom{2k}{k} \left(\frac{\hat{T}_0}{2mc^2} \right)^k . \tag{21}$$

In terms of momentum operators, the total relativistic energy operator of a free particle is

$$\hat{E} = mc^2 \sum_{k=0}^{\infty} \binom{2k}{k} \left(\frac{\hat{p}_0}{2mc} \right)^{2k} . \tag{22}$$

Obviously, this expression contains only even degrees of the momentum operator and hence cannot be linearized in terms of $\hat{p}_0$.

Moreover, in the most popular in traditional applications equation

$$\hat{E}^2 = \hat{p}^2 c^2 + m^2 c^4 \tag{23}$$

relativistic energy and momentum operators are present, not the nonrelativistic ones, applied deriving mentioned above Klein-Gordon and Dirac equations. Taking proper operators, this equation appears as identity, because

$$\hat{\gamma}^2 \left(mc^2 \right)^2 - \hat{\gamma}^2 \left(\hat{p}_0 c \right)^2 \equiv \left(mc^2 \right)^2 . \tag{24}$$

Finally, consider the expansion of the relativistic energy operator in terms of the relativistic momentum operator:

$$\hat{E} = \left(\hat{p}^2 c^2 + m^2 c^4 \right)^{1/2} = mc^2 + \frac{\hat{p}^2}{2m} - \frac{\hat{p}^4}{8m^3 c^2} + \cdots \tag{25}$$

If the second term in the right hand side is considered to be the nonrelativistic kinetic energy (as believed in mentioned approaches), we arrive at a strange, not consistent with SRT conclusion that the correction of this is negative, *i.e.* the relativistic kinetic energy of the particle is smaller than the nonrelativistic one. From the definition of the relativistic kinetic energy operator (21) it follows that the expectation value of relativistic kinetic energy, as necessary, is always larger than the nonrelativistic.

3. Relativistic Kinematics

Therefore, the present arguments have shown that the problem of relativistic dynamics application in quantum mechanics needs deeper investigation. The SRT considers free particles, therefore this problem works best for the start of SRT application in quantum mechanics.

From the Schrödinger equation for a free particle and present arguments it follows that two quantum mechanical operators—the first, dependent on time variable $i\hbar\partial/\partial t$, and the second, dependent on radius vector $-\hbar^2\Delta/2m$, are associated with the nonrelativistic kinetic energy of particle under consideration. Let us mark them as $\hat{T}_0(t)$ and $\hat{T}_0(\boldsymbol{r})$ correspondingly. Taking this into account opens two different possibilities for the same relativistic kinetic energy operator presentation:

$$\hat{T}(t) = mc^2 \left[\left(1 - \frac{2\hat{T}_0(t)}{mc^2} \right)^{-1/2} - 1 \right] \tag{26}$$

and

$$\hat{T}(\boldsymbol{r}) = mc^2\left[\left(1-\frac{2\hat{T}_0(\boldsymbol{r})}{mc^2}\right)^{-1/2}-1\right]. \tag{27}$$

Due to equivalence of introduced operators one can define the eigenvalues equation as

$$\hat{T}(t)\Psi(\boldsymbol{r},t) = \hat{T}(\boldsymbol{r})\Psi(\boldsymbol{r},t). \tag{28}$$

Let us call this the relativistic Schrödinger equation. The essential part of equation, independent of speed of light, is the Schrödinger equation for free particle:

$$\hat{T}_0(t)\Psi_0(\boldsymbol{r},t) = \hat{T}_0(\boldsymbol{r})\Psi_0(\boldsymbol{r},t). \tag{29}$$

Taking into account the expansions for these operators like given in Equation (21), one can present Equation (28) as

$$\sum_{k=1}^{\infty}\binom{2k}{k}\left(\frac{1}{2mc^2}\right)^k\left[\hat{T}_0^k(t)-\hat{T}_0^k(\boldsymbol{r})\right]\Psi(\boldsymbol{r},t) = 0. \tag{30}$$

After some transformation of commuting, due to dependence on different variables, the kinetic energy operators the equation takes the simplified form

$$\left[\sum_{k=1}^{\infty}\binom{2k}{k}\left(\frac{1}{2mc^2}\right)^k\sum_{j=1}^{k-1}\hat{T}_0^j(t)\hat{T}_0^{k-1-j}(\boldsymbol{r})\right]\left[\hat{T}_0(t)-\hat{T}_0(\boldsymbol{r})\right]\Psi(\boldsymbol{r},t) = 0, \tag{31}$$

leading to the conclusion that the eigenfunctions of the relativistic equation are the same as the corresponding eigenfunctions of the nonrelativistic equation, *i.e.*:

$$\Psi(\boldsymbol{r},t) = \Psi_0(\boldsymbol{r},t). \tag{32}$$

Due to separability of operators of both nonrelativistic and relativistic equations, the eigenfunctions are presentable as products of functions, dependent on time and spatial variables:

$$\Psi(\boldsymbol{r},t) = \Psi_{\mathcal{E}}(\boldsymbol{r})\Psi_{\mathcal{E}}(t). \tag{33}$$

As usual these functions are defined as eigenfunctions of corresponding stationary equations

$$\hat{T}(\boldsymbol{r})\Psi_{\mathcal{E}}(\boldsymbol{r}) = \mathcal{E}\Psi_{\mathcal{E}}(\boldsymbol{r}) \tag{34}$$

and

$$\hat{T}(t)\Psi_{\mathcal{E}}(t) = \mathcal{E}\Psi_{\mathcal{E}}(t). \tag{35}$$

The eigenfunctions of these operators are identical to the eigenfunctions of corresponding stationary nonrelativistic equations, but their eigenvalues are different. If we define the eigenvalue of the nonrelativistic equation as E, the eigenvalue of the relativistic equation, corresponding to the same eigenfunction, is

$$\frac{\mathcal{E}}{mc^2} = \left(1-\frac{2E}{mc^2}\right)^{-1/2}-1. \tag{36}$$

Due to the upper bound for nonrelativistic kinetic energy $E < mc^2/2$, this

equation implies that the set of eigenvalues of the relativistic stationary equation is restricted in comparison to the nonrelativistic set. This fact corresponds very well with the spirit of SRT.

To investigate the discrete spectrum, consider the problem of a free particle, trapped in the spherical well with impenetrable walls. The nonrelativistic stationary Schrödinger equation is

$$\hat{T}_0\left(r\theta\varphi\right)\psi_{nl\mu}\left(r\theta\varphi\right)=E_{nl}^{(0)}\psi_{nl\mu}\left(r\theta\varphi\right), \tag{37}$$

where

$$\hat{T}_0\left(r\theta\varphi\right)=-\frac{\left(\hbar c\right)^2}{2mc^2}\left[\frac{1}{r}\frac{\partial^2}{\partial r^2}r-\frac{\hat{L}^2\left(\theta\varphi\right)}{r^2}\right]. \tag{38}$$

Here and further, for the sake of simplicity, the conversion factor $\hbar c=197.3269788(12)$ MeVfm, as defined in [3], and rest energy of particle expressed in electronvolts, are used. For wave functions, written in spherical harmonics

$$\psi_{nl\mu}\left(r\theta\varphi\right)=u_{nl}\left(r\right)Y_{l\mu}\left(\theta\varphi\right), \tag{39}$$

the boundary condition is:

$$u_{nl}\left(r\right)=0 \text{ if } r=R, \tag{40}$$

where R is the radius of the spherical well. The solutions of this equation are the spherical Bessel functions. Boundary conditions define the spectrum of the nonrelativistic Schrödinger equation.

The Schrödinger equation with the relativistic kinetic energy operator has the same eigenfunctions but different corresponding eigenenergies:

$$\frac{\mathcal{E}_{nl}}{mc^2}=\left(1-\frac{2E_{nl}}{mc^2}\right)^{-1/2}-1. \tag{41}$$

Obviously, in the nonrelativistic approximation $\left(E_{nl}\ll mc^2/2\right)$, as necessary, $\mathcal{E}_{nl}\to E_{nl}$.

For angular momentum $l=0$ the solutions can be presented in analytical form:

$$E_{n0}=\frac{1}{2mc^2}\left(\frac{\pi\hbar c}{2R}\right)^2 n^2, n=1,2,3,\cdots, \tag{42}$$

and

$$\frac{\mathcal{E}_{n0}}{mc^2}=\left(1-\left(\frac{\pi\hbar c}{2Rmc^2}\right)^2 n^2\right)^{-1/2}-1. \tag{43}$$

This expression demonstrates that in a spherical well with impenetrable walls, the only allowed states are those corresponding to the quantum number

$$n<\frac{2Rmc^2}{\pi\hbar c}. \tag{44}$$

This does not exclude a case where there are no allowed states at all in such a well. It happens when $Rmc^2<\pi\hbar c/2$. Taking the given above value of conver-

sion factor, the right hand side of condition equals approximately 310 MeVfm Radius of well multiplied by mass of particle has to be larger than this value for at least one bound state to exist. On the other hand, in a corresponding nonrelativistic well there is an infinite number of bound states at any radius of well and mass of particle.

4. Conclusions

The operator of the introduced Schrödinger equation with relativistic kinematics is not invariant in respect of Lorentz transformations and from our consideration, it follows that construction of such operators, if possible, is immensely difficult. However, the Lorentz invariant theory is necessary for the description of ultrarelativistic processes and problems, like high energy phenomena obtainable in universe or the reactions in colliders. At high relativistic velocities, and hence high kinetic energies, the most interesting interactions among particles, responsible for surrounding us world structure and development, cannot play a remarkable role.

Therefore, the most actual applications of low energies quantum mechanics are obtained by solving the stationary Schrödinger equation, giving qualified description of bound states and excitation spectra of different quantum systems in huge energy intervals. Now, when experimental equipment is able to analyze different structures and phenomena with very high precision, the role played by relativistic effects stays remarkable and has to be investigated in a proper way. The first step in this direction is investigation of the stationary Schrödinger equation with the relativistic kinetic energy operator instead of the nonrelativistic one, present in the original equation. The obtained slight enough modifications of corresponding results of the original Schrödinger equation in low energies limit demonstrate high quality of nonrelativistic approach. In the larger energies region, the introduced innovation produces significant spectrum modifications and opens new possibilities for old problems of relativistic quantum mechanics solution.

The consideration of relativistic momentum operator, present in the known SRT equation $E^2 = m^2c^4 + p^2c^2$, as classical momentum leads to the conclusion that the first order correction of the nonrelativistic kinetic energy has the negative sign (Equation (1)), which means the expectation value of relativistic kinetic energy is smaller than the nonrelativistic one. This result, until now existing in applications for relativistic effects evaluation in atomic [3] and nuclear theory [4], creates "softer" than necessary kinetic energy and allows strange decisions concerning relativistic corrections of binding energies and excitations spectra of these quantum systems.

Our definition of the relativistic momentum operator classifies Klein-Gordon and Dirac equations as not completely relativistic. They are both invariant in respect of Lorentz transformations, but apply the definition of the nonrelativistic momentum operator instead of the relativistic one. This approach eliminates from equations basic for SRT dependence of relativistic energy and relativistic momentum on velocity, defined by Lorentz factor. Moreover, the Dirac equation

does not contain any input information about the electron, hence predicts the spin, equal $\hbar/2$, for all particles without any exemptions. The equation for free particle (7) in the nonrelativistic limit has to be consistent with corresponding Schrödinger equation, however, this cannot be established. The operator in front of the eigenfunction of right-hand side of this equation, seen as the relativistic free particle Hamiltonian, predicts the velocity of particle, equal to the speed of light c [2]. Finally, the Dirac equation is undefined for two- and more-particles system.

Therefore, new ideas of SRT application in quantum mechanics are necessary. As will be shown in following publications, our approach is applicable for the many-particle system and in the low kinetic energies approximation, reproduces the results of the corresponding nonrelativistic Schrödinger equation.

References

[1] Dirac, P.A.M. (1958) The Principles of Quantum Mechanics. Clarendon Press, Oxford.

[2] Messiah, A. (1965) Quantum Mechanics. Vol. 1, North-Holland, Amsterdam.

[3] Mohr, P.J., Newell, D.B. and Taylor, B.N. (2016) CODATA Recommended Values of the Fundamental Physical Constants: 2014. *Reviews of Modern Physics*, **88**, Article ID: 035009. https://doi.org/10.1103/RevModPhys.88.035009

[4] Carlson, J. and Schiavilla, R. (1998) Structure and Dynamics of Few-Nucleon Systems. *Reviews of Modern Physics*, **70**, 743-841. https://doi.org/10.1103/RevModPhys.70.743

Scientific Research Publishing

Submit or recommend next manuscript to SCIRP and we will provide best service for you:

Accepting pre-submission inquiries through Email, Facebook, LinkedIn, Twitter, etc.
A wide selection of journals (inclusive of 9 subjects, more than 200 journals)
Providing 24-hour high-quality service
User-friendly online submission system
Fair and swift peer-review system
Efficient typesetting and proofreading procedure
Display of the result of downloads and visits, as well as the number of cited articles
Maximum dissemination of your research work

Submit your manuscript at: http://papersubmission.scirp.org/
Or contact jamp@scirp.org

Scientific Research Publishing

Journal of Applied Mathematics and Physics, 2017, 5, 862-872
http://www.scirp.org/journal/jamp
ISSN Online: 2327-4379
ISSN Print: 2327-4352

Gravitation as Geometry or as Field

Walter Petry

Mathematical Institute of the University Duesseldorf, Duesseldorf, Germany
Email: wpetry@meduse.de

How to cite this paper: Petry, W. (2017) Gravitation as Geometry or as Field. *Journal of Applied Mathematics and Physics*, **5**, 862-872.
https://doi.org/10.4236/jamp.2017.54076

Received: January 22, 2017
Accepted: April 27, 2017
Published: April 30, 2017

Copyright © 2017 by author and Scientific Research Publishing Inc.
This work is licensed under the Creative Commons Attribution International License (CC BY 4.0).
http://creativecommons.org/licenses/by/4.0/

Open Access

Abstract

General relativity (GR) and gravitation in flat space-time (GFST) are covariant theories to describe gravitation. The metric of GR is given by the form of proper-time and the metric of GFST is a flat space-time form different from that of proper-time. The source of GR is the matter tensor and the Einstein tensor describes the gravitational field. The source of GFST is the total energymomentum including gravitation. The field is described by a non-linear differential operator of order two in divergence form. The results of the two theories agree for weak gravitational fields to the order of measurable accuracy. It is well-known that homogeneous, isotropic, cosmological models of GR start from a point singularity of the universe, the so called big bang. The density of matter is infinite. Therefore, our observable big universe implies an expansion of space, in particular an inflationary expansion in the beginning. Doubts are stated because infinities don't exist in physics. An explanation to the present, controversial discussion of expanding accelerating or non-accelerating universe as well as non-expanding universe is given. GFST starts in the beginning from a homogeneous, isotropic universe with uniformly distributed energy and no matter. In the course of time matter is created out of energy where the total energy is conserved. There is no singularity, *i.e.* no big bang. The space is flat and non-expanding.

Keywords

Gravitation, Cosmology, Flat Space, No Singularity, No Big Bang, Non-Expanding Universe

1. Introduction

Einstein's general theory of relativity is at present the most accepted theory of gravitation. The theory gives for weak gravitational fields, agreement with the corresponding experimental results. But the results for homogeneous, isotropic, cosmological models imply difficulties. So, the universe starts from a point singularity, *i.e.* the universe starts from a point with infinite density of matter. The

observed universe is very big. Hence, the space of the universe must expand very quickly which implies the introduction of an inflationary universe in the beginning. There are controversial discussions about the universe, e.g. is the universe accelerating or not. GFST uses a pseudo-Euclidean geometry and the proper time is defined similar to that of general relativity, *i.e.* space-time and proper time are different from one another. GFST starts from an invariant Lagrangian which gives by standard methods, the field equations of gravitation. The source is the total energy-momentum tensor including gravitation. The energy-momentum of gravitation is a tensor. The field is described by non-linear differential equations of order two in divergence form. The theory is generally covariant. The gravitational equations together with the conservation law of the total energy-momentum give the equations of motion for matter. The application of the theory implies for weak gravitational fields the same results as GR to experimental accuracy, e.g. gravitational red shift, deflection of light, perihelion precession, radar time delay, post-Newtonian approximation, gravitational radiation of a two-body system and the precession of the spin axis of a gyroscope in the orbit of a rotation body. But there are also differences of the results of these two theories. GFST gives non-singular, cosmological models. The covariance of GFST and the existence of non-singular cosmological models imply the possibility to interpret the solutions as expanding or as non-expanding space yielding an accelerating resp. non-expanding universe. GFST may e.g. be found in the book [1] and in the cited references. Additionally, non-singular, cosmological models are e.g. given in the articles [2] [3] [4] [5] [6].

Subsequently, homogeneous, isotropic, cosmological models will be summarized. Let us use the pseudo-Euclidean geometry. The resulting universe is non-singular under the assumption that the sum of the density parameters is greater than one, e.g. a little bit greater than one. It starts without matter and without radiation and all the energy is gravitational energy. Matter and radiation emerge from this energy by virtue of the conservation of the total energy. The space is flat and the interpretation of a non-expanding space is natural. But it is also possible to state an expansion of space by a suitable transformation as consequence of general covariance of the equations. Matter and radiation are generated from the beginning of the universe and the universe becomes hot. A certain time after the beginning matter and radiation decrease and the universe converges to dark energy as time goes to infinity. Hence, a universe given by GFST appears more natural than that received by GR which gives singular solution with infinite densities. The geometry of GR is in general non-Euclidean but the observed universe implies a flat space.

GR is well-known in contrast to GFST. Therefore, GFST and resulting cosmological models are shortly summarized in the next two sections. All these results can be found in the article [5].

Section 2 contains GFST; Section 3 contains cosmological models; Section 4 contains GR and Section 5 states GFST. Cosmological models of GR and GFST are compared with one another.

2. GFST

The theory of GFST is shortly summarized. The metric is the flat space-time given by

$$(\mathrm{d}s)^2 = -\eta_{ij}\mathrm{d}x^i \tag{1}$$

where (η_{ij}) is a symmetric tensor. Pseudo-Euclidean geometry has the form

$$(\eta_{ij}) = (1,1,1,-1). \tag{2}$$

Here, $(x^i) = (x^1, x^2, x^3)$ are the Cartesian coordinates and $x^4 = ct$. Let

$$\eta = \det(\eta_{ij}). \tag{3}$$

The gravitational field is described by a symmetric tensor (g_{ij}). Let (g^{ij}) be defined by

$$g_{ik}g^{kj} = \delta_i^j \tag{4}$$

and put similarly to (3)

$$G = \det(g_{ij}). \tag{5}$$

The proper time τ is defined by

$$(c\mathrm{d}\tau)^2 = -g_{ij}\mathrm{d}x^i\mathrm{d}x^j. \tag{6}$$

The Lagrangian of the gravitational field is given by

$$L(G) = -\left(\frac{-G}{-\eta}\right)^{1/2} g_{ij}g_{kl}g^{mn}\left(g^{ik}_{/m}g^{jl}_{/n} - \frac{1}{2}g^{ij}_{/m}g^{kl}_{/n}\right) \tag{7}$$

where the bar/denotes the covariant derivative relative to the flat space-time metric (1).

The Lagrangian of dark energy (given by the cosmological constant Λ) has the form

$$L(\Lambda) = -8\Lambda\left(\frac{-G}{-\eta}\right)^{1/2}. \tag{8}$$

Let

$$\kappa = 4\pi k/c^4 \tag{9}$$

and of matter of a perfect fluid are where κ is the gravitational constant. Then, the mixed energy-momentum tensor of gravitation, of dark energy and of matter of a perfect fluid are

$$T(G)^i_j = \frac{1}{8\kappa}\left[\left(\frac{-G}{-\eta}\right)^{1/2} g_{kl}g_{mn}g^{ir}\left(g^{km}_{/j}g^{ln}_{/r} - \frac{1}{2}g^{kl}_{/j}g^{mn}_{/r}\right) + \frac{1}{2}\delta^i_j L(G)\right] \tag{10a}$$

$$T(\Lambda)^i_j = \frac{1}{16\kappa}\delta^i_j L(\Lambda) \tag{10b}$$

$$T(M)^i_j = (\rho + p)g_{jk}u^k u^i + \delta^i_j pc^2. \tag{10c}$$

Here, ρ, p and u^i denote density, pressure and four-velocity of matter. It holds by (6)

$$c^2 = -g_{ij}u^i u^j. \tag{11}$$

Define the covariant differential operator

$$D^i_j = \left[\left(\frac{-G}{-\eta}\right)^{1/2} g^{kl} g_{jm} g^{mi}_{/l}\right]_{/k} \tag{12}$$

of order two. Then, the field equations for the potentials $\left(g_{ij}\right)$ have the form

$$D^i_j - \frac{1}{2}\delta^i_j D^k_k = 4\kappa T^i_j \tag{13}$$

where the total energy-momentum is the sum of the energy-momentum tensors of matter, gravitation and cosmological constant, *i.e.*,

$$T^i_j = T\left(G\right)^i_j + T\left(M\right)^i_j + T\left(\Lambda\right)^i_j. \tag{14}$$

Define the symmetric energy-momentum tensor

$$T\left(M\right)^{ij} = g^{ik}T\left(M\right)^j_k. \tag{15}$$

Then, the equations of motion in covariant form are

$$T\left(M\right)^k_{i/k} = \frac{1}{2}g_{kl/i}T\left(M\right)^{kl}. \tag{16}$$

In addition to the field Equations (13) and the equations of motion (16) the conservation law of the total energy-momentum holds, *i.e.*

$$T^k_{i/k} = 0. \tag{17}$$

The field equations of gravitation are formally similar to those of GR where T^i_j is the energy-momentum without that of gravitation since the energy-momentum of gravitation is not a tensor for GR. Furthermore, the differential operator is the Einstein tensor which may give a non-Euclidean geometry.

The results of this chapter may be found in the book [1] and in many other articles of the author, as e.g. in [5].

3. Homogeneous, Isotropic, Cosmological Models

In this chapter GFST is applied to homogeneous, isotropic, cosmological models. The pseudo-Euclidean geometry (1) with (2) is used. The matter tensor is given by perfect fluid with velocity

$$u^i = 0\left(i = 1,2,3\right) \tag{18}$$

and pressure p and density ρ with

$$\begin{aligned} p &= p_m + p_r, \\ \rho &= \rho_m + \rho_r \end{aligned} \tag{19}$$

where the indices m and r denote matter and radiation. The equations of state for matter (dust) and radiation are

$$p_m = 0,\ p_r = \frac{1}{3}\rho_r. \tag{20}$$

The potential are by virtue of (18) and the homogeneity and isotropy

$$g_{ij} = \begin{cases} a^2\left(t\right) & \left(i = j = 1,2,3\right) \\ -1/h\left(t\right) & \left(i = j = 4\right) \\ 0 & \left(i \neq j\right). \end{cases} \tag{21}$$

The four-velocity is by Equation (18) and Equation (6)

$$\left(u^i\right)=\left(0,0,0,ch^{1/2}\right). \tag{22}$$

Let $t_0=0$ be the present time and assume as initial conditions at present

$$a(0)=h(0)=1,\ \dot{a}(0)=H_0,\ \dot{h}(0)=\dot{h}_0,\ \rho_m(0)=\rho_{m0},\ \rho_r(0)=\rho_{r0} \tag{23}$$

where the dot denotes the time derivative, H_0 is the Hubble constant and $\dot{h}_0$ is a further constant, ρ_{m0} and ρ_{r0} denote the present densities of matter and radiation. It follows from (16) under the assumption that matter and radiation do not interact

$$\rho_m=\rho_{m0}/h^{1/2},\ \ \rho_r=3p_r=\rho_{r0}/\left(ah^{1/2}\right). \tag{24}$$

The field Equation (13) implies by the use of (21) the two nonlinear differential equations

$$\frac{\mathrm{d}}{\mathrm{d}t}\left(a^3h^{1/2}\frac{\dot{a}}{a}\right)=2\kappa c^4\left(\frac{1}{2}\rho_m+\frac{1}{3}\rho_r+\frac{\Lambda}{2\kappa c^2}\frac{a^3}{h^{1/2}}\right), \tag{25a}$$

$$\frac{\mathrm{d}}{\mathrm{d}t}\left(a^3h^{1/2}\frac{\dot{h}}{h}\right)=4\kappa c^4\left(\frac{1}{2}\rho_m+\rho_r+\frac{1}{8\kappa c^2}L(G)-\frac{\Lambda}{2\kappa c^2}\frac{a^3}{h^{1/2}}\right) \tag{25b}$$

where

$$L(G)=\frac{1}{c^2}a^3h^{1/2}\left(-6\left(\frac{\dot{a}}{a}\right)^2+6\frac{\dot{a}}{a}\frac{\dot{h}}{h}+\frac{1}{2}\left(\frac{\dot{h}}{h}\right)^2\right). \tag{26}$$

The expression $\frac{1}{16\kappa}L(G)$ is the density of gravitation. The conservation law of the total energy gives

$$\left(\rho_m+\rho_r\right)c^2+\frac{1}{16\kappa}L(G)+\frac{\Lambda}{2\kappa}\frac{a^3}{h^{1/2}}=\lambda c^2 \tag{27}$$

where λ is a constant of integration. Equations (25), (26) and (27) give by the use of the i initial conditions (23)

$$\frac{\dot{h}}{h}=-6\frac{\dot{a}}{a}+2\frac{4\kappa c^4\lambda t+\varphi_0}{2\kappa c^4\lambda t^2+\varphi_0 t+1} \tag{28}$$

with

$$\varphi_0=3H_0\left(1+\frac{1}{6}\frac{\dot{h}_0}{H_0}\right). \tag{29}$$

Integration of (28) yields

$$a^3h^{\frac{1}{2}}=2\kappa c^4\lambda t^2+\varphi_0 t+1. \tag{30}$$

Equation (27) gives for the present time $t_0=0$ by the use of the initial conditions (23)

$$\frac{1}{3}\left(8\kappa c^4\lambda-\varphi_0^2\right)=4\left[\frac{8}{3}\pi k\left(\rho_{m0}+\rho_{r0}+\frac{\Lambda c^2}{8\pi\mathrm{k}}\right)-H_0^2\right]. \tag{31}$$

It follows from (27) by the use of the standard definition of the density parameters of matter, radiation and the cosmological constant with the abbreviation

$$K_0 = \left(\Omega_m + \Omega_r + \Omega_\Lambda\right)/\Omega_m \tag{32}$$

the differential equation

$$\left(\frac{\dot{a}}{a}\right)^2 = \frac{H_0^2}{\left(2\kappa c^4 \lambda t^2 + \varphi_0 t + 1\right)^2}\left[-\Omega_m K_0 + \Omega_r a^2 + \Omega_m a^3 + \Omega_\Lambda a^6\right]. \tag{33a}$$

The initial condition is by (23)

$$a(0) = 1. \tag{33b}$$

The solution of (33) with (30) describes a homogeneous, isotropic, cosmological model by GFST.

Relation (31) can be rewritten in the form

$$\frac{8\kappa c^4 \lambda}{H_0^2} - \left(\frac{\varphi_0}{H_0}\right)^2 = 12\Omega_m K_0. \tag{34}$$

A necessary and sufficient condition to avoid singular solutions of (33) is

$$K_0 > 0 \tag{35}$$

which yields

$$2\kappa c^4 \lambda t^2 + \varphi_0 t + 1 > 0 \tag{36}$$

for all $t \in \mathbb{R}$. Hence, condition (35) implies a non-singular solution for all $t \in \mathbb{R}$, *i.e.* we get a non-singular cosmological model. It exists a $t_1 < t_0 = 0$ such that

$$\dot{a}(t_1) = 0. \tag{37}$$

Put $a_1 = a(t_1)$ then it follows from (33a) with $t = t_1$

$$\Omega_r a_1^2 + \Omega_m a_1^3 + \Omega_m a_1^6 = \Omega_m K_0. \tag{38}$$

It holds for all $t \in \mathbb{R}$

$$a(t) \geq a_1 > 0. \tag{39}$$

Subsequently assume

$$a_1 \ll a(0) = 1. \tag{40}$$

Then we get by virtue of (38)

$$K_0 \ll 1. \tag{41}$$

It follows from (32) by virtue of (41)

$$\Omega_r + \Omega_m + \Omega_\Lambda = 1 + \Omega_m K_0, \tag{42}$$

i.e. the sum of the density parameters is a little bit greater than one. Hence, $a(t)$ starts from a positive value, decreases to a small positive value, and then increases for all $t \in \mathbb{R}$.

The proper time from the beginning of the universe till time t is

$$\tilde{\tau}(t) = \int_{-\infty}^{t} 1/h^{1/2}(t)\,\mathrm{d}t. \tag{43}$$

The differential Equation (33a) is rewritten by the use of (30) in the form

$$\left(\frac{\dot{a}}{a}\right)^2 = H_0^2 \frac{1}{h}\left(-\frac{\Omega_m K_0}{a^6} + \frac{\Omega_r}{a^4} + \frac{\Omega_m}{a^3} + \Omega_\Lambda\right). \tag{44}$$

Hence, the differential equation for the function a by the use of the proper time is

$$\left(\frac{1}{a}\frac{\mathrm{d}a}{\mathrm{d}\tilde{\tau}}\right)^2 = H_0^2\left(-\frac{\Omega_m K_0}{a^6} + \frac{\Omega_r}{a^4} + \frac{\Omega_m}{a^3} + \Omega_\Lambda\right). \tag{45}$$

This differential equation is by virtue of (41) and a not too small function $a(t)$ identical with that of GR for a flat homogeneous, isotropic universe. Therefore, away from the beginning of the universe, the result for the universe agrees for GFST with that of GR. Under the above stated assumptions and $\Omega_r = 0$ the differential Equation (33) can analytically be solved. It follows that $a(t)$ starts from a small positive value at $-\infty$ and then it decreases for increasing $t$to $a_1 > 0$ at t_1. Finally it increases for $t > t_1$ to infinity as t goes to infinity. Relation (30) gives positive values $h(t)$ for all t. $h(t)$ starts from infinity at $-\infty$, decreases to a positive value and then it increases to infinity as t goes to infinity. The longer calculations are omitted and they can be found in the article [3].

The differential Equations (44) and (45) show that the condition (35) is important to avoid singularities. GR gives $K_0 = 0$ which yields the singularity of the model (big bang). We introduce in addition to the proper time $\tilde{\tau}$ the absolute time t' by

$$\mathrm{d}t' = \frac{1}{a(t)h^{1/2}(t)}\mathrm{d}t = \frac{1}{a(t)}\mathrm{d}\tilde{\tau}. \tag{46}$$

This gives for the proper time in the universe

$$(c\mathrm{d}\tau)^2 = -a(t)^2\left[|\mathrm{d}x|^2 - (\mathrm{d}ct')^2\right] \tag{47}$$

where $|\mathrm{d}x|$ denotes the Euclidean norm of the vector $\mathrm{d}x = (\mathrm{d}x_1, \mathrm{d}x_2, \mathrm{d}x_3)$.

Relation (47) implies that the absolute value of the light-velocity is equal to vacuum light-velocity c for all times t'.

The introduction of the absolute time t' in the differential Equation (45) gives

$$\left(\frac{\mathrm{d}a}{\mathrm{d}t'}\right)^2 = \frac{H_0^2}{a^2}\left(-\Omega_m K_0 + \Omega_r a^2 + \Omega_m a^3 + \Omega_\Lambda a^6\right). \tag{48}$$

Assume that a light ray is emitted at distance r at time t'_e resp. at time $t'_e + \mathrm{d}t'_e$ and it is received by the observer at time t' resp. at time $t' + \mathrm{d}t'$. Then, it follows

$$r = \int_{t'_e}^{t'} c\mathrm{d}t' = c(t' - t'_e),$$
$$r = \int_{t'_e+\mathrm{d}t'_e}^{t'+\mathrm{d}t'} c\mathrm{d}t' = c(t' + \mathrm{d}t' - t'_e - \mathrm{d}t'_e).$$

These two equations imply

$$\mathrm{d}t' = \mathrm{d}t'_e.$$

The age of the universe since the minimal value of $a(t)$ measured with absolute time t' till now

$$\Delta t' = \int_{t'_1}^{t'_0} \mathrm{d}t' = \int_{a_1}^{1} 1\Big/\left(\frac{\mathrm{d}a}{\mathrm{d}t'}\right)\mathrm{d}a = \frac{1}{H_0}\int_{a_1}^{1} a\mathrm{d}a\Big/\left(-\Omega_m K_0 + \Omega_r a^2 + \Omega_m a^3 + \Omega_\Lambda a^6\right)^{1/2}$$

$$\geq \frac{1}{H_0}\int_{a_1}^{1} a\mathrm{d}a\Big/\left(-\Omega_m K_0 + \left(\Omega_r + \Omega_m + \Omega_\Lambda\right)a^2\right)^{1/2} \approx \frac{1}{H_0}.$$

Therefore, the age of the universe measured with absolute time is greater than $1/H_0$ independent of the density parameters, *i.e.* there is no age problem.

We will now calculate the red shift of light emitted from a distant object at rest and received by the observer at present time. It is useful to introduce the absolute time. Assume that an atom at a distant object emits a photon at time t'_e. It follows from relation (46)

$$\mathrm{d}\tilde{\tau} = a\left(t'_e\right)\mathrm{d}t'. \tag{49}$$

Therefore, the energy of the emitted photon is

$$E \sim -g_{44}\frac{\mathrm{d}t'}{\mathrm{d}\tau} \sim a\left(t'_e\right)E_0.$$

The energy of the photon moving to the observer in the universe is constant by virtue of (47), *i.e.* by the constant light velocity. Then, the corresponding received frequency is

$$\nu = a\left(t'_e\right)\nu_0 \tag{50}$$

where ν_0 is the frequency emitted at the observer from the same atom. The red shift is given by

$$z = \nu_0/\nu - 1 = 1/a\left(t'_e\right) - 1. \tag{51}$$

Light emitted at distance r at time t'_e and received at $r = 0$ at time t'_0 has by the constant velocity of light the relation

$$r = c\left(t'_0 - t'_e\right).$$

This gives by Taylor expansion of $a\left(t'_e\right)$ in relation (51)

$$z = H_0\frac{r}{c} + \left(1 - \frac{1}{2}\frac{1}{H_0^2}\frac{\mathrm{d}^2 a\left(t'_0\right)}{\mathrm{d}t'^2_0}\right)\left(H_0\frac{r}{c}\right)^2.$$

Differentiation of equation (48) yields by neglecting small expressions

$$\frac{\mathrm{d}^2 a\left(t'_e\right)}{\mathrm{d}t'^2_e} \approx H_0^2\left(1 - \frac{1}{2}\Omega_m + \Omega_\Lambda\right).$$

This gives the red shift formula

$$z = H_0\frac{r}{c} + \frac{3}{4}\Omega_m\left(H_0\frac{r}{c}\right)^2. \tag{52}$$

The detailed calculations of Formula (52) can be found in the book [1].

Higher order Taylor expansion gives higher order red shift approximations. The red shift is already derived in the article [11] without Doppler Effect but

only by gravitation.

4. General Relativity

The theory of general relativity as well as the resulting cosmological models is well-known. Astronomical observations show that the universe is flat. Therefore, only flat space of general theory is stated. The curvature of the universe must be zero by the cosmological principle. This means that the sum of the density parameters is equal to one. The strong gravitational field in the neighbourhood of the singularity implies a high curvature which contradicts to a flat universe, *i.e.* with curvature zero. This problem is solved partly by the introduction of an inflationary expansion. Hence, either general relativity is not correct or the cosmological principle is not valid.

5. Field theory of Gravitation

GFST is a field theory which describes gravitation as a field in flat space-time. The theory is covariant and it is studied in the book [1], in the cited references there in and in the articles [2] [3] and [4]. This theory gives for weak gravitational fields to the lowest order of accuracy (measurable accuracy) the same results as general relativity. But there are differences to general relativity for strong gravitational fields, e.g. for the universe in the beginning. The source of the field equations of gravitation is the total energy-momentum including that of gravitational field which is a tensor for this theory. The universe starts without matter in the beginning and consists only of (gravitational) energy. In the course of time matter and radiation are created where the total energy is conserved. Singularities don't exist under the assumption that the sum of the density parameters is greater than one (at least a little bit greater which is subsequently assumed). Hence, there is no big bang. Models with and without cosmological constant are studied in the book [1]. By the use of the pseudo-Euclidean geometryas metric the solution yields a non-expanding universe. The red shift of distant objects in a non-expanding universe was already given in article [11]. It is worth to mention that by virtue of the covariance of the theory the non-singular results can be interpreted in a non-expanding and in an expanding space. The space of the theory is flat independent of the density parameters. The presently assumed density parameter of matter is ≈0.3. To avoid singular solutions of the cosmological model the density parameter of the cosmological constant must be ≈0.7 such that the sum of the two values is a little bit greater than one.

The present discussion of the universe about non-expanding or expanding with acceleration can be solved by GFST because non-expanding space seems to be the natural interpretation but the interpretation as expanding space is also possible. GR demands by virtue of the point -singularity an acceleration of the universe.

Article [10] contains further differences of the two theories.

A theory of gravitation in flat space-time (GFST) is given. The field is a tensor of rank 2 which is described on a flat space-time metric, e.g. the pseudo-Euclid-

ean geometry. The field equations have as source the total energy-momentum tensor inclusive that of gravitation which is a tensor. The conservation of the total energy-momentum tensor implies the equations of motion and reverse. The theory is generally covariant and the results of GFST and general relativity (GR) agree for weak fields to the lowest order of approximation. Homogeneous, isotropic, cosmological models of GFST are studied in the pseudo-Euclidean geometry. Assuming that the sum of the density parameters is a little bit greater than one the resulting cosmological models are non-singular. In the beginning of the universe no matter exists, *i.e.* all the energy is gravitation. In the course of time matter and radiation are generated from gravitational energy. The total energy is conserved. The space is flat and non-expanding. Certain time after the beginning the results of the two theories highly agree with one another under the assumption that the universe is flat. The general covariance of the theory gives the possibility to interpret the results in a non-expanding or in an expanding universe.

6. Conclusions

GFST is a field theory like Electrodynamics and GR is geometry. For weak fields, the two theories give approximately the same results under the assumption that the universe is flat. Astrophysical observations show that the universe is flat. Cosmological models of GR imply a singularity in the beginning of the universe with infinite matter density (big bang). Hence, in the neighbourhood of the singularity, there is a high curvature, *i.e.* space is not flat in the neighbourhood of the singularity. The cosmological principle implies that space is everywhere flat. Hence, we get a contradiction to GR or to the cosmological principle. The universe starts from a point-singularity. Therefore, space must expand or even inflationary expand by virtue of the big observed universe.

GFST is generally covariant, *i.e.* the space can be interpreted as non-expanding or as expanding. The density parameter of matter is at present assumed to be ≈ 0.3. Therefore, the density parameter of dark energy is ≈ 0.7 with the assumption that the sum of the density parameter is a little bit greater than one to imply non-singular cosmological models. Cosmological models of GR have a flat space under the assumption that the sum of the density parameters is equal to one. Therefore, GR and GFST give about the same values for the density parameters. But in the beginning of the universe, the solutions of GR and GFST are quite different. There exists a singularity (big bang) by GR and the solution of GFST is everywhere defined and regular, *i.e.* no bang. It is worth to mention that singularities are physically not allowed.

References

[1] Petry, W. (2014) A Theory of Gravitation in Flat Space-Time. Science PG 2014.

[2] Petry, W. (1981) Cosmological Models without Singularities. *General Relativity and Gravitation*, **13**, 1057-1071. https://doi.org/10.1007/BF00756365

[3] Petry, W. (1990) Nonsingular Cosmological Model with Matter Creation and En-

tropy Production. *General Relativity and Gravitation*, **22**, 1045-1965. https://doi.org/10.1007/BF00757815

[4] Petry, W. (1997) On the Hubble Law in a Nonexpanding Nonstationary Universe with Cosmological Constant. *Astrophysics and Space Science*, **254**, 305-317. https://doi.org/10.1023/A:1000938931517

[5] Petry, W. (2013) Cosmology with Bounce by Flat Space-Time Theory of Gravitation and a New Interpretation. *Journal of Modern Physics*, **4**, 20-25. https://doi.org/10.4236/jmp.2013.47A1003

[6] Petry, W. (2014) Gravitation in Flat Space-Time and General Relativity. *Journal of Applied Mathematics Physics*, **2**, 50-54.

[7] Lerner, E. (2005) Evidence for a Non-Expanding Universe: Surface Brightness Data from HUDF. *AIP Conference Proceedings*, **822**, 60. arXiv: astro-ph/0509611 https://doi.org/10.1063/1.2189123

[8] Petry, W. (2013) Modified Hubble Law. *Physics Essays*, **26**, 315-320. https://doi.org/10.4006/0836-1398-26.2.315

[9] Petry, W. (2015) Creation of a Non-Expanding, Non-Singular Universe. *Journal of Modern Physics*, **6**, 1085-1094. https://doi.org/10.4236/jmp.2015.68113

[10] Petry, W. (2016) Comparing Gravitation in Flat Space-Time with General Relativity. *Journal of Modern Physics*, **7**, 1492-1499. https://doi.org/10.4236/jmp.2016.712135

[11] Petry, W. (2007) Is the Universe Really Expanding? arXiv: 0705.4359

Scientific Research Publishing

Submit or recommend next manuscript to SCIRP and we will provide best service for you:

Accepting pre-submission inquiries through Email, Facebook, LinkedIn, Twitter, etc.
A wide selection of journals (inclusive of 9 subjects, more than 200 journals)
Providing 24-hour high-quality service
User-friendly online submission system
Fair and swift peer-review system
Efficient typesetting and proofreading procedure
Display of the result of downloads and visits, as well as the number of cited articles
Maximum dissemination of your research work

Submit your manuscript at: http://papersubmission.scirp.org/
Or contact jamp@scirp.org

Journal of Applied Mathematics and Physics, 2017, 5, 873-888
http://www.scirp.org/journal/jamp
ISSN Online: 2327-4379
ISSN Print: 2327-4352

Exact Time Domain Solutions of 1-D Transient Dynamic Piezoelectric Problems with Nonlinear Damper Boundary Conditions

Naum M. Khutoryansky, Vladimir Genis

Department of Engineering Technology, Drexel University, Philadelphia, PA, USA
Email: khutoryn@drexel.edu, genisv@drexel.edu

How to cite this paper: Khutoryansky, N.M. and Genis, V. (2017) Exact Time Domain Solutions of 1-D Transient Dynamic Piezoelectric Problems with Nonlinear Damper Boundary Conditions. *Journal of Applied Mathematics and Physics*, **5**, 873-888.
https://doi.org/10.4236/jamp.2017.54077

Received: March 14, 2017
Accepted: April 27, 2017
Published: April 30, 2017

Copyright © 2017 by authors and Scientific Research Publishing Inc.
This work is licensed under the Creative Commons Attribution International License (CC BY 4.0).
http://creativecommons.org/licenses/by/4.0/

Open Access

Abstract

Novel exact solutions of one-dimensional transient dynamic piezoelectric problems for thickness polarized layers and disks, or length polarized rods, are obtained. The solutions are derived using a time-domain Green's function method that leads to an exact analytical recursive procedure which is applicable for a wide variety of boundary conditions including nonlinear cases. A nonlinear damper boundary condition is considered in more detail. The corresponding nonlinear relationship between stresses and velocities at a current time moment is used in the recursive procedure. In addition to the exact recursive procedure that is effective for calculations, some new practically important explicit exact solutions are presented. Several examples of the time behavior of the output electric potential difference are given to illustrate the effectiveness of the proposed exact approach.

Keywords

Piezoelectric Layer, Transient Dynamic Problems, Time Domain Solutions, Green's Function Method, Nonlinear Boundary Conditions, Nonlinear Damper, Output Voltage

1. Introduction

Piezoelectric materials and devices have been widely used in many technical applications. Nowadays, the coupling between electrical and mechanical behaviors is used in different devices based both on the so-called "direct piezoelectric effect" or the "converse piezoelectric effect" [1] [2] [3] [4].

Some newer relevant applications include (among others) the high voltage generation from transient dynamic impact processes in vehicles [5].

Analysis of operating electrical and mechanical parameters of such processes can be done by using various analytical and numerical methods. Although analytical approaches are limited to rather simple geometries and other restrictions (homogeneous or piecewise-homogeneous bodies, linear governing equations, etc.), they often provide exact solutions.

Analytical methods have been successfully used for many transient dynamic one-dimensional piezoelectric problems [6]-[14]. Among analytical methods for transient dynamic piezoelectric problems, the Laplace transform methods play a very significant role. They solve boundary value problems in the frequency-domain, possibly for complex frequencies, using transformed boundary conditions for a piezoelectric body. After obtaining such solutions, the transformation back to the time-domain employs special methods for the inversion of Laplace transforms. However, using the Laplace transform methods is not instrumental even for one-dimensional problems if nonlinear boundary conditions are considered. Time-domain numerical methods (e.g., finite element or finite difference methods) that can be used under such conditions usually lack precision associated with the use of analytical methods. Therefore, development of time-domain analytical or semi-analytical methods combining advantages of analytical and numerical methods can be of interest for such problems.

In this paper, a time-domain Green's function method is implemented for solution of one-dimensional transient dynamic piezoelectric problems for thickness polarized disks or length polarized rods. This method stems from a time-domain representation formulas approach for transient dynamic piezoe-lectric problems described in [15]. For one-dimensional problems with a variety of boundary conditions including nonlinear ones, this method produces exact solutions which are shown below. Such solutions can be used both for analyses of longitudinal mode, piezoelectric devices and as benchmark solutions for numerical methods of piezoelectricity.

2. Representation Formulas

Consider a transversely isotropic homogeneous piezoelectric material (piezoelectric element) with the x_3-axis as the poling direction and the $x_1 - x_2$ plane as the isotropic plane. Let this piezoelectric material occupy a disk (or a cylinder) Ω bounded in x_3-direction by planes $x_3 = 0$ and $x_3 = h$ where $h > 0$ is the thickness of the disk (or the length of the cylinder). Consider a uniaxial strain state or a stress stress state in x_3 direction when there is only one non-zero component of strain γ_{33} or stress σ_{33} the others being zero. We assume that the non-zero stress and strain components, and also the displacement u_3 and electric displacement D_3 in the x_3-direction, and the electric potential ϕ, depend only on x_3 and t which is usually the case for a longitudinal mode piezoelectric element [16]:

$$\begin{aligned} &\sigma_{33} = \sigma_{33}(x_3, t), \quad D_3 = D_3(x_3, t), \\ &u_3 = u_3(x_3, t), \quad \phi = \phi(x_3, t) \text{ in } \Omega \end{aligned} \tag{1}$$

Under conditions (1), we can use the following one-dimensional constitutive equations (both for the uniaxial strain state and for the uniaxial stress state) that relate the mechanical and electrical fields in (1):

$$\sigma_{33} = Cu_{3,3} + e\phi_{,3}; \quad D_3 = eu_{3,3} - \epsilon\phi_{,3} \tag{2}$$

where coefficients are different for the uniaxial strain and uniaxial stress cases.

Then the corresponding equations of motions can be written as

$$\begin{aligned} &\rho\ddot{u}_3 - Cu_{3,33} - e\phi_{,33} = b_3; \\ &-D_{3,3} = \epsilon\phi_{,33} - eu_{3,33} = -q \quad \text{in } \Omega \end{aligned} \tag{3}$$

where $b_3 = b_3(x_3, t)$ and $q = q(x_3, t)$ denote the body force in x_3-direction and electric charge.

To simplify further notations we will denote x_3 and derivatives with respect to x_3 by x and the prime, respectively, and will skip subindex 3 for the elastic displacement, electric displacement and body force components presented in (3). Then system (3) becomes

$$\begin{aligned} &\rho\ddot{u} - Cu'' - e\phi'' = b; \\ &-D' = \epsilon\phi'' - eu'' = -q \quad \text{in } \Omega. \end{aligned} \tag{4}$$

The Green's functions for vector $\{u, \phi\}$ can be obtained using concentrated impulses instead of b or q in (4) when Ω is substituted by the infinite media.

Since ϕ'' can be expressed through u'' due to the second equation in (4), then the first equation in (4) can be presented as the one-dimensional wave equation for displacement u:

$$\rho\ddot{u} - C^D u'' = b - \frac{e}{\epsilon}q \tag{5}$$

where

$$C^D = C + \frac{e^2}{\epsilon}$$

is the Young's modulus measured at constant D.

The wave speed corresponding to Equation (5) is denoted below by

$$c = \sqrt{\frac{C^D}{\rho}}$$

The Green's function for u corresponding to load $\{b = \delta(x)\delta(t), q = 0\}$ is the well-known Green's function for the one-dimensional wave Equation (5):

$$U(x,t) = \frac{1}{2\rho c} H(t - |x|/c) \tag{6}$$

where $H(t)$ is the Heaviside step function (right-continuous), *i.e.* $H(t) = 0$ for $t < 0$ and $H(t) = 1$ for $t \geq 0$.

The corresponding Green's function for ϕ is calculated using the second equation in (4):

$$U_\phi(x,t) = \frac{e}{\epsilon} U(x,t) \tag{7}$$

Based on (6) and (7), the representation formula for the displacement vector

in 3-D case described in [15] reduces to the following expression for the displacement component $u_3(x,t) = u(x,t)$:

$$\begin{aligned} u(x,t) = & \frac{1}{2}\left[u(0,t-x/c)+u(h,t-(h-x)/c)\right] \\ & -\frac{1}{2\rho c}\int_{-\infty}^{t-x/c}\left[\sigma(0,\tau)+\frac{e}{\epsilon}D(0,\tau)\right]\mathrm{d}\tau \\ & +\frac{1}{2\rho c}\int_{-\infty}^{t-(h-x)/c}\left[\sigma(h,\tau)+\frac{e}{\epsilon}D(h,\tau)\right]\mathrm{d}\tau \\ & +\frac{1}{2\rho c}\int_0^h\int_{-\infty}^{t-|\xi-x|/c}\left[b(\xi,\tau)-\frac{e}{\epsilon}q(\xi,\tau)\right]\mathrm{d}\tau\mathrm{d}\xi \quad \text{in } \Omega, \end{aligned} \tag{8}$$

where σ_{33} is denoted by σ and it is taken into account that the outward normals to the lower and upper boundaries of the layer $0 \le x \le h$ have opposite directions.

In many practical applications, the electric volume charges are absent. Therefore, we consider henceforth only the case when $q = 0$. Then the terms related to D in the above expression can be simplified since, based on Equation (4) in this case, $D(x,t)$ is spatially uniform:

$$D(x,t) = D(t). \tag{9}$$

Due to the property (9) the representation formula (8) can be rewritten as

$$\begin{aligned} u(x,t) = & \frac{1}{2}\left[u(0,t-x/c)+u(h,t-(h-x)/c)\right] \\ & -\frac{1}{2\rho c}\int_{-\infty}^{t-x/c}\left[\sigma(0,\tau)+\frac{e}{\epsilon}D(\tau)\right]\mathrm{d}\tau \\ & +\frac{1}{2\rho c}\int_{-\infty}^{t-(h-x)/c}\left[\sigma(h,\tau)+\frac{e}{\epsilon}D(\tau)\right]\mathrm{d}\tau \\ & +\frac{1}{2\rho c}\int_0^h\int_{-\infty}^{t-|\xi-x|/c}b(\xi,\tau)\mathrm{d}\tau\mathrm{d}\xi \quad \text{in } \Omega. \end{aligned} \tag{10}$$

To obtain a representation formula for $\phi(x,t)$, let us consider an auxiliary function

$$\psi(x,t) = \phi(x,t) - \frac{e}{\epsilon}u(x,t) \tag{11}$$

that has the following connection to the electric displacement:

$$D = -\epsilon\psi'.$$

According to (3), $\psi'' = -D'/\epsilon = 0$. Then, using the corresponding Green's function $|x|/2$ and Equation (11), we get a representation formula for $\psi(x,t)$ involving only boundary value of function $\psi(x,t)$ and a spatially uniform electric displacement:

$$\psi(x,t) = \frac{1}{2}\left[\psi(0,t)+\psi(h,t)\right] + \frac{h-2x}{2\epsilon}D(t) \quad \text{in } \Omega. \tag{12}$$

Formulas (12) and (11) lead to the following expression for $\phi(x,t)$:

$$\begin{aligned} \phi(x,t) = & \frac{1}{2}\left[\phi(0,t)+\phi(h,t)\right] - \frac{e}{2\epsilon}\left[u(0,t)+u(h,t)\right] \\ & +\frac{e}{\epsilon}u(x,t)+\frac{h-2x}{2\epsilon}D(t) \quad \text{in } \Omega. \end{aligned} \tag{13}$$

After $u(x,t)$ is calculated, $\phi(x,t)$ can be determined using this calculated value, $D(t)$ and boundary values of $\phi(x,t)$.

The representation formula (10) allows us to get representation formulas for the velocity $v(x,t)=\dot{u}(x,t)$ and stress $\sigma(x,t)$. Differentiating (10) with respect to time provides the following representation formula for the velocity:

$$\begin{aligned} v(x,t)=&\frac{1}{2}\left[v(0,t-x/c)+v\left(h,t-(h-x)/c\right)\right]\\ &-\frac{1}{2\rho c}\left[\sigma(0,t-x/c)+\frac{e}{\epsilon}D(t-x/c)\right]\\ &+\frac{1}{2\rho c}\left[\sigma\left(h,t-(h-x)/c\right)+\frac{e}{\epsilon}D\left(t-(h-x)/c\right)\right]\\ &+\frac{1}{2\rho c}\int_0^h b\left(\xi,t-|\xi-x|/c\right)\mathrm{d}\xi \quad \text{in } \Omega. \end{aligned} \tag{14}$$

To get a representation formula for the stress we need to use the first contitutive equation from (2) (in the new notations introduced after equations (3)) and expression (13) which gives the following expression for the stress:

$$\begin{aligned} \sigma(x,t)&=Cu'(x,t)+e\left[\frac{e}{\epsilon}u'(x,t)-\frac{1}{\epsilon}D(t)\right]\\ &=C^D u'(x,t)-\frac{e}{\epsilon}D(t). \end{aligned} \tag{15}$$

After differentiating (10) with respect to x and substituting the result into (15) we get

$$\begin{aligned} \sigma(x,t)=&\frac{\rho c}{2}\left[v(0,t-x/c)+v\left(h,t-(h-x)/c\right)\right]\\ &+\frac{1}{2}\left[\sigma(0,t-x/c)+\sigma\left(h,t-(h-x)/c\right)\right]\\ &+\frac{e}{2\epsilon}\left[D(t-x/c)+D\left(t-(h-x)/c\right)-2D(t)\right]\\ &+\frac{1}{2}\int_0^h b\left(\xi,t-|\xi-x|/c\right)\mathrm{sgn}(x-\xi)\mathrm{d}\xi \quad \text{in } \Omega. \end{aligned} \tag{16}$$

A representation formula for $D(x,t)$ is not needed under assumption that $q=0$ since the electric displacement is uniform in space in this case and determined solely by the electric boundary conditions.

3. Boundary Equations

The velocity representation formula (14) generates two boundary equations when x tends to the upper and lower boundaries of the piezoelectric element, that is, when x tends to h or 0:

$$\begin{aligned} v(h,t)=&v(0,t-\theta)+\frac{1}{\rho c}\left[\sigma(h,t)-\sigma(0,t-\theta)\right]\\ &+\frac{e}{\rho c\epsilon}\left[D(t)-D(t-\theta)\right]+\frac{1}{\rho c}\int_0^h b(\xi,t-\theta+\xi/c)\mathrm{d}\xi, \end{aligned} \tag{17}$$

$$v(0,t) = v(h,t-\theta) + \frac{1}{\rho c}\left[\sigma(h,t-\theta) - \sigma(0,t)\right] + \frac{e}{\rho c \epsilon}\left[D(t-\theta) - D(t)\right] + \frac{1}{\rho c}\int_0^h b(\xi, t-\xi/c)\,\mathrm{d}\xi \tag{18}$$

where θ denotes the time taken by the elastic wave to travel the thickness of the piezoelectric layer:

$$\theta = \frac{h}{c}.$$

Similarly, the stress representation formula (16) generates the following boundary equations:

$$\sigma(h,t) = \sigma(0,t-\theta) + \rho c\left[v(h,t) - v(0,t-\theta)\right] + \frac{e}{\epsilon}\left[D(t-\theta) - D(t)\right] - \int_0^h b(\xi, t-\theta+\xi/c)\,\mathrm{d}\xi, \tag{19}$$

$$\sigma(0,t) = \sigma(h,t-\theta) + \rho c\left[v(h,t-\theta) - v(0,t)\right] + \frac{e}{\epsilon}\left[D(t-\theta) - D(t)\right] + \int_0^h b(\xi, t-\xi/c)\,\mathrm{d}\xi. \tag{20}$$

It is easy to verify that Equations (17) and (19), though presented in different forms, are equivalent. The same is true for the pair of Equations (18) and (20). Therefore, we shall use the equations in these pairs interchangeably.

We will not work with boundary equations that can be obtained directly from the displacement representation formula (10), since it is computationally more effective to determine at first unknown boundary values of the velocity $v(x,t)$, and then calculate unknown boundary values of the displacement $u(x,t)$ by integrating the boundary velocity over time (using also an initial condition for $u(x,t)$).

We also need to consider boundary values of the expression (13) for the electric potential. It is important to emphasize that two equations obtained from (13) when x tends to h or to 0 are equivalent and, therefore, they are presented below as one equation:

$$\phi(h,t) - \phi(0,t) = \frac{e}{\epsilon}\left[u(h,t) - u(0,t)\right] - \frac{h}{\epsilon}D(t) \tag{21}$$

The boundary equations presented above will be used in the next section to create an exact time domain solution procedure in the case when nonlinear damper boundary conditions are sprecified.

4. Nonlinear Damper Boundary Conditions and Exact Solutions

Suppose that the lower end face of the piezoelectric element is fixed to a nonlinear damper. Let F be a damping force acting on the lower end face which is defined by the following nonlinear relationship [17]:

$$F = -k_\alpha \left|v(0,t)\right|^\alpha \operatorname{sgn}\left(v(0,t)\right). \tag{22}$$

where $k_\alpha > 0$ is the damping constant, $\alpha > 0$ is the damping exponent, and

$\mathrm{sgn}(.)$ is the signum function defined for all real numbers (including 0 where its value is also 0). If $v(0,t) \neq 0$, the direction of F is opposite to $v(0,t)$. The exponent α has a value 1 for a linear damper, but may vary in practice in the interval $(0,2]$ [17] creating a set of possible boundary conditions at $x = 0$. We assume that the force F is uniformly distributed over the lower end face. Then (22) transforms into the following nonlinear (in general) boundary condition at the lower end face:

$$\sigma(0,t) = \frac{k_\alpha}{A} |v(0,t)|^\alpha \, \mathrm{sgn}(v(0,t)) \tag{23}$$

where A is the lower end face area.

Consider additional assumptions that will be used to get exact solutions for the damper boundary conditions based on the results of the previous section. We suppose that the values of u, σ, b, ϕ, D are defined for $-\infty < t < \infty$. In addition, let us assume henceforth that

$$u(x,t) = 0, \phi(x,t) = 0 \quad \text{if} \quad 0 < x < h, t < 0 \tag{24}$$

which means, based on (2) and (3), that σ, D and b are also zero inside the piezoelectric body at negative times. The next additional assumption is that

$$b(x,t) = 0 \tag{25}$$

inside the piezoelectric body at any time in the sense of generalized functions. This also includes the assumption that the initial conditions for the elastic displacement $u(x,t)$ are zero, as discussed in [15]. These assumptions will simplify using boundary Equations (17)-(20) for particular problems considered below.

Regarding the design of the piezoelectric element, we assume that it is a cylinder (or a rod) with two coated electrodes at $x = 0$ and $x = h$. The electrodes are considered to be of negligible thickness (from the mechanical point of view) and their deformation is neglected. The output voltage, which is defined as the electric potential difference between the lower and upper electrodes $\Delta\phi = \phi(0,t) - \phi(h,t)$, is of primary interest below.

The electric boundary condition at $x = 0$ corresponds to the grounded electrode:

$$\phi(0,t) = 0 \quad \text{if} \quad t \geq 0 \tag{26}$$

At the upper end face, the following mechanical boundary condition is used:

$$\sigma(h,t) = p(t) \quad \text{if} \quad t \geq 0 \tag{27}$$

where $p(t)$ is an applied normal stress load which is assumed to be known and negative.

The electric boundary condition at the upper end face $x = h$ is formulated as follows:

$$D(h,t) = 0 \quad \text{if} \quad t \geq 0. \tag{28}$$

So, based on (9), $D(t) = 0$.

Using the above assumptions the representation formulas (14) and (16) for

the velocity and stress take the following simplified forms:

$$v(x,t)=\frac{1}{2}\left[v(0,t-x/c)+v(h,t-(h-x)/c)\right] + \frac{1}{2\rho c}\left[p(t-(h-x)/c)-\sigma(0,t-x/c)\right] \quad \text{in } \Omega, \tag{29}$$

$$\sigma(x,t)=\frac{\rho c}{2}\left[v(0,t-x/c)+v(h,t-(h-x)/c)\right] + \frac{1}{2}\left[\sigma(0,t-x/c)+p(t-(h-x)/c)\right] \quad \text{in } \Omega \tag{30}$$

where all the time dependent functions are equal to zero for negative times.

In the representation formulas (29) and (30), there are three unknown boundary functions $v(0,t),\sigma(0,t)$ and $v(h,t)$ first two of which are related by Equation (23). Two additional equations needed for determination of these three functions will be derived below based on (17) and (18).

After the the velocity $v(x,t)$ is determined for any particular x over time, the corresponding displacement $u(x,t)$ can be obtained (due to the zero initial conditions) as

$$u(x,t)=\int_0^t v(x,\tau)\mathrm{d}\tau. \tag{31}$$

Boundary values of the displacement provide (according to (21) and (26)) the electric potential value at $x=h$:

$$\phi(h,t)=\frac{e}{\epsilon}\left[u(h,t)-u(0,t)\right] \tag{32}$$

4.1. An Exact Recursive Procedure

The solution of the above problem will be obtained by using an exact recursive procedure based on the following equations obtained from (17) and (18) under the boundary conditions (23) (26) (27) (28):

$$v(h,t)=2v(0,t-\theta)-v(h,t-2\theta)+\frac{1}{\rho c}\left[p(t)-p(t-2\theta)\right], \tag{33}$$

$$v(0,t)+\frac{k_\alpha}{\rho cA}\left|v(0,t)\right|^\alpha \operatorname{sgn}\left(v(0,t)\right)=v(h,t-\theta)+\frac{1}{\rho c}p(t-\theta). \tag{34}$$

There are two unknowns $v(h,t)$ and $v(0,t)$ at each time moment t in these equations. The right-hand sides of the equations are known at each time point since they contain either $p(t)$ or time-dalayed function values at $t-\theta$ that had to be determined at a previous step of the recursive process.

In order to simplify deriving next results, we need to introduce some additional notations:

$$\gamma=\frac{k_\alpha}{\rho cA},\quad \xi=v(0,t),\quad r=v(h,t-\theta)+\frac{1}{\rho c}p(t-\theta). \tag{35}$$

Then, Equation (34) reads as

$$\xi+\gamma\left|\xi\right|^\alpha \operatorname{sgn}(\xi)=r. \tag{36}$$

Let the left-hand side of Equation (36) be denoted by $f(\xi)$. Since $\alpha > 0$, $f(\xi)$ is a continuous strictly monotonically increasing function on $(-\infty, \infty)$ ranging from $-\infty$ to ∞. Therefore, for any real r, there exists one and only one solution of Equation (36) in $(-\infty, \infty)$.

Denote by Q_α the operator that tranforms r into this solution of equation (36). Thus, Q_α is the left inverse operator of the nonlinear operator acting on ξ in the left-hand side of Equation (36). If $\alpha = 2$, 1, $1/2$ or $1/3$, the corresponding expressions of $Q_\alpha r$ are very simple for computations:

$$\begin{cases} Q_2 r = \dfrac{1}{2\gamma}\left(-1+\sqrt{1+4|r|\gamma}\right)\operatorname{sgn}(r), \\ Q_1 r = \dfrac{r}{1+\gamma},\ Q_{1/2} r = \dfrac{1}{4}\left(-\gamma+\sqrt{\gamma^2+4|r|}\right)^2 \operatorname{sgn}(r), \\ Q_{1/3} r = -\gamma\left[\dfrac{1}{6}\left(108r+12\sqrt{12\gamma^3+81r^2}\right)^{1/3} - \dfrac{2\gamma}{\left(108r+12\sqrt{12\gamma^3+81r^2}\right)^{1/3}}\right]+r. \end{cases} \tag{37}$$

The calculation of $Q_\alpha r$ for other values of α can effectively be implemented using a symbolic computation software like Maple [18].

With help of the inverse operator Q_α Equation (34) can be rewritten in the following explicit form for calculating $v(0,t)$:

$$v(0,t) = Q_\alpha\left[v(h,t-\theta)+\frac{1}{\rho c}p(t-\theta)\right]. \tag{38}$$

Equation (38) combined with (33) creates the recursive procedure that can be used directly for calculations or can lead to building explicit exact solution for vector $\{v(0,t), v(h,t)\}$ step by step over consecutive time intervals $j\theta \le t < (j+1)\theta$ $(j = 0,1,2,\cdots)$. In doing so, it is helpful to substitute $v(0,t-\theta)$ in (33) by its expression obtained from (38) which provides the following recursive equation for $v(h,t)$:

$$\begin{aligned} v(h,t) = {} & 2Q_\alpha\left[v(h,t-2\theta)+\frac{1}{\rho c}p(t-2\theta)\right] \\ & -\left[v(h,t-2\theta)+\frac{1}{\rho c}p(t-2\theta)\right]+\frac{1}{\rho c}p(t), \end{aligned}$$

or, using the identity operator I (that leaves unchanged the element on which it operates),

$$v(h,t) = (2Q_\alpha - I)\left[v(h,t-2\theta)+\frac{1}{\rho c}p(t-2\theta)\right]+\frac{1}{\rho c}p(t). \tag{39}$$

4.2. Explicit Exact Solutions

Now we derive some explicit exact solutions for $v(h,t)$ and $v(0,t)$ corresponding to three practically important ranges of the duration t_1 of the stress load at $x = h$. Our goal is to present the boundary velocities directly through

the transient stress load at $x = h$ that generates the dynamic process in the piezoelectric body.

4.2.1. Case 1: $t_1 < 2\theta$

So, $p(t) = 0$ if $t \notin [0, 2\theta)$. Using the recursive Equation (39) under this condition for consecutive intervals $[2k\theta, 2(k+1)\theta)$, $k = 0, 1, 2, \cdots$, we finally obtain the following explicit expression for $v(h,t)$:

$$v(h,t) = \begin{cases} \dfrac{1}{\rho c} p(t) & \text{if} \quad 0 \le t < 2\theta, \\ (2Q_\alpha - I)^k \left[\dfrac{2}{\rho c} p(t - 2k\theta) \right] & \\ \text{if} \quad 2k\theta \le t < 2(k+1)\theta, \ k = 1, 2, \cdots. & \end{cases} \tag{40}$$

Substituting (40) into (38) we get the corresponding explicit expression for $v(0,t)$:

$$v(0,t) = \begin{cases} 0 & \text{if} \quad 0 \le t < \theta, \\ Q_\alpha (2Q_\alpha - I)^{k-1} \left[\dfrac{2}{\rho c} p(t - 2k\theta) \right] & \\ \text{if} \ (2k-1)\theta \le t < (2k+1)\theta, \ k = 1, 2, \cdots. & \end{cases} \tag{41}$$

4.2.2. Case 2: $t_1 < 4\theta$

In this case, $p(t) = 0$ if $t \notin [0, 4\theta)$. Acting similarly to section 4 we derive the following explicit exact solutions:

$$v(h,t) = \begin{cases} \dfrac{1}{\rho c} p(t) & \text{if} \quad 0 \le t < 2\theta, \\ (2Q_\alpha - I)^{k-1} \left[\dfrac{1}{\rho c} p(t - 2(k-1)\theta) \right. & \\ \left. + (2Q_\alpha - I) \left(\dfrac{2}{\rho c} p(t - 2k\theta) \right) \right] & \text{if} \ 2k\theta \le t < 2(k+1)\theta, k = 1, 2, \cdots; \end{cases} \tag{42}$$

$$v(0,t) = \begin{cases} 0 & \text{if} \quad 0 \le t < \theta, \\ Q_\alpha \left[\dfrac{2}{\rho c} p(t - \theta) \right] & \text{if} \quad \theta \le t < 3\theta, \\ Q_\alpha (2Q_\alpha - I)^{k-1} \left[\dfrac{1}{\rho c} p(t - 2k\theta + \theta) \right. & \\ \left. + (2Q_\alpha - I) \left(\dfrac{2}{\rho c} p(t - 2k\theta - \theta) \right) \right] & \\ \text{if} \ (2k-1)\theta \le t < (2k+1)\theta, \ k = 2, 3, \cdots. & \end{cases} \tag{43}$$

4.2.3. Case 3: $t_1 < 6\theta$

So, $p(t) = 0$ if $t \notin [0, 6\theta)$, and the corresponding exact solutions have the following closed form:

$$v(h,t)=\begin{cases}\dfrac{1}{\rho c}p(t) \quad \text{if} \quad 0\le t<2\theta,\\ \dfrac{1}{\rho c}p(t)+(2Q_\alpha-I)\left[\dfrac{2}{\rho c}p(t-2\theta)\right] \quad \text{if} \quad 2\theta\le t<4\theta,\\ (2Q_\alpha-I)^{k-1}\left[\dfrac{1}{\rho c}p(t-2(k-1)\theta)+(2Q_\alpha-I)\left[\dfrac{2}{\rho c}p(t-2k\theta)\right.\right.\\ \left.\left.+(2Q_\alpha-I)\left(\dfrac{2}{\rho c}p(t-2(k+1)\theta)\right)\right]\right]\\ \text{if} \quad 2(k+1)\theta\le t<2(k+2)\theta, k=1,2,\cdots;\end{cases} \tag{44}$$

$$v(0,t)=\begin{cases}0 \quad \text{if} \quad 0\le t<\theta,\\ Q_\alpha\left[\dfrac{2}{\rho c}p(t-\theta)\right] \quad \text{if} \quad \theta\le t<3\theta,\\ Q_\alpha\left[\dfrac{1}{\rho c}p(t-\theta)+(2Q_\alpha-I)\left(\dfrac{2}{\rho c}p(t-3\theta)\right)\right] \quad \text{if} \quad 3\theta\le t<5\theta,\\ Q_\alpha(2Q_\alpha-I)^{k-1}\left[\dfrac{1}{\rho c}p(t-2k\theta+\theta)\right.\\ +(2Q_\alpha-I)\left[\dfrac{2}{\rho c}p(t-2k\theta-\theta)\right.\\ \left.\left.+(2Q_\alpha-I)\left(\dfrac{2}{\rho c}p(t-2k\theta-3\theta)\right)\right]\right]\\ \text{if} \quad (2k+3)\theta\le t<(2k+5)\theta, \ k=1,2,\cdots.\end{cases} \tag{45}$$

Similar explicit formulas for $t_1\ge 6\theta$ are excessively cumbersome. In this case, it is easier to directly use the recursive procedure based on (33) and (38) which has the same simple form regardless of the transient load duration and also provides exact results.

5. Examples and Discussions

Consider some examples of using the results of the previous section for mathematical modeling of piezoelectric cylindrical devices installed in a car as proposed in [5]. These devices transform the mechanical energy of the moving pistons or crank-shafts into electrical energy, which will be stored in the capacitor or the battery charger. We consider the uniaxial stress state for a cylinder and assume that the material of the cylinder is PZT-5A [4]. In this case, parameters C,e,ϵ and ρ in Equations (3) have the following values:

$$C=5.32*10^{10}\ \text{N/m}^2;e=19.89\ \text{N/(V}\cdot\text{m)};$$
$$\epsilon=76.12*10^{-10}\ \text{farad/m};\ \rho=7750.0\ \text{kg/m}^3$$

Then the elastic wave speed c in the piezoelectric material is equal to $3684.06\ \text{m/s}$. Next, we take into account that the total force instantaneously applied to the top of a piston in an internal combustion engine is around 6300 pounds, which corresponds to approximately 28,640 N [19]. Suppose that this

force F_a is applied downward to a piezoelectric cylinder with a length of $h=1$ cm and a diameter $d=1$ cm. So, the area of the upper end face of the cylinder $A=\pi d^2/4=0.785$ cm^2. Assuming that F_a is uniformly distributed over the upper end face, we get the amplitude of the pressure impulse acting on the top of the cylinder: $p_a=364.66$ MPA. Let us assume that the applied normal stress load takes the form of the following rectangular compressive load (pressure) impulse:

$$p(t)=-p_a\left[H(t)-H(t-t_1)\right] \tag{46}$$

where t_1 is the duration of the pressure impulse.

We assume first that $\alpha=0.5$ and $k_\alpha=1000\ \mathrm{N\cdot s^{1/2}\cdot m^{-1/2}}$ (see, e.g., [20]) in the damper boundary conditions (23). Consider the following three values of t_1: $5, 10, 15$ μs. Since the transit time of elastic waves between the upper and lower end faces $\theta=2.71$ μs, then these three durations correspond to the three cases of explicit exact solutions considered in 4. The operator Q_α is calculated according to (37). The calculated results for the output voltage $V=\Delta\phi$ (in kV) based on these exact solutions are presented for $t\le 50$ μs in **Figures 1-3** below.

Comparing the graphs we can see that the maximum or peak value does not depend on the pressure impulse duration t_1. However, the number of peaks in each figure depends on the t_1. The time distance between two neighboring peaks is approximately equal to 2θ. After the pressure load is removed, there is an attenuation of the output voltage vibrations.

Now let us consider another set of the damper parameters: $\alpha=2.0$ and $k_\alpha=250\ \mathrm{N\cdot s^2\cdot m^{-2}}$. The parameters of the material and the impulse durations are the same as above. The operator Q_α is also calculated according to (37).

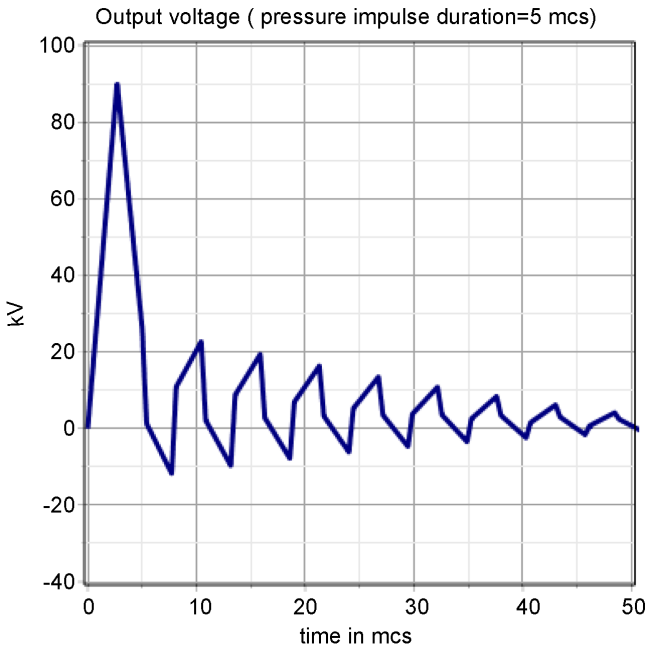

Figure 1. Output voltage for $\alpha=0.5, k_\alpha=1000\ \mathrm{N\cdot s^{1/2}\cdot m^{-1/2}}$ and $t_1=5$ μs.

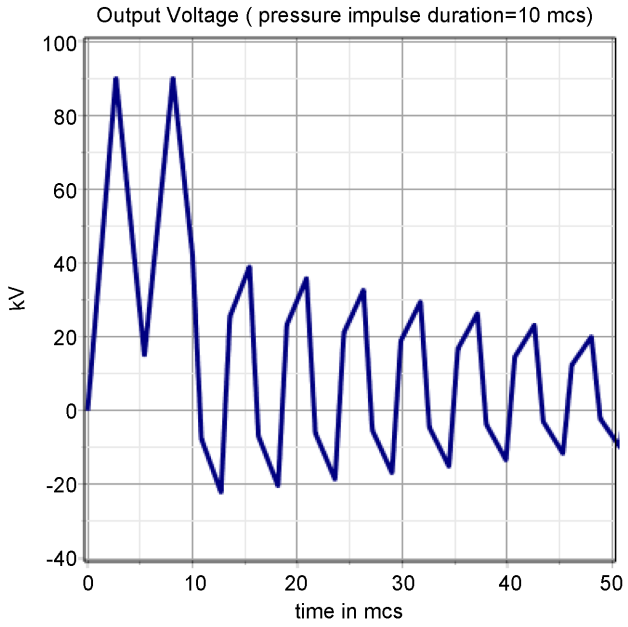

Figure 2. Output voltage for $\alpha = 0.5, k_\alpha = 1000\ \mathrm{N \cdot s^{1/2} \cdot m^{-1/2}}$ and $t_1 = 10\ \mu\mathrm{s}$.

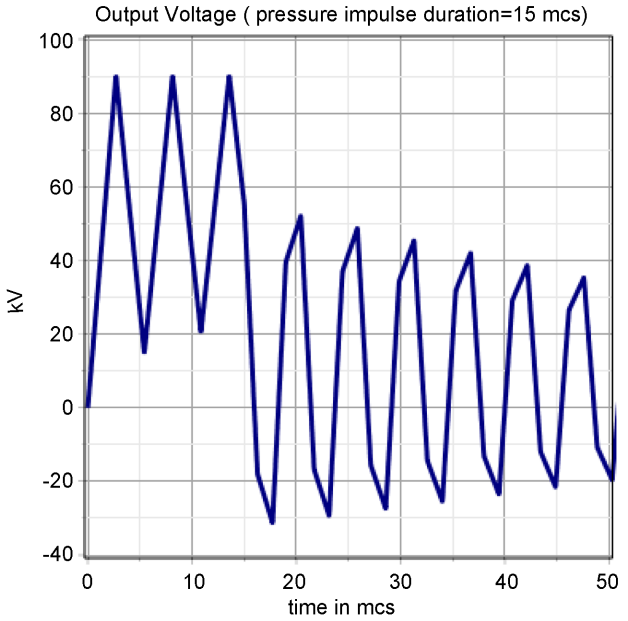

Figure 3. Output voltage for $\alpha = 0.5, k_\alpha = 1000\ \mathrm{N \cdot s^{1/2} \cdot m^{-1/2}}$ and $t_1 = 15\ \mu\mathrm{s}$.

The calculated results for the output voltage $V = \Delta\phi$ (in kV) are presented for $t \le 50\ \mu\mathrm{s}$ in **Figures 4-6**.

Comparison of these graphs shows that the maximum value of the output voltage does not depend on the pressure impulse duration t_1 which similar to the case when $\alpha = 0.5$. The difference is that now there is only one peak but its width depends on the t_1. After the pressure load is removed, the attenuation of the output voltage vibrations is very pronounced: the amplitude of vibrations after the load removal is almost negligible.

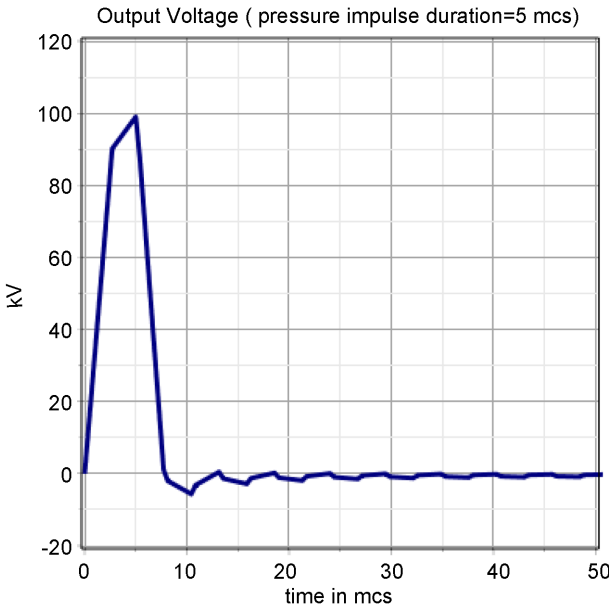

Figure 4. Output voltage for $\alpha = 2, k_\alpha = 250\ \mathrm{N \cdot s^2 \cdot m^{-2}}$ and $t_1 = 5\ \mu\mathrm{s}$.

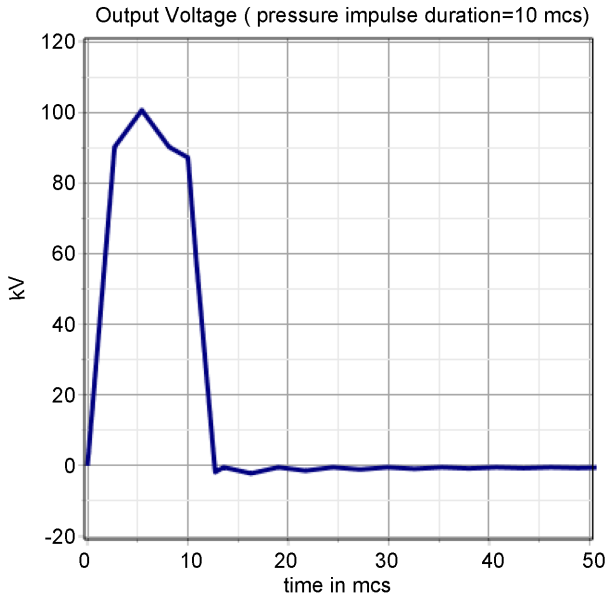

Figure 5. Output voltage for $\alpha = 2, k_\alpha = 250\ \mathrm{Ns^2m^{-2}}$ and $t_1 = 10\ \mu\mathrm{s}$.

6. Conclusion

One-dimensional transient dynamic piezoelectric problems for thickness polarized layers and disks, or length polarized rods, are considered here in the framework of a time-domain Green's function method. As the result, a novel exact analytical recursive procedure is derived which is applicable for a wide variety of boundary conditions including the nonlinear damper case. Some new practically important explicit exact solutions are presented. The effectiveness of the proposed exact approach is demonstrated by examples of the time behavior of the output electric potential difference between two electrodes coated at the

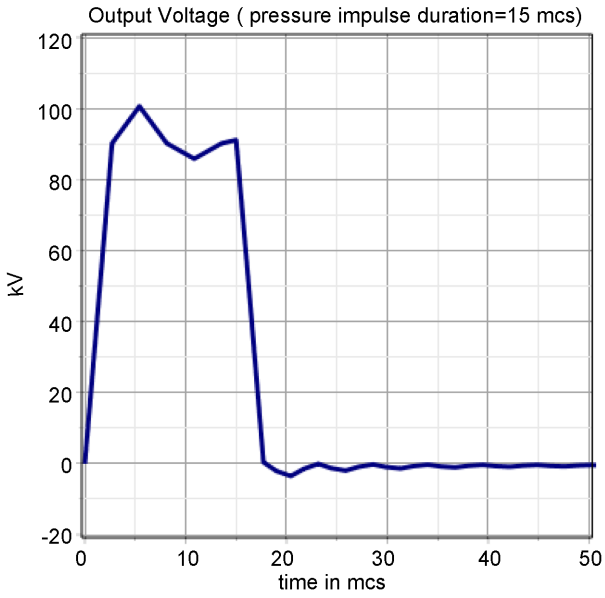

Figure 6. Output voltage for $\alpha = 2, k_{\alpha} = 250\ \mathrm{N \cdot s^2 \cdot m^{-2}}$ and $t_1 = 15\ \mu\mathrm{s}$.

end faces of a piezoelectric cylinder fixed to a nonlinear damper at one end, and subjected to impulsive loading at the other.

Acknowledgements

The authors would like to thank the anonymous reviewers for their comments.

References

[1] Mason, W.P. (1981) Piezoelectricity, Its History and Applications. *The Journal of the Acoustical Society of America*, **70**, 1561. https://doi.org/10.1121/1.387221

[2] Yang, J. (2006) Analysis of Piezoelectric Devices. World Scientific, Singapore. https://doi.org/10.1142/6156

[3] Fang, D., Wang, J. and Chen, W., Eds. (2013) Analysis of Piezoelectric Structures and Devices. De Gruyter, Berlin, Boston.

[4] Vijaya, M.S. (2013) Piezoelectric Materials and Devices: Applications in Engineering and Medical Sciences. CRC Press, Boca Raton.

[5] Genis, V. and Soukhomlinoff, A. (2010) United States Patent: 7679271—Piezoelectric Powered Vehicles and Motors, March 2010.

[6] Cook, E.G. (1956) Transient and Steady-State Response of Ultrasonic Piezoelectric Transducers. 1956 *IRE National Convention*, New York, 19-22 March 1956, 61-69. https://doi.org/10.1109/IRENC.1956.199155

[7] Filipczynski, L. (1960) Transients and the Equivalent Electrical Circuit of the Piezoelectric Transducer. *Acta Acustica united with Acustica*, **10**, 149-154.

[8] Redwood, M. (1961) Transient Performance of a Piezoelectric Transducer. *The Journal of the Acoustical Society of America*, **33**, 527-536. https://doi.org/10.1121/1.1908709

[9] Stuetzer, O.M. (1967) Multiple Reflections in a Free Piezoelectric Plate. *The Journal of the Acoustical Society of America*, **42**, 502. https://doi.org/10.1121/1.1910607

[10] Zhang, H.L., Li, M.X. and Ying, C.F. (1983) Complete Solutions of the Transient Behavior of a Transmitting Thickness-Mode Piezoelectric Transducer and Their

Physical Interpretations. *The Journal of the Acoustical Society of America*, **74**, 1105. https://doi.org/10.1121/1.390034

[11] Le, K.C. (1999) Vibrations of Shells and Rods. Springer, Berlin, Heidelberg. https://doi.org/10.1007/978-3-642-59911-8

[12] Ma, C.C., Chen, X.H. and Ing, Y.S. (2007) Theoretical Transient Analysis and Wave Propagation of Piezoelectric Bi-Materials. *International Journal of Solids and Structures*, **44**, 7110-7142.

[13] Ing, Y.S., Liao, H.F. and Huang, K.S. (2013) The Extended Durbin Method and Its Application for Piezoelectric Wave Propagation Problems. *International Journal of Solids and Structures*, **50**, 4000-4009.

[14] Gazonas, G.A., Wildman, R.A., Hopkins, D.A. and Scheidler, M.J. (2016) Longitudinal Impact of Piezoelectric Media. *Archive of Applied Mechanics*, **86**, 497-515. https://doi.org/10.1007/s00419-015-1042-3

[15] Khutoryansky, N.M. and Sosa, H. (1995) Dynamic Representation Formulas and Fundamental Solutions for Piezoelectricity. *International Journal of Solids and Structures*, **32**, 3307-3325.

[16] Yuan, F.G. (2016) Structural Health Monitoring (SHM) in Aerospace Structures. Elsevier Science, Amsterdam.

[17] Dixon, J. (2008) The Shock Absorber Handbook. John Wiley & Sons, Hoboken.

[18] Monagan, M.B., Geddes, K.O., Heal, K.M., Labahn, G., Vorkoetter, S.M., McCarron, J. and DeMarco, P. (2005) Maple 10 Programming Guide. Maplesoft, Waterloo, ON, Canada.

[19] Pulkrabek, W.W. (1997) Engineering Fundamentals of the Internal Combustion Engine. Prentice Hall, Upper Saddle River.

[20] Ho, C., Lang, Z.Q., Sapiński, B. and Billings, S.A. (2013) Vibration Isolation Using Nonlinear Damping Implemented by a Feedback-Controlled MR Damper. *Smart Materials and Structures*, **22**. https://doi.org/10.1088/0964-1726/22/10/105010

Scientific Research Publishing

Submit or recommend next manuscript to SCIRP and we will provide best service for you:

Accepting pre-submission inquiries through Email, Facebook, LinkedIn, Twitter, etc.
A wide selection of journals (inclusive of 9 subjects, more than 200 journals)
Providing 24-hour high-quality service
User-friendly online submission system
Fair and swift peer-review system
Efficient typesetting and proofreading procedure
Display of the result of downloads and visits, as well as the number of cited articles
Maximum dissemination of your research work

Submit your manuscript at: http://papersubmission.scirp.org/
Or contact jamp@scirp.org

Scientific Research Publishing

Journal of Applied Mathematics and Physics, 2017, 5, 889-899
http://www.scirp.org/journal/jamp
ISSN Online: 2327-4379
ISSN Print: 2327-4352

The Faraday Isolator, Detailed Balance and the Second Law

George S. Levy

Entropic Power, 3980 Del Mar Meadows, San Diego, CA, USA
Email: glevy@entropicpower.com

How to cite this paper: Levy, G.S. (2017) The Faraday Isolator, Detailed Balance and the Second Law. *Journal of Applied Mathematics and Physics*, **5**, 889-899.
https://doi.org/10.4236/jamp.2017.54078

Received: March 27, 2017
Accepted: April 27, 2017
Published: April 30, 2017

Copyright © 2017 by author and Scientific Research Publishing Inc.
This work is licensed under the Creative Commons Attribution International License (CC BY 4.0).
http://creativecommons.org/licenses/by/4.0/

Open Access

Abstract

A Faraday isolator is shown to develop a temperature difference between its input and output, but still complies with the second law when all the heat carriers, in this case, photons are homogeneous and indistinguishable. This result is a consequence of the H-theorem which assumes homogeneity and indistinguishability of particles. However, when a thermal feedback path is added, in which heat carriers have physical properties different from the photons in the isolator, then a heterogeneous system is formed not covered by the H-theorem, and the second law is violated.

Keywords

Faraday Isolator, Detailed Balance, Second Law, Non-Maxwellian, Entropy, H-Theorem, Statistical Mechanics, Perpetual Motion Machine, Statistical Symmetry, Indistinguishability

1. Introduction

Reciprocity in absorption and emission is a requirement of detailed balance and expressed by Kirchhoff law of radiation for any wavelength and for any direction.

$$\alpha(\omega,\theta,\varphi)=\varepsilon(\omega,\theta,\varphi) \tag{1}$$

In other words, the absorptivity α is equal to the emissivity ε for any value of frequency ω and polar coordinate angles θ and φ. This law is conventionally accepted, yet non-reciprocity of transmission and reflection has been the puzzlement [1] to scientists as it appears to violate the principle of detailed balance and the second law. Non-reciprocal devices are used in a multitude of applications, for example Faraday isolators and optical and microwave circulators. This paper discusses how such non-reciprocity leads to the breakdown of detailed balance and the second law.

The Faraday isolator is a non-reciprocal optical device, *i.e.*, a light diode. It

comprises an input linear polarizer, a polarization rotator and an output linear polarizer at 45˚ from the input polarizer. Light entering the isolator through the input is linearly polarized, then rotated by a 45˚ angle and exits unimpeded through the output polarizer. Light entering through the output is polarized, and then rotated another 45˚ thereby, encountering the first polarizer at a 90˚ angle and being stopped. The unidirectionality of the device seems to indicate that objects downstream of the light flow should get warmer and those upstream should get colder.

Wien [2] attempts to prove that Faraday isolators cannot violate the second law. He describes a thought experiment involving two black bodies A and B separated by a Faraday isolator comprised of polarizers X and Y and a Faraday rotator R. The polarizers are nicol prisms which, he assumes, transmit half of the light and reflect the other half. Wien's analysis assumes that the black bodies are initially at the same temperature. The analysis is illustrated in **Figure 1** in which the width of the channels corresponds to the magnitude of heat flow.

Half of the light coming from A is reflected back to A by the nicol X. The other half undergoes a 45˚ rotation, traverses nicol Y and reaches black body B.

Half of the light coming from B is reflected back to B by nicol Y. The second half is rotated by 45˚ and as it reaches nicol X, is totally reflected toward B. Wien then carelessly assumes that this polarized light crosses nicol Y and reaches B. He concludes that B receives three times more energy than A.

Wien's careless assumption is erroneous. This error is corrected by Rayleigh as described further below. In any case, it is instructive to continue with Wien's reasoning, and then discuss Rayleigh's correction.

To avoid a conflict with the second law, Wien proposes two solutions (original quote in French) [2]:

"On peut résoudre de deux façons différentes cette contradiction avec le second principe de la Thermodynamique.

Ou bien le magnétisme de la substance douée du pouvoir rotatoire est détruit par la radiation qui la traverse, c'est à dire que si la rotation est produite par des aimants permanents ces aimants sont affaiblis.

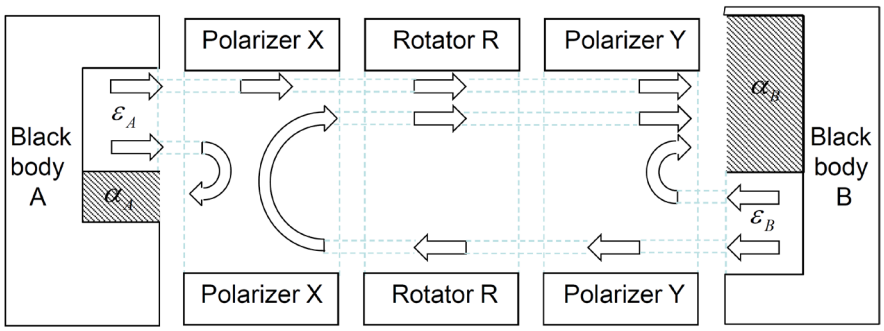

Figure 1. Wien's thought experiment using nicol prisms which transmit half of the light and reflect the other half. According to Wien, black body B receives three times more light than black body A. The figure shows the black bodies in an initial non-equilibrium state.

Ou tous les corps transparents doués du pouvoir rotatoire absorbent la lumière en faisant tourner son plan de polarization."

Translated to English, Wien proposes that, either light that goes through the rotator attenuates the magnetic field, or that the rotator absorbs light as a function of the rotation imparted to light.

Neither of his proposed solutions is acceptable. His first argument requires light to weaken the magnetic field, thereby impacting the bi-directional operation of the rotator. The complete elimination of the rotator's operation is obviously not possible because, then, Faraday isolators would not work. The partial reduction of the rotator's operation can easily be countered by increasing the length of the rotator to restore its function.

His second argument requires light to be asymmetrically absorbed by the rotator as a function of the orientations of the *non-local polarizers*. In other words, light from one of the polarizers would have to be preferentially absorbed compared to light from the other polarizer. There is no known physical mechanism by which this effect can be achieved.

Rayleigh [3] properly completes Wien's thought experiment, thereby correcting Wien's omission. As shown in **Figure 2** Rayleigh finds that, after the reflection from X, light acquires another 45˚ rotation as it traverses the rotator a third time and instead of crossing nicol Y and reaching B, light is reflected by nicol Y towards A.

At that point, the light has the correct polarization to cross nicol X and reach A. Surprisingly, Raleigh shows that the isolator is not unidirectional and he concludes that the two black bodies receive the same amount of light and the second law is not violated.

Rayleigh's argument leaves one to wonder how an isolator can function properly if *internal reflections cancel its unidirectional operation even under normal operation as a light diode*. Both Wien and Rayleigh's arguments are faulty as they rely on a non-working isolator design. In actual nicol-based isolators, light is not *reflected backward* by the nicols but *deflected and absorbed* by surrounding materials and collimators.

Mungan [1] asserts without a detailed proof that no violation of the second law occurs because heat from the hot object is absorbed by the isolator and

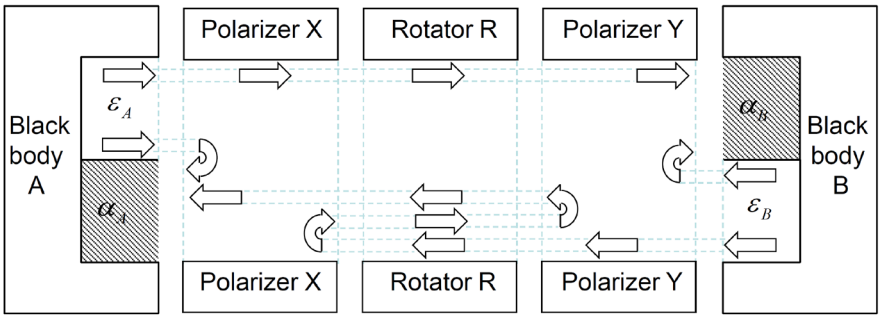

Figure 2. Rayleigh's thought experiment. Black bodies A and B receives the same amount of light. However, the design is faulty as the isolator is not unidirectional.

eventually re-radiated to the cold object, thereby reestablishing detailed balance.

2. Analysis of the Faraday Isolator

The analysis below provides a quantitative analysis of Mungan's argument and finds that Mungan is half right. Light is reradiated backward, but in insufficient amount to prevent a violation of detailed balance. The following thought experiment considers two black bodies A and B separated by a Faraday isolator. The isolator utilizes absorbing polarizers, thereby avoiding the reflection issue raised by the nicols employed by Wien and Rayleigh. The following analysis uses a large number of simple linear equations and is clarified by the drawings.

Before beginning the formal analysis, a baseline shall be established by analyzing a simpler device, that is one in which the polarization rotator within the Faraday isolator is replaced by a black body. Consider the system in Figure 3, comprised of black bodies A and B separated by a polarizer X, a blackbody Z, and a polarizer Y.

In this arrangement, Z replaces the polarization rotator. The dimensions of the transmission channels are intended to represent how much radiation flows through these channels.

Polarizers X and Y are ideal. They transmit half the light and absorb the remaining half. In the figure, emissivity is denoted by ε, absorptivity by α and transmissivity by τ. The system is in thermal equilibrium, therefore, $\varepsilon_A = \alpha_A$, $\varepsilon_B = \alpha_B$, $\varepsilon_{XA} = \alpha_{XB}$, $\varepsilon_{XZ} = \alpha_{XZ}$, $\varepsilon_{YB} = \alpha_{YB}$, $\varepsilon_{YZ} = \alpha_{YZ}$, $\varepsilon_{XA} = \alpha_{XB}$, $\varepsilon_{ZX} = \alpha_{ZX}$, and $\varepsilon_{ZY} = \alpha_{ZY}$. Therefore, the black bodies A and B are at the same temperature $T_A = T_B$ as per Stefan-Boltzmann law.

Let us now disturb the equilibrium state by suddenly replacing the black body Z with an ideal polarization rotator R as shown in Figure 4. We shall assume initially, as Wien and Rayleigh did, that the rotator is a perfect transmitter, and that it only rotates the plane of polarization without otherwise absorbing or emitting any light. Further down in this paper, we shall show that relaxing this assumption reduces the performance of the device but does not qualitatively change the conclusion of the experiment that detailed balance is violated.

In the instant immediately after the substitution, that is before the objects

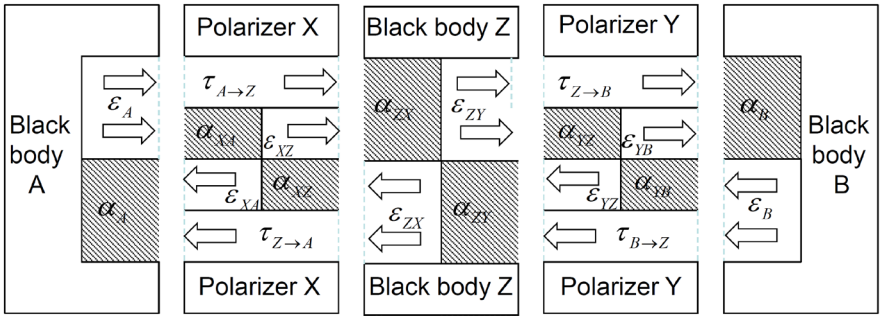

Figure 3. Replacing the polarization rotator Z of a Faraday isolator by a black body creates a perfectly symmetrical system in which two black bodies A and B reach isothermal equilibrium in compliance with detailed balance.

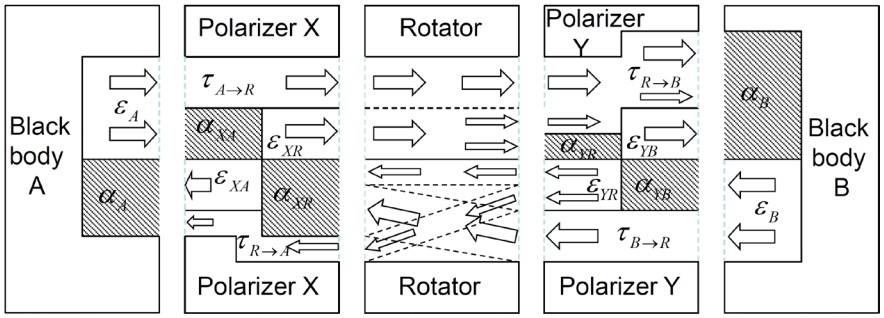

Figure 4. Reinserting the polarization rotator in the Faraday isolator breaks the system's symmetry allowing a temperature difference to develop between two black bodies A and B on either side of the isolator. Thermal equilibrium is reached when the forward flow of polarized light is compensated by a counter flow of non-polarized light that partially bypasses the input polarizer. The new equilibrium requires a temperature difference between A and B.

have time to change their temperatures, all emissivities remain the same but absorptivities can change. For example, ε_A is determined by the temperature of A before the substitution, therefore $\alpha_{XA} = \varepsilon_A/2$ must also be the same as before. However, $\alpha_A = \varepsilon_{XA} + \tau_{R\to A}$ must change immediately after the substitution because the polarizer transmits less light $\tau_{R\to A}$. A quick inspection of heat flow shows that A, being upstream in the light flow, absorbs less light immediately after the substitution, indicating that it will get colder after some time elapses. B is downstream, absorbs more light, indicating that it will get warmer. The following analysis solves the large number of linear equations that determine the thermal flow. The reader is invited to rely on the drawing to follow this analysis.

For the sake of simplicity, we define $\varepsilon_X = \varepsilon_{XA} = \varepsilon_{XR}$ because X is at the same temperature throughout. Similarly, $\varepsilon_Y = \varepsilon_{YB} = \varepsilon_{YR}$. Using these guidelines the following heat flow equations can be inferred by inspection from **Figure 3** (before the substitution) and from **Figure 4** (after the substitution). Polarizers are assumed to be ideal, allowing through half of non-polarized light, and absorbing the remaining half.

The amount of heat received by A and B immediately after the substitution can be quickly determined.

$$\alpha_A = \varepsilon_X + \frac{\varepsilon_Y}{2} \quad \text{(Note: } \varepsilon_X = \varepsilon_{XA} = \varepsilon_{XR};\ \varepsilon_Y = \varepsilon_{YB} = \varepsilon_{YR}\text{)} \tag{2}$$

and

$$\alpha_B = \varepsilon_Y + \frac{\varepsilon_X}{2} + \frac{\varepsilon_A}{2} \tag{3}$$

Since that the system was in equilibrium just before the substitution $\varepsilon_X = \varepsilon_Y$ (see **Figure 3**). Furthermore, since the polarizer is ideal, they transmit half of the light from the black bodies. The polarizers also absorb half of the light from the black bodies and emit half of the light. Hence $\varepsilon_X = \varepsilon_Y = \varepsilon_A/2$. At the instant immediately following the substitution all temperatures are the same as before the substitution and all emissivities remain the same. Using this information and combining (2) and (3) one can show that

$$\frac{\alpha_B}{\alpha_A} = \frac{5}{3} \tag{4}$$

which indicates that heat flows from A to B. Interestingly, the polarizers display the opposite tendency with X absorbing more light and Y absorbing less light. Since

$$\alpha_{XA} + \alpha_{XR} = \frac{1}{2}\varepsilon_A + \frac{1}{2}\varepsilon_{YR} + \frac{1}{2}\varepsilon_B \tag{5}$$

and

$$\alpha_{YB} + \alpha_{YR} = \frac{1}{2}\varepsilon_B + \frac{1}{2}\varepsilon_{XR} \tag{6}$$

one can show that

$$\frac{\alpha_{XA} + \alpha_{XR}}{\alpha_{YB} + \alpha_{YR}} = \frac{5}{3} \tag{7}$$

Immediately following the substitution, heat moves from black body A to black body B, away from the original equilibrium state. One can appreciate that a change does occur. The only way to prevent this shift in equilibrium is for the rotator R to behave exactly like the black body Z that it replaces (including being opaque to the polarized light that traverses it), which is obviously impossible even if the elements of the isolator including the polarizers and the rotator were not ideal. Eventually a new equilibrium is reached.

The question is what is the steady state of the black bodies A and B? Assuming zero net heat flow in or out of A, $\varepsilon_A = \alpha_A$:

$$\varepsilon_A = \alpha_A = \varepsilon_X + \frac{\varepsilon_Y}{2}. \tag{8}$$

Assuming zero net heat flow in or out of B, $\varepsilon_B = \alpha_B$:

$$\varepsilon_B = \alpha_B = \varepsilon_Y + \frac{\varepsilon_X}{2} + \frac{\varepsilon_A}{2}. \tag{9}$$

Subtracting Equation (9) from (8) produces

$$3\varepsilon_A - 2\varepsilon_B = \varepsilon_X - \varepsilon_Y. \tag{10}$$

Assuming zero net heat flow in or out of X, $2\varepsilon_X = \alpha_{XA} + \alpha_{XR}$:

$$2\varepsilon_X = \alpha_{XA} + \alpha_{XR} = \frac{\varepsilon_A}{2} + \frac{\varepsilon_Y}{2} + \frac{\varepsilon_B}{2}. \tag{11}$$

Assuming zero net heat flow in or out of Y, $2\varepsilon_Y = \alpha_{YB} + \alpha_{YR}$:

$$2\varepsilon_Y = \alpha_{YB} + \alpha_{YR} = \frac{\varepsilon_B}{2} + \frac{\varepsilon_X}{2}. \tag{12}$$

Subtracting Equation (12) from (11) yields

$$\frac{\varepsilon_A}{5} = \varepsilon_X - \varepsilon_Y. \tag{13}$$

Combining with (10) and solving for ε_A and ε_B we find that

$$\frac{\varepsilon_B}{\varepsilon_A} = \frac{7}{5} \tag{14}$$

indicating per Stefan-Boltzmann law that B is hotter than A, $T_B > T_A$. The polarizers are also at different temperatures. Combining Equations (13) and (8) produces:

$$\frac{\varepsilon_X}{\varepsilon_Y} = \frac{11}{8} \tag{15}$$

If one were to thermally clamp the two polarizers, forcefully setting $T_X = T_Y$ and $\varepsilon_X = \varepsilon_Y$, (as one may do in an experimental test of this effect) one would find from Equation (10):

$$\frac{\varepsilon_B}{\varepsilon_A} = \frac{3}{2} \tag{16}$$

This equilibrium state is illustrated in Figure 5 in which the dimensions are approximately proportional to the magnitude of the heat flows. One can see that B is warmer than A because ε_B is larger than ε_A. (This configuration may be more appropriate for an experiment involving film polarizers and rotators in a sandwich).

At room temperature, this difference in emissivity corresponds to a theoretical maximum temperature difference of 32˚C. Assuming polarizers and a rotator, each with a realistic transmissivity of 0.8, then one can show that $\varepsilon_B/\varepsilon_A = 1.256$ corresponding to a temperature ratio of $T_B/T_A = 1.058$ as per Stefan-Boltzmann law. At 300 K the temperature difference is $T_B - T_A = 17.6C$ which should easily be observable with careful calorimetric experimental procedures designed to avoid thermal shorts by convection and conduction. For an experiment running at room temperature the challenge is to find polarizers and rotators that operate at the corresponding black body radiation wavelength of about 10 microns.

Let us now revisit the assumption made by Wien and Rayleigh, and that was

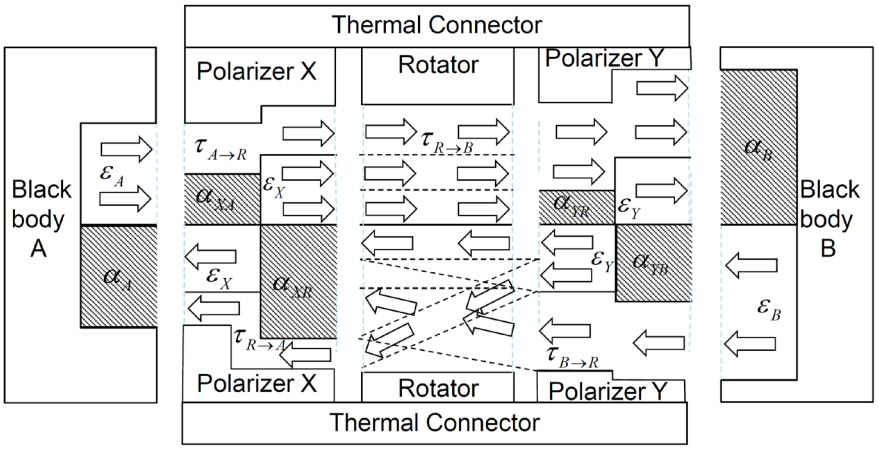

Figure 5. Thermally clamping the polarizers X and Y increases the temperature difference between A and B. The dimensions in the figure are approximately proportional to the conditions of Equation (16). The net flow of heat through the rotator is to the left, indicating that the system is not in static equilibrium and that heat flows to the right through the thermal connector.

also made in the analysis above. The rotator was assumed to be a perfect transmitter, and that it only rotates the plane of polarization without otherwise absorbing or emitting any light. Let us now consider the case of an imperfect isolator that partially behaves like a black body and partially like a perfect isolator. For example, we could combine **Figure 3** and **Figure 4** such that the rotator is 50% comprised of black body and 50% of perfect rotator. Clearly the performance of the Faraday isolator is degraded but some unidirectionality is retained and a difference in temperature between black bodies A and B still emerges and our conclusion that $T_B > T_A$ remains qualitatively unchanged.

The thought experiment above began with a modified Faraday isolator in which the rotator is replaced with an internal black body Z inserted between the two polarizers X and Y. This arrangement is perfectly symmetrical and isothermal equilibrium is reached. Replacing this internal black body with the rotator R introduces an asymmetry. Light flows preferentially in one direction causing a temperature difference between the two external black bodies A and B. Eventually a new equilibrium is reached with $T_B > T_A$, in which the forward flow of light is counterbalanced by a radiative counterflow of internally generated *non-polarized* light, half of which bypasses the blocking function of the input polarizer. (This explanation is different from Wien who incorrectly relied on a *polarized* counterflow). Statistical symmetry is restored. Mungan's assertion that the isolator would heat up and cause heat to flow backward thereby avoiding a violation of the second law, is shown to be unsubstantiated by the quantitative analysis above.

Reflective non-reciprocity is also well established for example in optical circulators and ferromagnetic optical materials. The reader is directed to [4] [5] [6] [7] [8] in particular to the non-reciprocal reflective thought experiment by Zhu and Fan [4]. The above discussion applies equally to reflective non-reciprocity.

The above discussion shows that a Faraday isolator placed between two black bodies causes the black body downstream to become hotter than the one upstream. The next question to be addressed is whether the second law and the principle of detailed balance are being violated. Two kinds of systems shall be discussed:

1. Homogeneous Faraday isolator systems.
2. Heterogeneous Faraday isolator systems.

3. Homogeneous Faraday Isolator Systems

Can this system convert heat to work, for example by placing a photoelectric device on the colder black body A to capture radiant thermal energy from the hotter black body B? The answer depends on the path taken by photons traveling from B to the photoelectric device on A.

The Faraday isolator carries thermal energy travels from the colder body A to the warmer body B. This shall be called the forward path. The path taken by photons traveling from B to the photoelectric device on A shall be called the reverse path.

If the reverse path is *homogenous* with the forward path, in other words, if the photons from B go through the Faraday isolator to reach the photoelectric device on A, then, these photons are indistinguishable from those in the forward path and no energy can be generated. This result complies with the H-theorem that requires homogeneity and indistinguishability of particles.

4. Heterogeneous Faraday Isolator Systems

If a heat engine is connected between A and B using a *reciprocal* photon or phonon flow channel, for example, a conventionally conducting material as shown in Figure 6, then useful work can be produced. The reason is that the heat phonons traveling through the thermal connectors are not affected by the non-reciprocity and they can be differentiated from the photons going through the isolator.

A Faraday isolator is a photon diode that produces a temperature difference between its input and output. Using a heterogeneous reverse path, this temperature difference can be used to convert heat to work. How is this concept different from the discredited idea that energy can be produced from the built-in potential in a semiconductor diode by connecting leads across the diode? In a diode, the carriers in the reverse path (the leads) have the same statistics as the ones in the forward path (the junction). The reverse path carriers are subjected to the same potential energy gradients as the diode's carriers. The electrical potentials at the contacts between the diode and the leads cancel out the diode built-in potential.

In contrast, the heat carriers in the system depicted in Figure 6 are different in the forward path and in the reverse path. In the forward path, the heat carriers are photons traveling through the non-reciprocal isolator and in the reverse path, they are phonons in a conventional reciprocal thermal conductor. The two kinds of heat carriers are physically different, have different statistics, and therefore, can be distinguished from each other. The H-theorem does not apply. Heat energy can be extracted from the system.

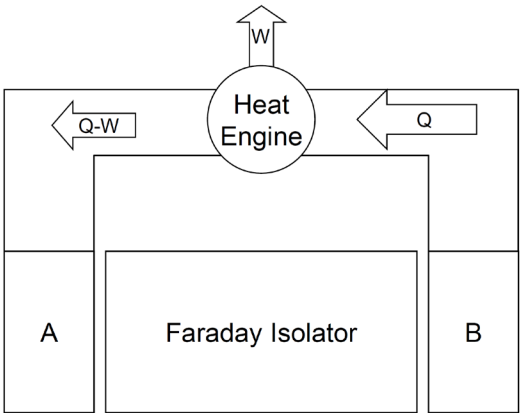

Figure 6. A heat engine can extract useful work from the non-reciprocal transmitter or reflector only if the connections to the heat engine do not go through the non-reciprocity. Such a system is heterogeneous and falls outside the coverage of the H-theorem.

5. Conclusions

This paper explores the limits of applicability of the second law. As stated by the H-Theorem, this law requires that the entropy of an isolated system can never decrease. The theorem, however, makes a crucially important assumption: the system must be homogeneous and its constituent particles indistinguishable. The Faraday isolator is used as a vehicle to exemplify two kinds of systems: the first, in which particles are homogeneously distributed and indistinguishable; the second, in which particles of different species such as fermions and bosons are heterogeneously distributed. This second kind of system falls outside of the H-Theorem.

The paper begins by showing that a temperature difference can arise spontaneously between two black bodies separated by a Faraday isolator.

If a heat engine is thermally connected to these black bodies by particles homogeneous with, and indistinguishable from those in the isolator, (*i.e.*, connecting photons traversing polarizers and rotator similarly configured as in the isolator) then the entire system conforms with the H-Theorem. The connecting photons produce the same temperature difference as those in the isolator. Even though a temperature difference does exist between the black bodies, this temperature difference cannot be communicated to the engine, and no useful work is generated in compliance with the second law.

This phenomenon is reminiscent of the built-in potential across a semiconductor junction. This potential is also unusable. The electrical carriers are homogeneous and indistinguishable throughout the system. Since electrical potential is a scalar field, contact potentials exactly cancel the built-in potential.

Both examples (isolator and semiconductor junction) describe homogeneous systems: the photons in the isolator behave the same as the photons in the thermal connector. Similarly, the electrons in the semiconductor junction have properties indistinguishable from the electrons in the electrical connectors. In such systems, voltage and temperature differences can occur spontaneously but are unusable to produce work. This result complies with the H-Theorem and the second law.

However, heterogeneous systems are not bound by the H-Theorem. As described in this paper, a Faraday isolator can produce a temperature difference between two black bodies. A heterogeneous system can be then formed by connecting a heat engine between the black bodies, using heat carriers with physical properties different from the photons in the isolator. The heat carriers could, for example, be heat phonons in a metallic conductor, not susceptible to the influence of the polarizers and the magnetic field in the rotator. The engine can then produce useful work.

The Faraday isolator is another example uncovered by the author, of heterogeneous systems falling outside the H-Theorem. These systems combine particles with different statistics such as fermions and bosons. In other publications [9] [10] the author shows that under proper conditions, a thermoelectric junction can spontaneously produce a detectable temperature difference even in the

absence of any electrical input. This effect has been observed in the lab [11] as a failure of the voltage-temperature Seebeck curve to pass through the origin. In the thermoelectric example, a heterogeneous system is formed when the thermal loop is closed by heat phonons in a thermally conductive medium. Since a thermometer can be viewed as a heat engine, the simple act of measuring a temperature difference output that arises without any electrical input constitutes a violation of the second law. Such violations are not mere microscopic fluctuations but have been observed [11] as large scale phenomena and dismissed as unexplained experimental error.

Acknowledgements

I thank my wife Penny for her unwavering support.

References

[1] Mungan, C.E. (1999) Faraday Isolators and Kirchhoff's Law: A Puzzle. https://www.usna.edu/Users/physics/mungan/_files/documents/Scholarship/FaradayIsolators.pdf

[2] Wien, W. (1900) Les lois théoriques du rayonnement, Rapports présentés au Congrès International de Physique, Paris, Vol. II, 29.

[3] Rayleigh (1901) On the Magnetic Rotation of Light and the Second Law of Thermodynamics. *Nature* (London), **64**, 577-578. https://doi.org/10.1038/064577e0

[4] Zhu, L. and Fan, S. (2014) Near-Complete Violation of Detailed Balance in Thermal Radiation. *Physical Review B*, **90**, Article Number: 220301. https://doi.org/10.1103/physrevb.90.220301

[5] Krichevtsov, B.B., Pavlov, V.V., Pisarev, R.V. and Gridnev, V.N. (1993) Spontaneous Non-Reciprocal Reflection of Light from Antiferromagnetic Cr_2O_3. *Journal of Physics*: *Condensed Matter*, **5**. https://doi.org/10.1088/0953-8984/5/44/014 http://iopscience.iop.org/article/10.1088/0953-8984/5/44/014/meta

[6] Dumelow, T. and Camley, R.E. (1996) Nonreciprocal Reflection of Infrared Radiation from Structures with Antiferromagnets and Dielectrics. *Physical Review B*, **54**, Article Number: 12232. https://doi.org/10.1103/PhysRevB.54.12232

[7] Stamps, R.L., Johnson, B.L. and Camley, R.E. (1991) Nonreciprocal Reflection from Semi-Infinite Antiferromagnets. *Physical Review B*, **43**, 3626. https://doi.org/10.1103/physrevb.43.3626

[8] He, C., Sun, X., Zhang, Z., Yuan, C., Lu, M., Chen, Y. and Sun, C. (2013) Nonreciprocal Resonant Transmission/Reflection Based on a One-Dimensional Photonic Crystal Adjacent to the Magneto-Optical Metal Film. *Optics Express*, **21**, Article No. 28933. https://doi.org/10.1364/OE.21.028933

[9] Levy, G.S. (2015) Anomalous Temperature Gradient in Non-Maxwellian Gases. In: *Ceramics for Energy Conversion*, *Storage*, *and Distribution Systems*, *Proceedings of the* 11*th International Conference on Ceramic Materials & Components for Energy & Environmental Applications*, Vancouver, BC, 14-19 June 2015, Wiley, Hoboken, Vol. 255.

[10] Levy, G.S. (2015) Quantum Game Beats Classical Odds—Thermodynamics Implications. *Entropy*, **17**, 7645-7657. https://doi.org/10.3390/e17117645

[11] Iwanaga, S., Toberer, E.S., LaLonde, A. and Snyder, G.J. (2011) A High Temperature Apparatus for Measurement of the Seebeck Coefficient. *Review of Scientific Instruments*, **82**, 1-6. https://doi.org/10.1063/1.3601358

Journal of Applied Mathematics and Physics, 2017, 5, 900-911
http://www.scirp.org/journal/jamp
ISSN Online: 2327-4379
ISSN Print: 2327-4352

Error Analysis and Variable Selection for Differential Private Learning Algorithm

Weilin Nie[1], Cheng Wang[2]

Huizhou University, Huizhou, China
Email: niewl@hzu.edu.cn, wangch@hzu.edu.cn

How to cite this paper: Nie, W.L. and Wang, C. (2017) Error Analysis and Variable Selection for Differential Private Learning Algorithm. *Journal of Applied Mathematics and Physics*, **5**, 900-911.
https://doi.org/10.4236/jamp.2017.54079

Received: February 14, 2017
Accepted: April 27, 2017
Published: April 30, 2017

Copyright © 2017 by authors and Scientific Research Publishing Inc.
This work is licensed under the Creative Commons Attribution International License (CC BY 4.0).
http://creativecommons.org/licenses/by/4.0/

Open Access

Abstract

In this paper, we construct a modified least squares regression algorithm which can provide privacy protection. A new concentration inequality is applied and the expected error bound is derived by error decomposition. Furthermore, via the error analysis, we find a method to choose an appropriate parameter ϵ to balance the error and privacy.

Keywords

Differential Privacy, Least Squares Regularization, Concentration Inequality, Error Decomposition

1. Introduction

Privacy protection attracts much attention in many branches of computer science. To deal with this, Dwork *et al.* proposed differential privacy in [1]. Soon [2] builds an exponential mechanism which is a useful approach to construct a differential private algorithm. The concept is introduced into learning theory in [3]. There, the authors consider output perturbation and object perturbation for ERM algorithms. Analysis of privacy and generalization for those algorithms also has been conducted. P. Jain and his collaborators have done a lot of work on differential private learning afterwards [4] [5] and etc. Recently, in [6], the authors find that the empirical average of the output from a differential private algorithm can converge to its expectation. And [7] provides another analysis of this convergence, which motivates our work.

In this paper, we consider the following statistical learning model (see [8] [9] for more details): The input space X is a compact metric space, and the output space is $Y \subset \mathbb{R}$ as a regression problem. Throughout the paper, we assume the output Y is uniformly bounded, *i.e.*, $|y| \le M$ for some $M > 0$ almost surely. On the sample space $Z := X \times Y$, we try to find a function $f : X \to Y$ via some

algorithms $\mathcal{A}$, reflecting the relationship between the input and output. Algorithm $\mathcal{A}$ relies on the random chosen sample $\mathbf{z}=\{z_i\}_{i=1}^m=\{(x_i,y_i)\}_{i=1}^m$, while the sample is drawn according to a distribution function ρ on Z. Furthermore, we assume there is a marginal distribution ρ_X on X and conditional distribution $\rho(y|x)$ on Y given some x.

Now we expect the algorithm can provide some privacy protection. We assume $\mathcal{A}$ satisfies the (ϵ,γ) differential private condition [1]. Denoting the Hamming distance between two sample sets $\{\mathbf{z}_1,\mathbf{z}_2\}$ is

$$d(\mathbf{z}_1,\mathbf{z}_2)=\#\{i=1,\cdots,m: z_{1,i}\neq z_{2,i}\},$$

i.e., there is only one element is different. Then (ϵ,γ)-differential private is defined as follows:

Definition 1 *A random algorithm $A: Z^m\to\mathcal{H}$ is (ϵ,γ)-differential private if for every two data sets $\mathbf{z}_1,\mathbf{z}_2$ satisfying $d(\mathbf{z}_1,\mathbf{z}_2)=1$, and every sets $\mathcal{O}\in\mathcal{H}$ we have*

$$\Pr\{A(\mathbf{z}_1)\in\mathcal{O}\}\leq \mathrm{e}^{\epsilon}\cdot\Pr\{A(\mathbf{z}_2)\in\mathcal{O}\}+\gamma.$$

Here $\mathcal{H}$ is a function space from X to Y, which is called the hypothesis space. In the sequel, we focus on the $(\epsilon,0)$-differential privacy with some $0<\epsilon<1$, which is always called ϵ-differential privacy for simplicity. How to choose an appropriate ϵ is a fundamental problem in differential private algorithms [10], and we will provide a method during our error estimation in the following sections.

2. Concentration Inequality

In this section, we study the error between average and expectation for an algorithm $\mathcal{A}$ providing ϵ-differential privacy. Our first result can be stated as follow:

Theorem 1 *If an algorithm $\mathcal{A}$ provides ϵ-differential privacy, and outputs a positive function $g_{z,\mathcal{A}}: X\times Y\to\mathbb{R}$ with bounded expectation $\mathbb{E}_{z,\mathcal{A}}g_{z,\mathcal{A}}\leq G$ for some $G>0$, where the expectation is taken over the sample via the algorithm output. Then*

$$\mathbb{E}_{z,\mathcal{A}}\left(\frac{1}{m}\sum_{i=1}^m g_{z,\mathcal{A}}(z_i)-\int_Z g_{z,\mathcal{A}}(z)\mathrm{d}\rho\right)\leq 2G\epsilon,$$

and

$$\mathbb{E}_{z,\mathcal{A}}\left(\int_Z g_{z,\mathcal{A}}(z)\mathrm{d}\rho-\frac{1}{m}\sum_{i=1}^m g_{z,\mathcal{A}}(z_i)\right)\leq 2G\epsilon.$$

Denote sample sets $\mathbf{w}_j=\{z_1,z_2,\cdots,z_{j-1},z_j',z_{j+1},\cdots,z_m\}$ for $j\in\{1,2,\cdots,m\}$. We observe that

$$\begin{aligned}\mathbb{E}_{z,\mathcal{A}}\left(\frac{1}{m}\sum_{i=1}^m g_{z,\mathcal{A}}(z_i)\right)&=\frac{1}{m}\sum_{i=1}^m\mathbb{E}_z\mathbb{E}_{\mathcal{A}}\left(g_{z,\mathcal{A}}(z_i)\right)\\&=\frac{1}{m}\sum_{i=1}^m\mathbb{E}_z\mathbb{E}_{z_i'}\int_0^{+\infty}\Pr_{\mathcal{A}}\{g_{z,\mathcal{A}}(z_i)\geq t\}\mathrm{d}t\end{aligned}$$

$$\leq \frac{1}{m}\sum_{i=1}^{m}\mathbb{E}_z\mathbb{E}_{z_i'}\int_0^{+\infty}\mathrm{e}^{\epsilon}\Pr_{\mathcal{A}}\left\{g_{w_i,\mathcal{A}}(z_i)\geq t\right\}\mathrm{d}t$$
$$= \mathrm{e}^{\epsilon}\frac{1}{m}\sum_{i=1}^{m}\mathbb{E}_{w_i}\mathbb{E}_{z_i}\mathbb{E}_{\mathcal{A}}\left(g_{w_i,\mathcal{A}}(z_i)\right) = \mathrm{e}^{\epsilon}\frac{1}{m}\sum_{i=1}^{m}\mathbb{E}_{w_i,\mathcal{A}}\mathbb{E}_{z_i}\left(g_{w_i,\mathcal{A}}(z_i)\right)$$
$$= \mathrm{e}^{\epsilon}\frac{1}{m}\sum_{i=1}^{m}\mathbb{E}_{w_i,\mathcal{A}}\int_Z g_{w_i,\mathcal{A}}(z)\mathrm{d}\rho = \mathrm{e}^{\epsilon}\frac{1}{m}\sum_{i=1}^{m}\mathbb{E}_{z,\mathcal{A}}\int_Z g_{z,\mathcal{A}}(z)\mathrm{d}\rho$$
$$= \mathrm{e}^{\epsilon}\mathbb{E}_{z,\mathcal{A}}\int_Z g_{z,\mathcal{A}}(z)\mathrm{d}\rho.$$

Then

$$\mathbb{E}_{z,\mathcal{A}}\left(\frac{1}{m}\sum_{i=1}^{m}g_{z,\mathcal{A}}(z_i)-\int_Z g_{z,\mathcal{A}}(z)\mathrm{d}\rho\right)$$
$$\leq\left(\mathrm{e}^{\epsilon}-1\right)\mathbb{E}_{z,\mathcal{A}}\left(\int_Z g_{z,\mathcal{A}}(z)\mathrm{d}\rho\right)\leq 2G\epsilon.$$

On the other hand,

$$\mathbb{E}_{z,\mathcal{A}}\int_Z g_{z,\mathcal{A}}(z)\mathrm{d}\rho = \frac{1}{m}\sum_{i=1}^{m}\mathbb{E}_z\mathbb{E}_{\mathcal{A}}\int_Z g_{z,\mathcal{A}}(z)\mathrm{d}\rho$$
$$= \frac{1}{m}\sum_{i=1}^{m}\mathbb{E}_{w_i}\mathbb{E}_{\mathcal{A}}\int_Z g_{w_i,\mathcal{A}}(z)\mathrm{d}\rho = \frac{1}{m}\sum_{i=1}^{m}\mathbb{E}_{w_i}\mathbb{E}_{\mathcal{A}}\int_Z g_{w_i,\mathcal{A}}(z_i)\mathrm{d}\rho(z_i)$$
$$= \frac{1}{m}\sum_{i=1}^{m}\mathbb{E}_{w_i}\mathbb{E}_{z_i}\mathbb{E}_{\mathcal{A}}\left(g_{w_i,\mathcal{A}}(z_i)\right) = \frac{1}{m}\sum_{i=1}^{m}\mathbb{E}_z\mathbb{E}_{z_i'}\int_0^{+\infty}\Pr_{\mathcal{A}}\left\{g_{w_i,\mathcal{A}}(z_i)\geq t\right\}\mathrm{d}t$$
$$\leq \frac{1}{m}\sum_{i=1}^{m}\mathbb{E}_z\mathbb{E}_{z_i'}\mathrm{e}^{\epsilon}\int_0^{+\infty}\Pr_{\mathcal{A}}\left\{g_{z,\mathcal{A}}(z_i)\geq t\right\}\mathrm{d}t$$
$$= \mathrm{e}^{\epsilon}\frac{1}{m}\sum_{i=1}^{m}\mathbb{E}_z\mathbb{E}_{\mathcal{A}}\left(g_{z,\mathcal{A}}(z_i)\right) = \mathrm{e}^{\epsilon}\mathbb{E}_{z,\mathcal{A}}\frac{1}{m}g_{z,\mathcal{A}}(z_i).$$

This leads to

$$\mathbb{E}_{z,\mathcal{A}}\left(\int_Z g_{z,\mathcal{A}}(z)\mathrm{d}\rho-\frac{1}{m}\sum_{i=1}^{m}g_{z,\mathcal{A}}(z_i)\right)$$
$$=\left(\mathrm{e}^{\epsilon}-1\right)\mathbb{E}_{z,\mathcal{A}}\frac{1}{m}\sum_{i=1}^{m}g_{z,\mathcal{A}}(z_j)\leq 2G\epsilon.$$

These verify our results.

Remark 1 *Similar results are proposed in* [6] *and* [7]. *However, there the authors limits the function to take value in* $[0,1]$ *or* $\{0,1\}$, *our result here extends theirs to the function taking value in* $\mathbb{R}^+$. *This makes our following error analysis implementable.*

3. Differential Private Learning Algorithm

In this section we consider the differential private least squares regularization algorithm. For a Mercer kernel K defined on $X\times X$, the function space $\mathcal{H}_K := \mathrm{span}\left\{K(x,\cdot), x\in X\right\}$ is the induced reproducing kernel Hilbert space (RKHS). Denote $K_x(y)=K(x,y)$ for any $x,y\in X$, and $\kappa=\sup_{x,y\in X}\sqrt{K(x,y)}$. It is well known that $f(x)=\langle f, K_x\rangle_K$ as the reproducing property. In the sequel, we always assume $|y|\leq M$ for some constant $M>0$. The least squares regularization algorithm, which has been extensively studied in such as [8] [11] [12] and etc. is:

$$f_{z,\lambda} = \arg\min_{f\in\mathcal{H}_K} \frac{1}{m}\sum_{i=1}^{m}\left(f(x_i)-y_i\right)^2 + \lambda\|f\|_K^2. \quad (1)$$

Denote π as a projection operator as we did in [13] [14]:

$$\pi\left(f(x)\right) = \begin{cases} M, & f(x) > M \\ f(x), & -M \le f(x) \le M \\ -M, & f(x) < -M \end{cases}.$$

Then we add a noise term b in the original algorithm (1) like the output perturbation algorithm in [3]:

$$f_{z,\mathcal{A}}(x) = \pi\left(f_{z,\lambda}(x)\right) + b \quad (2)$$

where the density of b is independent with z which will be clarified in the following analysis. Moreover, we take the following notation for simplicity:

$$\mathcal{E}(f) = \int_Z \left(f(x)-y\right)^2 \mathrm{d}\rho,\ \mathcal{E}_z(f) = \frac{1}{m}\sum_{i=1}^{m}\left(f(x_i)-y_i\right)^2.$$

Definition 2 *We denote Δf_z as the maximum infinite norm of difference when changing one sample point in z, i.e., if $d(\mathbf{z},\mathbf{z}')=1$,*

$$\Delta f_z = \sup_{z,z'}\|f_z - f_{z'}\|_\infty.$$

Then we have the following result:

Lemma 1 *Assume $\Delta\pi\left(f_{z,\lambda}(x)\right)$ is bounded, and b has density function proportion to $\exp\left\{-\frac{\epsilon|b|}{\Delta\pi\left(f_{z,\lambda}\right)}\right\}$, then algorithm (2) provides ϵ-differential privacy.*

The proof is just as Theorem 4 in [15]. For all possible function r, and $\mathbf{z},\mathbf{z}'$ differ in one element, then

$$\Pr\left\{f_{z,\mathcal{A}} = r\right\} = \Pr_b\left\{b = r - \pi\left(f_{z,\lambda}\right)\right\} \propto \exp\left(-\frac{\epsilon\left\|r-\pi\left(f_{z,\lambda}\right)\right\|_\infty}{\Delta\pi\left(f_{z,\lambda}\right)}\right),$$

and

$$\Pr\left\{f_{z',\mathcal{A}} = r\right\} = \Pr_b\left\{b = r - \pi\left(f_{z',\lambda}\right)\right\} \propto \exp\left(-\frac{\epsilon\left\|r-\pi\left(f_{z',\lambda}\right)\right\|_\infty}{\Delta\pi\left(f_{z',\lambda}\right)}\right).$$

So

$$\Pr\left\{f_{z,\mathcal{A}} = r\right\} \le \Pr\left\{\pi\left(f_{z',\mathcal{A}}\right) = r\right\} \times \mathrm{e}^{\frac{\epsilon\left\|\pi\left(f_{z,\lambda}\right)-\pi\left(f_{z',\lambda}\right)\right\|_\infty}{\Delta\pi\left(f_{z,\lambda}\right)}} \le \mathrm{e}^{\epsilon}\Pr\left\{f_{z',\mathcal{A}} = r\right\}.$$

Then the lemma is proved by a union bound.

Now we will bound the term $\Delta f_{z,\lambda}$.

Lemma 2 *For the function $f_{z,\lambda}$ obtained from algorithm (1), assume $\|f_{z,\lambda}\|_K \le R$ for any $\mathbf{z}\in Z^m$ for some $R \ge M$, and $0<\lambda\le 1$, we have*

$$\Delta f_{z,\lambda} \le \frac{2R\kappa^2(\kappa+1)}{\lambda m}.$$

Assume $f_{z,\lambda}$ and $f_{z',\lambda}$ are two results derived via algorithm (1) given any sample set $\boldsymbol{z}, \boldsymbol{z}'$ satisfying $d(\boldsymbol{z}, \boldsymbol{z}') = 1$. Without loss of generality, we set $\boldsymbol{z}' = (z_1, z_2, \cdots, z_{m-1}, z_{m'})$. Since the two functions are both the optimizer of algorithm (1), take derivative for f we have

$$\frac{2}{m}\sum_{i=1}^{m}\left(f_{z,\lambda}(x_i) - y_i\right)K_{x_i} + 2\lambda f_{z,\lambda} = 0$$

and

$$\frac{2}{m}\sum_{i=1}^{m-1}\left(f_{z',\lambda}(x_i) - y_i\right)K_{x_i} + \frac{2}{m}\left(f_{z',\lambda}(x'_m) - y'_m\right)K_{x_m} + 2\lambda f_{z',\lambda} = 0.$$

These lead to

$$\begin{aligned}&\frac{1}{m}\sum_{i=1}^{m}\left(f_{z,\lambda}(x_i) - f_{z',\lambda}(x_i)\right)K_{x_i} + \lambda\left(f_{z,\lambda} - f_{z',\lambda}\right)\\ &= \frac{1}{m}\left[\left(f_{z',\lambda}(x'_m) - y'_m\right)K_{x'_m} - \left(f_{z,\lambda}(x_m) - y_m\right)K_{x_m}\right].\end{aligned}$$

Take inner product with $f_{z,\lambda} - f_{z',\lambda}$ by both sides we have

$$\begin{aligned}&\frac{1}{m}\sum_{i=1}^{m}\left(f_{z,\lambda}(x_i) - f_{z',\lambda}(x_i)\right)^2 + \lambda\left\|f_{z,\lambda} - f_{z',\lambda}\right\|_K^2\\ &= \frac{1}{m}\left[\left(f_{z',\lambda}(x'_m) - y'_m\right)\left(f_{z,\lambda}(x'_m) - f_{z',\lambda}(x'_m)\right)\right.\\ &\qquad \left. - \left(f_{z,\lambda}(x_m) - y_m\right)\left(f_{z,\lambda}(x_m) - f_{z',\lambda}(x_m)\right)\right].\end{aligned}$$

This means

$$\begin{aligned}\lambda\left\|f_{z,\lambda} - f_{z',\lambda}\right\|_K^2 &\le \frac{1}{m}\left[\left|f_{z',\lambda}(x'_m) - y'_m\right| + \left|f_{z,\lambda}(x_m) - y_m\right|\right]\cdot\left\|f_{z,\lambda} - f_{z',\lambda}\right\|_\infty\\ &\le \frac{1}{m}\left(\left\|f_{z',\lambda}\right\|_\infty + \left\|f_{z,\lambda}\right\|_\infty + 2M\right)\kappa\left\|f_{z,\lambda} - f_{z',\lambda}\right\|_K.\end{aligned}$$

The last inequality is from the fact that

$$\|f\|_\infty = \sup_{x\in X} f(x) = \sup_{x\in X}\langle f, K_x\rangle_K \le \|K_x\|_K \cdot \|f\|_K \le \kappa\|f\|_K.$$

Since $\left\|f_{z,\lambda}\right\|_K \le R$, then $\left\|f_{z',\lambda}\right\|_K \le R$ as well. Therefore,

$$\left\|f_{z,\lambda} - f_{z',\lambda}\right\|_K \le \frac{1}{\lambda m}(2R\kappa + 2M)\kappa \le \frac{2R\kappa(\kappa+1)}{\lambda m}$$

for any $0 < \lambda \le 1$. So

$$\left\|f_{z,\lambda} - f_{z',\lambda}\right\|_\infty \le \frac{2R\kappa^2(\kappa+1)}{\lambda m}$$

for any $\boldsymbol{z}, \boldsymbol{z}'$, and our lemma holds.

It can be easily verified by discussion that

$$\left\|\pi\left(f_{z,\lambda}\right) - \pi\left(f_{z',\lambda}\right)\right\|_\infty \le \left\|f_{z,\lambda} - f_{z',\lambda}\right\|_\infty$$

for any $\boldsymbol{z}, \boldsymbol{z}'$, so we have the choice of noise b and the result for algorithm (2).

Proposition 1 *Assume* $\left\|f_{z,\lambda}\right\|_K \le R$ *for any* $\boldsymbol{z} \in Z^m$ *for some* $R \ge M$, *and* b *takes value in* $(-\infty, +\infty)$, *we choose the density of* b *to be*

$\frac{1}{\alpha}\exp\left(-\frac{\lambda m\epsilon|b|}{2R\kappa^2(\kappa+1)}\right)$, *where* $\alpha=\frac{4R\kappa^2(\kappa+1)}{\lambda m\epsilon}$, *then the algorithm* (2) *provides* ϵ *-differential privacy.*

The proof is by combining the two lemmas and the inequality above. And by simply calculation we can get the expression of α.

4. Error Analysis for Differential Private Learning Algorithm

In this section, we will study the expectation of the error between $\mathcal{E}(f_{z,\mathcal{A}})-\mathcal{E}(f_\rho)$, where $f_\rho=\int_Y y\mathrm{d}\rho(y|x)$ is the regression function which minimizes $\mathcal{E}(f)$. Firstly we shall introduce the error decomposition:

$$\begin{aligned}
&\mathcal{E}(f_{z,\mathcal{A}})-\mathcal{E}(f_\rho)\le\mathcal{E}(f_{z,\mathcal{A}})-\mathcal{E}(f_\rho)+\lambda\|f_{z,\lambda}\|_K^2\\
&\le\mathcal{E}(f_{z,\mathcal{A}})-\mathcal{E}_z(f_{z,\mathcal{A}})+\mathcal{E}_z(f_{z,\mathcal{A}})-\mathcal{E}_z(\pi(f_{z,\lambda}))\\
&\quad+\mathcal{E}_z(\pi(f_{z,\lambda}))+\lambda\|f_{z,\lambda}\|_K^2-\mathcal{E}(f_\rho)\\
&\le\mathcal{E}(f_{z,\mathcal{A}})-\mathcal{E}_z(f_{z,\mathcal{A}})+\mathcal{E}_z(f_{z,\mathcal{A}})-\mathcal{E}_z(\pi(f_{z,\lambda}))\\
&\quad+\mathcal{E}_z(f_{z,\lambda})+\lambda\|f_{z,\lambda}\|_K^2-\mathcal{E}(f_\rho)\\
&\le\mathcal{E}(f_{z,\mathcal{A}})-\mathcal{E}_z(f_{z,\mathcal{A}})+\mathcal{E}_z(f_{z,\mathcal{A}})-\mathcal{E}_z(\pi(f_{z,\lambda}))\\
&\quad+\mathcal{E}_z(f_\lambda)+\lambda\|f_\lambda\|_K^2-\mathcal{E}(f_\rho)\\
&\le\mathcal{R}_1+\mathcal{R}_2+\mathcal{S}+D(\lambda),
\end{aligned}\tag{3}$$

where f_λ is a function in $\mathcal{H}_K$ to be determined and

$$\mathcal{R}_1=\mathcal{E}(f_{z,\mathcal{A}})-\mathcal{E}_z(f_{z,\mathcal{A}}),$$

$$\mathcal{R}_2=\mathcal{E}_z(f_{z,\mathcal{A}})-\mathcal{E}_z(\pi(f_{z,\lambda})),$$

$$\mathcal{S}=\mathcal{E}_z(f_\lambda)-\mathcal{E}(f_\lambda),$$

$$D(\lambda)=\mathcal{E}(f_\lambda)-\mathcal{E}(f_\rho)+\lambda\|f_\lambda\|_K^2.$$

Here $\mathcal{R}_1$ and $\mathcal{R}_2$ involve the function $f_{z,\mathcal{A}}$ from random algorithm (2) so we call them random errors. $\mathcal{S}$ and $D(\lambda)$ are similar as classical ones in the past literature in learning theory and we still call them sample error and approximation error. In the following, we will study these errors respectively.

4.1. Error Bounds for Random Errors

Proposition 2 *For function* $f_{z,\mathcal{A}}$ *obtained from algorithm* (2) *with density of* b *as described in Proposition* 1, *we have*

$$\mathbb{E}_{z,\mathcal{A}}\mathcal{R}_1\le 8\epsilon\left(\frac{2R^2\kappa^4(\kappa+1)^2}{\lambda^2m^2\epsilon^2}+M^2\right).$$

Note that

$$\mathcal{R}_1=\int_Z(f_{z,\mathcal{A}}(x)-y)^2\,\mathrm{d}\rho-\frac{1}{m}\sum_{i=1}^m(f_{z,\mathcal{A}}(x_i)-y_i)^2,$$

analogous analysis to the proof of Theorem 1 tells us that

$$\begin{aligned}
&\mathbb{E}_{z,\mathcal{A}}\left(\int_Z\left(f_{z,\mathcal{A}}(x)-y\right)^2\mathrm{d}\rho-\frac{1}{m}\sum_{i=1}^m\left(f_{z,\mathcal{A}}(x_i)-|y_i\right)^2\right)\\
&\le\left(\mathrm{e}^{\epsilon}-1\right)\mathbb{E}_z\mathbb{E}_{\mathcal{A}}\frac{1}{m}\sum_{i=1}^m\left(\pi\left(f_{z,\lambda}(x_i)\right)+b-y_i\right)^2\mathrm{d}\rho\\
&=2\epsilon\mathbb{E}_z\mathbb{E}_b\left(b^2+b\left(\pi\left(f_{z,\lambda}(x_i)\right)-y_i\right)+\left(\pi\left(f_{z,\lambda}(x_i)\right)-y_i\right)^2\right)\\
&\le 2\epsilon\left(\frac{8R^2\kappa^4(\kappa+1)^2}{\lambda^2m^2\epsilon^2}+4M^2\right),
\end{aligned}$$

which verifies the proposition.

For the term $\mathcal{R}_2$, we have the same analysis.

Proposition 3 *For function* $f_{z,\mathcal{A}}$ *obtained from algorithm* (2) *with density of* b *as described in Proposition 1, we have*

$$\mathbb{E}_{z,\mathcal{A}}\mathcal{R}_2\le\frac{8R^2\kappa^4(\kappa+1)^2}{\lambda^2m^2\epsilon^2}.$$

Since

$$\begin{aligned}
\mathcal{R}_2&=\mathcal{E}_z\left(f_{z,\mathcal{A}}\right)-\mathcal{E}_z\left(\pi\left(f_{z,\lambda}\right)\right)\\
&=\frac{1}{m}\sum_{i=1}^m\left[\left(f_{z,\mathcal{A}}(x_i)-y_i\right)^2-\left(\pi\left(f_{z,\lambda}(x_i)\right)-y_i\right)^2\right]\\
&=\frac{1}{m}\sum_{i=1}^m b\left(b+2\pi\left(f_{z,\lambda}(x_i)\right)-2y_i\right)\\
&=b^2+2b\cdot\frac{1}{m}\sum_{i=1}^m\left(\pi\left(f_{z,\lambda}(x_i)\right)-y_i\right),
\end{aligned}$$

we have

$$\mathbb{E}_{z,\mathcal{A}}\mathcal{R}_2=\mathbb{E}_z\mathbb{E}_bb^2\le\frac{8R^2\kappa^4(\kappa+1)^2}{\lambda^2m^2\epsilon^2}.$$

And the proposition is proved.

4.2. Error Estimates for Sample Error and Approximation Error

Error estimates for sample error and approximation error have been extensively studied since [8]. Here we provide the proof for completeness. It is known that f_λ in the error decomposition (3) can be arbitrarily chosen in $\mathcal{H}_K$ in [12] [13] [14] and etc. Here we simply choose it to be the classical one

$$f_\lambda=\arg\min_{f\in\mathcal{H}_K}\mathcal{E}(f)+\lambda\|f\|_K^2.$$

From [16] [17] we have the expression of f_λ is

$$f_\lambda=\left(L_K+\lambda\right)^{-1}L_Kf_\rho,$$

where L_K is the operator defined on $L^2_{\rho_X}$ as

$$L_Kf(t)=\int_Xf(x)K(x,t)\mathrm{d}\rho_X.$$

[8] told us that L_K has a eigenvalue sequence $\{\mu_i\}_{i\ge1}$ satisfies $\mu_i>0$ $\mu_i\to0$ when $i\to\infty$, and $\|L_K\|\le\kappa^2$. Now we recall the Hoeffding inequality [18].

Lemma 3 *Let* ξ *be a random variable on a probability space* Z *satisfying* $\left|\xi(z)-\mathbb{E}\xi\right|\le B$ *for some* $B>0$ *for almost all* $z\in Z$, *then*

$$\Pr\left\{\left|\frac{1}{m}\sum_{i=1}^{m}\xi(z_i)-\mathbb{E}\xi\ge\varepsilon\right|\right\}\le 2\exp\left\{-\frac{m\varepsilon^2}{2B^2}\right\}.$$

Then we have the following analysis.

Proposition 4 *For* f_λ *and* f_ρ *defined as above, assume* $f_\rho\in L_K^r\left(L^2_{\rho_X}\right)$, *we have*

$$\mathbb{E}_{z,\mathcal{A}}\mathcal{S}+D(\lambda)\le\frac{8\sqrt{2\pi}M^2}{\sqrt{m}}+\lambda^{\min\{2r,1\}}\left(\kappa^{4r-2}+\kappa^{4r-4}+2\right)\left\|L_K^{-r}f_\rho\right\|_\rho^2.$$

Firstly we bound the sample error.

$$\begin{aligned}\mathcal{S}&=\mathcal{E}(f_\lambda)-\mathcal{E}_z(f_\lambda)\\&=\int_Z\left(f_\lambda(x)-y\right)^2\mathrm{d}\rho-\frac{1}{m}\sum_{i=1}^{m}\left(f_\lambda(x_i)-y_i\right)^2.\end{aligned}$$

Let $\xi(z)=-\left(f_\lambda(x)-y\right)^2$, since $\left|f_\rho(x)\right|=\left|\int_Y y\mathrm{d}\rho(y|x)\right|\le M$, and

$$\begin{aligned}\left\|f_\lambda\right\|_\infty&=\left\|\left(L_K+\lambda I\right)^{-1}L_Kf_\rho\right\|_\infty\\&\le\left\|\left(L_K+\lambda I\right)^{-1}L_K\right\|\cdot\left\|f_\rho\right\|_\infty\le M,\end{aligned}$$

we have $\left|\xi-\mathbb{E}\xi\right|\le 8M^2$. So from Hoeffding inequality there holds

$$\begin{aligned}&\Pr_z\left\{\left|\int_Z\left(f_\lambda(x)-y\right)^2\mathrm{d}\rho-\frac{1}{m}\sum_{i=1}^{m}\left(f_\lambda(x_i)-y_i\right)^2\right|\ge\varepsilon\right\}\\&\le 2\exp\left\{-\frac{m\varepsilon^2}{128M^4}\right\}.\end{aligned}$$

Then we have

$$\begin{aligned}\mathbb{E}_{z,\mathcal{A}}\mathcal{S}\le\mathbb{E}_z\left|\mathcal{S}\right|&=\int_0^{+\infty}\Pr_z\left\{\left|\mathcal{S}\right|\ge t\right\}\mathrm{d}t\\&=\int_0^{+\infty}2\exp\left\{-\frac{mt^2}{128M^4}\right\}\mathrm{d}t\le\frac{8\sqrt{2\pi}M^2}{\sqrt{m}}.\end{aligned}$$

For the approximation error, note that $\mathcal{E}(f_\lambda)-\mathcal{E}(f_\rho)=\left\|f_\lambda-f_\rho\right\|_\rho^2$ [9] which is independent with z and b, we have

$$\begin{aligned}\mathbb{E}_{z,\mathcal{A}}\mathcal{E}(f_\lambda)-\mathcal{E}(f_\rho)&=\left\|f_\lambda-f_\rho\right\|_\rho^2\\&=\left\|\left(L_K+\lambda I\right)^{-1}\left(L_K-\left(L_K+\lambda I\right)\right)f_\rho\right\|_\rho^2\\&=\lambda^2\left\|\left(L_K+\lambda I\right)^{-1}L_K^rL_K^{-r}f_\rho\right\|_\rho^2\\&\le\lambda^2\left\|\left(L_K+\lambda I\right)^{-1}L_K^r\right\|^2\left\|L_K^{-r}f_\rho\right\|_\rho^2\\&\le\begin{cases}\lambda^{2r}\left\|L_K^{-r}f_\rho\right\|_\rho^2, & r\le 1\\ \lambda^2\kappa^{4(r-1)}\left\|L_K^{-r}f_\rho\right\|_\rho^2, & r>1\end{cases}\\&\le\lambda^{\min\{2r,2\}}\left(\kappa^{4(r-1)}+1\right)\left\|L_K^{-r}f_\rho\right\|_\rho^2.\end{aligned}$$

On the other hand, in [8], the authors pointed out that $\|f\|_K = \left\|L_K^{-\frac{1}{2}} f\right\|_\rho$ for any $f \in \mathcal{H}_K$. So

$$\begin{aligned}
\mathbb{E}_{z,\mathcal{A}} \lambda \|f_\lambda\|_K^2 &= \lambda \left\|\left(L_K + \lambda I\right)^{-1} L_K f_\rho\right\|_K^2 \\
&= \lambda \left\|\left(L_K + \lambda I\right)^{-1} L_K^{\frac{1}{2}} f_\rho\right\|_\rho^2 \\
&\le \lambda \left\|\left(L_K + \lambda I\right)^{-1} L_K^{\frac{1}{2}+r}\right\|^2 \cdot \left\|L_K^{-r} f_\rho\right\|_\rho^2 \\
&\le \begin{cases} \lambda^{2r} \left\|L_K^{-r} f_\rho\right\|_\rho^2, & r \le \frac{1}{2} \\ \lambda \cdot \kappa^{4r-2} \left\|L_K^{-r} f_\rho\right\|_\rho^2, & r > \frac{1}{2} \end{cases} \\
&\le \lambda^{\min\{2r,1\}} \left(\kappa^{4r-2} + 1\right) \left\|L_K^{-r} f_\rho\right\|_\rho^2.
\end{aligned}$$

Combining the 3 bounds above, we can verify the proposition.

4.3. Convergence Result with Fixed ϵ

In our analysis for $\mathbb{E}_{z,\mathcal{A}} \mathcal{R}_1$ above, we indeed have the following result

$$\mathbb{E}_{z,\mathcal{A}} \mathcal{R}_1 \le \frac{16R^2\kappa^4 (\kappa+1)^2}{\lambda^2 m^2 \epsilon} + 2\epsilon \mathbb{E}_z \mathcal{E}_z \left(\pi\left(f_{z,\lambda}\right)\right).$$

Therefore, the error decomposition can be

$$\begin{aligned}
&\mathbb{E}_{z,\mathcal{A}} \left(\mathcal{E}\left(f_{z,\mathcal{A}}\right) - (1+2\epsilon)\mathcal{E}\left(f_\rho\right)\right) \\
&= \mathbb{E}_{z,\mathcal{A}} \left(\mathcal{R}_1 + \mathcal{R}_2 + \mathcal{S} + D(\lambda) - 2\epsilon\mathcal{E}\left(f_\rho\right)\right) \\
&\le \frac{16R^2\kappa^4 (\kappa+1)^2}{\lambda^2 m^2 \epsilon} + \frac{8R^2\kappa^4 (\kappa+1)^2}{\lambda^2 m^2 \epsilon^2} + \mathbb{E}_z 2\epsilon \left(\mathcal{E}_z\left(\pi\left(f_{z,\lambda}\right)\right) - \mathcal{E}\left(f_\rho\right)\right) + \mathbb{E}_z \left(\mathcal{S} + D(\lambda)\right) \\
&\le \frac{24R^2\kappa^4 (\kappa+1)^2}{\lambda^2 m^2 \epsilon^2} + 2\epsilon \mathbb{E}_z \left(\mathcal{E}_z\left(f_{z,\lambda}\right) + \lambda \left\|f_{z,\lambda}\right\|_K^2 - \mathcal{E}\left(f_\rho\right)\right) + \mathbb{E}_z \left(\mathcal{S} + D(\lambda)\right) \\
&\le \frac{24R^2\kappa^4 (\kappa+1)^2}{\lambda^2 m^2 \epsilon^2} + 2\epsilon \mathbb{E}_z \left(\mathcal{E}_z\left(f_\lambda\right) + \lambda \left\|f_\lambda\right\|_K^2 - \mathcal{E}\left(f_\rho\right)\right) + \mathbb{E}_z \left(\mathcal{S} + D(\lambda)\right) \\
&\le \frac{24R^2\kappa^4 (\kappa+1)^2}{\lambda^2 m^2 \epsilon^2} + (1+2\epsilon) \mathbb{E}_z \left(\mathcal{S} + D(\lambda)\right) \\
&\le \frac{24M^2\kappa^4 (\kappa+1)^2}{\lambda^3 m^2 \epsilon^2} + \frac{3\sqrt{2\pi} M^2 (1+2\epsilon)}{\sqrt{m}} + \lambda^{\min\{1,2r\}} \left(\kappa^{4r-2} + \kappa^{4r-4} + 2\right) \left\|L_K^{-r} f_\rho\right\|_\rho^2.
\end{aligned}$$

Then by choosing $\lambda = \left(\frac{1}{m}\right)^{2/\min\{4,3+2r\}}$ for balance we have the following result.

Theorem 2 *Let* $f_{z,\mathcal{A}}$ *derived from algorithm* (2), $f_{z,\lambda}$, f_λ *defined in the above subsections, and assume* $f_\rho \in L_K^r \left(L_{\rho_X}\right)$, *take* $\lambda = \left(\frac{1}{m}\right)^{2/\min\{4,3+2r\}}$, *there holds*

$$\mathbb{E}_{z,\mathcal{A}}\left(\mathcal{E}\left(f_{z,\mathcal{A}}\right)-\left(1+2\epsilon\right)\mathcal{E}\left(f_{\rho}\right)\right)\leq C_{\epsilon}\left(\frac{1}{m}\right)^{\min\left\{\frac{1}{2},\frac{4r}{3+2r}\right\}},$$

where constant

$$C_{\epsilon}=\frac{24M^{2}\kappa^{4}\left(\kappa+1\right)^{2}}{\epsilon^{2}}+8\sqrt{2\pi}M^{2}\left(1+2\epsilon\right)+\left(\kappa^{4r-2}+\kappa^{4r-4}+2\right)\left\|L_{K}^{-r}f_{\rho}\right\|_{\rho}^{2}.$$

4.4. Selection of ϵ and Total Error Bound

From the analysis for random error, sample error and approximation error above, we can obtain the whole error bound as follow.

Theorem 3 *Let* $f_{z,\mathcal{A}}$ *derived from algorithm* (2), $f_{z,\lambda}$, f_{λ} *defined in the above subsections, and assume* $f_{\rho}\in L_{K}^{r}\left(L_{\rho_{X}^{2}}\right)$, *take*

$$\lambda=\left(\frac{1}{m\epsilon}\right)^{2/\min\{4,3+2r\}},$$

and

$$\epsilon=\left(\frac{1}{\sqrt{m}}\right)^{\min\{1/3,4r/(3+6r)\}}$$

we have

$$\mathbb{E}_{z,\mathcal{A}}\left(\mathcal{E}\left(f_{z,\mathcal{A}}\right)-\mathcal{E}\left(f_{\rho}\right)\right)\leq\tilde{C}\left(\frac{1}{m}\right)^{\min\left\{\frac{1}{3},\frac{4r}{3+6r}\right\}},$$

where constant

$$\begin{aligned}\tilde{C}=&8\left(1+\sqrt{2\pi}\right)M^{2}+24M^{2}\kappa^{4}\left(\kappa+1\right)^{2}\\&+\left(\kappa^{4r-2}+\kappa^{4r-4}+2\right)\left\|L_{K}^{-r}f_{\rho}\right\|_{\rho}^{2}.\end{aligned}$$

It can be seen from error decomposition (3) that

$$\begin{aligned}\mathbb{E}_{z,\mathcal{A}}\left(\mathcal{E}\left(f_{z,\mathcal{A}}\right)-\mathcal{E}\left(f_{\rho}\right)\right)&\leq\mathbb{E}_{z,\mathcal{A}}\left(\mathcal{E}\left(f_{z,\mathcal{A}}\right)-\mathcal{E}\left(f_{\rho}\right)+\lambda\left\|f_{z,\lambda}\right\|_{K}^{2}\right)\\&\leq\mathbb{E}_{z,\mathcal{A}}\left(\mathcal{R}_{1}+\mathcal{R}_{2}+\mathcal{S}+D\left(\lambda\right)\right)\\&\leq 8\epsilon\left(\frac{2R^{2}\kappa^{4}\left(\kappa+1\right)^{2}}{\lambda^{2}m^{2}\epsilon^{2}}+M^{2}\right)+\frac{8R^{2}\kappa^{4}\left(\kappa+1\right)^{2}}{\lambda^{2}m^{2}\epsilon^{2}}\\&\quad+\frac{8\sqrt{2\pi}M^{2}}{\sqrt{m}}+\lambda^{\min\{2r,1\}}\left(\kappa^{4r-2}+\kappa^{4r-4}+2\right)\left\|L_{K}^{-r}f_{\rho}\right\|_{\rho}^{2}\\&\leq 8M^{2}\epsilon+\frac{24R^{2}\kappa^{4}\left(\kappa+1\right)^{2}}{\lambda^{2}m^{2}\epsilon^{2}}+\frac{8\sqrt{2\pi}M^{2}}{\sqrt{m}}\\&\quad+\lambda^{\min\{2r,1\}}\left(\kappa^{4r-2}+\kappa^{4r-4}+2\right)\left\|L_{K}^{-r}f_{\rho}\right\|_{\rho}^{2}.\end{aligned}$$

Since $\lambda\left\|f_{z,\lambda}\right\|_{K}^{2}\leq\mathcal{E}_{z}\left(f_{z,\lambda}\right)+\lambda\left\|f_{z,\lambda}\right\|_{K}^{2}\leq\mathcal{E}_{z}\left(0\right)\leq M^{2}$, we have $\left\|f_{z,\lambda}\right\|_{K}\leq\frac{M}{\sqrt{\lambda}}$, *i.e.*, we can choose $R=\frac{M}{\sqrt{\lambda}}$. Now take $\lambda=\left(\frac{1}{m\epsilon}\right)^{2/\min\{4,3+2r\}}$ and

$\epsilon = \left(\frac{1}{\sqrt{m}}\right)^{\min\{1/3, 4r/(3+6r)\}}$ for balance, and the result is proved.

5. Conclusions

Theorem 2, where ϵ is taken as a constant, reveals that the generalization error $\mathcal{E}\left(\pi\left(f_{z,\mathcal{A}}\right)\right)$ converges not to the one of regression function $\mathcal{E}\left(f_\rho\right)$, but a little different one $\left(1+2\epsilon\right)\mathcal{E}\left(f_\rho\right)$ in expectation.

It can be seen from the definition of differential privacy that algorithms will provide more privacy when ϵ tends to 0. However, Theorem 3 shows that ϵ cannot be too small, since the expected error will be very large accordingly. Hence our choice can be regarded as a balance between privacy protection and the expected error. In [19], the authors announce that ϵ also needs tend to 0 in some rates to keep generalization which matches our result.

Compared with previous learning theory results [12] [20] [21] [22] and etc., our learning rate is not so good since a perturbation term is introduced. However, in our result Theorem 1, we did not need a capacity condition as what we did in classical error analysis, *i.e.*, conditions on covering numbers, VC or Vγ dimensions. Instead the ϵ-differential private condition is adopted. So it may be capable and interesting for us to apply such condition to other learning algorithms.

Acknowledgements

This work is supported by NSFC (Nos. 11326096, 11401247), NSF of Guangdong Province in China (No. 2015A030313674), National Social Science Fund in China (No. 15BTJ024), Planning Fund Project of Humanities and Social Science Research in Chinese Ministry of Education (No. 14YJAZH040), Foundation for Distinguished Young Talents in Higher Education of Guangdong, China (No. 2016KQNCX162) and the Major Incubation Research Project of Huizhou University (No. hzux1201619).

References

[1] Dwork, C., McSherry, F., Nissim, K. and Smith, A. (2006) Calibrating Noise to Sensitivity in Private Data Analysis. In: Halevi, S. and Rabin, T., Eds., *Theory of Cryptography*, Springer, Berlin, 265-284.

[2] McSherry, F. and Talwar, K. (2007) Mechanism Design via Differential Privacy. *Proceedings of the* 48*th Annual Symposium on Foundations of Computer Science*, Providence, 21-23 October 2007, 94-103. https://doi.org/10.1109/focs.2007.66

[3] Chaudhuri, K., Monteleoni, C. and Sarwate, A.D. (2011) Differentially Private Empirical Risk Minimization. *Journal of Machine Learning Research*, **12**, 1069-1109.

[4] Jain, P. and Thakurta, A.G. (2013) Differentially Private Learning with Kernels. *JMLR*: *Workshop and Conference Proceedings*, **28**, 118-126.

[5] Jain, P. and Thakurta, A.G. (2014) Dimension Independent Risk Bounds for Differentially Private Learning. *Proceedings of the* 31*st International Conference on Machine Learning*, Beijing, 21-26 June 2014, 476-484.

[6] Dwork, C., Feldman, V., Hardt, M., Pitassi, T., Reingold, O. and Roth, A. (2015)

Preserving Statistical Validity in Adaptive Data Analysis. *ACM Symposium on the Theory of Computing*, Portland, 14-17 June 2015, 117-126. https://doi.org/10.1145/2746539.2746580

[7] Bassily, R., Nissim, K., Smith, A., Steinke, T., Stemmer, U. and Ullman, J. (2015) Algorithmic Stability for Adaptive Data Analysis.

[8] Cucker, F. and Smale, S. (2002) On the Mathematical Foundations of Learning. *Bulletin of the AMS*, **39**, 1-49. https://doi.org/10.1090/S0273-0979-01-00923-5

[9] Cucker, F. and Zhou, D.X. (2007) Learning Theory: An Approximation Theory Viewpoint. Cambridge University Press, Cambridge. https://doi.org/10.1017/CBO9780511618796

[10] Dwork, C. (2008) Differential Privacy: A Survey of Results. *International Conference on Theory and Applications of Models of Computation*, Xi'an, 25-29 April 2008, 1-19.

[11] Steinwart, I., Hush, D. and Scovel, C. (2009) Optimal Rates for Regularized Least Squares Regression. In: Dasgupta, S. and Klivans, A., Eds., *Proceedings of the* 22*nd Annual Conference on Learning Theory*, Montreal, 18-21 June 2009, 79-93.

[12] Wu, Q., Ying, Y. and Zhou, D.X. (2006) Learning Rates of Least-Square Regularized Regression. *Foundations of Computational Mathematics*, **6**, 171-192. https://doi.org/10.1007/s10208-004-0155-9

[13] Nie, W.L. and Wang, C. (2015) Constructive Analysis for Coefficient Regularization Regression Algorithms. *Journal of Mathematical Analysis and Applications*, **431**, 1153-1171.

[14] Wang, C. and Nie, W.L. (2014) Constructive Analysis for Least Squares Regression with Generalized K-Norm Regularization. *Abstract and Applied Analysis*, **2014**, Article ID: 458459. https://doi.org/10.1155/2014/458459

[15] Dwork, C. (2006) Differential Privacy. Springer, Berlin, 1-12.

[16] Smale, S. and Zhou, D.X. (2003) Estimating the Approximation Error in Learning Theory. *Analysis and Applications*, **1**, 17-41. https://doi.org/10.1142/S0219530503000089

[17] Smale, S. and Zhou, D.X. (2007) Learning Theory Estimates via Integral Operators and Their Applications. *Constructive Approximation*, **26**, 153-172. https://doi.org/10.1007/s00365-006-0659-y

[18] Hoeffding, W. (1963) Probability Inequalities for Sums of Bounded Random Variables. *Journal of the American Statistical Association*, **58**, 13-30. https://doi.org/10.1080/01621459.1963.10500830

[19] Wang, Y.-X., Lei, J. and Fienberg, S.E. (2015) Learning with Differential Privacy: Stability, Learn Ability and the Sufficiency and Necessity of ERM Principle.

[20] Wang, C. and Zhou, D.X. (2011) Optimal Learning Rates for Least Squares Regularized Regression with Unbounded Sampling. *Journal of Complexity*, **27**, 55-67.

[21] Hu, T., Fan, J., Wu, Q. and Zhou, D.X. (2015) Regularization Schemes for Minimum Error Entropy Principle. *Analysis and Applications*, **13**, 437-455. https://doi.org/10.1142/S0219530514500110

[22] Christmann, A. and Zhou, D.X. (2016) Learning Rates for the Risk of Kernel-Based Quantile Regression Estimators in Additive Models. *Analysis and Applications*, **14**, 449-477. https://doi.org/10.1142/S0219530515500050

Journal of Applied Mathematics and Physics, 2017, 5, 912-921
http://www.scirp.org/journal/jamp
ISSN Online: 2327-4379
ISSN Print: 2327-4352

Energy Conservation and Gravitational Wavelength Effect of the Gravitational Propagation Delay Analysis

Philipp Kornreich

1090 Wien, Austria
King of Prussia, PA 19406, USA
Email: pkornrei@syr.edu

How to cite this paper: Kornreich, P. (2017) Energy Conservation and Gravitational Wavelength Effect of the Gravitational Propagation Delay Analysis. *Journal of Applied Mathematics and Physics*, **5**, 912-921.
https://doi.org/10.4236/jamp.2017.54080

Received: February 14, 2017
Accepted: April 27, 2017
Published: April 30, 2017

Copyright © 2017 by author and Scientific Research Publishing Inc.
This work is licensed under the Creative Commons Attribution International License (CC BY 4.0).
http://creativecommons.org/licenses/by/4.0/

Open Access

Abstract

The motion of objects where the interaction propagated with a finite velocity was analyzed in my previous paper "The Contribution of the Gravitational Propagation Delay to Orbital and Center of Mass Motions". It is shown here that this analysis is valid for the case when the wavelength of the gravitational wave excited by the motion of the masses is much larger than the system of masses. It is also proven here that the conclusion reached in my previous paper conserves energy. Since this interaction is conservative, the energy is equal to the Hamiltonian. Therefore, the Hamiltonian is calculated and it is shown that the time derivative of the Hamiltonian is equal to zero. Thus, the Hamiltonian and therefore, the energy, are constants.

Keywords

Propagation Delay, Gravitation, Newtonian Mechanics, Lagrangian, Hamiltonian, Constants, Gravitational Waves

1. Introduction

It is determined here, that for the case when the wavelength of the gravitational wave generated by the motion of the point objects are much larger than the distance between objects, Newtonian Classical Mechanics gives accurate results. The correction to Classical Mechanics due to the curvature of space-time in this limit, is approximately the same size as the ratio of the Schwarzschild radius divided by the distance between objects. The curvature of space-time due to the masses is described by the General Relativity Theory. An equation for the wavelength of the gravitational wave generated by the motion of the objects is derived.

The motion of objects where the interaction propagated with a finite velocity was analyzed in my previous paper "The Contribution of the Gravitational Propagation Delay to Orbital and Center of Mass Motions" [1]. This analysis has been questioned if the result conserves energy. Here it is proven that the model in the above paper does conserve energy.

2. Comparison of Gravitational Wavelength and System Size

The gravitational interaction is modeled by the General Relativity Theory as a deformation of space-time caused by the presence of masses [2]. Mathematically, the space-time continuum is described by the geodetic tensor. The deformation of the space-time continuum by moving masses propagates as Gravitational Waves is schematically shown in **Figure 1**. Indeed, Einstein's equations have wave like solutions for space-time. Gravitational Waves have recently been measured [3].

The gravitational interaction propagates with the speed of light among objects. The obvious way to model this interaction is by the gravitational waves derived by the General Relativity Theory. However, for the objects considered in this paper, the gravitational waves generated by the motion of these objects have wavelengths very much larger than the size of the system of the objects, see **Figure 1**. Indeed, the reason that the Newtonian model is so successful is that the gravitational waves generated by systems described by the Newtonian Classical Mechanics [4] have wavelengths substantially longer than the size of the systems.

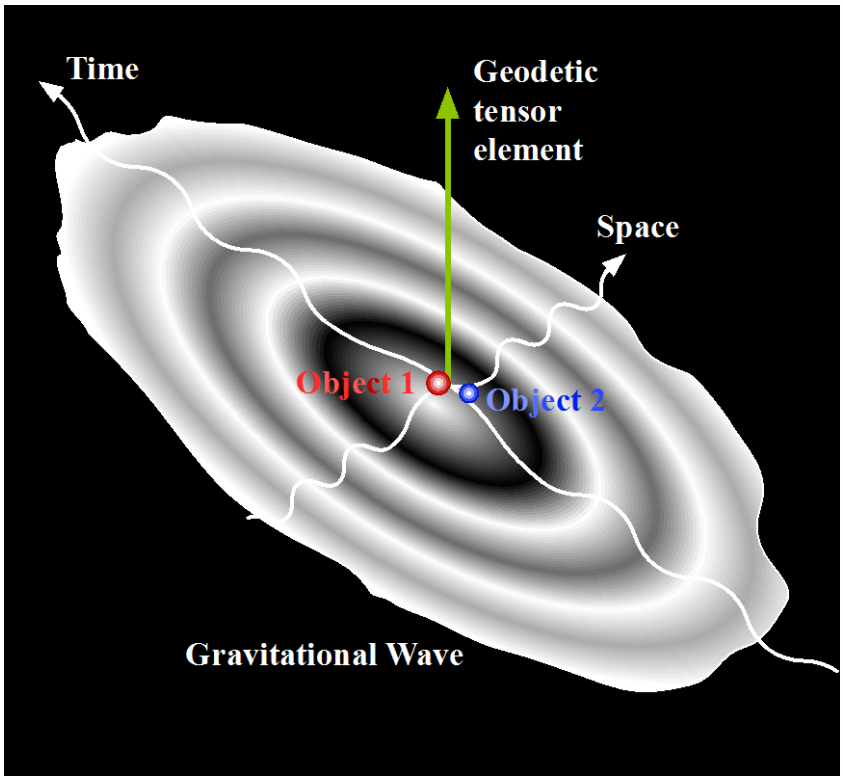

Figure 1. Schematic representation of a system with two objects in a deformed space-time continuum. The system consisting of Objects 1 and 2 is small compared to the wavelength of its gravitational wave. The coordinate axes follow the path of light beams.

The oscillating and orbiting objects will cause steady state gravitational waves in the space-time continuum surrounding the objects. At large distances from the objects, the steady state gravitational waves are spherical-wave like. An expression for the wavelengths of the gravitational waves generated by the systems is derived in Appendix **B**. The calculations in Appendix **B** are based on a derivation in Appendix **A**. The gravitational waves travel with the speed of light. The wavelength λ of this wave is derived in equation B 14b of Appendix **B** and the equation below:

$$\lambda = 2\pi R\sqrt{\frac{2R}{r_{ss}}} \tag{1}$$

where R is the average distance between objects and r_{ss} is the Schwarzschild radius of the sum of the masses of the objects. The Schwarzschild radius is given by:

$$r_{ss} = \frac{2\left(m_{\text{Object 1}} + M_{\text{Object 2}}\right)G}{c^2}. \tag{2}$$

The first result we have been seeking is given by Equation (1). For systems where the average distance R between objects is much larger than the Schwarzschild Radius r_{ss}, the wavelength λ of the Gravitational Wave is much larger than the system that generates the wave. For such systems, Newton's Classical Mechanics and the method to describe delayed interactions are very good mathematical models of nature.

For example, for the Earth Sun system R is approximately equal to twice the orbital semi major axis. The semi major axis is equal to one astronomical unit AU = 149,597,870,700 m. The solar Mass $M_{\odot}$ is equal to 1.989 × 1030 kg. The mass of the Earth ME is equal to 5.972 × 1024 kg. This results in a Schwarzschild radius r_{ss} which equals 2954.038 m. For the Earth Sun system the wavelength of the gravitational wave is 89426.148 times longer than the average orbital diameter. Thus, the size of the Earth Sun system is equal to a very small fraction of the wavelength of the steady state gravitational wave it excites.

To determine if one could use a Newtonian approximation to calculate the measured gravitational waves resulting from the two colliding galaxies R would have to be the distance between points in the galaxies, not the 410 Mpc distance to us. Also, for the observation of the deflection of light from a star by the solar mass the static form of the deformed space-time continuum through which the light passes would have to be calculated. By using the General Relativity Theory one obtains that light is deflected by the Solar mass. It is deflected by an angle of 4.24612 micro-radians, approximately equal to the Schwarzschild radius $r_{ss\odot}$ of the Sun divided by the Sun radius $R_{\odot}$.

3. Conservation of the Energy Analysis

The Wavelength of the Gravitational Wave generated by the system is substantially larger than the size of the system analyzed here. Since this interaction is conservative, the energy is equal to the Hamiltonian. First, the Hamiltonian is

calculated. Next, it is shown that the time derivative of the Hamiltonian is equal to zero. Thus, the Hamiltonian and therefore the energy are constants of the motion.

Here the initial steps of the propagation delay paper of reference [1] are restated:

The motion of the objects with a delayed interaction can be derived from a method similar to the Euler Lagrange model of Classical Mechanics [4]. One can develop a causal Lagrangian L_k that contains the effect of the delayed gravitational interaction. Since the propagation time of the gravitational interaction is very short compared to the orbital period, one can extend the Lagrangian L of the centrally symmetric Kepler problem [4] to include the propagation delay effect.

$$\begin{aligned} L &= \frac{1}{2}m\dot{x}_\mu \dot{x}_\mu + \frac{1}{2}M\dot{y}_\mu \dot{y}_\mu + \frac{mMG}{\sqrt{\left(x_\mu - y_\mu\right)\left(x_\mu - y_\mu\right)}} \\ \rightarrow L_k &= \frac{1}{2}m\dot{x}_{\mu k}\dot{x}_{\mu k} + \frac{1}{2}M\dot{y}_{\mu k}\dot{y}_{\mu k} + \frac{mMG}{2\sqrt{\left(x_{\mu k} - y_{\mu k-2}\right)\left(x_{\mu k} - y_{\mu k-2}\right)}} \\ &\quad + \frac{mMG}{2\sqrt{\left(y_{\mu k} - x_{\mu k-1}\right)\left(y_{\mu k} - x_{\mu k-1}\right)}} \end{aligned} \tag{3}$$

where summation over repeated Greek indices is implied. The Latin subscripts label discrete times. The single gravitational potential of the Kepler formulation is split into two potentials as shown in Equation (3). The first potential describes a gravitational interaction that was radiated by the Planet in the past at time $t_{k\text{-}2}$ and is sensed currently at time t_k by the Moon. The second potential describes a gravitational interaction that was radiated by the Moon in the past at time $t_{k\text{-}1}$ and is sensed currently at time t_k by the Planet. Thus, the Lagrangian L_k is causal. Half of each of these potentials as described by Dirac [5] is used.

An equation of motion similar to the Euler Lagrange equation of motion is derived by a least action method described in my paper "Reaction Mechanics for Point Objects" [6]. The Euler Lagrange method for the derivation of the equations of motion is most readily implemented using tensor notation. Here m is the mass and $x_{\mu k}$ is a component of the position vector $\boldsymbol{x}_k$ of the Moon at time step t_k and M is the mass and $y_{\mu k}$ is a component of the position vector $\boldsymbol{y}_k$ of the Planet at time step t_k. The time differences such as $t_k - t_{k-1}$ are propagation delays. The $t_k - t_{k-1}$ are finite time durations. The time steps such as $t_{k-2}, t_{k-1}, t_k, t_{k+1}$, and t_{k+2} are not necessarily consecutive. They are just time step labels. The time steps are not integer related. Bold letters such as $\boldsymbol{x}$ denote vectors, single superior dots such as $\dot{x} = \frac{\mathrm{d}x}{\mathrm{d}t}$ denote time derivatives and double superior dots such as $\ddot{x} = \frac{\mathrm{d}^2x}{\mathrm{d}t^2}$ denote second time derivatives.

The derivation of the Hamiltonian from the Lagrangian of Equation (3) is performed in Appendix **A**. The Hamiltonian Sum is the Legender transform [7] of the Sum of Lagrangians with respect to the current velocities for systems with delayed interactions. This calculation is performed in Appendix **A**. The time de-

rivative of the Hamiltonian Sum with respect to a current time t_k is given by Equation (A8) in Appendix A. Equation (A8) in the more compact vector form is rewritten below.

$$\frac{\mathrm{d}H}{\mathrm{d}t_k} = m\ddot{\boldsymbol{u}}_{1k}\cdot\dot{\boldsymbol{u}}_{1k} + \frac{mMG\left(\boldsymbol{u}_{1k}-\boldsymbol{u}_{2k-2}\right)\cdot\dot{u}_{1k}}{\left|\boldsymbol{u}_{1k}-\boldsymbol{u}_{2k-2}\right|^3} + \frac{mMG\left(\boldsymbol{u}_{2k}-\boldsymbol{u}_{1k+1}\right)\cdot\dot{\boldsymbol{u}}_{1k}}{\left|\boldsymbol{u}_{2k}-\boldsymbol{u}_{1k+1}\right|^3} + M\ddot{\boldsymbol{u}}_{2k}\cdot\dot{\boldsymbol{u}}_{2k} + \frac{mMG\left(\boldsymbol{u}_{2k}-\boldsymbol{u}_{1k-1}\right)\cdot\dot{u}_{2k}}{\left|\boldsymbol{u}_{2k}-\boldsymbol{u}_{1k-1}\right|^3} + \frac{mMG\left(\boldsymbol{u}_{1k}-\boldsymbol{u}_{2k+2}\right)\cdot\dot{u}_{2k}}{\left|\boldsymbol{u}_{1k}-\boldsymbol{u}_{2k+2}\right|^3} \tag{4}$$

The equations of motion of the Moon and Earth are given by Equations (A3). Equations (A3) are rewritten here in the more compact form in vector notation.

$$\begin{aligned} &\text{a)}\ m\ddot{\boldsymbol{u}}_{1k} + \frac{mMG\left(\boldsymbol{u}_{1k}-\boldsymbol{u}_{2k-2}\right)}{\left|\boldsymbol{u}_{1k}-\boldsymbol{u}_{2k-2}\right|^3} + \frac{mMG\left(\boldsymbol{u}_{2k}-\boldsymbol{u}_{1k+1}\right)}{\left|\boldsymbol{u}_{2k}-\boldsymbol{u}_{1k+1}\right|^3} = 0 \\ &\text{b)}\ M\ddot{\boldsymbol{u}}_{\mu k} + \frac{mMG\left(\boldsymbol{u}_{2k}-\boldsymbol{u}_{1k-1}\right)}{\left|\boldsymbol{u}_{2k}-\boldsymbol{u}_{1k-1}\right|^3} + \frac{mMG\left(\boldsymbol{u}_{1k}-\boldsymbol{u}_{2k+2}\right)}{\left|\boldsymbol{u}_{1k}-\boldsymbol{u}_{2k+2}\right|^3} = 0 \end{aligned} \tag{5}$$

By substituting the equations of motion of Equation (5) into Equation (4) one obtains:

$$\text{a)}\ \frac{\mathrm{d}H}{\mathrm{d}t_k} = 0 \quad \text{and thus} \quad H = \text{Constant} \tag{6}$$

The second result we are seeking is given above by Equation (6). Since this is a conservative system, the Hamiltonian is equal to the energy. The time derivative of the Hamiltonian is equal to zero. Therefore the Hamiltonian is a constant, and thus, the energy, too, is a constant.

4. Conclusion

It is shown here that the very successful Kepler Newtonian model, and thus the mathematical model analyzing the effect of the gravitational propagation delay is valid. This occurs in the case when the wavelengths of the gravitational waves excited by the motion of the masses which are much larger than the system of masses. For this range of system parameters, the extension of the Newtonian Gravitational potential that includes the gravitational propagation delay is also valid. It was questioned if the solution reached in the paper "The Contribution of the Gravitational Propagation Delay to Orbital and Center of Mass Motions" [1] conserved energy? This is a conservative system and therefore, the Ha- miltonian is equal to the energy. Here, the Hamiltonian sum has been calculated from the Lagrangian sum. It is shown that the time derivative of the Hamiltonian sum is equal to zero. This implies that the Hamiltonian sum is a constant. Therefore, the energy is constant and is conserved.

Acknowledgements

I thank my wife Marlene for our discussions about the subject matter of this paper, making the text more understandable for the reader. I also thank her for proof reading, for correcting my mistakes and for her assistance in formulating

this paper.

References

[1] Kornreich, P. (2016) The Contribution of the Gravitational Propagation Delay to Orbital and Center of Mass Motions. *Journal of Modern Physics*, **7**, 1909-1932. https://doi.org/10.4236/jmp.2016.714169

[2] Einstein, A., Lorentz, H.A., Weyl, H. and Minkowski, H. (1952) The Principles of Relativity. Dover Publishing, Minoeola.

[3] Abbott, B.P., *et al.* (2016) Observation of Gravitational Waves from a Binary Black Hole Merger. *Physical Review Letters*, **116**, Article ID: 061102.

[4] Goldstein, H. (1980) Classical Mechanics. Addison-Wesley Publishing Company, Reading MA.

[5] Dirac, P.A.M. (1938) Classical Theory of Radiating Electrons. *Proceedings of the Royal Society* (*London* A), **167**, 148-169. https://doi.org/10.1098/rspa.1938.0124

[6] Kornreich, P. (2017) Reaction Mechanics for Point Objects. *Journal of Applied Mathematical Physics*, **4**, 1909-1932.

[7] Callen, H. (1962) Thermodynamics. Wiley Co., Weinheim.

[8] Shen, S.W. (1995) Dynamics in a Discrete Nagumo Equation: Spatial Topological Chaos. *SIAM Journal of Applied Mathematics*, **55**, 1764-1781. https://doi.org/10.1137/S0036139994261757

Appendix A

To include the effect of both finite and infinitesimal time increments in the derivation of the equation of motion, a sum S of Lagrangians L_k is used. The method used here is similar to the discrete Nagumo equation [8]

$$S = \sum_{k=-\infty}^{k=\infty} L_k \tag{A1}$$

The equations of motion are obtained by inserting the sum of Lagrangians into an equation similar to the Euler Lagrange equations of motion for the Moon and the Planet.

$$\text{a)}\ \frac{\mathrm{d}}{\mathrm{d}t_k}\frac{\partial S}{\partial \dot{x}_{\mu k}} - \frac{\partial S}{\partial x_{\mu k}} = 0 \qquad \text{b)}\ \frac{\mathrm{d}}{\mathrm{d}t_k}\frac{\partial S}{\partial \dot{y}_{\mu k}} - \frac{\partial S}{\partial y_{\mu k}} = 0 \tag{A2}$$

This equation of motion was derived in my paper titled "Reaction Mechanics for Point Objects" [6]. By using the Lagrangians L_k of Equation (3) in the sum of Lagrangians S in Equation (A1), and substituting this sum into Equations (A2) one obtains the following discrete Nagumo [8] like equation of motion for the Moon and Planet respectively:

$$\begin{aligned}
&\text{a)}\ m\ddot{x}_{\mu k} + \frac{mMG\left(x_{\mu k} - y_{\mu k-2}\right)}{2\left[\left(x_{\nu k} - y_{\nu k\text{-}2}\right)\left(x_{\nu k} - y_{\nu k-2}\right)\right]^{\frac{3}{2}}} + \frac{mMG\left(x_{\mu k} - y_{\mu k+2}\right)}{2\left[\left(x_{\nu k} - y_{\nu k+2}\right)\left(x_{\nu k} - y_{\nu k+2}\right)\right]^{\frac{3}{2}}} = 0 \\
&\text{b)}\ M\ddot{y}_{\mu k} + \frac{mMG\left(y_{\mu k} - x_{\mu k-1}\right)}{2\left[\left(y_{\nu k} - x_{\nu k\text{-}1}\right)\left(y_{\nu k} - x_{\nu k-1}\right)\right]^{\frac{3}{2}}} + \frac{mMG\left(y_{\mu k} - x_{\mu k+1}\right)}{2\left[\left(y_{\nu k} - x_{\nu k+1}\right)\left(y_{\nu k} - x_{\nu k+1}\right)\right]^{\frac{3}{2}}} = 0
\end{aligned} \tag{A3}$$

In order to calculate the Hamiltonian [4] of this system, it is necessary to first calculate the components of the Reaction Mechanics momentums [6] $p_{\mu k}$ and $q_{\mu k}$ of the Moon and the Planet at time step t_k.

$$\text{a)}\ p_{\mu k} = \frac{\partial\left(L_k + L_{k+1}\right)}{\partial \dot{x}_{\mu k}} \qquad \text{b)}\ q_{\mu k} = \frac{\partial\left(L_k + L_{k+1}\right)}{\partial \dot{y}_{\mu k}} \tag{A4}$$

Only the current L_k and the future L_{k+1} Lagrangians are functions of the current coordinate components $x_{\mu k}$ and $y_{\mu k}$ of the Moon and Planet. By substituting Equation (3) for the Lagrangians L_k and L_{k+1} into equation A4 one obtains for the components of the Reaction Mechanics momentums.

$$\text{a)}\ p_{\mu k} = m\dot{x}_{\mu k} \qquad \text{b)}\ q_{\mu k} = M\dot{y}_{\mu k} \tag{A5}$$

The Hamiltonian sum H is equal to the Lagender transform [7] of the sum of Lagrangians S with respect to the velocity components.

$$\begin{aligned}
H = &\sum_{k=-\infty}^{k=\infty}\left(p_{\mu k}\dot{x}_{\mu k} + q_{\mu k}\dot{y}_{\mu k}\right) - \sum_{k=-\infty}^{k=\infty}\left(\frac{1}{2}m\dot{x}_{\mu k}\dot{x}_{\mu k} + \frac{1}{2}M\dot{y}_{\mu k}\dot{y}_{\mu k}\right) \\
&- \sum_{k=-\infty}^{k=\infty}\left[\frac{mMG}{2\sqrt{\left(x_{\mu k} - y_{\mu k-2}\right)\left(x_{\mu k} - y_{\mu k-2}\right)}} + \frac{mMG}{2\sqrt{\left(y_{\mu k} - x_{\mu k-1}\right)\left(y_{\mu k} - x_{\mu k-1}\right)}}\right] \\
&- \sum_{k=-\infty}^{k=\infty}\left[\frac{mMG}{2\sqrt{\left(x_{\mu k+2} - y_{\mu k}\right)\left(x_{\mu k+2} - y_{\mu k}\right)}} + \frac{mMG}{2\sqrt{\left(y_{\mu k+1} - x_{\mu k}\right)\left(y_{\mu k+1} - x_{\mu k}\right)}}\right]
\end{aligned} \tag{A6}$$

Using Equations (A5) in Equation (A6) and collecting terms in the resulting expression.

$$H=\sum_{k=-\infty}^{k=\infty}\left[\frac{p_{\mu k}p_{\mu k}}{2m}+\frac{q_{\mu k}q_{\mu k}}{2M}-\frac{mMG}{2\sqrt{\left(x_{\mu k}-y_{\mu k-2}\right)\left(x_{\mu k}-y_{\mu k-2}\right)}}\right.$$
$$-\frac{mMG}{2\sqrt{\left(y_{\mu k}-x_{\mu k-1}\right)\left(y_{\mu k}-x_{\mu k-1}\right)}}-\frac{mMG}{2\sqrt{\left(x_{\mu k+2}-y_{\mu k}\right)\left(x_{\mu k+2}-y_{\mu k}\right)}} \tag{A7}$$
$$\left.-\frac{mMG}{2\sqrt{\left(y_{\mu k+1}-x_{\mu k}\right)\left(y_{\mu k+1}-x_{\mu k}\right)}}\right]$$

Taking the time derivative with respect to a current time tk of the Hamiltonian sum in Equation (A7).

$$\frac{\mathrm{d}H}{\mathrm{d}t_k}=m\dot{x}_{\mu k}\ddot{x}_{\mu k}+\frac{mMG\left(x_{\mu k}-y_{\mu k-2}\right)\dot{x}_{\mu k}}{\left[\left(x_{\mu k}-y_{\mu k-2}\right)\left(x_{\mu k}-y_{\mu k-2}\right)\right]^{\frac{3}{2}}}+\frac{mMG\left(x_{\mu k}-y_{\mu k+1}\right)\dot{x}_{\mu k}}{\left[\left(y_{\mu k+1}-x_{\mu k}\right)\left(y_{\mu k+1}-x_{\mu k}\right)\right]^{\frac{3}{2}}}$$
$$+M\dot{y}_{\mu k}\ddot{y}_{\mu k}+\frac{mMG\left(y_{\mu k}-x_{\mu k-1}\right)\dot{y}_{\mu k}}{\left[\left(y_{\mu k}-x_{\mu k-1}\right)\left(y_{\mu k}-x_{\mu k-1}\right)\right]^{\frac{3}{2}}}+\frac{mMG\left(y_{\mu k}-x_{\mu k+2}\right)\dot{y}_{\mu k}}{\left[\left(x_{\mu k+2}-y_{\mu k}\right)\left(x_{\mu k+2}-y_{\mu k}\right)\right]^{\frac{3}{2}}} \tag{A8}$$

Equations (A8) and (A3) are rewritten as Equations (4) and (5) in the main text.

By substituting the equations of motion, Equations (A3) into Equation (A8) one obtains:

$$\text{a)}\ \frac{\mathrm{d}H}{\mathrm{d}t_k}=0 \qquad \text{and thus} \qquad H=\text{Constant} \tag{A9}$$

Since this is a conservative system, the Hamiltonian is equal to the energy. The time derivative of the Hamiltonian is equal to zero. Therefore, the Hamiltonian is a constant, and the energy, also is a constant.

Appendix B

Returning to Equation (A7) to investigate the relationship between the wavelength of the gravitational wave generated by the motion of the masses m and M, and the size of the system. It is assumed here that the wavelength of the gravitational wave is very much larger than the size of the system. In this limit the General Relativity Theory reverts to the Classical Mechanics model of nature. Therefore, one can use the much simpler Classical Mechanics for the calculations. For simplicity, neglecting the propagation delay and using the more compact vector notation one obtains for the equations of motions of the Moon and Earth from Equation (A7):

$$\begin{aligned} &\text{a)}\ \ddot{\boldsymbol{u}}_1 + \frac{MG\left(\boldsymbol{u}_1 - \boldsymbol{u}_2\right)}{\left(u_1^2 - 2u_1u_1 + u_1^2\right)^{\frac{3}{2}}} = 0 \\ &\text{b)}\ \ddot{u} - \frac{mG\left(\boldsymbol{u}_1 - \boldsymbol{u}_2\right)}{\left(u_1^2 - 2u_1u_1 + u_1^2\right)^{\frac{3}{2}}} = 0 \end{aligned} \tag{B1}$$

It is conventional to make a transformation of variables at this point:

$$\text{a)}\ \boldsymbol{q} = \boldsymbol{u}_1 - \boldsymbol{u}_2 \qquad \text{b)}\ \boldsymbol{Q} = \frac{m}{m+M}\boldsymbol{u}_1 + \frac{M}{m+M}\boldsymbol{u}_2 \tag{B2}$$

where $\boldsymbol{q}$ is the vectorial distance between objects and $\boldsymbol{Q}$ is the center of mass coordinate vector. Inverting Equations (B2).

$$\text{a)}\ \boldsymbol{u}_1 = \boldsymbol{Q} + \frac{M}{m+m}\boldsymbol{q} \qquad \text{b)}\ \boldsymbol{u}_2 = \boldsymbol{Q} - \frac{m}{m+M}\boldsymbol{q} \tag{B3}$$

Substituting equations B3a and B3b into Equations (B1).

$$\text{a)}\ \ddot{\boldsymbol{Q}} + \frac{M}{m\ +\ m}\ddot{\boldsymbol{q}} + \frac{MG\boldsymbol{q}}{q^3} = 0 \qquad \text{b)}\ \ddot{\boldsymbol{Q}} - \frac{m}{m+M}\ddot{\boldsymbol{q}} - \frac{mG\boldsymbol{q}}{q^3} = 0 \tag{B4}$$

First, subtract Equation (B4b) from Equation (B4a) and dot multiply the result by the vector $\boldsymbol{q}$. Next, subtract Equation (B4b) from Equation (B4a) and cross multiply the result by the vector $\boldsymbol{q}$. Last, multiply Equation (B4a) by m and equation B4b by M and add the resulting expressions.

$$\text{a)}\ \boldsymbol{q}\cdot\ddot{\boldsymbol{q}} + \frac{(m+M)G}{q} = 0 \qquad \text{b)}\ \boldsymbol{q}\times\ddot{\boldsymbol{q}} = 0 \qquad \text{c)}\ (m+M)\ddot{\boldsymbol{Q}} = 0 \tag{B5}$$

Equation B5c implies that the center of mass velocity $\dot{\boldsymbol{Q}}$ is a constant of the motion. Next, making a transformation to cylindrical coordinates.

$$\text{a)}\ q_1 = \rho\cos\theta \qquad \text{b)}\ q_2 = \rho\sin\theta \tag{B6}$$

Substituting equations B6 into Equations (B5a) and (B5b).

$$\begin{aligned} &\text{a)}\ \ddot{\rho} - \rho\dot{\theta}^2 + \frac{(m+M)G}{\rho^2} = 0 \qquad \text{b)}\ \hat{\boldsymbol{a}}_3\left(2\rho\dot{\rho}\dot{\theta} + \rho^2\ddot{\theta}\right) = 0 \\ &\text{c)}\ \frac{\mathrm{d}}{\mathrm{d}t}\rho^2\dot{\theta} = 0 \qquad \text{d)}\ \rho^2\dot{\theta} = \ell \qquad \text{e)}\ \dot{\theta} = \frac{\ell}{\rho^2} \end{aligned} \tag{B7}$$

Here λ is the angular momentum which is a constant of the motion. By substituting Equation (B7e) into Equation (B7a) one obtains the equation of motion.

$$\frac{\mathrm{d}^2\rho}{\mathrm{d}t^2}-\frac{\ell^2}{\rho^3}+\frac{(m+M)G}{\rho^2}=0 \tag{B8}$$

where ρ is the distance between objects. Approximating the distance between objects ρ by its average value R and a small oscillating portion rcos ω t.

$$\rho = R + r\cos\omega t \tag{B9}$$

The oscillation of the distance between objects is observed as an eccentric orbit where the distance between objects change periodically. Substituting Equation (B9) for the distance between objects ρ into Equation (B8) and expanding the resulting expression to first order in the small parameter $\frac{r}{R}\cos\omega t$.

$$-\omega^2 r\cos\omega t-\frac{\ell^2}{R^3}+\frac{3\ell^2}{R^4}r\cos\omega t+\frac{(m+M)G}{R^2}-\frac{2(m+M)G}{R^3}r\cos\omega t\approx 0 \tag{B10}$$

Collecting terms in Equation (B10):

$$\text{a)}\ -\omega^2+\frac{3\ell^2}{R^4}-\frac{2(m+M)G}{R^3}\approx 0 \qquad \text{b)}\ -\frac{\ell^2}{R^3}+\frac{(m+M)G}{R^2}\approx 0 \tag{B11}$$

Solving Equation (b11b) for the angular momentum λ and substituting the result into Equation (B11a).

$$\omega^2=\frac{(m+M)G}{R^3} \tag{B12}$$

Solving this equation for the oscillating frequency *f*:

$$\text{a)}\ f=\frac{1}{2\pi R}\sqrt{\frac{(m+M)G}{R}} \quad \text{where} \quad \text{b)}\ \omega=2\pi f \tag{B13}$$

The oscillating and orbiting objects will cause gravitational waves in the space-time continuum surrounding the objects, see **Figure 1**. The gravitational waves travel with the speed of light. The wavelength λ of this wave is equal to:

$$\text{a)}\ \lambda=\frac{c}{f} \qquad \text{b)}\ \lambda=2\pi R\sqrt{\frac{2R}{r_{ss}}} \tag{B14}$$

where R is the average distance between objects. Here r_{ss} is the Schwarzschild radius of the sum mass given by:

$$r_{ss}=\frac{2(m+M)G}{c^2} \tag{B15}$$

Equations (B14b) and (B15) are the results we are seeking. Equations (B14b) and (B15) are rewritten as Equations (1) and (2) in the main text.

Journal of Applied Mathematics and Physics, 2017, 5, 922-932
http://www.scirp.org/journal/jamp
ISSN Online: 2327-4379
ISSN Print: 2327-4352

Decay Rate for a Viscoelastic Equation with Strong Damping and Acoustic Boundary Conditions

Zhiyong Ma

College of Science, Shanghai Second Polytechnic University, Shanghai, China
Email: mazhiyong1980@hotmail.com

How to cite this paper: Ma, Z.Y. (2017) Decay Rate for a Viscoelastic Equation with Strong Damping and Acoustic Boundary Conditions. *Journal of Applied Mathematics and Physics*, **5**, 922-932.
https://doi.org/10.4236/jamp.2017.54081

Received: February 13, 2017
Accepted: April 27, 2017
Published: April 30, 2017

Copyright © 2017 by author and Scientific Research Publishing Inc.
This work is licensed under the Creative Commons Attribution International License (CC BY 4.0).
http://creativecommons.org/licenses/by/4.0/
Open Access

Abstract

This paper is concerned with a nonlinear viscoelastic equation with strong damping: $|u_t|^{\rho}u_{tt}-\Delta u-\Delta u_{tt}+\int_0^t g(t-s)\Delta u(x,s)\mathrm{d}s-\Delta u_t=0,$. The objective of the present paper is to provide some results on the long-time behavior to this equation with acoustic boundary conditions. By using the assumptions on the relaxation function due to Tatar [1], we show an arbitrary rate of decay with not necessary of an exponential or polynomial one and without the assumption $\int_0^{\infty}g(s)\mathrm{d}s<\frac{1}{2}$ condition. The result extends and improves some results given in Cavalcanti [2].

Keywords

Viscoelastic Equation, Decay Rate, Acoustic Boundary Condition

1. Introduction

In this paper, we investigate the following viscoelastic system with acoustic boundary conditons

$$|u_t|^{\rho}u_{tt}-\Delta u-\Delta u_{tt}+\int_0^t g(t-s)\Delta u(x,s)\mathrm{d}s-\Delta u_t=0,\quad (x,t)\in(0,+\infty), \tag{1.1}$$

$$\frac{\partial u_t}{\partial \nu}(x,t)=0\qquad (x,t)\in\Gamma\times[0,+\infty), \tag{1.2}$$

$$u(x,t)=0,\qquad (x,t)\in\Gamma_1\times[0,+\infty), \tag{1.3}$$

$$\frac{\partial u_{tt}}{\partial \nu}(x,t)+\frac{\partial u}{\partial \nu}(x,t)-\int_0^t g(t-s)\frac{\partial u}{\partial \nu}(x,s)\mathrm{d}s=y_t\quad (x,t)\in\Gamma_0\times[0,+\infty), \tag{1.4}$$

$$u_t(x,t)+p(x)y_t+q(x)y(x,t)=0\qquad (x,t)\in\Gamma_0\times[0,+\infty), \tag{1.5}$$

$$u(x,0)=u_0(x), u_t(x,0)=u_1(x), \quad x\in\Omega, \tag{1.6}$$

where $\Omega\subseteq\mathbb{R}^n\ (n=1,2)$ is a bounded domain with smooth boundary $\Gamma=\Gamma_0\bigcup\Gamma_1$, ν is the unit outward normal to Γ, the function g represents the kernel of a memory, p and q are specific functions, and ρ is a real number such that

$$1<\rho\le\frac{2}{n-2} \quad \text{if} \quad n\ge 3; \quad \rho>1 \quad \text{if} \quad n=1,2. \tag{1.7}$$

Our problem is of the form

$$f(u_t)u_{tt}-\Delta u-\Delta u_{tt}=0, \tag{1.8}$$

which has several modeling features. In the case, $f(u_t)$ is a constant; Equation (8) has been used to model extensional vibrations of thin rods (see Love [3], Chapter 20). In the case, $f(u_t)$ is not a constant; Equation (8) can model materials whose density depends on the velocity u_t, for instance, a thin rod which possesses a rigid surface and with an interior which can deform slightly. We refer the reader to Fabrizio and Morro [4] for several other related models.

Recently, Liu [5] considered the following viscoelastic problem with acoustic boundary conditions

$$u_{tt}-\Delta u+\int_0^t g(t-s)\Delta u(x,s)\mathrm{d}s=0, \quad (x,t)\in(0,+\infty), \tag{1.9}$$

$$u(x,t)=0, \qquad (x,t)\in\Gamma_1\times[0,+\infty), \tag{1.10}$$

$$\frac{\partial u}{\partial\nu}(x,t)-\int_0^t g(t-s)\frac{\partial u}{\partial\nu}(x,s)\mathrm{d}s=y_t \quad (x,t)\in\Gamma_0\times[0,+\infty), \tag{1.11}$$

$$u_t(x,t)+p(x)y_t+q(x)y(x,t)=0 \quad (x,t)\in\Gamma_0\times[0,+\infty), \tag{1.12}$$

$$u(x,0)=u_0(x),\ u_t(x,0)=u_1(x), \quad x\in\Omega, \tag{1.13}$$

the authors obtain an arbitrary decay rate of the energy. In the pioneering paper [6], Beale and Rosencrans considered the acoustic boundary condition (1.12) and the coupled impenetrability boundary condition (1.11) with a general form, which had the presence of y_{tt} in (1.2), in a study of the model for acoustic wave motion of a fluid interacting with a so-called locally reacting surface. Recently, many authors treated wave equations with acoustic boundary conditions, see [7] [8] [9] [10] and references therein. For instance, Rivera and Qin [10] proved the polynomial decay for the wave motion with general acoustic boundary conditions by using the Lyapunov functional technique. Frota and Larkin [8] established global solvability and the exponential decay for problems (1.9)-(1.13) with $g\equiv 0$. They overcame the difficulties which were arisen due to the absence of y_{tt} in (1.12) by using the degenerated second order equation. Recently, Park and Park [9] investigated problems (1.9)-(1.13) and proved general rates of decay which depended on the behavior of g, under the additional assumption of that $\int_0^{+\infty}g(s)\mathrm{d}s$.

Many authors have focused on the viscoelastic problem. In the pioneer work of Dafermos [11] [12], existence and asymptotic stability for a one-dimensional vis-

coelastic problem were proved but no rate of decay has been specified. Since then problems related to viscoelasticity have attracted a great deal of attention [13] [14] [15]. It seems all started with kernels of the form $g(t)=e^{-\beta t}$, $\beta>0$, then with kernels satisfying $-\xi_1 g(t)\le g'(t)\le -\xi_2 g(t)$, for all $t\ge 0$, for some constants ξ_1 and ξ_2 and some other conditions on the second derivative, Cavalcanti *et al.* [2] studied the following equation with Dirichlet boundary conditions

$$|u_t|^{\rho}u_{tt}-\Delta u-\Delta u_{tt}+g*\Delta u-\gamma\Delta u_t=0 \tag{1.14}$$

where $g*\Delta u=\int_0^t g(t-s)\Delta u(s)\mathrm{d}s$. They established a global existence result for $\gamma\ge 0$ and an exponential decay of energy for $\gamma>0$, and studied the interaction within the $|u_t|^{\rho}u_{tt}$ and the memory term $g*\Delta u$. Messaoudi and Tatar [16] established, for small initial data, the global existence and uniform stability of solutions to the equation

$$|u_t|^{\rho}u_{tt}-\Delta u-\Delta u_{tt}+g*\Delta u=b|u|^{p-2}u \tag{1.15}$$

with Dirichlet boundary condition, where $\gamma\ge 0,\rho,b>0,p>2$ are constants. In the case $b=0$ in (15), Messaoudi and Tatar [17] proved the exponential decay of global solutions to (15) without smallness of initial data, considering only the dissipation effect given by the memory.

In [18] [19], the condition has been replaced by $g'(t)\le -\xi(t)g(t)$, where $\xi(t)$ is a positive function. Similarly, Han and Wang [20] proved the energy decay for the viscoelastic equation with nonlinear damping

$$|u_t|^{\rho}u_{tt}-\Delta u-\Delta u_{tt}+g*\Delta u+|u_t|^{m}u_t=0, \tag{1.16}$$

with Dirichlet boundary condition, where $\rho>0,m>0$ are constants. Then Park and Park [21] established the general decay for the viscoelastic problem with nonlinear weak damping

$$|u_t|^{\rho}u_{tt}-\Delta u_{tt}-\Delta u+g*\Delta u+h(u_t)=0, \tag{1.17}$$

with the Dirichlet boundary condition, where $\rho>0$ is a constant. We also mention that Fabrizio and Polidoro [22] obtained the exponential decay result under the conditions that $g'(t)\le 0$ and $e^{\alpha t}g(t)\in L^1(0,+\infty)$ for some $\alpha>0$. Recently, Tatar [23] improved these results by removing the last condition and established a polynomial asymptotic stability. In fact, he considered the kernels having small flat zones and these zones are not too big (see also [24] for the case of coupled system). More recently, under the assumptions that $g'(t)\le 0$ and $g(t)\gamma(t)\in L^1(0,+\infty)$ for some nonnegative function $\gamma(t)$, Tatar [1] generalized these works to an arbitrary decay for wave equation with a viscoelastic damping term. Moreover, we would like to mention some results in [25]-[30].

The rest of our paper is organized as follows. In Section 2, we give some preparations for our consideration and our main result. The statements and the proofs of our main results will be given in Section 3.

For convenience, we denote the norm and scalar product in $L^2(\Omega)$ by $\|\cdot\|$ and $(\cdot,\cdot)$, respectively. C denotes a general positive constant, which may be different in different estimates.

2. Preliminaries and Main Result

For the memory kernel g we assume that:

(H_1) $g:\mathbb{R}^+\to\mathbb{R}^+$ is a non-increasing differentiable function satisfying that

$$g(0)>0,\ l=1-\int_0^{+\infty}g(s)\mathrm{d}s>0. \tag{2.1}$$

(H_2) suppose that there exists a nondecreasing function $\gamma(t)>0$ such that $\dfrac{\gamma'(t)}{\gamma(t)}=\eta(t)$ is a decreasing function and $\int_0^{+\infty}g(s)\gamma(s)\mathrm{d}s<+\infty$.

For the functions p and q, we assume that $p,q\in C(\Gamma_0)$ and $p(x)>0$ and $q(x)>0$ for all $x\in\Gamma_0$. This assumption implies that there exist positive constants $p_i,q_i\ (i=0,1)$ such that

$$p_0\le p(x)\le p_1,\ \ q_0\le q(x)\le q_1,\ \ x\in\Gamma_0. \tag{2.2}$$

We use the notation

$$V=\left\{u\in H^1(\Omega):u=0 \text{ on } \Gamma_1\right\},$$
$$(u,v)=\int_\Omega u(x)v(x)\mathrm{d}x,\ \text{ and }\ (u,v)_{\Gamma_0}=\int_{\Gamma_0}u(x)v(x)\mathrm{d}\Gamma.$$

Let λ and $\tilde{\lambda}$ be the smallest positive constants such that

$$\|u\|^2\le\lambda\|\nabla u\|^2,\qquad \|u\|_{\Gamma_0}^2\le\tilde{\lambda}\|\nabla u\|^2. \tag{2.3}$$

Firstly, we have the following existence and uniqueness results, it can be established by adopting the arguments of [2] [31].

Theorem 2.1 *Let* $(u_0,u_1)\in\left(V\bigcap H^2(\Omega)\right)\times V$. *Assume that* H_1,H_2 *and* (2.2) *hold. There exists a unique pair of functions* (u,y_t), *which is a solution to the problem* (1.1) *in the class*

$$u\in L^\infty\left(0,T,V\cap H^2(\Omega)\right),\quad u_t\in L^\infty(0,T,V), \tag{2.4}$$

$$u_{tt}\in L^\infty\left(0,T,L^2(\Omega)\right),\quad y,y^t\in L^2\left(\mathbb{R}^+;L^2(\Gamma_0)\right). \tag{2.5}$$

We introduce the modified energy functional

$$\begin{aligned}E(t)=&\frac{1}{\rho+2}\|u_t\|_{\rho+2}^{\rho+2}+\frac{1}{2}\left(1-\int_0^t g(s)\mathrm{d}s\right)\|\nabla u\|^2+\frac{1}{2}(g\circ\nabla u)(t)\\&+\frac{1}{2}\|\nabla u_t(t)\|^2+\frac{1}{2}\int_{\Gamma_0}q(x)|y(x,t)|^2\,\mathrm{d}\Gamma,\end{aligned} \tag{2.6}$$

where

$$(g\circ\nabla u)(t)=\int_0^t g(t-s)\|\nabla u(t)-\nabla u(s)\|^2\,\mathrm{d}s.$$

Clearly

$$\frac{\mathrm{d}}{\mathrm{d}t}E(t)=-\|\nabla u_t(t)\|^2-\frac{1}{2}g(t)\|\nabla u\|^2+\frac{1}{2}(g'\circ\nabla u)-\int_{\Gamma_0}py_t^2. \tag{2.7}$$

To state our main result, we introduce the following notations as in [32]. For every measurable set $\mathcal{A}\subset\mathbb{R}^+$, we define the probability measure $\hat{g}$ by

$$\hat{g}(\mathcal{A})=\frac{1}{1-l}\int_{\mathcal{A}}g(s)\mathrm{d}s. \tag{2.8}$$

The flatness set and the flatness rate of g are defined by

$$\mathcal{F}_g = \left\{ s \in \mathbb{R}^+ : g(s) > 0 \text{ and } g'(s) = 0 \right\} \tag{2.9}$$

and

$$\mathcal{R}_g = \hat{g}\left(\mathcal{F}_g\right) = \frac{1}{1-l}\int_{\mathcal{F}_g} g(s)\mathrm{d}s \tag{2.10}$$

respectively. We denote

$$G_\gamma(t) = \gamma(t)^{-1}\int_t^{+\infty} g(s)\gamma(s)\mathrm{d}s. \tag{2.11}$$

Now, we are in a position to state our main result.

Theorem 2.2 ([23]) *Let* $(u_0, u_1) \in \left(V \bigcap H^2(\Omega)\right) \times V$, *Assume that* (2.1)-(2.2) *hold and* $\mathcal{R}_g < \frac{1}{2}$. *If* $G_\gamma(0) < \frac{(1-l)(2-l)}{2}$, *then there exist positive constants* C *and* ν *such that*

$$E(t) \le C\gamma(t)^{-\nu}, \quad t \ge 0. \tag{2.12}$$

3. Arbitrary Rate of Decay

Now we define

$$\Phi(t) = \frac{1}{\rho+1}\int_\Omega |u_t|^\rho u_t u\mathrm{d}x + \int_\Omega \nabla u_t \cdot \nabla u\mathrm{d}x + \frac{1}{2}\int_{\Gamma_0} py^2\mathrm{d}\Gamma + \int_{\Gamma_0} uy\mathrm{d}\Gamma. \tag{3.1}$$

Using (1.1) and (3.1), we have

$$\begin{aligned}\Phi'(t) = {} & \frac{1}{\rho+1}\|u_t\|_{\rho+2}^{\rho+2} - \|\nabla u\|^2 + \|\nabla u_t\|^2 + \int_\Omega \nabla u\int_0^t g(t-s)\nabla u(s)\mathrm{d}s\mathrm{d}x \\ & + \int_\Omega \Delta u_t u\mathrm{d}\Gamma + 2\int_{\Gamma_0} uy_t\mathrm{d}\Gamma - \int_{\Gamma_0} q(x)y^2\mathrm{d}\Gamma.\end{aligned} \tag{3.2}$$

We use here the following identity due to [1], to give a better estimate for the term $\int_\Omega \nabla u\int_0^t g(t-s)\nabla u(s)\mathrm{d}s\mathrm{d}x$:

$$\begin{aligned}& \int_\Omega \nabla u\int_0^t g(t-s)\nabla u(s)\mathrm{d}s\mathrm{d}x \\ & = \frac{1}{2}\left(\int_0^t g(s)\mathrm{d}s\right)\|\nabla u\|^2 + \frac{1}{2}\int_0^t g(t-s)\|\nabla u(s)\|^2\mathrm{d}s - \frac{1}{2}(g\circ\nabla u)(t).\end{aligned} \tag{3.3}$$

From (2.1), (3.2) and (3.3), integration by parts and Young's inequality, we derive for any $\delta_0 > 0$,

$$\begin{aligned}\Phi'(t) \le {} & \frac{1}{\rho+1}\|u_t\|_{\rho+2}^{\rho+2} + (1+\delta_0)\|\nabla u_t(t)\|^2 - \left(\frac{1+l}{2} - \delta_0\tilde{\lambda}\right)\|\nabla u\|^2 \\ & + \frac{1}{2}\int_0^t g(t-s)\|\nabla u(s)\|^2\mathrm{d}s - \frac{1}{2}(g\circ u)(t) \\ & + \frac{1}{\delta_0}\|y_t\|_{\Gamma_0}^2 - \int_{\Gamma_0} q(x)y^2\mathrm{d}\Gamma.\end{aligned} \tag{3.4}$$

As in [5], we have:

Lemma 3.1 *For* $u \in H_0^1(\Omega)$, *we have*

$$\int_\Omega \left(\int_0^t g(t-s)\big(u(t)-u(s)\big)\mathrm{d}s \right)^2 \mathrm{d}x \le \lambda(1-l)(g\circ\nabla u)(t). \tag{3.5}$$

Now we define the functional

$$\Psi(t) = \int_\Omega \left(\Delta u_t - \frac{1}{\rho+1}|u_t|^\rho u_t \right) \int_0^t g(t-s)\big(u(t)-u(s)\big)\mathrm{d}s\mathrm{d}x. \tag{3.6}$$

It follows from (1.1) and (3.6) that

$$\begin{aligned}
\Psi'(t) &= \int_\Omega \Delta u_t \int_0^t g'(t-s)\big(u(t)-u(s)\big)\mathrm{d}s\mathrm{d}x - \left(\int_0^t g(s)\mathrm{d}s \right) \|\nabla u_t\|^2 \\
&\quad + \left(1 - \int_0^t g(s)\mathrm{d}s \right) \int_\Omega \nabla u(t) \cdot \left(\int_0^t g(t-s)\big(\nabla u(t)-\nabla u(s)\big)\mathrm{d}s \right) \mathrm{d}x \\
&\quad + \int_\Omega \left(\int_0^t g(t-s)\big(\nabla u(t)-\nabla u(s)\big)\mathrm{d}s \right)^2 \mathrm{d}x - \frac{\int_0^t g(s)\mathrm{d}s}{\rho+1} \|u_t\|_{\rho+2}^{\rho+2} \\
&\quad + \int_\Omega \nabla u_t \int_0^t g(t-s)\big(\nabla u(t)-\nabla u(s)\big)\mathrm{d}s\mathrm{d}x \\
&\quad - \int_\Omega \frac{1}{\rho+1}|u_t|^\rho u_t \int_0^t g'(t-s)\big(u(t)-u(s)\big)\mathrm{d}s\mathrm{d}x \\
&\quad - \int_{\Gamma_0} y_t \left(\int_0^t g(t-s)\big(u(t)-u(s)\big)\mathrm{d}s \right) \mathrm{d}\Gamma \\
&= I_1 - I_2 + \left(1 - \int_0^t g(s)\mathrm{d}s \right) I_3 + I_4 - I_5 + I_6 - I_7 - I_8.
\end{aligned} \tag{3.7}$$

For any $\delta > 0$, we have

$$I_1 \le \delta \|\nabla u_t(t)\|^2 - \frac{g(0)}{4\delta}\lambda\big(g'(s)\circ\nabla u\big)(t). \tag{3.8}$$

For all measurable sets $\mathcal{A}$ and $\mathcal{F}$ such that $\mathcal{A} = \mathbb{R}^+ \setminus \mathcal{F}$, I_3, I_4 and I_6 can be estimated as in [1]:

$$\begin{aligned}
I_3 &\le \delta_1 \|\nabla u\|^2 + \frac{1-l}{4\delta_1} \int_\Omega \int_{\mathcal{A}_t} g(t-s)\big|\nabla u(t)-\nabla u(s)\big|^2 \mathrm{d}s\mathrm{d}x \\
&\quad + \frac{3}{2}(1-l)\hat{g}(\mathcal{F})\|\nabla u\|^2 + \frac{1}{2}\int_{\mathcal{F}_t} g(t-s)\|\nabla u(s)\|^2 \mathrm{d}s, \quad \delta_1 > 0,
\end{aligned} \tag{3.9}$$

$$\begin{aligned}
I_4 &\le \left(1 + \frac{1}{\delta_2} \right)(1-l)\int_\Omega \int_{\mathcal{A}_t} g(t-s)\big|\nabla u(t)-\nabla u(s)\big|^2 \mathrm{d}s\mathrm{d}x \\
&\quad + (1+\delta_2)(1-l)\hat{g}(\mathcal{F})\int_\Omega \int_{\mathcal{F}_t} g(t-s)\big|\nabla u(t)-\nabla u(s)\big|^2 \mathrm{d}s\mathrm{d}x, \quad \delta_2 > 0,
\end{aligned} \tag{3.10}$$

$$\begin{aligned}
I_6 &\le \delta_1 \|\nabla u_t\|^2 + \frac{1}{4\delta_1} \int_\Omega \int_{\mathcal{A}_t} g(t-s)\big|\nabla u(t)-\nabla u(s)\big|^2 \mathrm{d}s\mathrm{d}x \\
&\quad + \frac{3}{2}\hat{g}(\mathcal{F})\|\nabla u_t\|^2 + \frac{1}{2}\int_{\mathcal{F}_t} g(t-s)\|\nabla u(s)\|^2 \mathrm{d}s, \quad \delta_1 > 0,
\end{aligned} \tag{3.11}$$

where $\hat{g}$ is defined in (2.8). For any $\delta > 0$,

$$I_7 \le \delta \|\nabla u_t(t)\|^2 - \frac{g(0)}{4\delta}\lambda\big(g'(s)\circ\nabla u\big)(t). \tag{3.12}$$

For I_8, for $\delta_3, \delta_4 > 0$, we use a different estimate as

$$
\begin{aligned}
I_8 &= \int_{\Gamma_0} y_t \left(\int_{\mathcal{A}_t} g(t-s)\big(u(t)-u(s)\big)\mathrm{d}s \right)\mathrm{d}\Gamma \\
&\quad + \int_{\Gamma_0} y_t \left(\int_{\mathcal{F}_t} g(t-s)\big(u(t)-u(s)\big)\mathrm{d}s \right)\mathrm{d}\Gamma \\
&\le \frac{1}{2}\|y_t\|^2_{\Gamma_0} + \frac{\tilde{\lambda}(1-l)}{2}\int_\Omega\int_{\mathcal{A}_t} g(t-s)\big|\nabla u(t)-\nabla u(s)\big|^2 \mathrm{d}s\mathrm{d}x \\
&\quad + \frac{1}{4\delta_3}\hat{g}(\mathcal{F})\|y_t\|^2_{\Gamma_0} \\
&\quad + \delta_3\tilde{\lambda}\hat{g}(\mathcal{F})\|\nabla u\|^2 + \frac{1}{4\delta_4}\|y_t\|^2_{\Gamma_0} \\
&\quad + \delta_4\tilde{\lambda}(1-l)\int_{\mathcal{F}_t} g(t-s)\|\nabla u(s)\|^2 \mathrm{d}s.
\end{aligned} \tag{3.13}
$$

Taking into account these estimates in (3.6), let t_* be a number such that $\int_0^{t_*} g(s)\mathrm{d}s = g_*$, we obtain that

$$
\begin{aligned}
\Psi'(t) &\le \left(-\frac{g_*}{2}+\delta_1\right)\|\nabla u_t\|^2 - \frac{g_*}{\rho+1}\|u_t\|^{\rho+2}_{\rho+2} \\
&\quad + \left\{(1-g_*)\left(\delta_1 + \frac{3}{2}(1-l)\hat{g}(\mathcal{F})\right) + \delta_3\tilde{\lambda}\hat{g}(\mathcal{F}) + \delta\right\} \\
&\quad \times \|\nabla u\|^2 (1-l)\left(\frac{1-g_*}{4\delta_1} + \frac{1+\delta_2}{\delta_2} + \frac{\tilde{\lambda}}{2}\right)\int_\Omega\int_{\mathcal{A}_t} g(t-s)\big|\nabla u(t)-\nabla u(s)\big|^2 \mathrm{d}s\mathrm{d}x \\
&\quad - \frac{3}{4\delta} g(0)\lambda(g'\circ\nabla u)(t) \\
&\quad + (1+\delta_2)(1-l)\hat{g}(\mathcal{F})\int_\Omega\int_{\mathcal{F}_t} g(t-s)\big|\nabla u(t)-\nabla u(s)\big|^2 \mathrm{d}s\mathrm{d}x \\
&\quad + \left(\frac{1-g_*}{2} + \delta_4\tilde{\lambda}(1-l)\right)\int_{\mathcal{F}_t} g(t-s)\|\nabla u(s)\|^2 \\
&\quad + \left(\frac{1}{2} + \frac{\hat{g}(\mathcal{F})}{4\delta_3} + \frac{1}{4\delta_4}\right)\|y_t\|^2_{\Gamma_0}.
\end{aligned} \tag{3.14}
$$

Let

$$
I(t) = \int_\Omega\int_0^t G_\gamma(t-s)\big|\nabla u(s)\big|^2 \mathrm{d}s\mathrm{d}x, \tag{3.15}
$$

and $G_\gamma(t)$ is given in (2.11), we define the following functional

$$
F(t) = ME(t) + \varepsilon\Phi(t) + \Psi(t) + \epsilon I(t), \tag{3.16}
$$

then we know from [1] that

$$
\begin{aligned}
I'(t) &\le G_\gamma(0)\|\nabla u\|^2 - \eta(t)\int_0^t G_\gamma(t-s)\|\nabla u(s)\|^2 \mathrm{d}s \\
&\quad - \int_0^t g(t-s)\|\nabla u(s)\|^2 \mathrm{d}s.
\end{aligned} \tag{3.17}
$$

At the same time, we have the following lemmas.

Lemma 3.2 *For M large enough, there exist two positive constants ρ_1 and ρ_2 such that*

$$
\rho_1\big(E(t)+I(t)\big) \le F(t) \le \rho_2\big(E(t)+I(t)\big). \tag{3.18}
$$

Proof. See, e.g. Liu [5].

Proof of Theorem 2.2 By using (2.7), (3.4), (3.13)-(3.16), a series of com-

putations yields, for $t \geq t_*$,

$$\begin{aligned}
F'(t) \leq & \left(\frac{M}{2}-\frac{3}{4\delta}g(0)\lambda\right)(g'\circ\nabla u)(t)-\left(\frac{g_*}{\rho+1}-\frac{\varepsilon}{1+\rho}\right)\|u_t(t)\|_{\rho+2}^{\rho+2} \\
& -\left[\frac{M}{2}+\frac{g_*}{2}-\delta_1-\varepsilon(1+\delta_0)\right]\|\nabla u_t(t)\|^2 \\
& +(1+\delta_2)(1-l)\hat{g}(\mathcal{F})\int_\Omega\int_{\mathcal{F}_t}g(t-s)|\nabla u(t)-\nabla u(s)|^2\,\mathrm{d}s\mathrm{d}x \\
& +\left\{(1-g_*)\left(\delta_1+\frac{3}{2}(1-l)\hat{g}(\mathcal{F})\right)+\delta_3\tilde{\lambda}\hat{g}(\mathcal{F})+\delta+eG_\gamma(0)-\varepsilon\left(\frac{1+l}{2}-\delta_0\tilde{\lambda}\right)\right\}\|\nabla u\|^2 \\
& +(1-l)\left(\frac{1-g_*}{4\delta_1}+\frac{1+\delta_2}{\delta_2}+\frac{\tilde{\lambda}}{2}\right)\int_\Omega\int_{\mathcal{A}_t}g(t-s)|\nabla u(t)-\nabla u(s)|^2\,\mathrm{d}s\mathrm{d}x \\
& -\left(\epsilon-\frac{\varepsilon}{2}\right)\int_0^t g(t-s)\|\nabla u(s)\|^2\,\mathrm{d}s-\frac{\varepsilon}{2}(g\circ\nabla u)(t)\left(\frac{1-g_*}{2}+\delta_4\tilde{\lambda}(1-l)\right)\int_{\mathcal{F}_t}g(t-s)\|\nabla u(s)\|^2\,\mathrm{d}s\mathrm{d}x \\
& -\epsilon\eta(t)-\varepsilon\int_{\Gamma_0}q(x)y^2\mathrm{d}\Gamma-\left[Mp_0-\frac{\varepsilon}{\delta_0}-\left(\frac{1}{2}+\frac{\hat{g}(\mathcal{F})}{4\delta_3}+\frac{1}{4\delta_4}\right)\right]\|y_t\|_{\Gamma_0}^2.
\end{aligned} \tag{3.19}$$

For $n \in \mathbb{N}$, as in [32] we introduce the sets

$$\mathcal{A}_n = \left\{s \in \mathbb{R}^+ : ng'(s)+g(s) \leq 0\right\}. \tag{3.20}$$

It is easy to see that

$$\bigcup_n \mathcal{A}_n = \mathbb{R}^+ \setminus \left\{\mathcal{F}_g \cup \mathcal{N}_g\right\}, \tag{3.21}$$

where $\mathcal{F}_g$ is given in (2.9) and $\mathcal{N}_g$ is the null set where g' is not defined. Additionally, we denote $\mathcal{F}_n = \mathbb{R}^+ \setminus \mathcal{A}_n$, then

$$\lim_{n\to\infty}\hat{g}(\mathcal{F}_n) = \hat{g}(\mathcal{F}_g), \tag{3.22}$$

since $\mathcal{F}_{n+1} \subset \mathcal{F}_n$ for all n and $\bigcap_n \mathcal{F}_n = \mathcal{F}_g \cup \mathcal{N}_g$. Then, we take $\mathcal{A} = \mathcal{A}_n$ and $\mathcal{F} = \mathcal{F}_n$ in (3.18), it follows that

$$\begin{aligned}
F'(t) \leq & \left(\frac{M}{2}-\frac{3}{4\delta}g(0)\lambda\right)(g'\circ\nabla u)(t)-\left(\frac{g_*}{\rho+1}-\frac{\varepsilon}{\rho+1}\right)\|u_t(t)\|_{\rho+2}^{\rho+2} \\
& -\left[\frac{M}{2}+\frac{g_*}{2}-\delta_1-\varepsilon(1+\delta_0)\right]\|\nabla u_t(t)\|^2 \\
& -\left(\epsilon-\frac{1+\varepsilon-g_*}{2}-\delta_4\tilde{\lambda}(1-l)\right)\int_0^t g(t-s)\|\nabla u(s)\|^2\,\mathrm{d}s \\
& +\left\{(1-g_*)\left(\delta_1+\frac{3}{2}(1-l)\hat{g}(\mathcal{F}_n)\right)+\delta_3\tilde{\lambda}\hat{g}(\mathcal{F}_n)+\delta+eG_\gamma(0)\right. \\
& \quad \left.-\left[\sigma+(1-\sigma)\right]\varepsilon\frac{1+l}{2}+\varepsilon\delta_0\tilde{\lambda}\right\}\|\nabla u\|^2 \\
& +(1-l)\left(\frac{1-g_*}{4\delta_1}+\frac{1+\delta_2}{\delta_2}+\frac{\tilde{\lambda}}{2}\right)\int_\Omega\int_{\mathcal{A}_t}g(t-s)|\nabla u(t)-\nabla u(s)|^2\,\mathrm{d}s\mathrm{d}x \\
& -\left(\frac{\varepsilon}{2}-(1+\delta_2)(1-l)\hat{g}(\mathcal{F}_n)\right)(g\circ\nabla u)(t) \\
& -\epsilon\eta(t)I(t)-\varepsilon\int_{\Gamma_0}q(x)y^2\mathrm{d}\Gamma-\left[Mp_0-\frac{\varepsilon}{\delta_0}-\left(\frac{1}{2}+\frac{\hat{g}(\mathcal{F}_n)}{4\delta_3}+\frac{1}{4\delta_4}\right)\right]\|y_t\|_{\Gamma_0}^2,
\end{aligned} \tag{3.23}$$

for some $0<\delta<1$. Since $\mathcal{R}_g=\hat{g}\left(\mathcal{F}_g\right)<\frac{1}{2}$, we can choose ε,δ_2 small enough and n,t_* large enough such that

$$\frac{\varepsilon}{2}-\left(1+\delta_2\right)\left(1-l\right)\hat{g}\left(\mathcal{F}_n\right)\geq 0 \tag{3.24}$$

and

$$\frac{3}{2}\left(1-l\right)\left(1-g_*\right)\hat{g}\left(\mathcal{F}_n\right)-\sigma\varepsilon\frac{1+l}{2}<0 \tag{3.25}$$

with $\sigma=\frac{3\left(1-l\right)\left(1-g_*\right)}{2g_*\left(1+l\right)}$. Note that for t_* large enough. Furthermore, we require that

$$\begin{aligned}\frac{1+\varepsilon-g_*}{2}+\delta_4\tilde{\lambda}\left(1-l\right)\leq\epsilon\leq\frac{1}{G_\gamma\left(0\right)}\Bigg(&\left(1-\sigma\right)\varepsilon\frac{1+l}{2}\\&-\left(1-g_*\right)\delta_1-\delta_3\tilde{\lambda}\hat{g}\left(\mathcal{F}_n\right)-\varepsilon\delta_0\tilde{\lambda}+\delta\Bigg).\end{aligned} \tag{3.26}$$

Combining (3.24) and (3.25), we obtain

$$\left(1-g_*\right)\left(\delta_1+\frac{3}{2}\left(1-l\right)\hat{g}\left(\mathcal{F}_n\right)\right)+\delta_3\tilde{\lambda}\hat{g}\left(\mathcal{F}_n\right)+\delta+eG_\gamma\left(0\right)-\varepsilon\frac{1+l}{2}+\varepsilon\delta_0\tilde{\lambda}<0 \tag{3.27}$$

Choose our constants properly so that:

$$\frac{M}{2}-\frac{3}{4\delta}g\left(0\right)\lambda\geq\frac{M}{4}, \tag{3.28}$$

$$Mp_0-\frac{\varepsilon}{\delta_0}-\left(\frac{1}{2}+\frac{\hat{g}\left(\mathcal{F}_n\right)}{4\delta_3}+\frac{1}{4\delta_4}\right)\geq 0, \tag{3.29}$$

$$\left(1-l\right)\left(\frac{1-g_*}{4\delta_1}+\frac{1+\delta_2}{\delta_2}+\frac{\tilde{\lambda}}{2}\right)-\frac{M}{4n}<0 \tag{3.30}$$

together with (3.22) yield

$$F'\left(t\right)\leq -C_1E\left(t\right)-\epsilon\eta\left(t\right)I\left(t\right),\quad t\geq t_*. \tag{3.31}$$

As $\eta\left(t\right)$ is decreasing, we have $\eta\left(t\right)\leq\eta\left(0\right)$ for all $t\geq t_*$. Then (3.30) becomes

$$F'\left(t\right)\leq -\frac{C_1}{\eta\left(0\right)}\eta\left(t\right)E\left(t\right)-\epsilon\eta\left(t\right)I\left(t\right),\quad t\geq t_*.$$

Since $F\left(t\right)$ is equipped with $E\left(t\right)+I\left(t\right)$, we get

$$F'\left(t\right)\leq -C_2\eta\left(t\right)F\left(t\right), \tag{3.32}$$

integrating (3.31) over $\left[t_*,t\right]$ yields

$$F\left(t\right)\leq e^{-C_2\int_{t_*}^{t}\eta(s)\mathrm{d}s}F\left(t_*\right),\quad t\geq t_*.$$

Then using the left hand side inequality in (3.17), we get

$$\rho_1\left(E\left(t\right)+I\left(t\right)\right)\leq e^{-C_2\int_{t_*}^{t}\eta(s)\mathrm{d}s}F\left(t_*\right),\quad t\geq t_*.$$

By virtue of the continuity and boundedness of $E(t)$ in the interval $[0,t_*]$, we conclude that

$$E(t) \le C\gamma^{-\nu}(t), \quad t \ge 0 \tag{3.33}$$

for some positive constants C and ν.

Acknowledgements

This work was in part supported by Shanghai Second Polytechnical University and the key discipline "Applied Mathematics" of Shanghai Second Polytechnic University with contract number XXKZD1304.

References

[1] Tatar, N. (2011) Arbitrary Decays in Linear Viscoelasticity. *Journal of Mathematical Physics*, **52**, Article ID: 013502.

[2] Cavalcanti, M.M., Domingos Cavalcanti, V.N. and Ferreira, J. (2001) Existence and Uniform Decay for a Non-Linear Viscoelastic Equation with Strong Damping. *Mathematical Methods in the Applied Sciences*, **24**, 1043-1053. https://doi.org/10.1002/mma.250

[3] Love, A.E.H. (1944) A Treatise on the Mathematical Theory of Elasticity. Dover, New York.

[4] Fabrizio, M. and Morro, A. (1992) Mathematical Problems in Linear Viscoelasticity. SIAM Studies in Applied Mathematics, No. 12, Philadelphia.

[5] Liu, W. (2014) Arbitrary Rate of Decay for a Viscoelastic Equation with Acoustic Boundary Conditions. *Applied Mathematics Letters*, **38**, 155-161. https://doi.org/10.1090/S0002-9904-1974-13714-6

[6] Beale, J.T. and Rosencrans, S.I. (1974) Acoustic Boundary Conditions. *Bulletin of the AMS*, **80**, 1276-1278.

[7] Frota, C.L. and Goldstein, J.A. (2000) Some Nonlinear Wave Equations with Acoustic Boundary Conditions. *Journal of Differential Equations*, **164**, 92-109. https://doi.org/10.1006/jdeq.1999.3743

[8] Frota, C.L. and Larkin, N.A. (2006) Uniform Stabilization for a Hyperbolic Equation with Acoustic Boundary Conditions in Simple Connected Domains. In: Cazenave, T., Costa, D., Lopes, O., Manásevich, R., Rabinowitz, P., Ruf, B. and Tomei, C., Eds., *Contributions to Nonlinear Analysis*, Vol. 66, Birkhauser, Basel, 297-312. https://doi.org/10.1007/3-7643-7401-2_20

[9] Park, J.Y. and Park, S.H. (2011) Decay Rate Estimates for Wave Equations of Memory Type with Acoustic Boundary Conditions. *Nonlinear Analysis*, **74**, 993-998.

[10] Munoz Rivera, J.E. and Qin, Y. (2003) Polynomial Decay for the Energy with an Acoustic Boundary Condition. *Applied Mathematics Letters*, **16**, 249-256.

[11] Dafermos, C.M. (1970) Asymptotic Stability in Viscoelasticity. *Archive for Rational Mechanics and Analysis*, **37**, 297-308. https://doi.org/10.1007/BF00251609

[12] Dafermos, C.M. (1970) An Abstract Volterra Equation with Applications to Linear Viscoelasticity. *Journal of Differential Equations*, **7**, 554-569.

[13] Berrimi, S. and Messaoudi, S.A. (2006) Existence and Decay of Solutions of a Viscoelastic Equation with a Nonlinear Source. *Nonlinear Analysis*, **64**, 2314-2331.

[14] Cavalcanti, M.M., Domingos Cavalcanti, V.N. and Martinez, P. (2008) General Decay Rate Estimates for Viscoelastic Dissipative Systems. *Nonlinear Analysis*, **68**, 177-193.

[15] Liu, W.J. and Sun, Y. (2014) General Decay of Solutions for a Weak Viscoelastic Equation with Acoustic Boundary Conditions. *Zeitschrift für Angewandte Mathematik und Physik*, **65**, 125-134. https://doi.org/10.1007/s00033-013-0328-y

[16] Messaoudi, S.A. and Tatar, N.-E. (2007) Global Existence and Uniform Stability of Solutions for a Quasilinear Viscoelastic Problem. *Mathematical Methods in the Applied Sciences*, **30**, 665-680. https://doi.org/10.1002/mma.804

[17] Messaoudi, S.A. and Tatar, N.-E. (2009) Exponential Decay for a Quasilinear Viscoelastic Equation. *Mathematische Nachrichten*, **282**, 1443-1450. https://doi.org/10.1002/mana.200610800

[18] Messaoudi, S.A. (2008) General Decay of Solutions of a Viscoelastic Equation. *Journal of Mathematical Analysis and Applications*, **341**, 1457-1467.

[19] Wu, S.T. (2012) General Decay of Energy for a Viscoelastic Equation with Damping and Source Terms. *Taiwanese Journal of Mathematics*, **16**, 113-128.

[20] Han, X. and Wang, M. (2009) General Decay of Energy for a Viscoelastic Equation with Nonlinear Damping. *Mathematical Methods in the Applied Sciences*, **32**, 346-358. https://doi.org/10.1002/mma.1041

[21] Park, J.Y. and Park, S.H. (2009) General Decay for Quasiliear Viscoelastic Equations with Nonlinear Weak Damping. *Journal of Mathematical Physics*, **50**, 1-10. https://doi.org/10.1063/1.3187780

[22] Fabrizio, M. and Polidoro, S. (2002) Asymptotic Decay for Some Differential Systems with Fading Memory. *Applicable Analysis*, **81**, 1245-1264. https://doi.org/10.1080/0003681021000035588

[23] Tatar, N. (2008) Polynomial Stability without Polynomial Decay of the Relaxation Function. *Mathematical Methods in the Applied Sciences*, **31**, 1874-1886. https://doi.org/10.1002/mma.1018

[24] Yu, S.Q. (2009) Polynomial Stability of Solutions for a System of Non-Linear Viscoelastic Equations. *Applicable Analysis*, **88**, 1039-1051. https://doi.org/10.1080/00036810903114825

[25] Araújo, R.O., Ma, T. and Qin, Y. (2013) Long-Time Behavior of a Quasilinear Viscoelastic Equation with Past History. *Journal of Differential Equations*, **254**, 4066-4087.

[26] Cavalcanti, M.M., Domingos Cavalcanti, V.N., Prates Filho, J.A. and Soriano, J.A. (2001) Existence and Uniform Decay Rates for Viscoelastic Problems with Non-Linear Boundary Damping. *Differential and Integral Equations*, **14**, 85-116.

[27] Chueshov, I. and Lasiecka, I. (2008) Long-Time Behavior of Second Order Evolution Equations with Nonlinear Damping. Vol. 195, Memoirs of the American Mathematical Society, Providence.

[28] Munoz Rivera, J.E., Lapa, E.C. and Barreto, R. (1996) Decay Rates for Viscoelastic Plates with Memory. *Journal of Elasticity*, **44**, 61-87. https://doi.org/10.1007/BF00042192

[29] Wu, S.T. (2011) General Decay of Solutions for a Viscoelastic Equation with Nonlinear Damping and Source Terms. *Acta Mathematica Scientia*, **31**, 1436-1448.

[30] Han, X. and Wang, M. (2009) Global Existence and Uniform Decay for a Nonlinar Viscoelastic Equation with Damping. *Nonlinear Analysis*, **70**, 3090-3098.

[31] Qin, Y., Feng, B. and Zhang, M. (2014) Uniform Attractors for a Non-Autonomous Viscoelastic Equation with a Past History. *Nonlinear Analysis*, **101**, 1-15.

[32] Pata, V. (2006) Exponential Stability in Linear Viscoelasticity. *Quarterly of Applied Mathematics*, **6**, 499-513. https://doi.org/10.1090/S0033-569X-06-01010-4

Scientific Research Publishing

Journal of Applied Mathematics and Physics, 2017, 5, 933-938
http://www.scirp.org/journal/jamp
ISSN Online: 2327-4379
ISSN Print: 2327-4352

A Note on the Cosmological Constant in $f(R)$ Gravity

Peter K. F. Kuhfittig

Department of Mathematics, Milwaukee School of Engineering, Milwaukee, Wisconsin, USA
Email: kuhfitti@msoe.edu

How to cite this paper: Kuhfittig, P.K.F. (2017) A Note on the Cosmological Constant in $f(R)$ Gravity. *Journal of Applied Mathematics and Physics*, **5**, 933-938.
https://doi.org/10.4236/jamp.2017.54082

Received: March 14, 2017
Accepted: April 27, 2017
Published: April 30, 2017

Copyright © 2017 by author and Scientific Research Publishing Inc.
This work is licensed under the Creative Commons Attribution International License (CC BY 4.0).
http://creativecommons.org/licenses/by/4.0/

Open Access

Abstract

The starting point in this note is $f(R)$ modified gravity in a cosmological setting. We assume a spatially flat universe to describe late-time cosmology and the perfect-fluid equation of state $p=\omega\rho$ to model the hypothesized dark energy. Given that on a cosmological scale, $f(R)$ modified gravity must remain close to Einstein gravity to be consistent with observation, it was concluded that either (1) Einstein's cosmological constant was the only acceptable model for the accelerated expansion, or that (2) the equation of state for dark energy was far more complicated than the perfect-fluid model and might even exclude a constant ω.

Keywords

Cosmological Constant, $f(R)$ Gravity

1. Introduction

The discovery that our universe is undergoing an accelerated expansion [1] [2] has led to a renewed interest in modified theories of gravity. One of the most important of these, $f(R)$ modified gravity, replaces the Ricci scalar R in the Einstein-Hilbert action

$$S_{\mathrm{EH}}=\int\sqrt{-g}\,R\mathrm{d}^4x$$

by a nonlinear function $f(R)$:

$$S_{f(R)}=\int\sqrt{-g}\,f(R)\mathrm{d}^4x.$$

(For a review, see Refs. [3] [4] [5].)

An alternative to the modified gravity model is the hypothesis that the acceleration is due to a negative pressure dark energy, implying that $\ddot{a}>0$ in the

Friedmann equation

$$\frac{\ddot{a}(t)}{a(t)}=-\frac{4\pi}{3}(\rho+3p).$$

(We are using units in which $c=G=1$.) In the equation of state $p=\omega\rho$, $\ddot{a}>0$ corresponds to the range of values $\omega<-1/3$, referred to as *quintessence dark energy*. The case $\omega=-1$ is equivalent to assuming Einstein's cosmological constant. It has been forcefully argued by Bousso [6] that the cosmological constant is the best model for dark energy. In this note, we go a step further and propose that $f(R)$ modified gravity implies that $\omega=-1$ is the only allowed value in the equation of state $p=\omega\rho$.

2. The Solution

For convenience of notation, we start with the spherically symmetric line element

$$\mathrm{d}s^2=-\mathrm{e}^{2\Phi(r)}\mathrm{d}t^2+\frac{\mathrm{d}r^2}{1-b(r)/r}+r^2\left(\mathrm{d}\theta^2+\sin^2\theta\mathrm{d}\phi^2\right). \tag{1}$$

It was shown by Lobo [7] that under the assumption that $\Phi'(r)\equiv 0$, the Einstein field equations are

$$\rho(r)=F(r)\frac{b'(r)}{r^2}, \tag{2}$$

$$p_r(r)=-F(r)\frac{b(r)}{r^3}+F'(r)\frac{rb'(r)-b(r)}{2r^2}-F''(r)\left(1-\frac{b(r)}{r}\right), \tag{3}$$

and

$$p_t(r)=-\frac{F'(r)}{r}\left(1-\frac{b(r)}{r}\right)+\frac{F(r)}{2r^3}\left[b(r)-rb'(r)\right], \tag{4}$$

where $F=\frac{\mathrm{d}f}{\mathrm{d}R}$. The curvature scalar R is given by

$$R(r)=\frac{2b'(r)}{r^2}. \tag{5}$$

For our purposes, a more convenient form of the line element is

$$\mathrm{d}s^2=-\mathrm{e}^{\nu(r)}\mathrm{d}t^2+\mathrm{e}^{\lambda(r)}\mathrm{d}r^2+r^2\left(\mathrm{d}\theta^2+\sin^2\theta\mathrm{d}\phi^2\right). \tag{6}$$

Here the Einstein field equations can be written [8]

$$8\pi\rho=\mathrm{e}^{-\lambda}\left(\frac{\lambda'}{r}-\frac{1}{r^2}\right)+\frac{1}{r^2}, \tag{7}$$

$$8\pi p_r=\mathrm{e}^{-\lambda}\left(\frac{1}{r^2}+\frac{\nu'}{r}\right)-\frac{1}{r^2} \tag{8}$$

and

$$8\pi p_t=\frac{1}{2}\mathrm{e}^{-\lambda}\left[\frac{1}{2}(\nu')^2+\nu''-\frac{1}{2}\lambda'\nu'+\frac{1}{r}(\nu'-\lambda')\right]. \tag{9}$$

Then if $\nu' \equiv 0$, Lobo's equations become

$$8\pi\rho(r) = F(r)\left[e^{-\lambda}\left(\frac{\lambda'}{r} - \frac{1}{r^2}\right) + \frac{1}{r^2}\right], \tag{10}$$

$$8\pi p_r(r) = F(r)\left[e^{-\lambda}\frac{1}{r^2} - \frac{1}{r^2}\right] + \frac{F'(r)}{2}\lambda' e^{-\lambda} - F''(r)e^{-\lambda} \tag{11}$$

and

$$8\pi p_t(r) = -\frac{F'(r)}{r}e^{-\lambda} - \frac{F(r)}{2r}\lambda' e^{-\lambda}. \tag{12}$$

Now substituting into the equation of state $p = \omega\rho$, we obtain

$$\begin{aligned} &\omega F(r)\left[e^{-\lambda}\left(\frac{\lambda'}{r} - \frac{1}{r^2}\right) + \frac{1}{r^2}\right] \\ &= F(r)\left[\frac{e^{-\lambda}}{r^2} - \frac{1}{r^2}\right] + \frac{F'(r)}{2}\lambda' e^{-\lambda} - F''(r)e^{-\lambda}. \end{aligned} \tag{13}$$

This equation can be rewritten as follows:

$$F''(r) - \frac{1}{2}F'(r)\lambda' + F(r)\left[\omega\frac{\lambda'}{r} + (\omega+1)\frac{1}{r^2}\left(e^{\lambda} - 1\right)\right] = 0. \tag{14}$$

Since we are dealing with a cosmological setting, we may assume the FLRW model, so that $\nu \equiv 0$:

$$ds^2 = -dt^2 + a^2(t)\left[\frac{dr^2}{1-kr^2} + r^2\left(d\theta^2 + \sin^2\theta d\phi^2\right)\right]. \tag{15}$$

Observe that we now have

$$e^{\lambda} = a^2(t)\frac{1}{1-kr^2} \tag{16}$$

and

$$\lambda = \ln a^2(t) + \ln\left(1-kr^2\right)^{-1}, \tag{17}$$

so that

$$\lambda' = \frac{2kr}{1-kr^2}, \tag{18}$$

which is independent of time. The significance of the special value $\omega = -1$ in Equation (14) now becomes apparent: the entire equation has become time independent, *i.e.*,

$$F''(r) - \frac{kr}{1-kr^2}F' - \frac{2k}{1-kr^2}F = 0. \tag{19}$$

(For later reference, observe that if $k = 0$, then $F(r) = c_1 + c_2 r$.) The solution of Equation (19) is

$$\begin{aligned} F(r) = c_1 &\cos\left[\sqrt{2}\ln\left(|k|r + \sqrt{k^2r^2 - 1}\right)\right] \\ &+ c_2 \sin\left[\sqrt{2}\ln\left(|k|r + \sqrt{k^2r^2 - 1}\right)\right], \quad k \neq 0. \end{aligned} \tag{20}$$

This solution can also be written

$$F(r)=c\sin\left[\sqrt{2}\ln(|k|r+\sqrt{k^2r^2-1}+\phi\right], \tag{21}$$

where $c=\sqrt{c_1^2+c_2^2}$ and $\phi=\tan^{-1}(c_1/c_2)$.

3. Staying Close to Einstein Gravity

In a cosmological setting, $f(R)$ modified gravity must remain close to Einstein gravity to be consistent with observation. In this section, we wish to show that it is possible, at least in principle, to choose the arbitrary constants in Equation (21) so that this goal is achieved.

The sinusoidal solution (21) has a large period and a small slope, especially for large r. To confirm this statement, observe that the function

$$g(r)=\sin\left[\sqrt{2}\ln\left(|k|r+\sqrt{k^2r^2-1}\right)\right]\sim\sin(\ln r) \tag{22}$$

for large r. So both $g'(r)$ and $g''(r)$ approach zero as $r\to\infty$. As a result, $\sin(\ln r)$ has the approximate form $ar+b$ on any interval that is not excessively large, and since the slope a is small in absolute value, we have

$$ar+b\approx b,\quad -1\le b\le 1. \tag{23}$$

We can now show that it is possible in principle to choose the arbitrary constants c and ϕ in such a way that $F(r)$ remains close to unity and both F' and F'' close to zero on one complete period.

Let $\phi=0$, so that

$$F(r)=c\sin\left[\sqrt{2}\ln\left(|k|r+\sqrt{k^2r^2-1}\right)\right]. \tag{24}$$

First observe that $F(r)=0$ whenever

$$\sqrt{2}\ln\left(|k|r+\sqrt{k^2r^2-1}\right)=n\pi$$

for all integers n. Solving for r, we get

$$r=\frac{1}{|k|}\cosh\frac{n\pi}{2}.$$

Now choose a particular n for which $F(r)\ge 0$ on the interval $[r_1,r_2]$, where

$$r_1=\frac{1}{|k|}\cosh\frac{n\pi}{2}\quad\text{and}\quad r_2=\frac{1}{|k|}\cosh\frac{(n+1)\pi}{2}. \tag{25}$$

Next, subdivide the interval $[r_1,r_2]$ into i subintervals I_i each of which is small enough so that b remains in a narrow range. Then on each separate subinterval, construct a tangent line $a_ir+b_i\approx b_i$ near the midpoint, thereby ensuring that $b_i\ne 0$. (See **Figure 1**) So we may now choose $c_i=1/b_i$ for the arbitrary constant c. We then repeat the procedure on the interval $[r_2,r_2+\pi]$, so that $F(r)\approx 1$ on the entire period $[r_1,r_2+\pi]$. Since both F' and F'' are close to zero [from Equation (22)], the periodicity of $F(r)$ guarantees that our $f(R)$ modified gravity is close to Einstein gravity for all r.

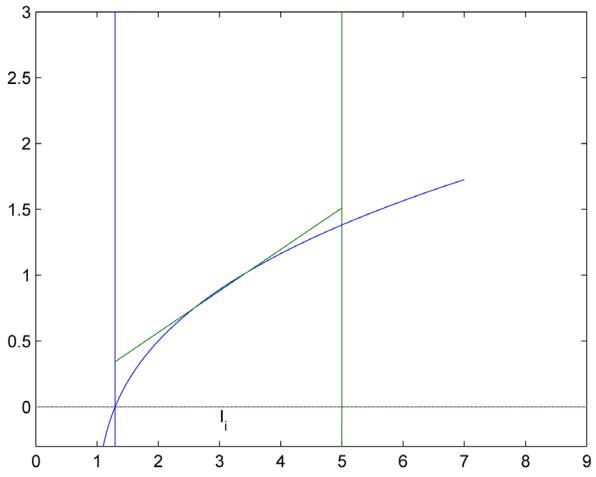

Figure 1. The line segment $a_i r + b_i$ on the interval I_i (not drawn to scale).

4. The Cosmological Constant

Suppose we return to Equation (14) and substitute Equations (16)-(18). Then we obtain

$$F'' - \frac{kr}{1-kr^2}F' + F\left[\omega\frac{2k}{1-kr^2} + \frac{\omega+1}{r^2}\left(a^2(t)\frac{1}{1-kr^2} - 1\right)\right] = 0. \tag{26}$$

While we normally assume that $k \neq 0$, it is noted in Ref. [3] that $k = 0$, representing a spatially flat universe, is not a dramatic departure from generality when it comes to late-time cosmology.

With $k = 0$, the time-dependent solution is

$$\begin{aligned} F(r) = c_1 \exp\left[(-\ln r)\left(\frac{1}{2}\sqrt{4\omega - 4a^2\omega - 4a^2 + 5} - \frac{1}{2}\right)\right] \\ + c_2 \exp\left[(\ln r)\left(\frac{1}{2}\sqrt{4\omega - 4a^2\omega - 4a^2 + 5} + \frac{1}{2}\right)\right]. \end{aligned} \tag{27}$$

In the special case $\omega = -1$, $F(r) = c_1 + c_2 r$, in agreement with Equation (19) with $k = 0$.

In the previous section, we dealt with a time-independent solution due to the assumption $\omega = -1$. This allowed our $f(R)$ modified model to remain close to Einstein gravity at least in principle. By contrast, solution (27) is time dependent. So if $\omega \neq -1$, we are dealing with two possibilities:

(a) if $\omega > -1$, there is no real solution;

(b) if $\omega < -1$, then the $f(R)$ model is far removed from Einstein gravity, *i.e.*, if $a^2(t)$ increases indefinitely, then the first term in solution (27) goes to zero, while the second term gets large. So $F(r)$ cannot remain close to unity.

We conclude that $\omega = -1$ in the equation of state $p = \omega\rho$ is the only allowed value. Since this note deals with rather reasonable assumptions, the only plausible objection to this conclusion is that the equation of state for dark energy is much more complicated than the perfect-fluid equation of state $p = \omega\rho$. This possibility was also raised by Lobo [5], who stated that a mixture of various in-

teracting non-ideal fluids may be necessary. This could imply that dark energy is dynamic in nature, thereby forcing us to exclude models with constant ω, including the cosmological constant.

5. Conclusions

The starting point in this note is $f(R)$ modified gravity in a cosmological setting. We also assume a spatially flat universe to describe late-time cosmology [3]; thus $k=0$ in the FLRW model. Our key assumption is the perfect-fluid equation of state $p=\omega\rho$ to describe the hypothesized dark energy. While $\omega<-1/3$ is sufficient to yield an accelerated expansion, it is concluded that $\omega=-1$ is the only value which allows our solution to remain close enough to Einstein gravity to be consistent with observation.

Weighing the above assumptions, we conclude that either (1) Einstein's cosmological constant is the only acceptable model for dark energy, or that (2) the equation of state is far more complicated than the above perfect-fluid equation and may even exclude a constant ω.

References

[1] Riess, A.G., *et al.* (1998) Observational Evidence from Supernovae for an Accelerating Universe and a Cosmological Constant. *Astronomical Journal*, **116**, 1009-1038. https://doi.org/10.1086/300499

[2] Perlmutter, S.J., *et al.* (1999) Measurements of Ω and Λ from 42 High-Red Shift Supernovae. *The Astrophysical Journal*, **517**, 565-586. https://doi.org/10.1086/307221

[3] Sotiriou, T.P. and Faraoni, V. (2010) $f(R)$ Theories of Gravity. *Reviews of Modern Physics*, **82**, 451-457. https://doi.org/10.1103/RevModPhys.82.451

[4] Nojiri, S. and Odintsov, S.D. (2007) Introduction to Modified Gravity and Gravitational Alternative for Dark Energy. *International Journal of Geometric Methods in Modern Physics*, **4**, 115. https://doi.org/10.1142/S0219887807001928

[5] Lobo, F.S.N. (2008) The Dark Side of Gravity: Modified Theories of Gravity. arXiv: 0807.1640.

[6] Bousso, R. (2012) The Cosmological Constant Problem, Dark Energy and the Landscape of String Theory. arXiv: 1203.0307.

[7] Lobo, F.S.N. and Oliveira, M.A. (2009) Wormhole Geometries in $f(R)$ Modified Theories of Gravity. *Physical Review D*, **80**, Article No.: 104012. https://doi.org/10.1103/physrevd.80.104012

[8] Rahaman, F., Chakraborty, K., Kuhfittig, P.K.F., Shit, G.C. and Rahman, M. (2014) A New Deterministic Model of Strange Stars. *European Physical Journal C*, **74**, 3126. https://doi.org/10.1140/epjc/s10052-014-3126-6

Journal of Applied Mathematics and Physics, 2017, 5, 939-952
http://www.scirp.org/journal/jamp
ISSN Online: 2327-4379
ISSN Print: 2327-4352

Classical Fundamental Unique Solution for the Incompressible Navier-Stokes Equation in $\mathbb{R}^N$

Waleed S. Khedr

Independent Researcher, Cairo, Egypt
Email: waleedshawki@yahoo.com

How to cite this paper: Khedr, W.S. (2017) Classical Fundamental Unique Solution for the Incompressible Navier-Stokes Equation in $\mathbb{R}^N$. *Journal of Applied Mathematics and Physics*, **5**, 939-952.
https://doi.org/10.4236/jamp.2017.54083

Received: March 21, 2017
Accepted: April 27, 2017
Published: April 30, 2017

Copyright © 2017 by author and Scientific Research Publishing Inc.
This work is licensed under the Creative Commons Attribution International License (CC BY 4.0).
http://creativecommons.org/licenses/by/4.0/

Open Access

Abstract

We present a class of non-convective classical solutions for the multidimensional incompressible Navier-Stokes equation. We validate such class as a representative for solutions of the equation in bounded and unbounded domains by investigating the compatibility condition on the boundary, the smoothness of the solution inside the domain and the boundedness of the energy. Eventually, we show that this solution is indeed the unique classical solution for the problem given some appropriate and convenient assumptions on the data.

Keywords

Fluid Mechanics, Navier-Stokes Equation, Fundamental Solutions

1. Introduction

In this article, a well known model is to be investigated that represents the flow of an incompressible fluid in both bounded and unbounded domains of $\mathbb{R}^N$. This model is commonly called the Navier-Stokes equation following the French engineer Navier who was the first to propose this model. This model was investigated later by Poisson and de Saint Venant. However, Stokes was the one who justified the model based on the principles of continuum mechanics. By advent of 1930, the interest in this model increased significantly and outstanding results were obtained by Leray, Hopf, Ladyzhenskaya and Finn.

This equation describes the flow of what is so called the Newtonian fluid. These are the fluids that exhibit shearing stress due to the presence of frictional forces. Frictional forces within fluids are consequences of its viscosity. Also, the gradient of the velocity represents a measure for the relative motion of the fluid's particles. Moreover, deformation of fluids is commonly associated with internal

and external body forces; the internal force is what we refer to as the pressure of the fluid. The derivation of the Navier-Stokes equation is a natural application of Newton's second law of motion, the balance of momentum and the mass conservation, which eventually leads to the definition of the Cauchy stress tensor. In Newtonian fluids, this stress tensor is a function in the pressure, the viscosity and the gradient of the velocity. For a convenient physical background about the basics of continuum mechanics and how we derive the Navier-Stokes equation we propose [1] [2]. Also a very interesting work from a physical point of view can be found in [3] [4]. In particular, the work of Kambe in [4] was the source of inspiration for the ideas in this article.

This model poses a serious challenge when it comes to proving the existence and the smoothness of its solution. This problem was perfectly addressed by Ladyzhenskaya in two dimensional spaces among many other issues in higher dimensional spaces [5]. However, a decisive answer in the three-dimensional space or higher remains unavailable. It is almost impossible to enlist all the results obtained for this equation. Therefore, we suggest for the interested reader to review the monographs [5] [6] [7] and the references within for much more details.

Recently, the interest in this equation is not fading at all. There are persistent efforts to clarify the properties of the solution, especially its smoothness. Among many respectful results, we mention the outstanding analysis by Tao in [8], the work of Constantin in [9] [10] [11]. A very interesting result for partial regularity of suitable weak solutions was obtained by Caffarelli in [12].

In this article the idea is simple. **A** class of possible solutions is proposed and then it is proved that it indeed represents **the** unique classical solution of the problem. Most of the results are obtained by considering standard theories of partial differential equations. Some of the results in the monograph [7] are also used repeatedly. In the next section a statement of the problem is introduced along with some definitions, notations and employed functional spaces. Afterwards, the proofs of the main results are established.

2. Statement of the Problem

The spatial domain is Ω which is either a bounded region in $\mathbb{R}^N$ or the whole of $\mathbb{R}^N$ and this point shall be specified explicitly. For the sake of conciseness, the notation Ω_t is used to denote $\Omega_t = \{(\boldsymbol{x},t) : \boldsymbol{x} \in \Omega, t \in (0,\infty)\}$. Clearly, such notation should not be taken to imply a moving boundary. The main model equation is in the form

$$\begin{cases} \boldsymbol{v}_t + (\boldsymbol{v}\cdot\nabla)\boldsymbol{v} = \mu\Delta\boldsymbol{v} - \nabla p + \boldsymbol{f} \quad \text{in } \Omega_t, \\ \boldsymbol{\omega} = \nabla\times\boldsymbol{v} \quad \text{in } \Omega_t, \\ \boldsymbol{v}(\boldsymbol{x},0) = \boldsymbol{v}_0(\boldsymbol{x}) \quad \text{and} \quad \boldsymbol{\omega}_0(x) = \nabla\times\boldsymbol{v}_0(x) \quad \text{in } \Omega, \\ \boldsymbol{v}(\boldsymbol{x},t) = \boldsymbol{v}^*(\boldsymbol{x}_{N-1},t) \quad \text{on } \partial\Omega_t, \\ \nabla\cdot\boldsymbol{v} = \nabla\cdot\boldsymbol{\omega} = 0 \quad \text{in } \bar{\Omega}_t \end{cases} \tag{1}$$

where the last equation in the above model is what many authors commonly refer to as the **incompressibility condition** or the **solenoidal condition**. The first

term in the first equation is the acceleration of the fluid's flow in time, the second is the convective term that represents the acceleration of the flow in space, the third represents the diffusion scaled by the kinematic viscosity constant μ, the fourth is the pressure, and the last one represents the total of the external body forces. The initial profile is denoted by $\boldsymbol{v}_0$ and the boundary datum is denoted by $\boldsymbol{v}^*$. The solution $\boldsymbol{v}$ is the vector field representing the velocity of the flow in each direction, and its rotation $\boldsymbol{\omega}$ is the vorticity. Note that $\nabla \cdot \boldsymbol{\omega} = 0$ in $\bar{\Omega}_t$ by compatibility.

The well known Lebesgue spaces $L^q(\Omega)$ will be used repeatedly to represent the functions with bounded mean of order q. The Sobolev space $H^m(\Omega)$ is used to represent functions with bounded derivatives such that for a vector field $\boldsymbol{v} = \{v_1, \cdots, v_N\}$ one has $\partial^{|\alpha|} v_i \in L^2(\Omega)$ for every $|\alpha| = 1, \cdots, m$ and $i = 1, \cdots, N$. This motivates the usage of the space $V^m(\Omega)$, which is a well known space of functions in the theory of incompressible fluids as a representative for divergence free (solenoidal) bounded vector fields such that
$V^m(\Omega) = \{\boldsymbol{v} \in H^m(\Omega) : \nabla \cdot \boldsymbol{v} = 0 \text{ in } \Omega\}$.

By laws of classical mechanics, the energy generated by a moving object is proportional to the square of its velocity. Hence, the energy $E(t)$ generated by the flow $\boldsymbol{v}$ is defined as follows

$$E(t) = \int_\Omega |\boldsymbol{v}(\boldsymbol{x}, t)|^2 \, \mathrm{d}\boldsymbol{x}. \tag{2}$$

Recall that the above integral represents the norm of $\boldsymbol{v}$ in the Lebesgue space $L^2(\Omega)$. The smoothness of $\boldsymbol{v}_0(\boldsymbol{x})$ is such that

$$\boldsymbol{v}_0(\boldsymbol{x}) \in \mathbf{C}^2(\bar{\Omega}) \cap V^{N+2}(\Omega). \tag{3}$$

The smoothness of the boundary datum $\boldsymbol{v}^*(\boldsymbol{x}_{N-1}, t)$ is such that

$$\boldsymbol{v}^*(\boldsymbol{x}_{N-1}, t) \in \mathbf{C}^\infty(\partial\Omega_t) \text{ and } \boldsymbol{v}^*(\cdot, t) \sim t^{-K^*} \text{ for any } K^* > 1. \tag{4}$$

Finally, the forcing term $\boldsymbol{f}$ is smooth in space and time such that

$$\boldsymbol{f}(\boldsymbol{x}, t) \in \mathbf{C}^1\left([0, \infty]; \mathbf{C}^1(\bar{\Omega}) \cap H^3(\Omega)\right) \text{ and } \boldsymbol{f}(\cdot, t) \sim t^{-K} \text{ for any } K > 0. \tag{5}$$

Note that the intersections in the above conditions are not really required in the case of bounded domain since boundedness of the domain and continuity of the functions are enough to imply boundedness in the sense of the mean. However, these requirements are of significant importance in the case of unbounded domain as will be shown later.

The target is to define a class of possible solutions to Model Equation (1) from which $\boldsymbol{v}$, $\boldsymbol{\omega}$ and p can be concluded. Once $\boldsymbol{v}$ is obtained, then p can easily be recovered from the main model. The validity of this solution as a meaningful physical solution will be investigated when inserted in the main model. A meaningful solution is a unique and smooth solution that vanishes as $t \to \infty$, and in the case of unbounded domain it vanishes as $|\boldsymbol{x}| \to \infty$ as well.

Remark. The **curl** operator or the rotation of a vector field has a physical meaning only in three dimensional space. However, it will be used in $\mathbb{R}^N$ for the sake of generality. Most of the results depend on the **curl** operator in the sense

of a differential operator without direct exposure to its definition. Note that the main interest is to find the velocity, which means that any use of the rotation, in spite of its significance in this work, is nothing more than a transient step. It can always be assumed that the space is three dimensional when needed, and a generalization becomes possible by reverting back to the results of the velocity. In particular, some of the vorticity ideas introduced in [7] are adopted in this study.

3. Main Results

In this section a class of possible solutions is proposed and the insertion of these solutions in the main model is investigated to check where they will lead to. This is initiated by the statement of the following claim.

Claim 1. The unique solution of Model Equation (1) is in the form $\boldsymbol{v}(\boldsymbol{x},t)=\psi(\boldsymbol{x},t)\boldsymbol{u}(t)$ where $\psi:\mathbb{R}^N\times\mathbb{R}\to\mathbb{R}$ is a scalar field and $\boldsymbol{u}=(u_1(t),\cdots,u_N(t))$ is a vector field such that, at least, $\psi(\boldsymbol{x},t)\in\mathbf{C}^2(\bar{\Omega}_t)$ and $\boldsymbol{u}\in\mathbf{C}(\mathbb{R})$.

An important question in the theory of Navier-Stokes equation is the ability to verify the compatibility condition on the boundary with minimum restrictions on the flux passing through the boundary especially if $\partial\Omega$ is divided into several parts ([6], p. 4-8). This condition is a natural consequence of the incompressibility of the flow. Hence, it takes the form

$$\int_{\partial\Omega}(\boldsymbol{v}\cdot\vec{\boldsymbol{n}})\mathrm{d}\boldsymbol{x}_{N-1}=0, \tag{6}$$

where $\vec{\boldsymbol{n}}$ is the outward unit vector normal to $\partial\Omega$. This motivates the introduction of the following lemma.

Lemma 1 (Tangential flow). Let Ω be an arbitrary domain, $\psi(\boldsymbol{x},t):\mathbb{R}^N\times\mathbb{R}\to\mathbb{R}$ be any scalar field such that $\psi\in\mathbf{C}^1(\bar{\Omega})$ and let $\boldsymbol{u}(t)=(u_1(t),\cdots,u_N(t))$ be any vector field independent of $\boldsymbol{x}$. The Compatibility Condition (6) is satisfied for every divergence free vector field $\boldsymbol{v}(\boldsymbol{x},t):\mathbb{R}^N\times\mathbb{R}\to\mathbb{R}^N$ in the form $\boldsymbol{v}=\psi(\boldsymbol{x},t)\boldsymbol{u}(t)$. In particular, on every part of $\partial\Omega$, $\boldsymbol{v}$ and its rotation $\boldsymbol{\omega}$ are tangents to $\partial\Omega$ such that $\boldsymbol{v}\cdot\vec{\boldsymbol{n}}=\boldsymbol{\omega}\cdot\vec{\boldsymbol{n}}=0$.

Proof. Given that $\boldsymbol{v}=\psi(\boldsymbol{x},t)\boldsymbol{u}(t)$ is divergence free such that $\nabla\cdot\boldsymbol{v}=0$ leads to

$$\sum_{i=1}^{N}\frac{\partial\psi}{\partial x_i}u_i=0. \tag{7}$$

Identity (7) can be used to deduce that $(\boldsymbol{v}\cdot\nabla)\boldsymbol{v}=(\nabla\boldsymbol{v})\boldsymbol{v}=\boldsymbol{0}$. Upon dot product by $\boldsymbol{v}$ one obtains

$$0=(\nabla\boldsymbol{v})\boldsymbol{v}\cdot\boldsymbol{v}=(\nabla\boldsymbol{v})^{\mathrm{T}}\boldsymbol{v}\cdot\boldsymbol{v}=\frac{1}{2}\boldsymbol{v}\cdot\nabla|\boldsymbol{v}|^2=\frac{1}{2}\nabla\cdot(|\boldsymbol{v}|^2\boldsymbol{v}), \tag{8}$$

and when integrated over Ω for any $t>0$ provides

$$0=\int_{\Omega}\nabla\cdot(|\boldsymbol{v}|^2\boldsymbol{v})\mathrm{d}\boldsymbol{x}=\int_{\partial\Omega}(|\boldsymbol{v}|^2\boldsymbol{v}\cdot\vec{\boldsymbol{n}})\mathrm{d}\boldsymbol{x}_{N-1}, \tag{9}$$

which is a true identity for every arbitrary Ω, ψ and $\boldsymbol{u}$ and for every $t>0$. On the other hand, given that $(\boldsymbol{v}\cdot\nabla)\boldsymbol{v}=0$, one can use the identity

$$\frac{1}{2}\nabla|\boldsymbol{v}|^2=(\boldsymbol{v}\cdot\nabla)\boldsymbol{v}+\boldsymbol{v}\times\nabla\times\boldsymbol{v}=\boldsymbol{v}\times\boldsymbol{\omega}, \tag{10}$$

where $\boldsymbol{\omega}=\nabla\times\boldsymbol{v}$, which upon dot product by $\boldsymbol{\omega}$ provides

$$\nabla\cdot\left(|\boldsymbol{v}|^2\boldsymbol{\omega}\right)=0,$$

where we used also that $\nabla\cdot\boldsymbol{\omega}=0$. Integrate over Ω for any $t>0$ to get

$$0=\int_\Omega\nabla\cdot\left(|\boldsymbol{v}|^2\boldsymbol{\omega}\right)\mathrm{d}\boldsymbol{x}=\int_{\partial\Omega}\left(|\boldsymbol{v}|^2\boldsymbol{\omega}\cdot\vec{\boldsymbol{n}}\right)\mathrm{d}\boldsymbol{x}_{N-1}, \tag{11}$$

which is true for arbitrary Ω, ψ and $\mathbf{u}$. Now, since $\nabla\cdot\mathbf{v}=0$ one also has

$$0=\int_\Omega(\nabla\cdot\boldsymbol{v})\mathrm{d}\boldsymbol{x}=\int_{\partial\Omega}(\boldsymbol{v}\cdot\vec{\boldsymbol{n}})\mathrm{d}\boldsymbol{x}_{N-1}. \tag{12}$$

Identity (10) implies that $\nabla|\boldsymbol{v}|^2$ is orthogonal to the space spanned by $\boldsymbol{v}$ and $\boldsymbol{\omega}$. Combine Identities (9), (11) and (12), and exclude the cases $|\boldsymbol{v}|=1$ and $|\boldsymbol{v}|=0$ by the arbitrariness of the choice to deduce that it is necessary that $\boldsymbol{v}\cdot\vec{\boldsymbol{n}}=0$; that is to say $\boldsymbol{v}$ is tangential to every part of $\partial\Omega$. It can also be deduced that either $\boldsymbol{v}=\boldsymbol{\omega}$ on every part of $\partial\Omega$ (this actually means $\boldsymbol{v}=\boldsymbol{\omega}=0$ on $\partial\Omega$), or $\boldsymbol{\omega}\cdot\vec{\boldsymbol{n}}=0$ on every part of $\partial\Omega$. Both cases imply that $\boldsymbol{\omega}\cdot\vec{\boldsymbol{n}}=0$ on every part of $\partial\Omega$. Hence, both $\boldsymbol{v}$ and $\boldsymbol{\omega}$ are tangential to the boundary.

Remark. As pointed out, the question of verifying the Compatibility Condition (6) on the boundary of Ω is an important open question in the mathematical theory of Navier-Stokes equation. Some results were obtained to justify the validity of such compatibility under certain restrictions on the flux of the flow in terms of the viscosity of the fluid, for details on this issue refer to [6]. In the present case, the compatibility is naturally achieved given, of course, that the solution of Model Equation (1) is indeed in the form proposed in Claim 1. This shall be verified by the statements of the following theorems.

Theorem 2 (Bounded Domain). Let $\Omega\subset\mathbb{R}^N$ be a bounded domain with sufficiently smooth boundaries $\partial\Omega$ and let $\Omega_t=\Omega\times(0,\infty)$. Suppose $\boldsymbol{v}_0(\boldsymbol{x})$, $\boldsymbol{v}^*(\boldsymbol{x}_{N-1},t)$ and $\boldsymbol{f}(\boldsymbol{x},t)$ satisfy Conditions (3), (4) and (5) respectively. If $\boldsymbol{v}(\boldsymbol{x},t)$ is in the form proposed in Claim 1, then Model Equation (1) has a classical solution $(\boldsymbol{v},\boldsymbol{\omega},p)$ with bounded energy $E(t)$ such that $\boldsymbol{v}(\boldsymbol{x},t)\in\mathbf{C}^\infty(\bar{\Omega}_t)$, $\boldsymbol{\omega}(\boldsymbol{x},t)\in\mathbf{C}^\infty(\bar{\Omega}_t)$ and $p(\boldsymbol{x},t)\in C^1\left([0,\infty];C^3(\bar{\Omega})\right)$. In particular, the exact solution is given by solving the following system

$$\begin{cases}\left.\begin{aligned}&\boldsymbol{\omega}_t=\mu\Delta\boldsymbol{\omega}+\nabla\times\boldsymbol{f}\\&\Delta\boldsymbol{v}=-\nabla\times\boldsymbol{\omega}\\&\Delta p=\nabla\cdot\boldsymbol{f}\end{aligned}\right\}&\text{in }\Omega_t,\\ \left.\begin{aligned}&\boldsymbol{v}(\boldsymbol{x},t)=\boldsymbol{v}^*(\boldsymbol{x}_{N-1},t)\\&\boldsymbol{\omega}(\boldsymbol{x},t)=\nabla\times\boldsymbol{v}^*(\boldsymbol{x}_{N-1},t)\end{aligned}\right\}&\text{on }\partial\Omega_t,\\ \boldsymbol{\omega}(\boldsymbol{x},0)=\boldsymbol{\omega}_0(\boldsymbol{x})=\nabla\times\boldsymbol{v}_0(x)&\text{in }\bar{\Omega},\\ \nabla\cdot\boldsymbol{v}=\nabla\cdot\boldsymbol{\omega}=0&\text{in }\bar{\Omega}_t\end{cases} \tag{13}$$

where ∇p can be defined uniquely in terms of the values of $\boldsymbol{v}$ and $\boldsymbol{f}$ on the boundary. Moreover, if $\boldsymbol{f}\in\mathbf{C}^\infty(\bar{\Omega}_t)$ then $p\in C^\infty(\bar{\Omega}_t)$.

Proof. The proof is quite simple and it depends mostly on classical results and the standard theory of linear parabolic and elliptic equations of second order. If $\boldsymbol{v}=\psi(\boldsymbol{x},t)\boldsymbol{u}(t)$, then by virtue of Identity (7) one has $(\boldsymbol{v}\cdot\nabla)\boldsymbol{v}=0$. Hence, the main equation takes the form

$$\boldsymbol{v}_t=\mu\Delta\boldsymbol{v}-\nabla p+\boldsymbol{f}. \tag{14}$$

Apply the divergence operator to get

$$\Delta p=\nabla\cdot\boldsymbol{f}, \tag{15}$$

where the incompressibility condition $\nabla\cdot\boldsymbol{v}=0$ is used. By the standard theory of elliptic equations, if $\boldsymbol{f}$ satisfies Condition (5), then $p\in C^1\left([0,\infty];C^3\left(\bar{\Omega}\right)\right)$. However, if $\boldsymbol{f}\in\mathbf{C}^\infty\left(\bar{\Omega}_t\right)$, then p is actually $C^\infty\left(\bar{\Omega}_t\right)$, for details on such equation see ([13], pp. 326-343). This concludes one part of System (13), however, a further discussion on a unique definition of p will be introduced at the end of this proof.

Now, revert to Equation (14) and apply the **curl** operator to get

$$\boldsymbol{\omega}_t=\mu\Delta\boldsymbol{\omega}+\nabla\times\boldsymbol{f}, \tag{16}$$

which is the first equation in System (13). Finally, given the incompressibility of $\boldsymbol{v}$ and applying a simple vector identity lead to the third equation in System (13) that is

$$-\Delta\boldsymbol{v}=\nabla\times\boldsymbol{\omega}. \tag{17}$$

The fundamental solution $\boldsymbol{\omega}$ to Equation (16) with initial profile $\boldsymbol{\omega}_0$ and force $\nabla\times\boldsymbol{f}$ is given formally by

$$\begin{aligned}\boldsymbol{\omega}(\boldsymbol{x},t)=&\left(4\pi\mu t\right)^{-\frac{N}{2}}\int_\Omega \mathrm{e}^{-\frac{|x-y|^2}{4\mu t}}\nabla\times\boldsymbol{v}_0(\boldsymbol{y})\mathrm{d}\boldsymbol{y}\\&+\int_0^t\left(4\pi\mu(t-s)\right)^{-\frac{N}{2}}\int_\Omega \mathrm{e}^{-\frac{|x-y|^2}{4\mu(t-s)}}\nabla\times\boldsymbol{f}(\boldsymbol{y},s)\mathrm{d}\boldsymbol{y}\mathrm{d}s.\end{aligned} \tag{18}$$

As explained in ([14], Chapter 7), because of the smoothing property of the Gaussian kernel, it is enough to have a contentious data under the integral sign to guarantee that $\boldsymbol{\omega}\in\mathbf{C}^\infty\left(\bar{\Omega}_t\right)$, which is what has been already assumed. Given the assumptions on the growth of $\boldsymbol{f}$ in time and the form of Formula (18), the solution $\boldsymbol{\omega}\to 0$ as $t\to\infty$. Moreover, the continuity of the data, the clear decay in time and the assumed boundedness of Ω imply that $|\boldsymbol{\omega}|<C$ in $\bar{\Omega}_t$, which implies actually that $\boldsymbol{\omega}\in L^2(\Omega)$ for every $t>0$. Uniqueness of $\boldsymbol{\omega}$ as per Expression (18) is not clear unless we insert the boundary datum $\nabla\times\boldsymbol{v}^*$ explicitly in Expression (18). This can be done by introducing the auxiliary variable $\mathbf{w}=\boldsymbol{\omega}-\nabla\times\boldsymbol{v}^*$ for which one obtains a homogeneous heat equation. Anyhow, the presence of any form of boundary conditions guarantees the uniqueness of $\boldsymbol{\omega}$. Moreover, since $\boldsymbol{\omega}$ is actually a derivative of $\boldsymbol{v}$, then it suffices to show that $\boldsymbol{v}$ is unique, which is our main concern, to conclude the uniqueness of $\boldsymbol{\omega}$.

Now, go back to Equation (17). By virtue of the results obtained above for $\boldsymbol{\omega}$ and the standard theory of elliptic equations one directly concludes that $\boldsymbol{v}\in\mathbf{C}^\infty\left(\bar{\Omega}_t\right)$, for more details see ([13], pp. 326-343). Such regularity, the boundedness of Ω and the global decay of $\boldsymbol{\omega}$ in time imply that $\boldsymbol{v}$ is bounded in

$L^2(\Omega)$ for every $t>0$, which in turn implies the boundedness of the energy of the flow $E(t)$ as defined by Expression (2). Since $\boldsymbol{\omega}\in L^2(\Omega)$, then ([7], Proposition 2.16]) can be used to conclude that a formal solution for Equation (17) takes the form

$$\boldsymbol{v}(\boldsymbol{x},t)=\frac{1}{\omega_N}\int_\Omega \frac{\boldsymbol{x}-\boldsymbol{y}}{|\boldsymbol{x}-\boldsymbol{y}|^N}\times\boldsymbol{\omega}(\boldsymbol{y},t)\,\mathrm{d}\boldsymbol{y}, \tag{19}$$

where ω_N is the area of the unit sphere in $\mathbb{R}^N$. The solution $\boldsymbol{v}$ can be enforced to take the values $\boldsymbol{v}^*$ on the boundary in a standard manner by introducing Dirichlet Green's function. We refrain from discussing these details being highly dependent on the choice of the domain. The uniqueness of $\boldsymbol{v}$ follows by the presence of the boundary condition $\boldsymbol{v}^*$, for details see [13] [14].

Finally, go back to Equation (15) to solve for p. In this case one only needs to calculate $\nabla p\cdot\vec{\mathbf{n}}$ from the main model by knowing the values of $\boldsymbol{v}_t$, $\Delta\boldsymbol{v}$ and $\boldsymbol{f}$ on the boundary. This provides a form of boundary conditions for p which consequently guarantees its uniqueness up to a constant, for details see [14]. The infinite differentiability of p also follows from the main model and the fact that $\boldsymbol{v}\in\mathbf{C}^\infty(\bar{\Omega}_t)$ provided, of course, that $\boldsymbol{f}\in\mathbf{C}^\infty(\bar{\Omega}_t)$ as well. If $\boldsymbol{f}=0$, then p is certainly $C^\infty(\bar{\Omega}_t)$. This completes the proof.

Remark. As explained in the proof of *Theorem 2*, the uniqueness of $\boldsymbol{\omega}$ follows by the ability to define $\boldsymbol{v}$ uniquely. The order of solving the equations in System (13) is not really important since none of the quantities $(\boldsymbol{v},\omega,p)$ induces the other; they act simultaneously. Another way of solvability can be introduced by which one can obtain the same results. This can be a topic for a future study.

The problem of proving the existence of regular and smooth enough solutions for the Navier-Stokes equation in bounded domain was exhaustively investigated as pointed out in the introduction. The real problem was to prove the boundedness of the solution in an unbounded domain, clearly because of the unboundedness of the domain itself. This fact manifests the need to show that the solution's support is bounded in $\mathbb{R}^N$, or equivalently to show that the solution $\boldsymbol{v}$ decays rapidly as $|\boldsymbol{x}|\to\infty$.

The solution obtained in *Theorem* 2 represents a perfect candidate as a solution for Model Equation (1) in unbounded domains also except for one issue. One needs to prove the boundedness of $\boldsymbol{v}$ in $L^2(\mathbb{R}^N)$ for every $t>0$ so that the boundedness of the energy $E(t)$ can be claimed, and also to ensure that the solution does indeed vanish as $|\boldsymbol{x}|\to\infty$. For $\boldsymbol{v}$ to be bounded in $L^2(\mathbb{R}^N)$, it should attain a rate of decay, at least, $|\boldsymbol{v}|\le C(1+|\boldsymbol{x}|)^{-(N+\delta)/2}$ for any $\delta>0$. One can argue that some of the results in the literature require a rate of decay higher than that for the surface integrals to vanish; these restrictions can be dropped because these integrals already vanish by virtue of *Lemma 1*, (see [7], Lemma 1.5]). However, this does not mean that rapid rates of decay are not achievable, they are achievable as demonstrated next.

In order to derive such an estimate one goes back to Formula (19) that represents the fundamental solution for $\boldsymbol{v}$. If $|\boldsymbol{\omega}|\le C$ then it is expected that

the outcome of this integral will provide nothing less than a linear rate of growth for $|\boldsymbol{v}|$, which is a bad answer to the problem in hand. Therefore, Formula (18) shall be used to help us estimate some rates of decay for $\boldsymbol{\omega}$ and consequently for $\boldsymbol{v}$ so that boundedness in $L^2(\Omega)$ can be proved for every $t>0$.

Theorem 3 (The Domain $\mathbb{R}^N$). *Suppose all the conditions of Theorem* 2 *are satisfied for* $\Omega=\mathbb{R}^N$. *Then there exists a classical solution* $(\boldsymbol{v},\boldsymbol{\omega},p)$ *for Model Equation* (1) *represented by the System* (13) *and defined as*

$$\boldsymbol{\omega}(\boldsymbol{x},t)=h(t)\int_{\mathbb{R}^N}\mathrm{e}^{\frac{|\boldsymbol{x}-\boldsymbol{y}|^2}{4\mu t}}\boldsymbol{\omega}_0(\boldsymbol{y})\mathrm{d}\boldsymbol{y}+\int_0^t h(t-s)\int_{\mathbb{R}^N}\mathrm{e}^{\frac{|\boldsymbol{x}-\boldsymbol{y}|^2}{4\mu(t-s)}}\boldsymbol{g}(\boldsymbol{y},s)\mathrm{d}\boldsymbol{y}\mathrm{d}s, \quad (20)$$

and

$$\boldsymbol{v}(\boldsymbol{x},t)=\frac{1}{\omega_N}\int_{\mathbb{R}^N}\frac{\boldsymbol{x}-\boldsymbol{y}}{|\boldsymbol{x}-\boldsymbol{y}|^N}\times\boldsymbol{\omega}(y,t)\mathrm{d}y, \quad (21)$$

where $h(t)=(4\pi\mu t)^{-\frac{N}{2}}$, $\boldsymbol{g}=\nabla\times\boldsymbol{f}$ and ω_N is the surface area of a unit sphere. The pressure p can be defined from Model Equation (1) up to a constant where $\nabla p\cdot\vec{\mathrm{n}}$ can be specified uniquely in terms of the values of $\boldsymbol{v}$ and $\boldsymbol{f}$ on the boundary. Moreover, the energy of the flow $E(t)$ is bounded for every $t>0$ where $\boldsymbol{v}$ grows at most as $|\boldsymbol{v}|\sim(1+|\boldsymbol{x}|)^{-(N+6)/2}$.

Proof. The proof of smoothness and uniqueness is identical to the one introduced in the proof of *Theorem 2* and it follows by the standard theory of linear second order elliptic and parabolic equations. The focus here will be on proving the boundedness in $L^2(\mathbb{R}^N)$ for both $\boldsymbol{\omega}$ and $\boldsymbol{v}$, which necessarily entails an estimation of appropriate decay rates as pointed out in the preceding discussion. Since $\boldsymbol{f}\in\mathbf{C}^1([0,\infty];H^3(\mathbb{R}^N))$, then $\boldsymbol{g}\in\mathbf{C}([0,\infty];H^2(\mathbb{R}^N))$. By assumption, $\boldsymbol{v}_0\in V^{N+2}(\mathbb{R}^N)$ which implies that $\boldsymbol{\omega}_0\in V^{N+1}(\mathbb{R}^N)$ and since $N\geq 2$ for meaningful physical interpretation, then at least $\boldsymbol{\omega}_0\in V^3(\mathbb{R}^N)$. Hence, $\boldsymbol{\omega}\in L^2((0,\infty];V^4(\mathbb{R}^N))$ as per the standard theory of linear second order parabolic equations, for details refer to ([13], Theorem 6, p. 386). Now, it is needed to show that $\boldsymbol{v}$ is bounded in $L^2(\mathbb{R}^N)$ for every $t>0$. There are two ways to show this; in one of them a rough estimate will be provided for the minimum rate of decay of $\boldsymbol{v}$ given the assumptions on the data.

The first direction depends on the results in ([7], Theorems 3.4 and 3.6). In these theorems a regularization technique by mollifiers along with energy estimates were used to prove global in time existence. In particular, ([7], Theorem 3.4) states that if $\boldsymbol{v}_0\in V^m$ and $m\geq[N/2]+2$, then there exists a unique continuous solution locally in time such that this is true up to $T\leq C(\|\boldsymbol{v}\|_m)^{-1}$, which coincides with the assumptions on $\boldsymbol{v}_0$. The local existence of a unique continuous solution was extended to a global in time existence in ([7], Theorem 3.6) given that

$$\int_0^T|\boldsymbol{\omega}(x,t)|_{L^\infty(\Omega_t)}\mathrm{d}t\leq C$$

and such that $\boldsymbol{v}\in\mathbf{C}^1((0,T];\mathbf{C}^2(\Omega)\cap V^m(\Omega))$. Since $\boldsymbol{\omega}_0$ and $\boldsymbol{g}$ are bounded in $L^2(\mathbb{R}^N)$ for every $t>0$, then it follows that there exists a ball $B\subset\mathbb{R}^N$ such that the supports of $\boldsymbol{g}$ and $\boldsymbol{\omega}_0$ are entirely inside B_t where $B_t=B\times[0,\infty]$. Hence, the integrals in Formula (20) can be restricted to the ball

B, apply Hölder's inequality, maximize the exponential term which is bounded for every $\boldsymbol{x}, \boldsymbol{y} \in B$ and for every $t > 0$, and with some estimation procedures it becomes easy to find an estimate of the form $|\boldsymbol{\omega}(\boldsymbol{x}, t)| \le Ch(t)$ in the whole of $\mathbb{R}^N$ and for every $t > 0$. Since $h(t)$ is a decreasing function in time then by assuming a simple scale of time one obtains

$$\int_0^\infty |\boldsymbol{\omega}(\boldsymbol{x}, t)|_{L^\infty(\bar{\Omega}_t)} \mathrm{d}t \le C \int_1^\infty h(\tau) \mathrm{d}\tau \le C.$$

It follows that all the conditions of ([7], Theorem 3.4, Theorem 3.6) are satisfied such that $\boldsymbol{v}$ exists globally in time and such that $\boldsymbol{v} \in V^{N+2}(\mathbb{R}^N)$ for every $t > 0$, which implies the boundedness of the energy $E(t)$ for every $t > 0$ as well.

The second way is trying to get an estimate for $\boldsymbol{v}$ in terms of $|\boldsymbol{x}|$ to confirm the boundedness in $L^2(\mathbb{R}^N)$. Consider the following argument: fix t in Expression (20), calculate $\nabla \boldsymbol{\omega}$, which is in $L^2(\mathbb{R}^N)$ for every $t > 0$ because $\boldsymbol{\omega} \in V^4(\Omega)$. Take the absolute value of both sides, perform some manipulation to the integrands, use $\boldsymbol{x} \cdot \boldsymbol{y} \le |\boldsymbol{x}||\boldsymbol{y}|$ and maximize the time integral (the integrand is a decreasing function in time) so that one finally gets the term with the highest power for $|\boldsymbol{x}|$ as follows

$$\begin{aligned} |\nabla \boldsymbol{\omega}| &\le H(t) \int_B |\boldsymbol{x}| \left(\left| 1 + \frac{|\boldsymbol{y}|}{|\boldsymbol{x}|} \right|^2 \right)^{\frac{1}{2}} \mathrm{e}^{-\frac{|\boldsymbol{x}-\boldsymbol{y}|^2}{4\mu t}} \left(|\boldsymbol{\omega}_0(\boldsymbol{y})|_{L^\infty(B)} + |\boldsymbol{g}(\boldsymbol{y}, t)|_{L^\infty(B_t)} \right) \mathrm{d}\boldsymbol{y} \\ &\le H(t) \mathrm{M}(|\boldsymbol{x}|) |\boldsymbol{x}| C\left(|B|, |\boldsymbol{\omega}_0|_{L^\infty(B)} + |\boldsymbol{g}|_{L^\infty(B_t)} \right) \\ &\le C \mathrm{M}(|\boldsymbol{x}|) |\boldsymbol{x}|, \end{aligned}$$

where $\mathrm{M}(|\boldsymbol{x}|)$ is the collection of every possible appearance of any power of $|\boldsymbol{x}|$ after the integration. Since $\nabla \boldsymbol{\omega}$ is in $L^2(\mathbb{R}^N)$ as pointed out, then to obtain a decreasing integrand when calculating the L^2-norm of this derivative it is necessary that $\mathrm{M}(|\boldsymbol{x}|)$ is decreasing in $|\boldsymbol{x}|$ such that it is at least $\mathrm{M}(|\boldsymbol{x}|) \sim (1 + |\boldsymbol{x}|)^{-\frac{N+2+\delta}{2}}$ for some $\delta > 0$. But $\boldsymbol{\omega}$ is in $L^2(\mathbb{R}^N)$ as well, and the integrands of the above estimate are the same except for the terms with positive powers of $|\boldsymbol{x}|$. That is to say that $|\boldsymbol{\omega}| \le C\mathrm{M}(|\boldsymbol{x}|) \sim (1 + |\boldsymbol{x}|)^{-\frac{N+2+\delta}{2}}$. Incorporate this estimate in Expression (21) of the solution $\boldsymbol{v}$ and one can readily see that $|\boldsymbol{v}| \sim (1 + |\boldsymbol{x}|)^{-\frac{N+\delta}{2}}$ as desired, which in turn confirms the boundedness of the energy $E(t)$ for every $t > 0$ and implies the decay of $\boldsymbol{v}$ as $|\boldsymbol{x}| \to \infty$.

However, since $\boldsymbol{\omega} \in V^4(\mathbb{R}^N)$, then we actually have $D^4 \boldsymbol{\omega} \in L^2(\mathbb{R}^N)$ for every $t > 0$. This means that we can differentiate Formula (20) four times and repeat the same argument as above to conclude that we actually have $\mathrm{M}(|\boldsymbol{x}|) \sim (1 + |\boldsymbol{x}|)^{-\frac{N+8+\delta}{2}}$ which in turn leads to $|\boldsymbol{v}| \sim (1 + |\boldsymbol{x}|)^{-\frac{N+6+\delta}{2}}$ and this completes the proof.

Remark. Better estimates for the decay of $\boldsymbol{v}$ can be obtained by repeating the same procedure described above for higher order derivatives of $\boldsymbol{\omega}$ which, of course, entails higher assumptions on the data so that we can claim the boundedness of the considered derivative apriori. On the other hand, the assumptions

on the smoothness of the forcing term $\boldsymbol{f}$ can be relaxed. It is enough to assume that $\boldsymbol{f}\in\mathbf{C}^1\left(\left[0,\infty\right];\mathbf{C}^1\left(\mathbb{R}^N\right)\cap H^1\left(\mathbb{R}^N\right)\right)$ so that one obtains $\boldsymbol{g}\in\mathbf{C}\left(\left[0,\infty\right];L^2\left(\mathbb{R}^N\right)\right)$, which is sufficient to conclude that $\boldsymbol{\omega}\in L^2\left(\left(0,\infty\right];V^2\left(\mathbb{R}^N\right)\right)$. The boundedness of $\nabla\boldsymbol{\omega}$ in $L^2\left(\mathbb{R}^N\right)$ is enough to deduce a sufficient decay estimate for $\boldsymbol{v}$ as shown above. The introduced assumptions were chosen for consistency with the standard theory and the Embedding Theorem, and in the same time to illustrate the estimation procedure. For more information review ([13], pp. 382-386).

We managed to prove that our solution is indeed **a** classical solution of Model Equation (1). Here come some important questions, what if there exists another solution in a more general form? Moreover, does the choice of the domain or the choice of the boundary data play a role in the uniqueness of the solution? The answer to these questions is addressed by the statement of the next theorem.

Theorem 4 (Uniqueness). Let $\Omega\subseteq\mathbb{R}^N$ be an arbitrary domain. Suppose $\boldsymbol{v}_0$, $\boldsymbol{v}^*$ and $\boldsymbol{f}$ are satisfying Conditions (3), (4) and (5) respectively. Then Claim 1 is true and the unique classical solution of Model Equation (1) is in the form $\boldsymbol{v}\left(\boldsymbol{x},t\right)=\psi\left(\boldsymbol{x},t\right)\boldsymbol{u}\left(t\right)$. This solution is defined as per Theorems 2 and 3.

Proof. The proof here depends on our results in *Theorems* 2 and 3, and also on ([7], Theorems 3.4 and 3.6). By virtue of the assumptions on the data and our results in *Theorems* 2 and 3, it is clear that our solution $\boldsymbol{v}$ satisfies all the conditions in [7] for every $t\in\left(0,\infty\right]$.

Assume that there exists a more general solution than the proposed one and denote it by $\boldsymbol{v}^g$. Such solution should definitely inherit the smoothness proved in [7] as well. That is to say that $\boldsymbol{v}^g\in\mathbf{C}^1\left(\left(0,\infty\right];\mathbf{C}^2\cap V^m\right)$ and such that $\left(\boldsymbol{v}^g,\boldsymbol{\omega}^g,p^g\right)$ is the triad solution of Model Equation (1) with boundary datum $\boldsymbol{v}^*$ and initial profile $\boldsymbol{v}_0$. Let $\boldsymbol{w}=\boldsymbol{v}-\boldsymbol{v}^g$ and let $q=p-p^g$. Hence, $\boldsymbol{w}$ has zero boundary and initial data and it obeys the equation

$$\boldsymbol{w}_t-\mu\Delta\boldsymbol{w}+\nabla q=\left(\boldsymbol{v}^g\cdot\nabla\right)\boldsymbol{v}^g. \tag{22}$$

Dot product the above equation by $\boldsymbol{v}^g$ and integrate by parts over any arbitrary domain Ω to get

$$\int_\Omega\boldsymbol{v}^g\cdot\left(\boldsymbol{w}_t-\mu\Delta\boldsymbol{w}+\nabla q\right)\mathrm{d}\boldsymbol{x}=\frac{1}{2}\int_{\partial\Omega}\left|\boldsymbol{v}^g\right|^2\boldsymbol{v}^g\cdot\vec{\boldsymbol{n}}\mathrm{d}\boldsymbol{x}_{N-1}=\frac{1}{2}\int_{\partial\Omega}\left|\boldsymbol{v}\right|^2\boldsymbol{v}\cdot\vec{\boldsymbol{n}}\mathrm{d}\boldsymbol{x}_{N-1}=0, \tag{23}$$

where we used the Divergence theorem in the right hand side, the facts that $\nabla\cdot\boldsymbol{v}^g=0$ and that $\boldsymbol{v}^g=\boldsymbol{v}^*=\boldsymbol{v}$ on the boundary, and the results of *Lemma* 1. Now, recalling that $\nabla\cdot\boldsymbol{\omega}^g=0$ and using the vector identity

$$\nabla\left|\boldsymbol{v}^g\right|^2=2\left(\boldsymbol{v}^g\cdot\nabla\right)\boldsymbol{v}^g+2\boldsymbol{v}^g\times\boldsymbol{\omega}^g, \tag{24}$$

one can dot product Equation (22) by $\boldsymbol{\omega}^g$ and integrate as above to get

$$\begin{aligned}\int_\Omega\boldsymbol{\omega}^g\cdot\left(\boldsymbol{w}_t-\mu\Delta\boldsymbol{w}+\nabla q\right)\mathrm{d}\boldsymbol{x}&=\frac{1}{2}\int_{\partial\Omega}\left|\boldsymbol{v}^g\right|^2\boldsymbol{\omega}^g\cdot\vec{\boldsymbol{n}}\mathrm{d}\boldsymbol{x}_{N-1}\\&=\frac{1}{2}\int_{\partial\Omega}\left|\boldsymbol{v}^*\right|^2\nabla\times\boldsymbol{v}^*\cdot\vec{\boldsymbol{n}}\mathrm{d}\boldsymbol{x}_{N-1}\\&=\frac{1}{2}\int_{\partial\Omega}\left|\boldsymbol{v}\right|^2\boldsymbol{\omega}\cdot\vec{\boldsymbol{n}}\mathrm{d}\boldsymbol{x}_{N-1}=0,\end{aligned} \tag{25}$$

where *Lemma 1* is used again. Identities (23) and (25) imply one of three possibilities. Either $\boldsymbol{v}^g = \boldsymbol{\omega}^g = 0$ which is excluded for being trivial, or $\boldsymbol{w}_t - \mu\Delta\boldsymbol{w} + \nabla q = 0$ almost everywhere. The third possibility is $\boldsymbol{w}_t - \mu\Delta\boldsymbol{w} + \nabla q$ being orthogonal to the space spanned by $\boldsymbol{v}^g$ and $\boldsymbol{\omega}^g$, which by Equation (22) implies that $\left(\boldsymbol{v}^g \cdot \nabla\right)\boldsymbol{v}^g$ is orthogonal to $\boldsymbol{\omega}^g$ and $\boldsymbol{v}^g$.

Let us start with $\boldsymbol{w}_t - \mu\Delta\boldsymbol{w} + \nabla q = 0$ almost everywhere. Multiply this equation by $\boldsymbol{w}$, integrate by parts over Ω, employ the Divergence theorem and recall that $\boldsymbol{w} = 0$ on $\partial\Omega$ to get

$$\frac{1}{2}\frac{\mathrm{d}}{\mathrm{d}t}\int_\Omega |\boldsymbol{w}|^2 \,\mathrm{d}\boldsymbol{x} + \mu\int_\Omega |\nabla\boldsymbol{w}|^2 \,\mathrm{d}\boldsymbol{x} = -\int_{\partial\Omega} q\boldsymbol{w}\cdot\vec{\boldsymbol{n}}\,\mathrm{d}\boldsymbol{x}_{N-1} = 0.$$

This readily implies that $\boldsymbol{w} = 0$ almost everywhere. But by the results obtained for $\boldsymbol{v}$ and $\boldsymbol{v}^g$, one concludes that at least $\boldsymbol{w} \in \mathbf{C}^2\left(\bar{\Omega}\right)$ which implies that $\boldsymbol{w}$ is identically zero. Hence, the solution $\boldsymbol{v}$ is the unique solution for Model Equation (1) in this case.

Now, if $\boldsymbol{v}^g$ and $\boldsymbol{\omega}^g$ are orthogonal to $\left(\boldsymbol{v}^g \cdot \nabla\right)\boldsymbol{v}^g$, then by Identity (24) we deduce that $\nabla\left|\boldsymbol{v}^g\right|^2$ is orthogonal to the space spanned by $\boldsymbol{v}^g$ and $\boldsymbol{\omega}^g$ everywhere, which is equivalent to the nature of the solution $\boldsymbol{v}$. This means that $\nabla|\boldsymbol{v}|^2$ and $\nabla\left|\boldsymbol{v}^g\right|^2$ are parallel to each other on the boundary. Since both solutions coincide at the boundary and both are extended continuously to the interior of the domain, then it is not hard to conclude that $\boldsymbol{v}^g = \boldsymbol{v}$ everywhere, which is the aim of this proof. Assume not. Let $\boldsymbol{\theta} = \boldsymbol{\omega} - \boldsymbol{\omega}^g$ so that the difference equation for $\boldsymbol{\omega}$ takes the form

$$\boldsymbol{\theta}_t - \mu\Delta\boldsymbol{\theta} = \left(\boldsymbol{v}^g \cdot \nabla\right)\boldsymbol{\omega}^g - \left(\boldsymbol{\omega}^g \cdot \nabla\right)\boldsymbol{v}^g. \tag{26}$$

where $\left(\boldsymbol{\omega}^g \cdot \nabla\right)\boldsymbol{v}^g - \left(\boldsymbol{v}^g \cdot \nabla\right)\boldsymbol{\omega}^g = -\nabla\times\left(\boldsymbol{v}^g \cdot \nabla\right)\boldsymbol{v}^g$. Use the vector identity

$$\nabla\left(\boldsymbol{v}^g \cdot \boldsymbol{\omega}^g\right) = \left(\nabla\boldsymbol{v}^g\right)^{\mathrm{T}}\boldsymbol{\omega}^g + \left(\nabla\boldsymbol{\omega}^g\right)^{\mathrm{T}}\boldsymbol{v}^g,$$

and given the incompressibility of $\boldsymbol{v}^g$ one also has

$$\nabla\boldsymbol{\omega}^g\boldsymbol{\omega}^g = \frac{1}{2}\nabla\left|\boldsymbol{\omega}^g\right|^2 - \boldsymbol{\omega}^g \times\left(\nabla\times\boldsymbol{\omega}^g\right) = \frac{1}{2}\nabla\left|\boldsymbol{\omega}^g\right|^2 + \boldsymbol{\omega}^g \times\Delta\boldsymbol{v}^g.$$

Use these two identities, bearing in mind the incompressibility, to find that

$$\begin{aligned}
\boldsymbol{v}^g \cdot\left(\nabla\boldsymbol{\omega}^g\boldsymbol{v}^g - \nabla\boldsymbol{v}^g\boldsymbol{\omega}^g\right) &= \left(\nabla\boldsymbol{\omega}\right)^{\mathrm{T}}\boldsymbol{v}^g\cdot\boldsymbol{v}^g - \frac{1}{2}\nabla\left|\boldsymbol{v}^g\right|^2\cdot\boldsymbol{\omega}^g \\
&= \nabla\left(\boldsymbol{v}^g\cdot\boldsymbol{\omega}^g\right)\cdot\boldsymbol{v}^g - \left(\nabla\boldsymbol{v}^g\right)^{\mathrm{T}}\boldsymbol{\omega}^g\cdot\boldsymbol{v}^g - \frac{1}{2}\nabla\left|\boldsymbol{v}^g\right|^2\cdot\boldsymbol{\omega}^g \\
&= \nabla\cdot\left(\left(\boldsymbol{v}^g\cdot\boldsymbol{\omega}^g\right)\boldsymbol{v}^g - \frac{1}{2}\left|\boldsymbol{v}^g\right|^2\boldsymbol{\omega}^g\right) - \nabla\boldsymbol{v}^g\boldsymbol{v}^g\cdot\boldsymbol{\omega}^g \\
&= \nabla\cdot\left(\left(\boldsymbol{v}^g\cdot\boldsymbol{\omega}^g\right)\boldsymbol{v}^g - \frac{1}{2}\left|\boldsymbol{v}^g\right|^2\boldsymbol{\omega}^g\right) \\
&\quad -\frac{1}{2}\nabla\left|\boldsymbol{v}^g\right|^2\cdot\boldsymbol{\omega}^g + \left(\boldsymbol{v}^g\times\boldsymbol{\omega}^g\right)\cdot\boldsymbol{\omega}^g \\
&= \nabla\cdot\left(\left(\boldsymbol{v}^g\cdot\boldsymbol{\omega}^g\right)\boldsymbol{v}^g - \left|\boldsymbol{v}^g\right|^2\boldsymbol{\omega}^g\right) \\
&= \nabla\cdot G_1\left(\boldsymbol{v}^g, \boldsymbol{\omega}^g\right).
\end{aligned} \tag{27}$$

Now recall that we are discussing the possibility in which $\nabla\left|\boldsymbol{v}^g\right|^2$ is orthogonal to $\boldsymbol{v}^g$ and $\boldsymbol{\omega}^g$ such that $C\nabla\left|\boldsymbol{v}^g\right|^2=\left(\mathbf{v}^g\times\boldsymbol{\omega}^g\right)$. Following the same steps as above one can write

$$\begin{aligned}\boldsymbol{\omega}^g\cdot\left(\nabla\boldsymbol{\omega}^g\boldsymbol{v}^g-\nabla\boldsymbol{v}^g\boldsymbol{\omega}^g\right)&=\nabla\cdot\left(\left|\boldsymbol{\omega}^g\right|^2\boldsymbol{v}^g-\left(\boldsymbol{v}^g\cdot\boldsymbol{\omega}^g\right)\boldsymbol{\omega}^g\right)-\left(\boldsymbol{\omega}^g\times\Delta\boldsymbol{v}^g\right)\cdot\boldsymbol{v}^g\\&=\nabla\cdot\left(\left|\boldsymbol{\omega}^g\right|^2\boldsymbol{v}^g-\left(\boldsymbol{v}^g\cdot\boldsymbol{\omega}^g\right)\boldsymbol{\omega}^g\right)-\left(\boldsymbol{v}^g\times\boldsymbol{\omega}^g\right)\cdot\Delta\boldsymbol{v}^g\\&=\nabla\cdot\left(\left|\boldsymbol{\omega}^g\right|^2\boldsymbol{v}^g-\left(\boldsymbol{v}^g\cdot\boldsymbol{\omega}^g\right)\boldsymbol{\omega}^g\right)-C\nabla\left|\boldsymbol{v}^g\right|^2\cdot\Delta\boldsymbol{v}^g\\&=\nabla\cdot\left(\left|\boldsymbol{\omega}^g\right|^2\boldsymbol{v}^g-\left(\boldsymbol{v}^g\cdot\boldsymbol{\omega}^g\right)\boldsymbol{\omega}^g-C\left|\boldsymbol{v}^g\right|^2\Delta\boldsymbol{v}^g\right)\\&=\nabla\cdot G_2\left(\boldsymbol{v}^g,\boldsymbol{\omega}^g\right).\end{aligned}\tag{28}$$

Now, dot product Equation (26) by $\boldsymbol{v}^g$, use Identity (27), integrate over Ω and use the Divergence theorem to reach

$$\int_\Omega\boldsymbol{v}^g\cdot\left(\boldsymbol{\theta}_t-\mu\Delta\boldsymbol{\theta}\right)\mathrm{d}\boldsymbol{x}=\int_{\partial\Omega}G_1\left(\boldsymbol{v}^g,\boldsymbol{\omega}^g\right)\cdot\vec{\boldsymbol{n}}\mathrm{d}\boldsymbol{x}_{N-1}=\int_{\partial\Omega}G_1\left(\boldsymbol{v},\boldsymbol{\omega}\right)\cdot\vec{\boldsymbol{n}}\mathrm{d}\boldsymbol{x}_{N-1}.\tag{29}$$

Also dot product Equation (26) by $\boldsymbol{\omega}^g$, use Identity (28), integrate over Ω and use the Divergence theorem to get

$$\int_\Omega\boldsymbol{\omega}^g\cdot\left(\boldsymbol{\theta}_t-\mu\Delta\boldsymbol{\theta}\right)\mathrm{d}\boldsymbol{x}=\int_{\partial\Omega}G_2\left(\boldsymbol{v}^g,\boldsymbol{\omega}^g\right)\cdot\vec{\boldsymbol{n}}\mathrm{d}\boldsymbol{x}_{N-1}=\int_{\partial\Omega}G_2\left(\boldsymbol{v},\boldsymbol{\omega}\right)\cdot\vec{\boldsymbol{n}}\mathrm{d}\boldsymbol{x}_{N-1}.\tag{30}$$

Now, reverse the Divergence theorem in the surface integrals that include values of $\boldsymbol{v}$ and $\boldsymbol{\omega}$ and reverse all the steps made to conclude G_1 and G_2 to obtain identities in the form

$$\int_\Omega\boldsymbol{v}^g\cdot\left(\boldsymbol{\theta}_t-\mu\Delta\boldsymbol{\theta}\right)\mathrm{d}\boldsymbol{x}=\int_\Omega\boldsymbol{v}\cdot\nabla\times\left(\left(\boldsymbol{v}\cdot\nabla\right)\boldsymbol{v}\right)\mathrm{d}\boldsymbol{x}=0,\tag{31}$$

and similarly

$$\int_\Omega\boldsymbol{\omega}^g\cdot\left(\boldsymbol{\theta}_t-\mu\Delta\boldsymbol{\theta}\right)\mathrm{d}\boldsymbol{x}=\int_\Omega\boldsymbol{\omega}\cdot\nabla\times\left(\left(\boldsymbol{v}\cdot\nabla\right)\boldsymbol{v}\right)\mathrm{d}\boldsymbol{x}=0.\tag{32}$$

Now, there are three other possibilities. The trivial solution; that is $\boldsymbol{v}^g=\boldsymbol{\omega}^g=0$ and it is excluded. Another one is $\boldsymbol{\theta}_t-\mu\Delta\boldsymbol{\theta}=0$ and this one is equivalent to $\boldsymbol{w}_t-\mu\Delta\boldsymbol{w}+\nabla q=0$ because the uniqueness of $\boldsymbol{v}$ implies the uniqueness of $\boldsymbol{\omega}$ and vice versa. It remains that $\nabla\times\left(\left(\boldsymbol{v}^g\cdot\nabla\right)\boldsymbol{v}^g\right)$ is orthogonal to the space spanned by $\boldsymbol{v}^g$ and $\boldsymbol{\omega}^g$. But we already have $\left(\boldsymbol{v}^g\cdot\nabla\right)\boldsymbol{v}^g$ orthogonal to $\boldsymbol{v}^g$ and $\boldsymbol{\omega}^g$, which implies that $\left(\boldsymbol{v}^g\cdot\nabla\right)\boldsymbol{v}^g$ and its rotation (**curl**) are parallel to each other. By definition, the **curl** operator is the unique vector field for which $\left(\nabla\boldsymbol{s}-\nabla\boldsymbol{s}^{\mathrm{T}}\right)\boldsymbol{a}=\left(\nabla\times\boldsymbol{s}\right)\times\boldsymbol{a}$ for every vector field $\boldsymbol{a}$ ([1], p. 32). If $\boldsymbol{s}=\lambda\left(\nabla\times\boldsymbol{s}\right)$, then let $\boldsymbol{a}=\boldsymbol{s}=\lambda\nabla\times\boldsymbol{s}$ to get $\nabla\boldsymbol{s}=\nabla\boldsymbol{s}^{\mathrm{T}}$ which in turn implies that $\nabla\times\boldsymbol{s}=0$ then $\boldsymbol{s}=0$ as well. Hence, it is necessary that $\left(\boldsymbol{v}^g\cdot\nabla\right)\boldsymbol{v}^g=0$ which implies that $\boldsymbol{v}^g=\boldsymbol{v}$. This completes the proof.

Remark. In the proof of uniqueness one can argue that the statement of the proof was given in the sense of classical solutions, and such that there still exists another solution in a weaker form. While this may sound true, but in fact it is not. The basic idea of the proof is based on using the coincidence on the boundary and then moving back to the interior. Assuming the existence of a weaker solution does not change the fact that it is going to coincide with the proposed

one on the boundary. However, further investigation on this specific point will be introduced in a future study.

4. Conclusions and Suggestions

A class of possible solutions for the incompressible Navier-Stokes equation in bounded and unbounded regions of $\mathbb{R}^N$ is proposed. It was demonstrated that for such class of vector fields, the flux of the energy of the flow is orthogonal to the space spanned by $\boldsymbol{v}$ and its associated rotation $\boldsymbol{\omega}$. It was also proved that $\boldsymbol{v}$ and $\boldsymbol{\omega}$ are tangential to the boundary such that $\boldsymbol{v}\cdot\vec{\boldsymbol{n}} = \boldsymbol{\omega}\cdot\vec{\boldsymbol{n}} = 0$.

An investigation of the validity of this class of vector fields as a candidate for a solution to the incompressible Navier-Stokes equation was carried out in both bounded and unbounded domains. Given plausible assumptions on the data and a forcing term in the case of unbounded domains, it turned out that this class of solutions represents perfectly a classical solution of the problem. Verification was established for the infinite differentiability, the uniqueness and the boundedness of the energy in appropriate spaces in light of well known and standard theories. An appropriate estimate was also given for the minimum rate of decay of the solution $\boldsymbol{v}$ as $|\boldsymbol{x}| \to \infty$. Moreover, global existence in time and the corresponding rate of decay were quite obvious in the deduced formulas.

Finally, it was proved that this class of solutions represents actually the unique classical solution of the incompressible Navier-Stokes equation. In light of the non-convective nature of the proposed solution and the uniqueness argument under arbitrary settings, the incompressible Navier-Stokes equation can safely be reduced to a linear equation. This point is quite interesting and it motivates further investigations on a possible relation between incompressibility and convection in fluid mechanics.

Acknowledgements

Sincere thanks to the members of JAMP for their professional performance, and special thanks to managing editor *Hellen Xu* for a rare attitude of high quality.

References

[1] Gurtin, M. (1982) An Introduction to Continuum Mechanics, Mathematics in Science and Engineering. Academic Press, Cambridge.

[2] Kambe, T. (2007) Elementary Fluid Mechanics. World Scientific Publishing, Singapore.

[3] Kambe, T. (2010) A New Formulation of Equations of Compressible Fluids by Analogy with Maxwell's Equations. *Fluid Dynamics Research*, **42**. https://doi.org/10.1088/0169-5983/42/5/055502

[4] Kambe, T. (1983) Axisymmetric Vortex Solution of Navier-Stokes Equation. *Journal of Physical Society of Japan*, **53**, 13-15. https://doi.org/10.1143/JPSJ.53.13

[5] Ladyzhenskaya, O. (1969) The Mathematical Theory of Viscous Incompressible Flow, Translated from the Russian by Richard A. Silverman, Mathematics and its Applications. 2nd Edition, Gordon and Breach.

[6] Galdi, G.P. (2011) An Introduction to the Mathematical Theory of the Navier-

Stokes Equations. Springer Monographs in Mathematics, Springer New York.

[7] Majda, A.J. and Bertozzi, L. (2001) Vorticity and Incompressible Flow. Cambridge Texts in Applied Mathematics, Cambridge University Press, Cambridge. https://doi.org/10.1017/CBO9780511613203

[8] Tao, T. (2016) Finite Time Blowup for an Averaged Three-Dimensional Navier-Stokes Equation. *Journal of American Mathematical Society*, **29**, 601-674. https://doi.org/10.1090/jams/838

[9] Constantin, P. and Fefferman, C. (1993) Direction of Vorticity and the Problem of Global Regularity for the Navier-Stokes Equations. *Indiana University Mathematics Journal*, **42**, 775-789. https://doi.org/10.1512/iumj.1993.42.42034

[10] Constantin, P. (1990) Navier-Stokes Equations and Area of Interfaces. *Communications in Mathematical Physics*, **129,** 241-266. https://doi.org/10.1007/BF02096982

[11] Constantin, P. (2001) Some Open Problems and Research Directions in the Mathematical Study of Fluid Dynamics, Mathematics Unlimited-2001 and Beyond. Springer Verlag, Berlin, 353-360.

[12] Caffarelli, L., Kohn, R. and Nirenberg, L. (1982) Partial Regularity of Suitable Weak Solutions of the Navier-Stokes Equations. *Communication on Pure & Applied Mathematics*, **35**, 771-831. https://doi.org/10.1002/cpa.3160350604

[13] Evans, L. (2010) Partial Differential Equations. 2nd Edition, Graduate Studies in Mathematics. *American Mathematical Society*, **19**. https://doi.org/10.1090/gsm/019

[14] John, F. (1978) Partial Differential Equations. Vol. 1, 4th Edition, Applied Mathematical Sciences, Springer US, New York. https://doi.org/10.1007/978-1-4684-0059-5

Journal of Applied Mathematics and Physics, 2017, 5, 953-965
http://www.scirp.org/journal/jamp
ISSN Online: 2327-4379
ISSN Print: 2327-4352

Biomechanical Study of Vertebral Compression Fracture Using Finite Element Analysis

Hiromitsu Takano[1], Ikuho Yonezawa[1], Mitsugu Todo[2], Muhammad Hazli Mazlan[3,4], Tatsuya Sato[1], Kazuo Kaneko[1]

[1]Division of Spine Surgery, Department of Orthopedic Surgery, School of Medicine, Juntendo University, Tokyo, Japan
[2]Research Institute for Applied Mechanics, Kyushu University, Kasuga-City, Japan
[3]Interdisciplinary Graduate School of Engineering Sciences, Kyushu University, Kasuga-City, Japan
[4]Faculty of Electrical and Electronic Engineering, University Tun Hussein Onn Malaysia, Parit Raja, Malaysia
Email: yoza@juntendo.ac.jp

How to cite this paper: Takano, H., Yonezawa, I., Todo, M., Mazlan, M.H., Sato, T. and Kaneko, K. (2017) Biomechanical Study of Vertebral Compression Fracture Using Finite Element Analysis. *Journal of Applied Mathematics and Physics*, **5**, 953-965.
https://doi.org/10.4236/jamp.2017.54084

Received: March 16, 2017
Accepted: April 27, 2017
Published: April 30, 2017

Copyright © 2017 by authors and Scientific Research Publishing Inc.
This work is licensed under the Creative Commons Attribution International License (CC BY 4.0).
http://creativecommons.org/licenses/by/4.0/
Open Access

Abstract

This research aimed to mechanically analyze vertebral stress concentration in one healthy subject and one subject with osteoporotic first lumbar (L1) vertebral compression fracture by using finite element analysis (FEA). We constructed three-dimensional image-based finite element (FE) models (Th12L2) by using computed tomographic (CT) digital imaging and communications in medicine (DICOM) for each patient and then conducted exercise stress simulations on the spine models. The loadings on the 12th thoracic vertebra (Th12) due to compression, flexion, extension, lateral bending, and axial rotation were examined within the virtual space for both spine models. The healthy and vertebral compression fracture models were then compared based on the application of equivalent vertebral stress. The comparison showed that vertebral stress concentration increased with all stresses in the vertebral compression fracture models. In particular, compression and axial rotation caused remarkable increases in stress concentration in the vertebral compression fracture models. These results suggest that secondary vertebral compression fractures are caused not only by bone fragility but possibly also by the increase in vertebral stress concentration around the site of the initial fracture.

Keywords

Biomechanics, Finite Element Analysis, Vertebral Compression Fracture

1. Introduction

With the recent aging of the population, the trend toward increasing numbers of patients with osteoporosis has made fragility fractures a major problem in society. Bone fractures cause loss of motor functions and other ailments that mar-

kedly lower patient quality of life and lead to invalidity among many of the elderly, making fractures a grave concern in a society which is ageing. The diagnosis of osteoporosis demands methods of discovering and preventing bone fractures early. However, presently, no valid method of diagnosis has been established to quantitatively evaluate the extent of fracture risk due to the mechanical phenomenon of bone destruction. Moreover, the incidence of secondary compression fractures after vertebral fractures is high. This is thought to be caused by bone fragility by osteoporosis. Finite element analysis (FEA) has been introduced in the field of biomechanics over the last few decades. This methodology has been utilized in many clinical applications and gained popularity especially in the prediction of vertebral strength due to its subtle relationships that exist between structure and functionality under a variety of conditions. Moreover, due to the complexity and difficulty of *in-vitro* and *in-vivo* experiments, FEA seems to give more promising results. Furthermore, this computational approach reduces the cost and danger of other testing procedures, allowing one to achieve certain individualization when organ geometry and specific loading condition can be fully customized by means of medical image treatment and biomechanics simulation technology. The reliability of FEA is subsequently strengthened by the recent finding which demonstrated its better correlations to vertebral strength then Dual-energy X-ray absorptiometry (DXA) approach [1]. In this study, FE models were constructed that reflect the bone density distribution and spinal shape of one healthy subject and one subject with vertebral compression fracture for the purpose of mechanically analyzing vertebral stress concentration. This research aimed to mechanically analyze vertebral stress concentration in one healthy subject and one subject with osteoporotic first lumbar (L1) vertebral compression fracture by using FEA.

2. Materials and Methods

2.1. Patient-Specific FE Modeling

Bone geometrical features were extracted from computed tomographic (CT) digital imaging and communications in medicine (DICOM) by using Mechanical Finder (MF) software (Research Center of Computational Mechanics Co. Ltd. Japan) [2]. Individual complex bone shapes and heterogeneous bone density distributions were considered in this bone modeling procedure. Heterogeneous bone density distributions are related to the Young's modulus of bone and vary between cancellous bones and around the regions between the cortical and cancellous bones. To reflect this heterogeneity in the finite element analysis (FEA), the MF software program was used to calculate the apparent bone density and determine the Young's modulus of each element separately [3] [4] [5]. Two sets of spinal models of healthy and osteoporotic subjects were developed. Written informed consent, permission, and cooperation were obtained from a 29-year-old Japanese male healthy subject (weight, 78 kg and height, 176 cm) and an 86-year-old Japanese female patient with osteoporosis and first lumbar (L1) vertebral compression fracture (weight, 47 kg and height, 160 cm; fish-type fracture;

Figure 1). To create the FE models, CT scan images of the patients' vertebrae, from the 12th thoracic vertebra (Th12) to the second lumbar vertebra (L2), were obtained. The three-dimensional (3-D) image-based FE models were then constructed based on the extracted bone edges of the region of interest (ROI) around the outer region of the cortical bone on the CT scan images, to obtain the anatomical structure of the spinal bone. Because of the structural complexity of the vertebrae, we adopted tetrahedral elements instead of cubic elements to represent the smooth surface of the spinal bone [6]. The trabecular and inner portion of the cortical bone were modeled by using 3-mm linear tetrahedral elements. Triangular shell elements with a thickness of 0.4 mm were also adopted on the outer surface of the cortex to represent the thin cortical shell [7]. On average, the healthy spinal and osteoporotic models had 804,467 and 790,408 tetrahedral solid elements, and 105,252 and 103,844 triangular shell elements, respectively.

2.2. Calculation of the Bone Material Properties of the Spine FE Models

The bone density of an element was determined from the average CT value (Hounsfield units [HU]) of 17 points, which was composed of the center and four points distributed on four lines connecting the center point to each apex of the tetrahedral element [8]. The bone density of each FE was computed based on the relationship.

Poisson's ratio was set to a constant value of 0.4, according to that used by Keyak *et al.* [5], Reilly and Burstein [9], and Van Buskirk and Ashman [10]. The elastic modulus of each finite element was determined based on the relationship between Young's modulus, (*Mpa*), and the bone density provided by Keyak *et al.* [11] (Table 1).

Figure 1. Lateral view of plain CT scan images performed during initial examination.

As Young's modulus is defined by individual elements one by one as described earlier, the heterogeneity of Young's modulus in the femoral bone can be directly reflected in the FE models. Meanwhile, the yield stress (*Mpa*) of the models was calculated from the bone density as proposed by Keyak *et al.* [5]. The final FE models consisted of the T12-L2 vertebrae, intervertebral disks and facet joints (Figure 2). The material properties of the intervertebral disk and facet joint are listed in Table 2.

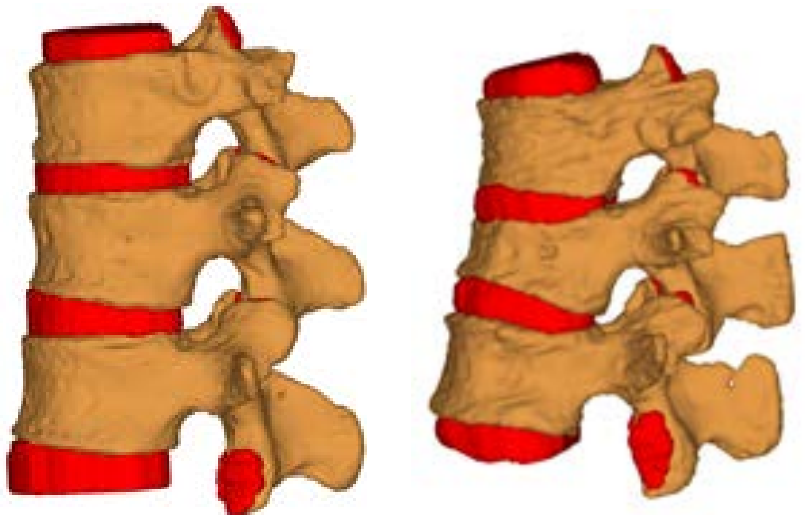

(a) (b)

Figure 2. Three-dimensional finite-element model: (a) healthy subject (b) osteoporotic subject.

Table 1. Spine material properties.

Young's modulus E (MPa)	Bone density p (g/cm^3)
$E = 0.01$	$p = 0.0$
$E = 33900p^2$	$0.0 < p \le 0.27$
$E = 5307p + 469$	$0.27 < p \le 0.6$
$E = 10200p^{2.01}$	$0.6 \le p$
Yield stress σ (MPa)	Bone density p (g/cm^3)
$\sigma = 1.0 \times 10^{20}$	$p \le 0.2$
$\sigma = 137p^{1.88}$	$0.2 < p \le 0.317$
$\sigma = 114p^{1.72}$	$0.317 \le p$
Poisson's ratio	Bone density p (g/cm^3)
0.4	$0.0 \le p$

Table 2. Material properties of the finite-element models.

Material	Young's modulus	Poisson's ratio
Intervertebral disc	8.4 MPa	0.45
Facet joint	11 MPa	0.2

2.3. Analysis

The FE models were loaded with a compressive force of 1000 N and four rotational/moment loadings on the superior surface of the T12 intervertebral disk to stimulate the four physiological motions/functions of the spine, which represent the movement of flexion, extension, lateral bending, and axial rotation. The inferior side of the L2 intervertebral disk was rigidly fixed. The loading details are listed and depicted in **Table 3** and **Figure 3**, respectively [12]. The biomechanical effects of the osteoporotic bone model were analyzed and compared with those of the healthy bone model. Drucker-Prager stress distributions on the vertebrae were evaluated [13]. In order to evaluate the stress distribution within and between the vertebral bodies, 30 points (10 points for each vertebra) were selected to extract the average Drucker-Prager stress. This point represented a square plate that could measure the average stress distribution distributed uniformly throughout its square volume. The plate was placed in parallel to the vertebral end plates. The distance between each of the plate was set to 5 mm. **Figure 4** is Young's modulus distributions.

The main procedures for FEA statistical analysis are as follows:

1) Bone edges are extracted from the ROI defined from the CT DICOM data.

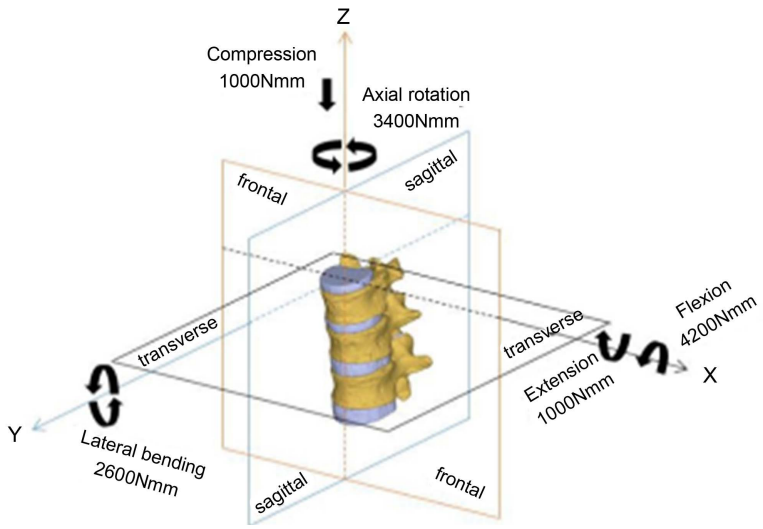

Figure 3. Five basic vertebral physiological motions.

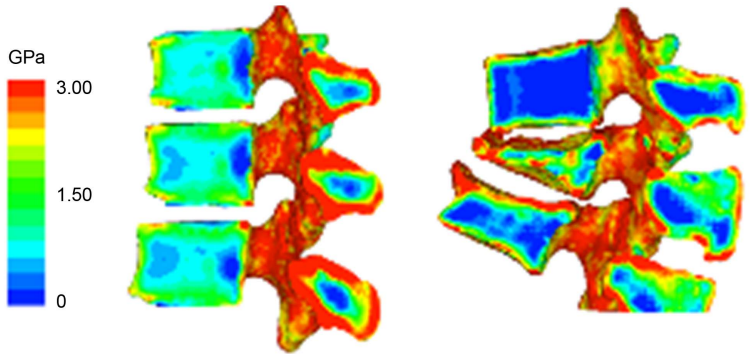

Figure 4. Young's modulus distribution.

Table 3. Loading conditions [12].

Motion	Flexion	Extension	Lateral bending	Axial rotation
Loading (N.m)	4.2	1.0	2.6	3.4

2) Three-dimensional image-based FE model contour data are calculated from the bone edge extraction data.

3) Mesh segmentation is applied to the contour data, and a 3-D image-based FE model is constructed.

4) Material properties are bestowed on each element based on conversion equations for the properties of the selected materials.

5) Loads and boundary conditions are established.

6) Statistical processing for each element is conducted based on established methods (*i.e.*, static response analysis and linear regression).

7) From these statistical results, information on aspects such as fracture load, strain distribution, and stress distribution is derived.

3. Results

The load transfer properties (stress and strain) significantly differed between the healthy vertebrae and the osteoporotic vertebrae in five different vertebral physiological motions (**Figure 5**). In general, the osteoporotic subject tended to produce higher stress and strain than the healthy subject in all physiological movements. The maximum Drucker-Prager stresses (**Figure 6**) for the healthy subject were 6.45, 10.05, 1.69, 3.03, and 6.48 MPa for compression, flexion, lateral bending, and axial rotation, respectively. Meanwhile, the Drucker-Prager stresses for the osteoporotic subject were 16.85, 10.61, 2.25, 3.90, and 7.96 MPa for compression, flexion, lateral bending, and axial rotation, respectively. The largest relative difference (**Figure 7**) was found in compression activity (161%), followed by axial rotation (23%), flexion (6%), lateral bending (29%), and extension (33%) activities. The minimum principle strains (**Figure 8**) for the healthy subject were −3590, −1560, −334, −843, and −637 μs train for compression, flexion, extension, lateral bending, and axial rotation, respectively. Replicating the same distribution pattern as that of the Drucker-Prager stress distributions, the osteoporotic subject had a relatively higher minimum principle strain than the healthy subject. Topping the list (**Figure 7**) was axial rotation (801%), followed by compression (1816%), flexion (727%), extension (321%), and lateral bending vertebral motion (632%). The result of the average Drucker-Prager stress distributions are shown in **Figure 9**. The results showed that the greatest Drucker-Prager stress for both subjects was found during compression. For the osteoporotic subject, this stress was substantially higher under relatively similar level of compressive loading, approximately 5 times higher for the osteoporotic than for the healthy subject. It is also important to note that the least relative stress difference was 50% under similar extensive loading, with the osteoporotic subject exhibiting higher stress than the healthy subject. The high degree of these stresses were then correlated with the high

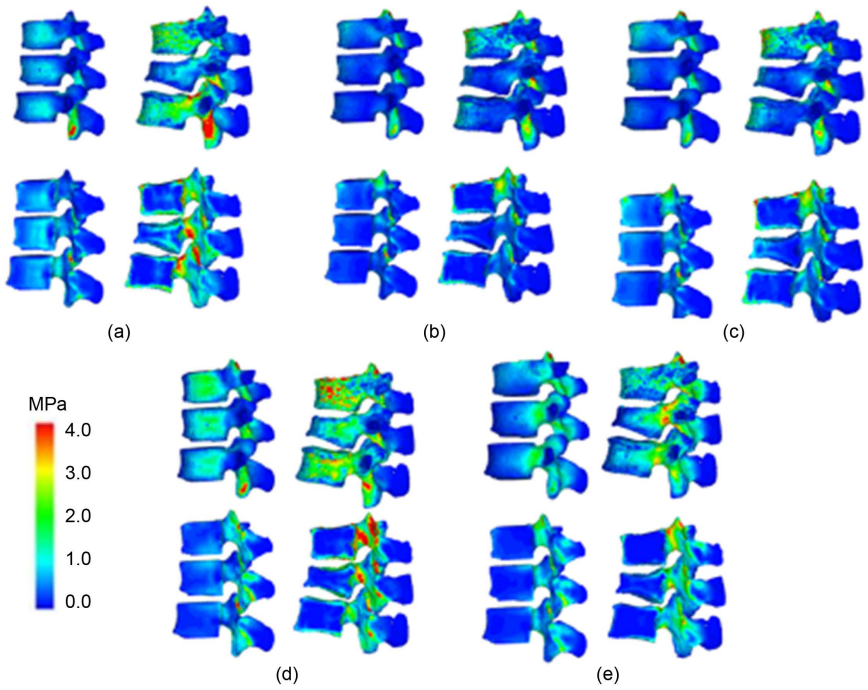

Figure 5. The cross-sectional view of the Drucker-Prager stress distribution on the vertebral body in five different vertebral physiological motions: (a) compression; (b) extension, (c) flexion; (d) lateral bending; and (e) axial rotation.

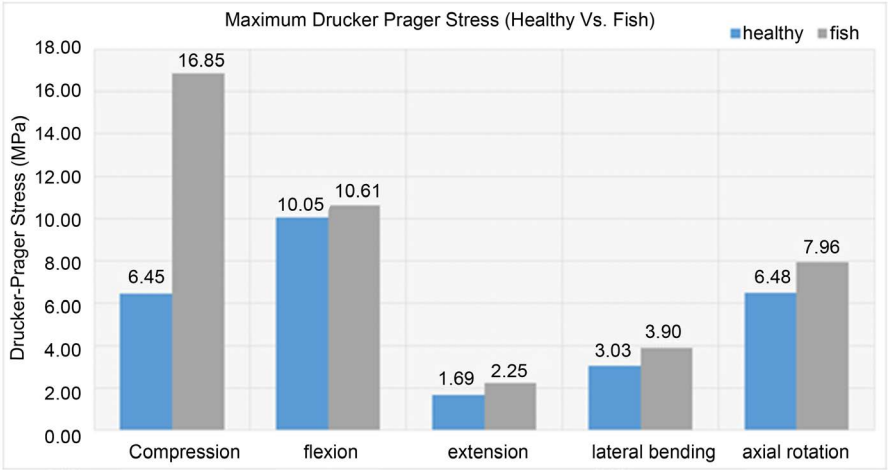

Figure 6. Drucker-Prager stress on the vertebral body of the healthy and osteoporotic subjects.

degree of principle strain. That is, the Drucker-Prager stress values were directly proportional to the principle strain values, and most of the time, the strains were concentrated in the middle of the trabecular region for each of the vertebrae.

4. Discussion

The recent developments in computational dynamics technology has made possible the use of FEA to conduct a mechanical bone analysis that reflects the complex structural morphology and material properties of bones. Indeed, through

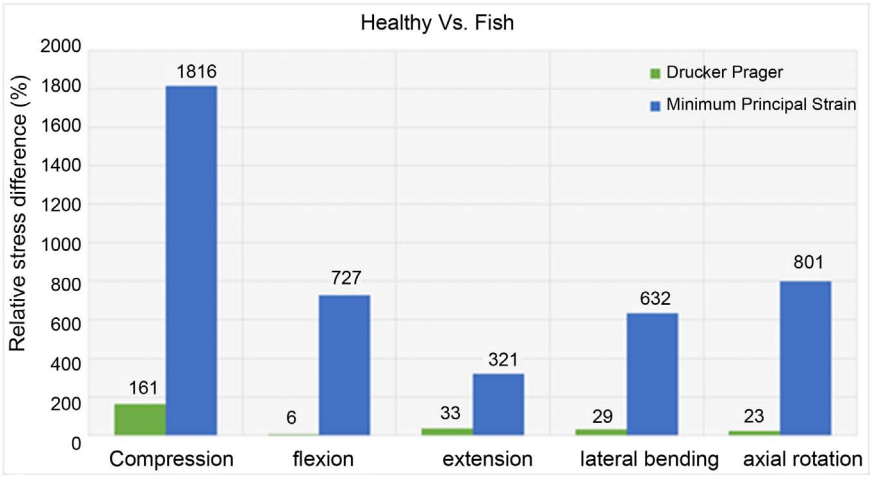

Figure 7. Relative stress difference (%) between the osteoporotic and healthy subjects.

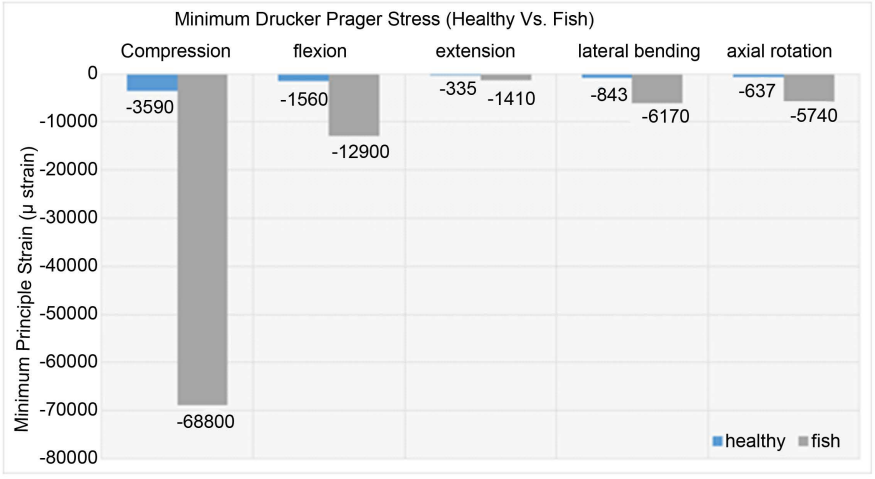

Figure 8. Minimum Principle strain on the vertebral body of the healthy and osteoporotic subjects.

such applications, various mechanical experiments and FEA on vertebral compression fractures have been performed. The method involves conducting FEA structural analysis on 3-D bone models constructed based on DICOM data procured from quantitative CT bone analysis. Then, the intensity of external forces applied in any direction or at any strength are quantitatively examined [14] [15] [16]. First, the CT based 3-D bone structure and bone density distribution can be assessed. Simultaneously, bone density can be evaluated at each tetrahedral element by collecting CT values for bone mass phantoms and plotting them on a calibration curve that correlates the CT value of each tetrahedral element to bone density. Thus, based on the calibration curve, CT values can be converted to bone density data. The bone density data can be arranged just like in a patient's bone in each area of the 3-D bone model derived from the DICOM data. Computer processing can then reproduce a 3-D bone image with structure and density distribution identical to that of the subject. Further processing can be done to construct FE models, against which virtual loads and boundary

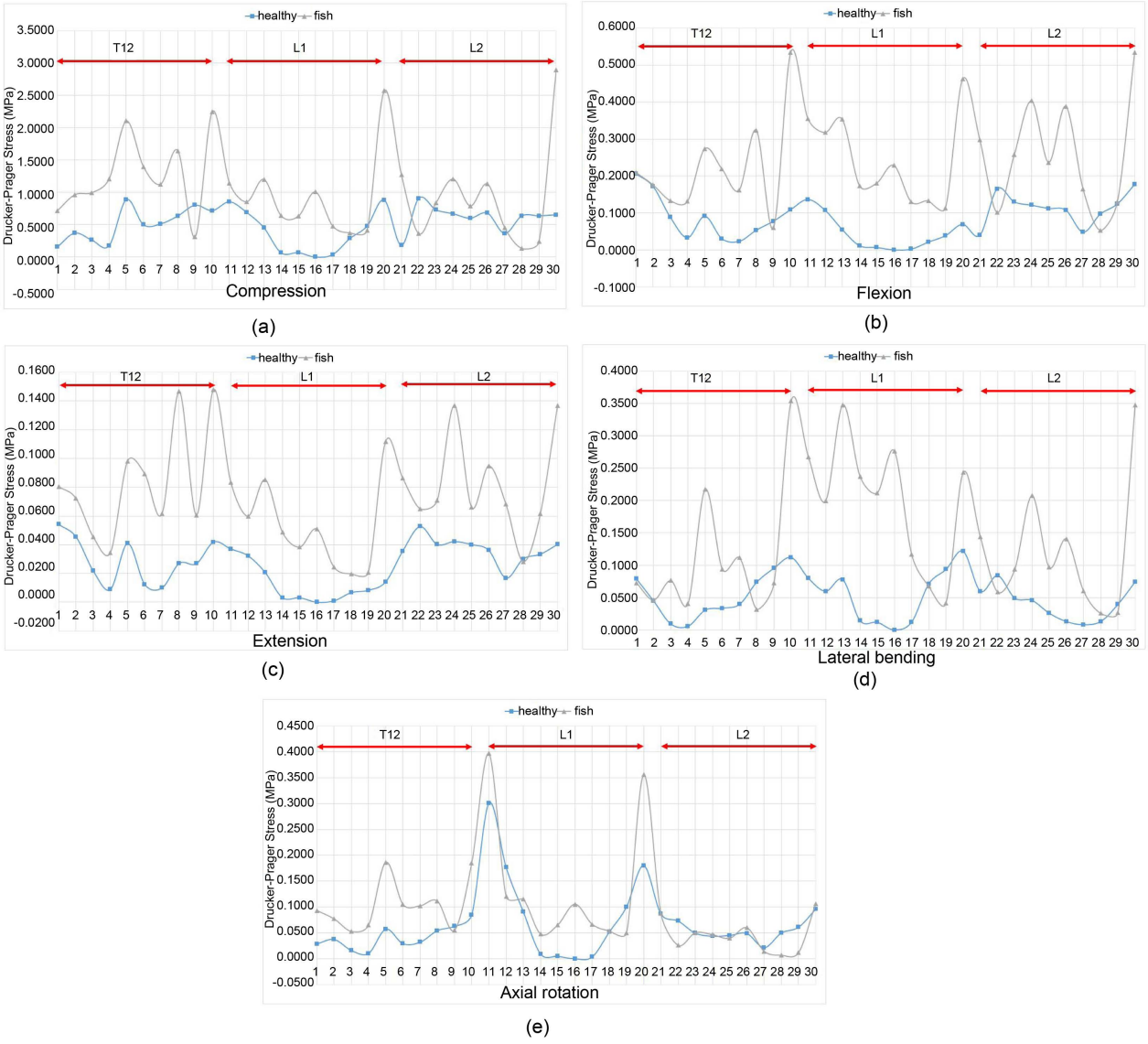

Figure 9. Average Drucker-Prager stress distributions in the vertebral body of the healthy and osteoporotic subjects, measured from the superior end plate of T12 to the inferior end plate of L2: (a) compression, (b) flexion, (c) extension, (d) lateral bending, and (e) axial rotation.

conditions can be established. Then, items such as strain distribution, stress distribution, yield load, and fracture load can be quantitatively assessed. Recently, some attempts have been made to understand the pathology of osteoporosis and judge therapeutic effects in individual patients based on CT data [17] [18] [19]. Other methods have involved the use of implants for surgical evaluations [20] [21] [22] [23] [24]. The first attempt to use FEA in bone strength analysis was made by Brekelmans *et al.* [25], whose analysis of the proximal end of the femur was far more accurate than the standard application of beam theory. Keyak [26] published a study in which the accuracy of FEA using CT of the proximal end of the femur was simultaneously tested along with the load testing of vertebrae samples from fresh cadavers. Another study involving lumbar vertebrae samples from fresh cadavers showed that CT-based FEA was highly accurate and corre-

lated highly with vertical compression test results [27]. However, hitherto reports of FE models of osteoporotic vertebrae have mainly focused on individual vertebrae, and no reports have considered vertebrae shape or spinal alignment. In this study, models of a set of three vertebrae were constructed, and further analyses of vertebrae shape and alignment were conducted with respect to vertebral compression fracture models.

Lindsay *et al.* [28] reported that novel vertebral fractures occur through natural processes at a rate of 19.2% and that after initial vertebrae fractures, the probability of developing secondary compression fractures is extremely high. The results of this study indicated that all the stresses associated with compression, flexion, extension, lateral bending, and axial rotation observed in vertebral compression fracture models resulted in increases in stress concentration in adjacent vertebrae. Thus, it is thought that the occurrence of secondary vertebral compression fractures is due not only to bone fragility but also to alterations in the stress concentrated on adjacent vertebrae due to changes in alignment after the initial vertebral fracture. Considering that hitherto studies on stress loading have not investigated stresses caused by factors besides compression, flexion, and extension [29] [30] and as we have confirmed particularly an increase in stress concentration due to compression and axial rotation, as well as from the perspective of providing guidance on daily activities after vertebral fractures, we believe new insight has been gained.

These phenomena were proven to be well correlated with the deterioration of bone structural strength and reduced bone mass as characterized by osteoporosis. The limitations of this study are a small sample size and we don't have experimental validations. We will study far more sample after this. Validation study is very difficult, but we hope to try cadaver study.

5. Conclusion

The osteoporotic vertebral model with L1 vertebral compression fracture has significantly affected the load transfer pattern (stress and strain) distributions within the vertebral body. By utilizing the stress and strain distributions of the healthy subject as a comparison tool, we found that the osteoporotic subject seemed to exhibit extremely higher stresses and strains than the healthy subject under the five basic vertebral physiological motions. Worsening this condition was the accompanying uneven stress distribution within and between the vertebral bodies. Therefore, we strongly suggest that for the osteoporotic subject, the risk of vertebral fracture can occur at any time even with daily living activities.

Acknowledgements

Written informed consent was obtained from the patient for publication of this paper and any accompanying images.

Conflict of Interest

The authors report no conflict of interest concerning the findings specified in

this paper.

References

[1] Crawford, R.P., Cann, C.E. and Keaveny, T.M. (2003) Finite Element Models Predict *in Vitro* Vertebral Body Compressive Strength Better than Quantitative Computed Tomography. *Bone*, **33**, 744-750. https://doi.org/10.1016/S8756-3282(03)00210-2

[2] Tawara, D., Sakamoto, J., Murakami, H., Kawahara, N., Oda, J. and Tomita, K. (2010) Mechanical Evaluation by Patient-Specific Finite Element Analysis Demonstrates Therapeutic Effects for Osteoporotic Vertebrae. *Journal of the Mechanical Behavior of Biomedical Materials*, **3**, 31-40. https://doi.org/10.1016/j.jmbbm.2009.03.001

[3] Carter, D.R. and Hayes, W.C. (1997) The Compressive Behavior of Bone as Two-Phase of Porous Structure. *The Journal of Bone and Joint Surgery*, **59**, 954-962. https://doi.org/10.2106/00004623-197759070-00021

[4] Keller, T.S. (1994) Predicting the Compressive Mechanical Behavior of Bone. *Journal of Biomechanics*, **27**, 1159-1168. https://doi.org/10.1016/0021-9290(94)90056-6

[5] Keyak, J.H., Rossia, S.A., Jones, K.A. and Skinner, H.B. (1998) Prediction of Femoral Fracture Load Using Automated Finite Element Modeling. *Journal of Biomechanics*, **31**, 125-133. https://doi.org/10.1016/S0021-9290(97)00123-1

[6] Ulrich, D., Rietbergen, B.V., Weinans, H. and Ruegsegger, P. (1998) Finite Element Analysis of Trabecular Bone Structure: A Comparison of Image-Based Meshing Techniques. *Journal of Biomechanics*, **31**, 1187-1192. https://doi.org/10.1016/S0021-9290(98)00118-3

[7] Imai, K., Ohnishi, I., Yamamoto, S. and Nakamura, K. (2008) *In Vivo* Assessment of Lumbar Vertebral Strength in Elderly Women Using Computed Tomography-Based Nonlinear Finite Element Model. *Spine*, **33**, 27-32. https://doi.org/10.1097/BRS.0b013e31815e3993

[8] Bessho, M., Ohnishi, I., Matsuyama, J., Matsumoto, T. and Imai, K. (2007) Prediction of Strength and Strain of Proximal Femur by a CT-Based Finite Element Method. *Journal of Biomechanics*, **3**, 31-40.

[9] Reilly, D.T. and Burstein, A.H. (1975) The Elastic and Ultimate Properties of Compact Bone Tissue. *Journal of Biomechanics*, **8**, 393-405. https://doi.org/10.1016/0021-9290(75)90075-5

[10] Van Buskirk, W.C.V. and Ashman, R. (1981) The Elastic Moduli of Bone. *American Society of Mechanical Engineers*, **45**, 131-143.

[11] Keyak, J.H., Lee, I.Y. and Skinner, H.B. (1994) Correlations between Orthogonal Mechanical Properties and Density of Trabecular Bone: Use of Different Densitometric Measures. *Journal of Biomedical Materials Research*, **28**, 1329-1336. https://doi.org/10.1002/jbm.820281111

[12] Han, K.S., Rohlmanna, A., Zandera, T. and Taylorb, W.R. (2013) Lumbar Spinal Loads Vary with Body Height and Weight. *Medical Engineering and Physics*, **35**, 969-977. https://doi.org/10.1016/j.medengphy.2012.09.009

[13] Mazlan, M.H., Todo, M., Takano, H. and Yonezawa, I. (2014) Finite Element Analysis of Osteoporotic Vertebrae with First Lumber (L1) Vertebral Compression Fracture. *International Journal of Applied Physics and Mathematics*, **4**, 267-274.

[14] Bauera, J.S., Sidorenkoc, I., Muellerd, D., Bauma, T., Isseverb, A.S., Ecksteinf, F., Rummeny, E.J., Link, T.M. and Raeth, C.W. (2014) Prediction of Bone Strength by CT and MDCT-Based Finite-Element Models: How Much Spatial Resolution Is

Needed. *European Journal of Radiology*, **83**, 36-42.
https://doi.org/10.1016/j.ejrad.2013.10.024

[15] Brouwers, J.E.M., Lambers, F.M., Rietbergen, B.V., Ito, K. and Huiskes, R. (2009) Comparison of Bone Loss Induced by Ovariectomy and Neurectomy in Rats Analyzed by *in Vivo* Micro-CT. *Journal of Orthopaedic Research*, **27**, 1521-1527.
https://doi.org/10.1002/jor.20913

[16] Sairyo, K., Goel, V.K., Masuda, A., Vishnubhotla, S., Faizan, A., Biyani, A., Ebraheim, N., Yonekura, D., Murakami, R. and Terai, T. (2006) Three-Dimensional Finite Element Analysis of the Pediatric Lumbar Spine. Part I: Pathomechanism of Apophyseal Bony Ring Fracture. *European Spine Journal*, **15**, 923-929.

[17] Green, J.O., Diab, T., Allen, M.R., Vidakovic, B., Burr, D.B. and Guldberg, R.E. (2012) Three Years of Alendronate Treatment Does Not Continue to Decrease Microstructural Stresses and Strains Associated with Trabecular Microdamage Initiation beyond Those at 1 Year. *Osteoporosis International*, **23**, 2313-2320.

[18] Imai, K. (2011) Vertebral Fracture Risk and Alendronate Effects on Osteoporosis Assessed by a Computed Tomography-Based Nonlinear Finite Element Method. *Journal of Bone and Mineral Metabolism*, **29**, 645-651.
https://doi.org/10.1007/s00774-011-0281-9

[19] Tawara, D., Sakamoto, J., Murakami, H., Kawahara, N. and Tomita, K. (2011) Patient Specific Finite Element Analyses Detect Significant Mechanical Therapeutic Effects on Osteoporotic Vertebrae during a Three-Year Treatment. *Journal of Biomechanical Science and Engineering*, **6**, 248-261. https://doi.org/10.1299/jbse.6.248

[20] Alizadeh, M., Kadir, M.R.A., Fadhli, M.M., Fallahiarezoodar, A., Azmi, B., Murali, M.R. and Kamarul, T. (2013) The Use of X-Shaped Cross-Link in Posterior Spinal Constructs Improves Stability in Thoracolumbar Burst Fracture: A Finite Element Analysis. *Journal of Orthopaedic Research*, **31**, 1447-1454.

[21] Choi, K.C., Ryu, K.S., Lee, S.H., Kim, Y.H., Lee, S.J. and Park, C.K. (2013) Biomechanical Comparison of Anterior Lumbar Interbody Fusion: Stand-Alone Interbody Cage versus Interbody Cage with Pedicle Screw Fixation: A Finite Element Analysis. *BMC Musculoskeletal Disorders*, **14**, 220-229.
https://doi.org/10.1186/1471-2474-14-220

[22] Lin, H.M., Pan, Y.N., Liub, C.L., Huangc, L.Y., Huang, C.H. and Chen, C.S. (2013) Biomechanical Comparison of the K-ROD and Dynesys Dynamic Spinal Fixator Systems: A Finite Element Analysis. *Bio-Medical Materials and Engineering*, **23**, 495-505.

[23] Wilke, H.J., Wenger, K. and Claes, L. (1998) Testing Criteria for Spinal Implants Recommendations for the Standardization of *In Vitro* Stability Testing of Spinal Implants. *European Spine Journal*, **7**, 148-154.

[24] Zhang, L., Yang, G., Wub, L. and Yu, B. (2010) The Biomechanical Effects of Osteoporosis Vertebral Augmentation with Cancellous Bone Granules or Bone Cement on Treated and Adjacent Non-Treated Vertebral Bodies: A Finite Element Evaluation. *Clinical Biomechanics*, **25**, 166-172.
https://doi.org/10.1016/j.clinbiomech.2009.10.006

[25] Brekelmans, W.A., Poort, H.W. and Slooff, T.J. (1972) A New Method to Analyze the Mechanical Behavior of Skeletal Parts. *Acta Orthopaedica Scandinavica*, **43**, 301-317.

[26] Keyak, J.H. (2001) Improved Prediction of Proximal Femoral Fracture Load Using Nonlinear Finite Element Models. *Medical Engineering and Physics*, **23**, 165-173.
https://doi.org/10.1016/S1350-4533(01)00045-5

[27] Silva, M.J., Wang, C., Keaveny, T.M. and Hayes, W.C. (1994) Direct and Computed

Tomography Thickness Measurements of the Human, Lumbar Vertebral Shell and End Plate. *Bone*, **15**, 409-414.

[28] Lindsay, R., Silverman, S.L., Cooper, C., Hanley, D.A., Barton, I., Broy, S.B., Licata, A., Benhamou, L., Geusens, P., Flowers, K., Stracke, H. and Seeman, E. (2001) Risk of New Vertebral Fracture in the Year Following a Fracture. *Journal of the American Medical Association*, **285**, 320-323. https://doi.org/10.1001/jama.285.3.320

[29] Garo, A., Arnoux, P.J., Wagnac, E. and Aubin, C.E. (2011) Calibration of the Mechanical Properties in a Finite Element Model of a Lumbar Vertebra under Dynamic Compression up to Failure. *Medical and Biological Engineering and Computing*, **49**, 1371-1379. https://doi.org/10.1007/s11517-011-0826-z

[30] Wagnac, E., Arnoux, P.J., Garo, A. and Aubin, C.E. (2012) Finite Element Analysis of the Influence of Loading Rate on a Model of the Full Lumbar Spine under Dynamic Loading Conditions. *Medical and Biological Engineering and Computing*, **50**, 903-915. https://doi.org/10.1007/s11517-012-0908-6

Scientific Research Publishing

Submit or recommend next manuscript to SCIRP and we will provide best service for you:

Accepting pre-submission inquiries through Email, Facebook, LinkedIn, Twitter, etc.
A wide selection of journals (inclusive of 9 subjects, more than 200 journals)
Providing 24-hour high-quality service
User-friendly online submission system
Fair and swift peer-review system
Efficient typesetting and proofreading procedure
Display of the result of downloads and visits, as well as the number of cited articles
Maximum dissemination of your research work

Submit your manuscript at: http://papersubmission.scirp.org/
Or contact jamp@scirp.org

Journal of Applied Mathematics and Physics, 2017, 5, 966-989
http://www.scirp.org/journal/jamp
ISSN Online: 2327-4379
ISSN Print: 2327-4352

Exact Solution for Thermal Stagnation-Point Flow with Surface Curvature and External Vorticity Effects

Ronald Ming Cho So[1], Elizabeth Wing Sze Kam[2*]

[1]Mechanical Engineering Department, the Hong Kong Polytechnic University, Hong Kong, China
[2]Department of Mathematical Sciences, Rensselaer Polytechnic Institute, Troy, NY, USA
Email: mmmcso@polyu.edu.hk, *kamwingsze@gmail.com

How to cite this paper: So, R.M.C. and Kam, E.W.S. (2017) Exact Solution for Thermal Stagnation-Point Flow with Surface Curvature and External Vorticity Effects. *Journal of Applied Mathematics and Physics*, **5**, 966-989.
https://doi.org/10.4236/jamp.2017.54085

Received: February 19, 2017
Accepted: April 27, 2017
Published: April 30, 2017

Copyright © 2017 by authors and Scientific Research Publishing Inc.
This work is licensed under the Creative Commons Attribution International License (CC BY 4.0).
http://creativecommons.org/licenses/by/4.0/

Open Access

Abstract

Exact solution of the steady Navier-Stokes equations has been obtained for the thermal stagnation-point flow at the leading edge of a turbine blade under the assumptions of constant nose radius and external vorticity, and fluid properties independent of temperature. The solutions reveal that curvature affects local heat transfer and skin friction while external vorticity does not. The effect of external vorticity is to shift the zero skin friction point away from the stagnation point. This solution is valid for all Reynolds number, external vorticity, and nose radius. In the limit of nose radius going to infinity and external vorticity, going to zero, the exact solution for two-dimensional plane stagnation-point flow is recovered identically. In addition, it can be shown that the velocity field around the stagnation point of a rotating curved surface is the same as that around the stagnation point of a stationary curved surface with an external vorticity which equals to twice of the rotational speed. This realization renders the present solution equally valid for thermal stagnation-point flow at the leading edge of centrifugal impeller blades.

Keywords

Navier-Stokes Equations, Exact Solutions, Thermal Stagnation-Point Flow, Displacement Effect

1. Introduction

Frequently, in the past, two-dimensional calculation methods were used to determine the gas-side heat transfer coefficient on turbine blades [1]. All these methods, whether based on the integral or differential equations, were derived on the assumption that the flow is steady and the static pressure variation across

the boundary layer has very little effect on the flow, and hence can be neglected [2]. Measurements of two-dimensional turbulent boundary layers along plane surfaces lend support to this assumption [3]. However, when these methods were used to calculate flows along curved surfaces, they were found to be inadequate comparing with measured data [2]. The reason is that existing two-dimensional method neglects the effect of curvature on the mean flow streamlines. This neglect is justifiable in laminar flows [4] [5] if $k\delta \ll 1$. On the other hand, the neglect of the effect of streamline curvature is not justifiable in the case of turbulent flows [6] even when $k\delta \ll 1$.

Striking effects of curvature have been observed in turbulent boundary-layer flow over convex and concave surfaces [7] [8]. Boundary layer measurements showed that large convex curvature in the mean flow streamlines leads to vanishing shear stress in regions where the mean velocity gradient is still substantial [7], while large concave curvature promotes the formation of Taylor-Gortler type instabilities [8]. As a result, various attempts were made by different investigators to account for the effect of streamline curvature in two-dimensional turbulent shear flows [9]-[14]. Attempt to use these techniques to calculate flow around compressor blades was first made in [13], and good correlations were obtained between measured and calculated results. Furthermore, these techniques were extended to model heat transfer on curved surfaces alone [14] and curved surfaces with swirl [15]. Again, good correlations were obtained between measured and calculated heat transfer results. In view of this, the same technique has also been used to predict the flow and heat transfer around axial flow turbine blades where Coriolis effects are absent [15].

Generally, the solution of the two-dimensional plane stagnation-point flow [16] [17] [18] is used to provide initial conditions for heat transfer calculations along turbine blades. This assumption is valid as long as the surface curvature is considered to have negligible effect on the boundary-layer flow around the blades. With the introduction of improved techniques mentioned above [9]-[15], it is evident that, to be consistent with the improved techniques, the effect of surface curvature on the stagnation-point flow cannot be neglected.

The boundary layer thickness in a stagnation-point flow is given by $\delta = 2.4\sqrt{\nu/a}$; therefore, it can be seen that the neglect of curvature effect is valid only if $\sqrt{\nu/a}$ is much less than the radius of curvature of the surface at the stagnation point [18]. In the leading edge of a turbine blade, the nose radius is very small and the above condition is not necessary true. As a result, surface curvature may have a significant effect on the flow and heat transfer downstream of the forward stagnation of a turbine blade. In addition to being affected by surface curvature (k), the flow and heat transfer at the leading edge are also influenced by free stream vorticity (Ω) in the flow approaching the turbine blades. Therefore, to obtain the correct initial conditions for subsequent heat transfer calculations around the blades using any one of the previously mentioned techniques [9]-[15], the effect of k and Ω on the flow and heat transfer

at the leading edge have to be considered and analyzed.

Effect of surface curvature on stagnation-point flow was first examined in [4] [5]. Assuming that $Re \gg 1$ and $k\delta \ll 1$, the analysis in [4] [5] proceeded to expand the stream function in terms of $1/Re$. The problem was then solved using the technique of matched asymptotic expansions and the results gave the second-order effect on heat transfer coefficient and skin friction due to surface curvature. Further, second-order effect due to flow displacement and free-stream Ω was also evaluated [4] [5]. Subsequently, other investigators [19] [20] [21] have also carried out analysis on the same problem invoking the same assumptions, but using different methods to solve the problem. The results obtained by these investigators were no different than those presented earlier [4] [5]. In some cases [19] [20], the results were shown to be less accurate because of the assumptions the investigators had to invoke to simplify the problem.

The effect of constant external Ω on two-dimensional plane stagnation-point flow was also attempted and an exact solution to the governing equations was obtained [22]. Unlike the perturbation solution mentioned previously [4] [5], the exact solution, without accounting for the effect of flow displacement, is valid for all Re [22]. Further, it was found that the effect of external Ω on the flow was to shift the zero skin friction point away from the stagnation point; however, no attempt had been made to analyze the heat transfer problem [22]. On the other hand, a complete second-order analysis of the problem was carried out and it showed that if displacement effect were also included [23], the shift of the zero skin friction point from the stagnation point is greater than that predicted in [22]. A thorough discussion of most second-order effects has been presented in [23] where the flows considered are not limited to stagnation-point flows.

In spite of the fairly complete second-order treatment of stagnation-point flow on curved surfaces [4] [5] [23], the analysis is rather limiting because of the assumptions of $Re \gg 1$ and $k\delta \ll 1$. These assumptions could lead to two sources of error in the prediction of gas-side heat transfer coefficients on turbine blades. The obvious source is the inaccurate estimate of the heat transfer coefficient at the leading edge, which may or may not be too critical depending on the value of Re and $k\delta$ at the nose. A second source of error is associated with the incorrect estimate of initial conditions for subsequent convective heat transfer calculations on the rest of the blade. The effect of this error on the calculated heat transfer coefficient is difficult to estimate, and it could be more severe as Re decreases and $k\delta$ increases at the leading edge. Consequently, there is a need for a more exact theory that can correctly account for the effect of surface curvature and external Ω on thermal stagnation-point flows at the leading edge of turbine blades.

The objective of the present paper, therefore, is to investigate the effect of surface curvature and constant external Ω on heat transfer at the leading edge of axial flow turbine blades. To simplify the problem, the flow near the leading edge of the blade is approximated by the flow around a two-dimensional cylinder of

the same radius as the nose. Also, the flow is assumed to be steady and laminar, and the fluid properties are assumed constant over the temperature range of interest. As the first attempt, the assumption of laminar flow at the stagnation point and its immediate vicinity is reasonable. It is shown that exact solutions to the governing equations could be obtained and that these solutions would reduce to the exact solution with constant Ω [22] as $k \to 0$, and to the classical solutions [15] [16] [17] [18] in the limit of zero surface curvature and zero external Ω. Thus formulated, the solutions are valid for all values of *Re*, $k\delta$ and Ω. Once this solution is obtained, it is shown that the formulation can be extended to analyze the thermal stagnation-point flow at the leading edge of centrifugal impeller blades.

2. The Governing Equations

The governing equations describing the steady incompressible flow and temperature fields near the forward stagnation point of a two-dimensional cylinder of constant radius *R* can be written with respect to a co-ordinate system attached to the cylinder as shown in **Figure 1**. In component form, the full set of steady Navier-Stokes equations [24] is reduced to:

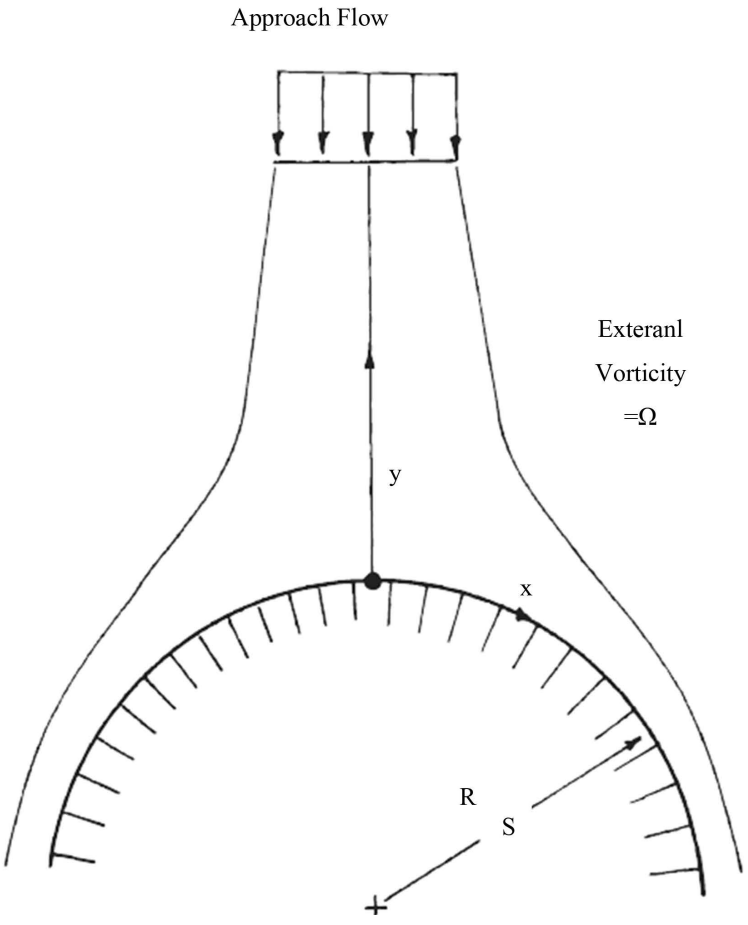

Figure 1. Curvilinear co-ordinate system for a stationary surface.

$$u_x + (hv)_y = 0, \tag{1}$$

$$uu_x + v(hu)_y = -\rho^{-1}p_x + v\left[h^{-1}u_{xx} + hu_{yy} + ku_y - k^2h^{-1}u + 2kh^{-1}v_x\right], \tag{2}$$

$$uv_x + hvv_y - ku^2 = -\rho^{-1}hp_y + v\left[h^{-1}v_{xx} + hv_{yy} + kv_y - k^2h^{-1}v - 2kh^{-1}u_x\right], \tag{3}$$

$$uT_x + hvT_y = \alpha\left[h^{-1}T_{xx} + hT_{yy} + kT_y\right], \tag{4}$$

where subscripts denote partial differentiation, k is positive for convex and negative for concave curvature, and viscous dissipation of heat has been assumed negligible. The boundary conditions are no slip at the wall, uniform flow and temperature far upstream of the stagnation point, and inviscid flow with a constant Ω outside a shear layer close to the wall.

Assuming constant fluid properties allow the velocity field equations to be decoupled from the temperature field equation. A complete solution to the aerodynamic problem, *i.e.* Equations (1)-(3), can be obtained by first finding a solution to the outer inviscid flow and then proceeding to determine the flow in the viscous region near the wall. Once the velocity field near the stagnation point is known heat transfer to or from the cylinder surface can be obtained by solving Equation (4) with the appropriate temperature boundary conditions.

3. The Inviscid Solution

Since the flow in the outer region is inviscid, the stream function, $\Psi(x, y)$, satisfies the Poisson equation, which can be written as

$$h^{-1}\left(h^{-1}\Psi_x\right)_x + h^{-1}\left(h\Psi_y\right)_y = -\Omega, \tag{5}$$

where the stream function is defined by

$$u = \Psi_y, \tag{6}$$

$$hv = -\Psi_x. \tag{7}$$

The boundary conditions are

$$\Psi = 0 \quad \text{on the body,} \tag{8}$$

$$\Psi(x, y) \sim \Psi_\infty \quad \text{far upstream.} \tag{9}$$

This problem can be considered properly set for an elliptic differential equation, and a solution for Ψ can be sought in the form

$$\Psi(x, y) = P(x)Q(y) + \Omega S(y). \tag{10}$$

Substituting (10) into (5) gives

$$-\frac{P''}{P} = \frac{h^2Q''}{Q} + \frac{khQ'}{Q} = n^2, \tag{11}$$

$$h^2S'' + khS' = -h^2, \tag{12}$$

where the primes denote ordinary differentiation with respect to x for P, and to y for Q and S. If the solution for $\Psi(x, y)$ is to approach the classical two-dimensional plane stagnation-point flow solution when $k \to 0$ and $\Omega \to 0$, then

it can be shown that the only meaningful solution for (11) is given by $n=0$. With $n=0$, solutions for $P(x)$ and $Q(y)$ are

$$P(x)=a_1 x, \tag{13}$$

$$Q(y)=\frac{a_2 \ln h}{k}, \tag{14}$$

where a_1 and a_2 are arbitrary constants. Since the homogeneous solution of (12) is identical to that obtained for Q and Ω is constant, it can be easily shown that only the particular integral of Equation (12) is of interest. A particular solution of (12) is given by

$$S(y)=-\frac{y(1+h)}{4k}+\frac{\ln h}{2k^2}. \tag{15}$$

As a result, the solution for Ψ with boundary conditions (8) and (9) can be written as:

$$\Psi(x,y)=\frac{ax}{k}\ln h-\frac{\Omega y(1+h)}{4k}+\frac{\Omega}{2k^2}\ln h, \tag{16}$$

where a is an arbitrary constant. It should be pointed out that in the limit of $k\to 0$, Equation (16) reduces to the solution given in [22], or

$$\lim_{k\to 0}\Psi = axy-\frac{1}{2}\Omega y^2. \tag{17}$$

Therefore, when $\Omega=0$, Equation (17) reduces to the classical potential solution for two-dimensional plane stagnation-point flow.

The velocity field is given by

$$u=\frac{ax}{h}-\frac{\Omega y(1+h)}{2h}, \tag{18}$$

$$v=-\frac{a\ln h}{kh}, \tag{19}$$

and the pressure field is obtained by integrating the Euler equations which are the inviscid counterparts of (2) and (3). With the help of (18) and (19), the pressure field can be written as:

$$p_0-p=\frac{1}{2}\rho\left[\frac{a^2x^2}{h^2}+\frac{a\Omega x}{k}\frac{2h^2\ln h-h^2+1}{h^2}+\frac{\Omega^2}{4k^2}\frac{h^4-4h^2\ln h-1}{h^2}+\frac{a^2(\ln h)^2}{k^2h^2}\right], \tag{20}$$

where p is the pressure and p_0 is the pressure at the stagnation point. It should be noted that even when $\Omega\to 0$ the velocity u downstream of the stagnation point is not uniform as could be seen from Equation (18). This is necessary because curvature gives rise to a "centrifugal force" that is balanced by a normal pressure gradient.

4. Viscous Flow and Heat Transfer

Equations (18)-(20) represent a complete solution to the inviscid problem. Once the inviscid solution is known, the next task is to focus on the viscous flow and

heat transfer near the surface. Since the inviscid solution does not satisfy the no-slip condition at the wall, a viscous solution that is valid at and near the surface will be sought. This solution has to approach (18) and (19) for large y, and in this limit, the vorticity also approaches Ω in the external flow. In order not to impose any conditions on Re, $k\delta$, and Ω, an exact solution to the governing Navier-Stokes Equations (1)-(3) is sought in the viscous layer. The pressure terms in the momentum equations are eliminated by cross-differentiating (2) and (3), and the resulting vorticity equation is given by

$$\begin{aligned} &h^2uu_{xy}+h^3vu_{yy}+kh^2uv_y+kh^2vu_y-huv_{xx}-h^2vv_{xy}+hkvv_x+2khuu_x \\ &=v\left[hu_{xxy}+ku_{xx}+h^3u_{yyy}+2kh^2u_{yy}-k^2hu_y+k^3u+khv_{xy}-k^2v_x-v_{xxx}-h^2v_{xyy}\right], \end{aligned} \tag{21}$$

where use has been made of Equation (1). Stagnation-point flow near the surface is, therefore, given by the solution of (21) subject to the boundary conditions

$$u(x,y)=v(x,0)=0, \tag{22a}$$

$$\left.\begin{aligned} &u(x,y)\to\frac{ax}{h}-\frac{\Omega y(1+h)}{2h} \\ &h^{-1}v_x-h^{-1}(hu)_y\to\Omega \end{aligned}\right\} \text{ for large } y. \tag{22b, c}$$

Once the velocity field is known, the stagnation-point heat transfer problem can be analyzed by solving Equation (4) subject to the conditions of an isothermal body and a uniform temperature in the external flow.

As in the case of plane flows with or without the effect of Ω [15] [16] [17] [18] [22], a similar solution to Equation (21) is sought such that the velocity and temperature fields can be written as:

$$u=axF'(\eta)-\Omega\sqrt{\frac{\nu}{a}}\frac{G(\eta)}{h}, \tag{23}$$

$$v=-\sqrt{a\nu}\frac{F(\eta)}{h}, \tag{24}$$

$$T=T_w+(T_\infty-T_w)\Theta(\eta), \tag{25}$$

where $\eta=\left(\sqrt{a/\nu}\right)y$ is the similarity variable, $h=1+ky=1+K\eta$ and $K=\left(\sqrt{\nu/a}\right)k$. Substituting Equations (23)-(25) into (21) and (4), the following equations for $F(\eta)$, $G(\eta)$, and $\Theta(\eta)$ are obtained,

$$F''''+\frac{F+2K}{h}F'''+\frac{K(F-K)-hF'}{h^2}F''-\frac{K^2(F-K)+KhF'}{h^3}F'=0, \tag{26}$$

$$G''+\frac{F-K}{h}G''+\frac{K(F-K)}{h^2}G'-\frac{hF''+KF'}{h^2}G=0, \tag{27}$$

$$\Theta''+\frac{FPr+K}{h}\Theta'=0, \tag{28}$$

where the primes denote ordinary differentiation with respect to η. The conditions that $T(x,0)=T_w$, $T(x,\text{large } y)=T_\infty$ and (22) give the necessary boundary conditions for (26)-(28).

It is not convenient to choose $G(\eta)$ at large η as one of the outer boun-

dary conditions for G because its value at large η is dependent on displacement. As a result, the outer boundary conditions for G are defined by the functions $G'(\eta)$ and $G''(\eta)$ at large η. In terms of η, the boundary conditions for F, G, and Θ can then be written as

$$\text{at } \eta = 0 : F(0) = 0, \tag{29a}$$

$$F'(0) = 0, \tag{29b}$$

$$G(0) = 0, \tag{29c}$$

$$\Theta(0) = 0, \tag{29d}$$

$$\text{at large } \eta : F'(\eta) = h^{-1}, \tag{30a}$$

$$F''(\eta) = -Kh^{-2}, \tag{30b}$$

$$G'(\eta) = h, \tag{30c}$$

$$G''(\eta) = K, \tag{30d}$$

$$\Theta(\eta) = 1. \tag{30e}$$

The viscous flow and heat transfer problem at the stagnation point is reduced to solving three ordinary differential equations governing $F(\eta)$, $G(\eta)$ and $\Theta(\eta)$, and subject to boundary conditions (29) and (30). Thus formulated, solutions of these equations will represent exact solutions to the thermal stagnation-point problem at the leading edge of axial flow turbine blades.

5. Numerical Integration of the Governing Equations

The ordinary differential equations governing F, G, and Θ are highly nonlinear and analytic solutions for (26)-(28) are not easily obtainable and are not presently available. However, numerical technique could be used to simulate the solutions for (26)-(28). Since numerical solutions of ordinary differential equations is far better developed than those of highly nonlinear partial differential equations, such as the Navier-Stokes equations, and a lot more accurate, therefore, numerical solutions of (26)-(28) are both accurate and reliable.

To further simplify the governing equations for numerical analysis, a transformation first put forward in [20] is adopted. If the new similarity variable is denoted by

$$\zeta = \frac{\ln(1 + K\eta)}{K}, \tag{31}$$

and the new functions for F, G, and Θ are written as

$$f(\zeta) = F(\eta), \tag{32}$$

$$g(\zeta) = G(\eta), \tag{33}$$

$$\theta(\zeta) = \Theta(\eta), \tag{34}$$

then it can be easily shown that in terms of f, g, and θ, (26)-(28) become

$$f''' + (f - 4K) f'' + (4K^2 - 2Kf - f') f'' = 0, \tag{35}$$

$$g''' + (f - 4K)g'' - 2K(f - 2K)g' - f''g = 0, \tag{36}$$

$$\theta'' + f Pr\theta' = 0. \tag{37}$$

The boundary conditions can be obtained from (29) and (30) with the help of (31)-(34). The transformed boundary conditions are given by

$$\text{at } \zeta = 0: f(0) = 0, \tag{38a}$$

$$f'(0) = 0, \tag{38b}$$

$$g(0) = 0, \tag{38c}$$

$$\theta(0) = 0, \tag{38d}$$

$$\text{at large } \zeta: f'(\zeta) = 1, \tag{39a}$$

$$f''(\zeta) = 0, \tag{39b}$$

$$g'(\zeta) = \exp(2K\zeta), \tag{39c}$$

$$g''(\zeta) = 2K\exp(2K\zeta), \tag{39d}$$

$$\theta(\zeta) = 1, \tag{39e}$$

where the primes now denote differentiation with respect to ζ. Equations (35)-(37) are much simplified compared to (26)-(28). However, they are still highly nonlinear and two additional initial conditions each, namely, $f'''(0)$, $f''(0)$ and $g''(0)$, $g'(0)$ are required for the numerical integration of (35) and (36). Fortunately, a first integral of (35) and (36) can be obtained, whereas such is not possible for (26) and (27). These integrals can be used to estimate one of the required initial conditions for the integrations of (35) and (36).

Integrating (35) and (36) once from 0 to ζ and making use of (38a-38d) gives

$$f'' + ff'' - f'^2 - K\left[4f' - 4Kf + 2\int_0^\zeta ff''\mathrm{d}\zeta\right] = f'''(0) - 4Kf''(0) = C, \tag{40}$$

$$g'' + fg' - f'g - K\left[4g' + 2(f - 2K)g - 2\int_0^\zeta gf'\mathrm{d}\zeta\right] = g''(0) - 4Kg'(0) = C_1. \tag{41}$$

The constants C and C_1 can be determined by evaluating (40) and (41) at large ζ and making use of (39a-39e) and the following conditions.

Since the effect of displacement have not been included in the present formulation for $f(\zeta)$, it follows from (39a) that

$$f(\zeta) = \zeta - \delta^* \text{ at large } \zeta, \tag{42a}$$

where δ^* is the displacement thickness for the $K \neq 0$ but $\Omega = 0$ case. Also, the condition of constant in the external flow gives

$$f'''(\zeta) = 0 \text{ at large } \zeta. \tag{42b}$$

On the other hand, the displacement effect on $g(\zeta)$ can be easily analyzed and it will be carried out in the following analysis.

From (39c) it can be shown that

$$g(\zeta) = \frac{1}{2K}\left[\exp(2K\zeta) - \exp(2K\delta^*)\right] \text{ at large } \zeta, \tag{43a}$$

if displacement effect on g (ζ) are neglected, and

$$g(\zeta)=\frac{1}{2K}\left[\exp(2K\zeta)-1\right] \text{ at large } \zeta, \tag{43b}$$

if displacement effect on $g(\zeta)$ are included. In the absence of curvature, (43a) reduces to the result given in [22] where displacement effect is not included, and (43b) reduces to the result presented in [4] [5] where displacement effect is accounted for. Therefore, two sets of solutions for $g(\zeta)$ will be obtained depending on whether $g(\zeta)$ is taken to satisfy (43a) or (43b) at large ζ in the evaluation of C_1.

With the conditions for f and g defined at large ζ, it can be easily shown that C and C_1 are given by

$$C=f'''(0)-4Kf''(0)=-1-2K\int_0^{\zeta} ff''\mathrm{d}\zeta+4K^2, \tag{44}$$

$$\begin{aligned} C_1 &= g''(0)-4Kg'(0) \\ &= \frac{1}{2K}\left[\exp(2K\delta^*)-1\right]-(\delta^*-2K)\exp(2K\delta^*) \\ &\quad +2K\int_0^{\zeta}\left[gf'-\frac{1}{2K}\left\{\exp(2K\zeta)-\exp(2K\delta^*)\right\}\right]\mathrm{d}\zeta, \end{aligned} \tag{45a}$$

if displacement effect on g is neglected, or

$$C_1=-\delta^*-2K\left\{1-\int_0^{\zeta}\left[gf'-\frac{1}{2K}\left\{\exp(2K\zeta)-\exp(2K\delta^*)\right\}\right]\mathrm{d}\zeta\right\}, \tag{45b}$$

if displacement effect on g is included. It should be pointed out that in the limit of $K\to 0$, as expected, (45a,b) reduce to $C_1=0$ and $C_1=-\delta_0^*$, respectively.

In the limit of $K\to 0$, (40) and (41) together with (44) and (45a) reduce to the equations analyzed in [22]. According to [4], the solution given in [22] can only account for the kinematic effect of external Ω. If the dynamic effect were to be analyzed, then the displacement effect on g cannot be neglected. In other words, C_1 has to be evaluated from (45b). The second-order equation for vorticity effect analyzed in [4] [5] is inhomogeneous. However, it was shown in [4] [5] that the inhomogeneous part of the second-order equation is given by $-\delta_0^*$. This is different from the present analysis. According to (45b), the result $C_1=-\delta_0^*$ is true only when $K=0$; in other words, only for two-dimensional plane stagnation-point flow. Therefore, the approximate treatment [4] [5] can only be interpreted as accounting for the displacement effect resulting from a two-dimensional plane stagnation-point flow, and not that at the leading edge of turbine blades.

From this discussion, it can be seen that the present formulation for the stagnation-point flow problem including surface curvature and external Ω effects indeed approaches the two limiting cases of $K=0$, $\Omega\neq 0$ and $K=0$, $\Omega=0$ correctly. Therefore, the solutions obtained are exact and are valid for all values of Re, $k\delta$, and Ω. In addition, the solutions correctly account for the boundary-layer displacement effect at the stagnation point.

Although one additional initial condition each is required for the integration of (40) and (41), these two equations are not convenient to solve numerically because they involve the integrals of f and g. As a result, (35) and (36) are solved, and (44) and (45) are used to estimate the initial values for $f''(0)$ and $\theta'(0)$ once the initial guesses on $f''(0)$ and $g'(0)$ are known. The integrals in (44) and (45) are evaluated from the previous iterations for f and g. A fourth-order Runge-Kutta technique is used to start the integration of (35) - (37) using the approximate results given in [4] [5] as initial guesses for $f''(0)$, $g'(0)$, and $\theta'(0)$. Subsequent integration of the equations is performed by a predictor-corrector method that has accuracy in both predictor and corrector of $O\left(\Delta\zeta^5\right)$. Details of this method are outlined in [25]. The complete integration of equations (35)-(37) is iterated with different initial conditions until the outer boundary conditions (39a)-(39e) are satisfied. The outer boundary conditions are considered satisfied when numerical values at the last two consecutive outer steps agree to within 2×10^{-5}. When this condition is reached, convergent solutions for f, g, and θ are obtained.

6. Discussion of Results

Equations (35)-(37) with boundary conditions (38) and (39) are solved for thirteen different values of K; namely, $K = 0, \pm0.015, \pm0.03, \pm0.05, \pm0.1, \pm0.2, \pm0.3$, at a $Pr = 0.7$. The integration of f, g, and θ are carried out to $\zeta = 10$ for all values of K except $K = -0.1, -0.2$ and -0.3, and the outer boundary conditions are applied there instead of at $\zeta\to\infty$. For large negative values of K, integrations are carried out to $\zeta = 12$; this choice of ζ is satisfactory because f, g, and θ approach their outer boundary conditions very rapidly even for large values of $|K|$. For all the cases considered, it is found that f, g, and θ approach their free stream value around $\zeta = 8$. Hence, the choice of $\zeta = 10$ or 12 for all integrations is more than adequate.

Local heat transfer and skin friction can be evaluated from

$$\dot{q} = \kappa\left(\frac{\partial T}{\partial y}\right)_{y=0}, \tag{46}$$

$$\tau_w = \mu\left(\frac{\partial T}{\partial y}\right)_{y=0}. \tag{47}$$

With the help of (23), (25) and equations (32)-(34), (46) and (47) can be reduced to

$$\dot{q} = \kappa\left(T_\infty - T_w\right)\sqrt{\frac{a}{v}}\theta'(0), \tag{48}$$

$$\tau_w = \rho a\sqrt{av}xf''(0) - \mu\Omega g'(0). \tag{49}$$

It can be seen from (49) that the effect of external Ω is to shift the zero shear point away from the stagnation point, which is located at $x = 0$. The shear stress that is responsible for this shift is designated $\left(\tau_w\right)_v$ and is given by,

$$\left(\tau_w\right)_v = -\mu\Omega g'(0). \tag{50}$$

The calculated value is $\left(\tau_w\right)_v = -1.4065\mu\Omega$ with displacement effect on g included, and is $\left(\tau_w\right)_v = -0.6079\mu\Omega$ when displacement effect is neglected. These results show that $\left(\tau_w\right)_v$ is not affected by K but depends on Ω and the displacement. They validate the approximate analysis results of [4] [5], and show that, indeed, the effect of curvature on $g'(0)$ is negligible.

If the origin of the coordinate axes is located at the zero-shear point and the new x coordinate is denoted by $\bar{x}$, then (49) can be rewritten as

$$\bar{\tau} = \rho a\sqrt{av}\bar{x}f''(0). \tag{51}$$

Denoting the local heat transfer and skin friction of the $K = 0$ case by a subscript "o", the following relations for the ratio of local heat transfer and skin friction with and without curvature effect included are obtained

$$\frac{\dot{q}}{\dot{q}_o} = \frac{\theta'(0)}{\theta_o'(0)}, \tag{52}$$

$$\frac{\bar{\tau}}{\bar{\tau}_o} = \frac{f''(0)}{f_o''(0)}. \tag{53}$$

These results are shown in **Figure 2** and **Figure 3**, respectively.

In the approximate analysis of [4] [5], the inviscid surface velocity in the immediate vicinity of the stagnation point was expanded in the form

$$u(x,0) = u_{11}x + u_{12}x^2 + O\left(x^3\right), \tag{54}$$

where u_{11} has the dimension of (time)$^{-1}$ and u_{12} has the dimension of (length)$^{-1}$ (time)$^{-1}$. Using this expansion, the approximate analysis gives rise to the following expressions for the local heat transfer and skin friction ratios; namely,

$$\frac{\dot{q}}{\dot{q}_o} = 1 - 0.258356K + 1.810687\frac{v^{1/2}\Omega u_{12}}{u_{11}^{5/2}}, \tag{55}$$

$$\frac{\bar{\tau}}{\bar{\tau}_o} = 1 - 1.552226K + 4.743353\frac{v^{1/2}\Omega u_{12}}{u_{11}^{5/2}}. \tag{56}$$

On first examination, it seems that the approximate results of [4] [5] are quite reasonable because one would indeed expect the effect of external Ω to be felt by the local heat flux and the wall shear. The approximate analysis [4] [5] showed that, in addition to shifting the zero-shear point away from the stagnation point, external Ω also influences local heat transfer and skin friction. However, on closer examination, it could be seen that the inviscid solution (18)-(20) deduced from the present analysis gives an inviscid surface velocity of $u(x,0) = ax$ only. This implies that the last term in (55) and (56) should be identically zero; *i.e.*, $u_{12} \equiv 0$. In other words, assuming (54) for $u(x,0)$, as suggested in [4] [5], is incorrect; at least in the immediate vicinity of the stagnation point. Setting $u_{12} = 0$ reduce the equations for local heat flux (55) and local shear stress (56) to:

$$\frac{\dot{q}}{\dot{q}_o} = 1 - 0.258356K, \tag{57}$$

$$\frac{\overline{\tau}}{\overline{\tau}_o} = 1 - 1.552226K. \tag{58}$$

These results are shown in Figure 2 and Figure 3 for comparison.

It can be seen in Figure 2 that the exact wall heat flux decrease with K for $K > 0$ is faster than that predicted by the approximate analysis [4] [5], and the opposite is true for $K < 0$. But as shown in Figure 3, there is no discernible difference between the exact result for wall shear stress and that obtained from the approximate analysis [4] [5]. However, on close examination, a consistent difference does exist, especially for large K. This is evident from the results tabulated in Table 1 where the values of $f''(0)$ and $\theta'(0)$ are reported to the fourth decimal point. The approximate results [4] [5], which are denoted by a subscript VD, are also listed in Table 1 for comparison. It can be seen that the approximate results are correct for values of K up to $|K| = 0.015$. Thereafter, they deviate from the exact solutions. The variations are small for small values of $|K|$,

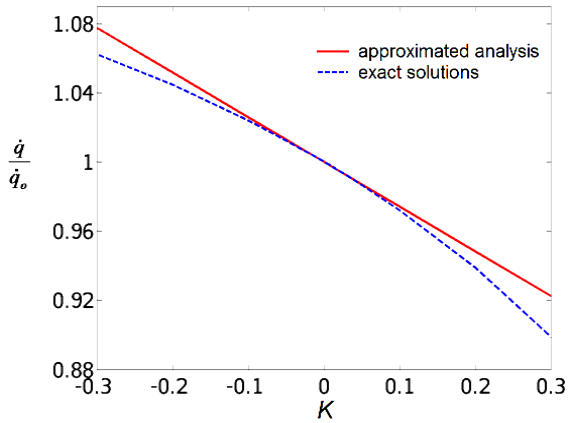

Figure 2. Wall heat flux, $\dot{q}/\dot{q}_o$, at different values of K (red solid line—approximate analysis [4] [5]; blue dashed line—exact solutions).

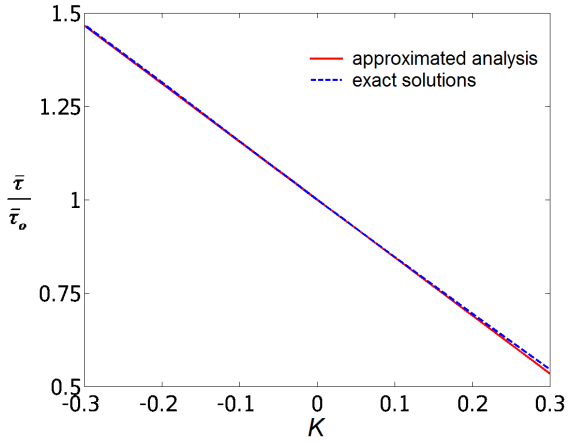

Figure 3. Wall shear stress, $\overline{\tau}/\overline{\tau}_o$, at different values of K (red solid line—approximate analysis [4] [5]; blue dashed line—exact solutions).

Table 1. A comparison of $f''(0)$ and $\theta'(0)$ with approximate results deduced from [4] [5] for different values of *K*.

	K												
	−0.3	−0.2	−0.1	−0.05	−0.03	−0.15	0	0.15	0.03	0.05	0.1	0.2	0.3
$f''(0)$	1.8092	1.6188	1.4250	1.3286	1.2901	1.2613	1.2326	1.2039	1.1753	1.1372	1.0426	0.8553	0.6717
$f''_{VD}(0)$	1.8066	1.6152	1.4239	1.3283	1.2900	1.2613	1.2326	1.2039	1.1752	1.1369	1.0413	0.8499	0.6586
$\theta'(0)$	0.5268	0.5781	0.5078	0.5021	0.4996	0.4978	0.4959	0.4959	0.4920	0.4892	0.4820	0.4656	0.4457
$\theta'_{VD}(0)$	0.5343	0.5215	0.5087	0.5023	0.4997	0.4978	0.4959	0.4959	0.4920	0.4895	0.4895	0.4702	0.4574

but increase as $|K|$ increases. These small differences are significant because in the course of numerically integrating (35) and (37), it is found that, if the approximate values are used for $f''(0)$ and $\theta'(0)$, the numerical results fail to approach the boundary conditions at ζ = 10 or 12 correctly and still satisfy the accuracy criteria imposed on $f''(\zeta)$, $f'''(\zeta)$, and $\theta(\zeta)$. The situation gets worse when $|K|$ increases and at $|K| \geq 0.1$ the numerical computations fail to converge to a meaningful solution. Consequently, it can be concluded that the approximate analysis of [4] [5] gives the correct slope for $\overline{\tau}/\overline{\tau}_o$ and $\dot{q}/\dot{q}_o$ at *K* = 0 only. This was pointed out in [21] where the authors concluded that there is actually no justification for attaching any significance to the curvature of the curves for $\overline{\tau}/\overline{\tau}_o$ and $\dot{q}/\dot{q}_o$ when they are deduced from any one of the known approximate methods [19] [20] [21].

The higher wall shear given by the exact analysis is a direct consequence of the more favorable pressure gradient seen by the flow for a given *K*. From (2) it can be deduced that the pressure gradient at the wall along the flow direction is given by

$$\rho^{-1}\left(\frac{\partial p}{\partial x}\right)_{y=0} = \nu\left(\frac{\partial^2 u}{\partial y^2}\right)_{y=0} + \nu k\left(\frac{\partial u}{\partial y}\right)_{y=0}. \tag{59}$$

With the help of (23) and equations (31) - (33), it can be shown that (59) reduces to

$$\rho^{-1}\left(\frac{\partial p}{\partial x}\right)_{y=0} = a^2 x\left[f'''(0) - 2Kf''(0)\right] - \nu\Omega\left[g''(0) - 2Kg'(0)\right]. \tag{60}$$

Again, the effect of external Ω is to shift the zero pressure gradient point away from the stagnation point. Consequently, (60) can be written as

$$\frac{\left(\partial p/\partial x\right)_{y=0}}{\rho a^2 \overline{x}} = f'''(0) - 2Kf''(0), \tag{61}$$

while the corresponding result deduced from the approximate analysis [4] [5] is

$$\left[\frac{\left(\partial p/\partial x\right)_{y=0}}{\rho a^2 \overline{x}}\right]_{VD} = -1 + 1.880488K. \tag{62}$$

These results are plotted in **Figure 4**. They show that the decrease in favorable pressure gradient with *K*, for $K > 0$, is faster for the exact solution than for the

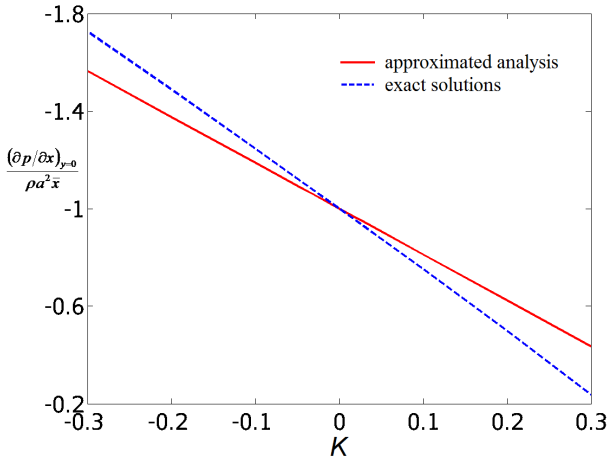

Figure 4. Wall pressure gradient ratio, $(\partial p/\partial x)_{y=0}/\rho a^2 \bar{x}$, at different values of K (red solid line—approximate analysis [4] [5]; blue dashed line—exact solutions).

approximate analysis. The opposite is true for $K < 0$.

Some sample plots of f, f', f'', g, g', and q for three different values of K are shown in **Figures 5-10**, respectively. They clearly demonstrate the effect of curvature on these profiles. Therefore, if the plane stagnation-point-flow solution is used as initial conditions for subsequent heat transfer calculations around turbine blades, the error incurred could be substantial, depending on the nose curvature and the external Ω. The latter effect would shift the zero shear point and the zero pressure gradient point away from the stagnation point, and this could have an impact on transition to turbulence and local separation. However, curvature would affect the wall shear, the wall heat flux, the pressure distribution around the leading edge and, more importantly, the boundary layer thickness in the vicinity of the stagnation point (**Figure 6**). This means that if the $K = 0$ solution is used as initial conditions, a wrong estimate of the velocity profile and momentum and displacement thicknesses would have been used for subsequent heat transfer calculation around turbine blades. The seriousness of this error is best illustrated by examining the variation of the displacement thickness ratio, δ^*/δ_o^*, with K for the case $\Omega = 0$ (**Figure 11**), which clearly underlines the importance of including surface curvature effect in the calculation of leading edge heat transfer.

Finally, consider the determination of "a" which is as yet undefined. To accomplish this, consider the flow along the stagnation streamline toward a circular cylinder in the absence of external vorticity. In the vicinity of the stagnation point, the velocity along the stagnation streamline as given by (i) the plane stagnation-point flow inviscid solution, (ii) the present inviscid solution, and (iii) the potential solution around a cylinder, can be written as

(i) $\dfrac{V_o^p}{V_\infty} = -\dfrac{ay}{V_\infty}$ (plane wall)

(ii) $\dfrac{V_o^c}{V_\infty} = -\dfrac{aR^2 \ln(1+y/R)}{V_\infty (R+y)}$ (curved wall)

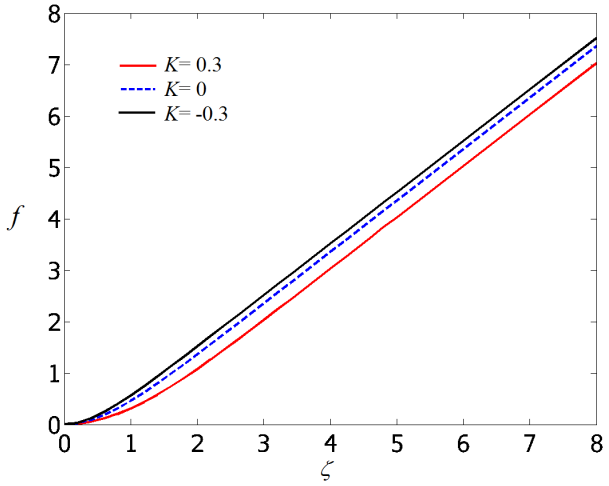

Figure 5. Effects of surface curvature on f (red solid line—$K = 0.3$; blue dashed line—$K = 0$; black solid line—$K = -0.3$).

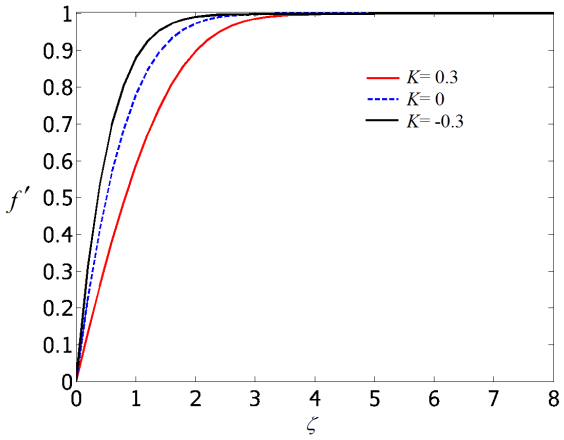

Figure 6. Effects of surface curvature on f' (red solid line—$K = 0.3$; blue dashed line—$K = 0$; black solid line—$K = -0.3$).

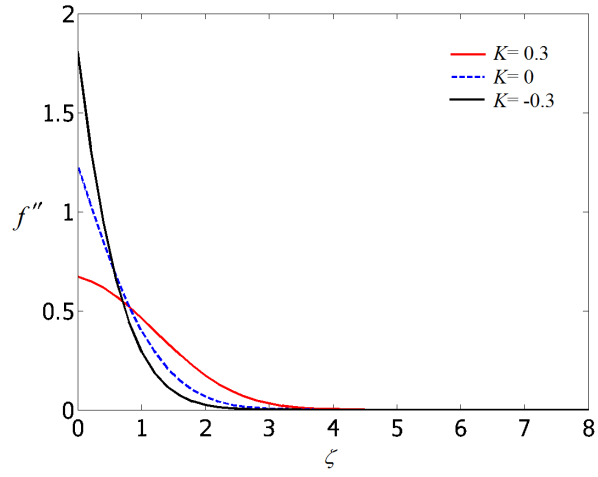

Figure 7. Effects of surface curvature on f'' (red solid line—$K = 0.3$; blue dashed line—$K = 0$; black solid line—$K = -0.3$).

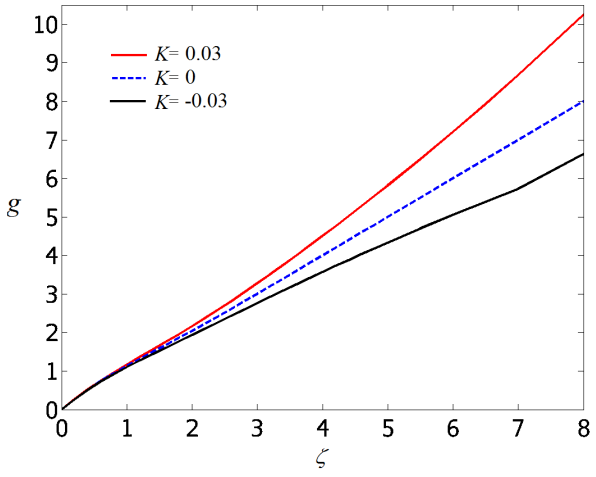

(a)

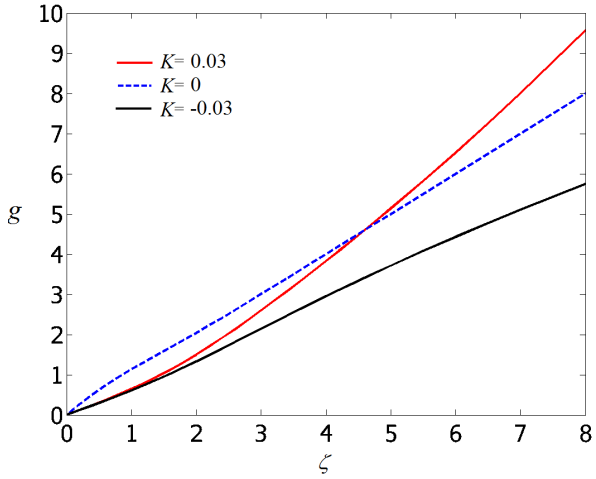

(b)

Figure 8. (a) Effects of surface curvature on g with displacement effect (red solid line—K = 0.03; blue dashed line—K = 0; black solid line—K = −0.03); Effects of surface curvature on g without displacement effect (red solid line—K = 0.03; blue dashed line—K = 0; black solid line—K = −0.03).

(iii) $\dfrac{V_o}{V_\infty} = -\dfrac{y(y+2R)}{(R+y)^2}$ (cylinder)

where V_∞ is the velocity far upstream and V_o^p, V_o^c, V_o are the velocities along the stagnation streamlines for the three cases (i), (ii), (iii) considered, respectively. For very small y, the above relations reduce to

$$\frac{V_o^p}{V_\infty} = \frac{V_o^c}{V_\infty} = \frac{V_o}{V_\infty} = -\frac{2y}{R} = -\frac{ay}{V_\infty}, \tag{63}$$

thus giving,

$$a = \frac{2V_\infty}{R}. \tag{64}$$

Therefore, "a" can be determined from knowledge of the approach flow and the nose radius.

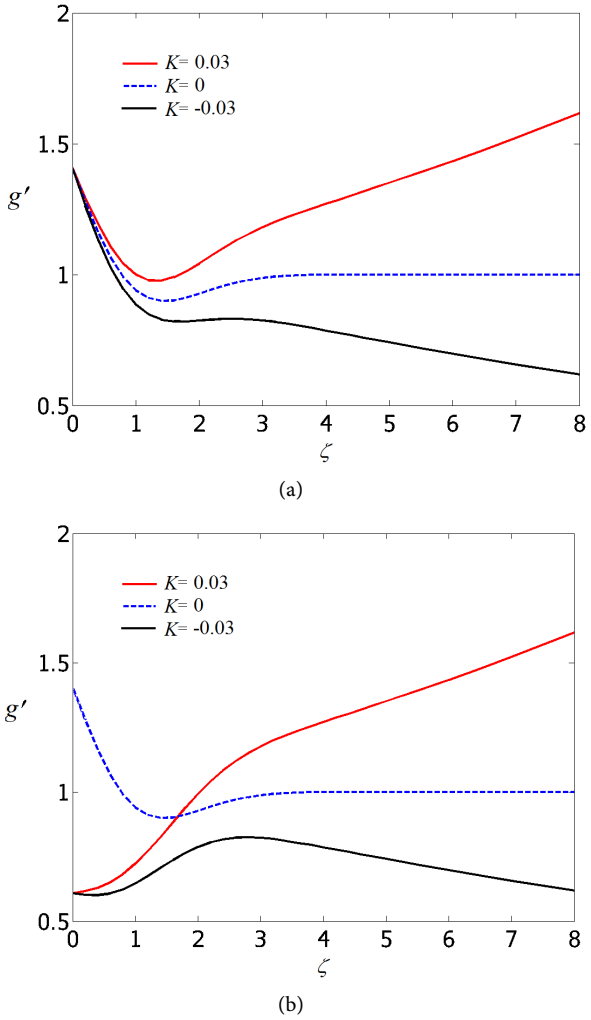

Figure 9. (a) Effects of surface curvature on g' with displacement effect (red solid line—$K = 0.03$; blue dashed line—$K = 0$; black solid line—$K = -0.03$); (b) Effects of surface curvature on g' without displacement effect (red solid line—$K = 0.03$; blue dashed line—$K = 0$; black solid line—$K = -0.03$).

At this point, it can be concluded that the thermal stagnation-point flow problem at the leading edge of axial flow turbine blades has been correctly and completely solved. This leads to exact solutions for the governing Navier-Stokes equations under the assumption of steady flow, small nose radius, constant external Ω, and any *Re*.

7. Extention to Centrifugal Impeller Blades

The present analysis is formulated for a stationary curved surface with a uniform flow having a constant Ω approaching the surface. Therefore, it is directly applicable to leading edge problems in axial flow turbines where Coriolis force effect are absent in the viscous flow and heat transfer around turbine blades. However, this is not true for a radial flow machine, and it would seem that the present analysis could not be applied to study the leading edge problem of cen-

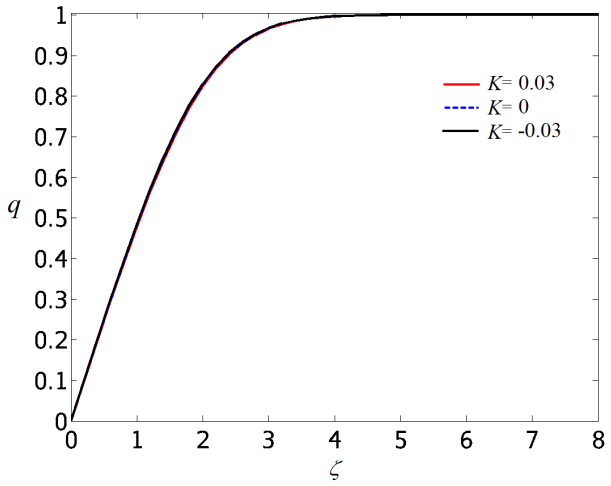

Figure 10. Effects of surface curvature on q (red solid line—K = 0.03; blue dashed line—K = 0; black solid line—K = −0.03).

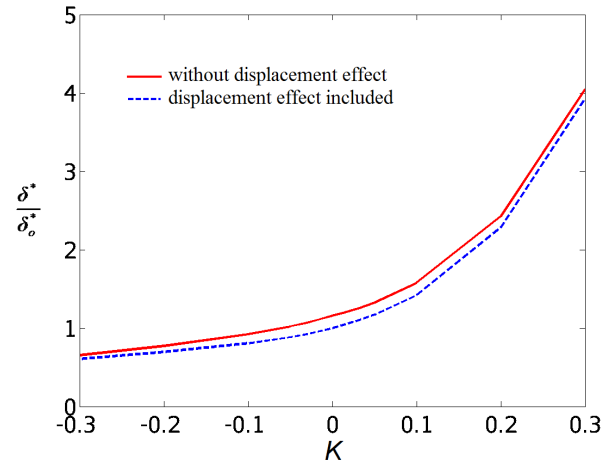

Figure 11. Effects of surface curvature on the displacement thickness ratio, δ^*/δ_o^*, for the case $\Omega = 0$ (red solid line—without displacement effect; blue dashed line—displacement effect included).

trifugal impeller blades. Fortunately, there are similarities between a uniform shear flow toward a stationary surface and a uniform flow toward a rotating surface that would allow the use of the present results for the study of flows toward rotating curved surfaces.

To appreciate this, consider the steady thermal stagnation-point flow with a uniform velocity approaching a two-dimensional curved surface rotating at a constant speed of $\Omega/2$. The equations governing the two-dimensional flow can be written with respect to a coordinate system attached to the rotating surface (**Figure 12**) and obeying the right-hand rule. If u and v are again used to denote the relative velocities along x and y direction, respectively, then the steady state equations can be written as

$$u_x + (hv)_y = 0, \tag{65}$$

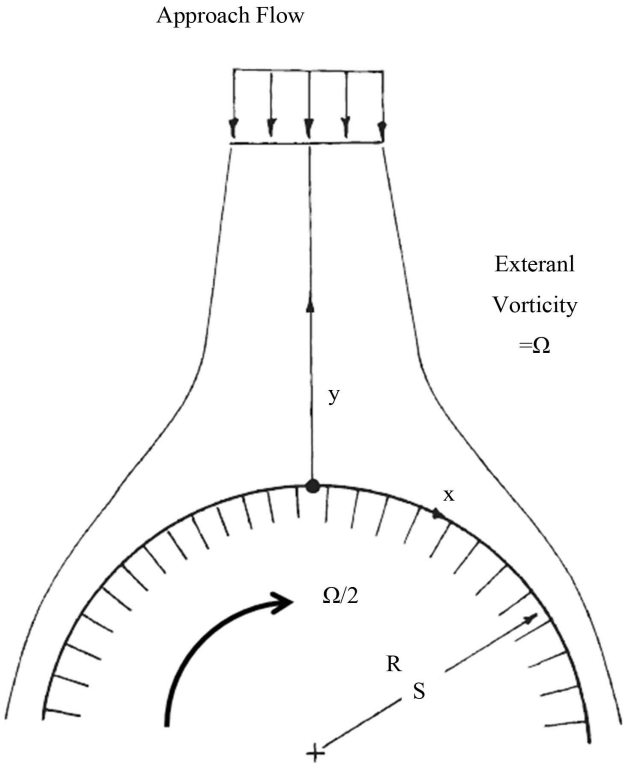

Figure 12. Curvilinear co-ordinate system for a rotating surface with constant speed of $\Omega/2$.

$$uu_x + v(hu)_y - h\Omega v = -\rho^{-1}p_x^* + v\left[h^{-1}u_{xx} + hu_{yy} + ku_y - k^2h^{-1}u + 2kh^{-1}v_x\right], \quad (66)$$

$$uv_x + hvv_y - ku^2 + h\Omega u = -\rho^{-1}hp_y^* + v\left[h^{-1}v_{xx} + hv_{yy} + kv_y - k^2h^{-1}v - 2kh^{-1}u_x\right], \quad (67)$$

$$uT_x + hvT_y = \alpha\left[h^{-1}T_{xx} + hTv_{yy} + kT_y\right], \quad (68)$$

$$\text{where} \quad p^* = p - \frac{1}{2}\rho r^2\left(\frac{\Omega}{2}\right)^2, \quad (69)$$

is the reduced pressure and r is the radial distance from the axis of rotation. As before, k is taken to be constant. Since the flow is two-dimensional, there is only one component of vorticity and it is normal to the plane of flow. This component is given by

$$h^{-1}v_x - h^{-1}(hu)_y = \Omega, \quad (70)$$

in the inviscid flow region.

With the problem thus formulated, it can be easily seen that the inviscid flow is again governed by the Poisson Equation (5) with boundary conditions given by (8) and (9). Therefore, the inviscid velocity field is given by (18) and (19) and the pressure field is obtained by integrating (66) and (67) with the kinematic viscosity $\nu \equiv 0$. The result is

$$p_o^* - p^* = \frac{1}{2}\rho\left[\frac{a^2x^2}{h^2} + \frac{a\Omega x}{k}\frac{4h^2\ln h - h^2 + 1}{h^2} - \frac{\Omega^2}{4k^2}\frac{h^4 + 1}{2h^2} + \frac{a^2(\ln h)^2}{k^2h^2}\right]. \quad (71)$$

By cross-differentiating Equations (66) and (67) to eliminate p^*, it can be shown that the resulting vorticity equation is again given by (21) because the Coriolis force terms are zero as a result of the continuity equation (65). The boundary conditions are the same as (22). In view of this, the velocity field around the stagnation point of a rotating curved surface is the same as that around the stagnation point of a stationary curved surface with an approach flow having a constant Ω equal to twice the rotational speed. Since the temperature field as defined by (68) only depends on the velocity field, the resulting solution of (68) would also be the same as that obtained before, provided the thermal boundary conditions remain the same. The pressure field will be different and is given by the integral of (66) and (67) once the velocity field is known.

From the above discussion, it can be seen that the present exact analysis can also be extended to study the steady heat transfer and viscous flow around the stagnation point at the leading edge of centrifugal impeller blades.

8. Conclusions

The problem of a steady thermal stagnation-point flow at the leading edge of an axial flow turbine under the influence of a constant external Ω has been analyzed. It is shown that exact solutions to the steady governing Navier-Stokes equations can be obtained if the nose radius is constant. Heat transfer and skin friction results obtained for the curvature parameter K ranging from $-0.3 \le K \le 0.3$ show that, within this range, the linear relation between wall shear and K given by the approximate analysis of [4] [5] is essentially correct. However, the decrease of wall heat flux with K for $K > 0$ is faster than that predicted in [4] [5], and the opposite is true for $K < 0$. Consequently, the exact results show that the approximate analysis is correct only in the determination of the slopes of the variation of wall shear and local heat transfer with K at $K = 0$.

External Ω gives rise to a wall shear stress that is responsible for shifting the zero skin friction point away from the stagnation point. Although the wall shear is a function of external Ω and displacement, it is independent of curvature. Besides this effect, external Ω has no other effect on wall shear and local heat transfer. This is contrary to the results given in [4] [5], which revealed that external Ω also has a second-order effect on wall shear and wall heat flux. This error in the analysis detailed in [4] [5] could be traced to its incorrect proposed expansion for the inviscid surface velocity in the immediate vicinity of the stagnation point. If a correct expansion is proposed, the approximate results are consistent with the exact solutions, at least to the lowest order.

Surface curvature also influences the wall static pressure distribution in the vicinity of the stagnation point. It is found that convex curvature decreases the favorable pressure gradient, but concave curvature increases it. This implies that the flow near the leading edge of turbine blades (whose curvature is convex) will be more susceptible to laminar separation than the corresponding flow toward a plane surface. In addition, surface curvature affects the velocity and temperature profiles and the thickness of the viscous layer. All these underline the impor-

tance of including surface curvature and external Ω effect in the heat transfer calculation around turbine blades.

Finally, it is shown that the present analysis can also be applied to study the steady leading edge stagnation-point flow problem in centrifugal impeller blades. With the exception of the pressure field, the solution to the impeller blade problem is identical to that of the axial flow turbine blade.

Acknowledgements

The first author would like to acknowledge the support given him by the Mechanical Engineering Department, the Hong Kong Polytechnic University, Hong Kong, during his stay as Visiting Chair Professor from September to October of 2016.

References

[1] van Driest, E.R. (1959) Convective Heat Transfer in Gases. In: Lin, C.C., Ed., *High Speed Aerodynamics and Jet Propulsion*, Vol. 5, Princeton University Press, Princeton, NJ, 339.

[2] Kline, S.J., Morkovin, M.V., Sovran, G. and Cockrell, D.J. (1968) v.1. Methods, Predictions, Evaluation, and Flow Structure. *Proceedings of the Stanford Conference on Computation of Turbulent Boundary Layers*, AFOSR-IFP, 1, 18-19.

[3] Coles, D.E. and Hirst, E.A. (1968) v.2.Compiled Data. *Proceedings of the Stanford Conference on Computation of Turbulent Boundary Layers*, AFOSR-IFP, 2.

[4] Van Dyke, M. (1962) Higher Approximations in Boundary Layer Theory, Part I: General Analysis. *Journal of Fluid Mechanics*, **14**, 161-177. https://doi.org/10.1017/S0022112062001147

[5] Van Dyke, M. (1962) Higher Approximations in Boundary Layer Theory, Part II: Application to Leading Edges. *Journal of Fluid Mechanics*, **14**, 481-495. https://doi.org/10.1017/S0022112062001391

[6] Bradshaw, P. (1973) Effect of Streamline Curvature on Turbulent Flow. AGARDograph 169.

[7] So, R.M.C. and Mellor, G.L. (1973) Experiment on Convex Curvature Effect in Turbulent Boundary Layers. *Journal of Fluid Mechanics*, **60**, 43-62. https://doi.org/10.1017/S0022112073000030

[8] So, R.M.C. and Mellor, G.L. (1975) Experiment on Turbulent Boundary Layers on a Concave Wall. *Aeronautical Quarterly*, **26**, 25-40. https://doi.org/10.1017/S0001925900007174

[9] Bradshaw, P. (1969) The Analogy between Streamline Curvature and Buoyancy in Turbulent Shear Flow. *Journal of Fluid Mechanics*, **36**, 177-191. https://doi.org/10.1017/S0022112069001583

[10] Rastogi, A.K. and Whitelaw, J.H. (1971) Procedure for Predicting the Influence of Longitudinal Curvature on Boundary Layer Flows. ASME Paper 71-WA/FE-37.

[11] Irwin, H.P.A.H. and Arnot Smith, P. (1975) Prediction of the Effect of Streamline Curvature on Turbulence. *Physics of Fluids*, **18**, 624-630. https://doi.org/10.1063/1.861202

[12] So, R.M.C. and Mellor, G.L. (1978) Turbulent Boundary Layers with Large Streamline Curvature Effect. *Zeitschrift für angewandte Mathematik und Physik ZAMP*,

29, 54-74. https://doi.org/10.1007/BF01797303

[13] Johnston, J.P. and Eide, S.A. (1976) Turbulent Boundary Layers on Centrifugal Compressor Blades, Prediction of the Effect of Surface Curvature and Rotation. *Journal of Fluids Engineering*, **98**, 374-381.

[14] So, R.M.C. (1981) Heat Transfer Modeling for Turbulent Shear Flows on Curved Surfaces. *Zeitschrift für angewandte Mathematik und Physik ZAMP*, **32**, 514-532. https://doi.org/10.1007/BF00947018

[15] Koosinlin, M.L., Launder, B.E. and Sharma, B.I. (1974) Prediction of Momentum, Heat and Mass Transfer in Swirling, Turbulent Boundary Layers. *Journal of Heat Transfer*, **96**, 204-209. https://doi.org/10.1115/1.3450165

[16] Hiemenz, K. (1911) Die Grenzschicht an einem in den gleichformigen Flussigkeitsstrom eingetauchten geraden Kreiszylinder. *Dingler's Polytechnical Journal*, **326**, 321.

[17] Howarth, L. (1938) On the Calculation of the Steady Flow in the Boundary Layer near the Surface of a Cylinder in a Stream. Aeronautical Research Council, R. & M. 1632.

[18] Schlichting, H. (1960) Boundary Layer Theory. 4th Edition, McGraw-Hill Book Company, New York, London, 78.

[19] Massey, B.S. and Clayton, B.R. (1965) Laminar Boundary Layers and Their Separation from Curved Surfaces. *Journal of Basic Engineering*, **87**, 483-493. https://doi.org/10.1115/1.3650580

[20] Schultz-Grunow, F. and Breuer, W. (1965) Laminar Boundary Layers on Cambered Walls. In: Holt, M., Ed., *Basic Developments in Fluid Dynamics*, Vol. 1, 377-436.

[21] Narasimha, R. and Ojha, S.K. (1967) Effect of Longitudinal Surface Curvature on Boundary Layers. *Journal of Fluid Mechanics*, **29**, 187-199. https://doi.org/10.1017/S0022112067000710

[22] Stuart, J.T. (1959) The Viscous Flow Near a Stagnation Point When the External Flow Has Uniform Vorticity. *Journal of the Aerospace Sciences*, **26**, 124-125. https://doi.org/10.2514/8.7963

[23] van Dyke, M. (1969) Higher-Order Boundary Layer Theory. *Annual Review of Fluid Mechanics*, **1**, 265-292. https://doi.org/10.1146/annurev.fl.01.010169.001405

[24] Goldstein, S. (1965) Modern Developments in Fluid Dynamics. Vo. 1, Dover Publications, Inc., New York, 119.

[25] Ralston, A. and Wilf, H.S. (1960) Mathematical Methods for Digital Computers. John Wiley Sons, Inc., New York, London, 93.

a_1	Arbitrary constant defined in Equation (13)
a_2	Arbitrary constant defined in Equation (14)
a	Arbitrary constant defined in Equation (16)
C, C_1	Integration constants defined in Equation (40) and Equation (41)
C_p	Specific heat of fluid at constant pressure
$f(\zeta)$	Transformed similar velocity function defined in Equation (32)
$F(\eta)$	Similar velocity function defined in Equations (23) and (24)
$g(\zeta)$	Transformed similar velocity function defined in Equation (33)
$G(\eta)$	Similar velocity function defined in Equation (23)
$h = 1 + ky$	Metric coefficient
k	Surface curvature
$K = k\sqrt{\nu/a}$	Normalized surface curvature
L	Characteristic length
p	Static pressure
p_0	Static pressure at the stagnation point
$Pr = \nu/\alpha$	Prandtl number
$\dot{q}$	Wall heat flux
$\dot{q}_0$	Wall heat flux for the $k = 0$ case
$Re = U_r L/\nu$	Reynolds number
T	Fluid temperature
T_w	Wall temperature
T_∞	Fluid temperature far away from the wall
u	Velocity along x-direction
U_r	Characteristic velocity
v	Velocity along y-direction
x, y	Coordinates measured along the wall and normal to the wall, respectively
α	Thermal diffusivity of fluid
δ	Thickness of viscous layer
δ^*	Displacement thickness for the $\Omega = 0$ case
$\eta = y\sqrt{a/\nu}$	Similarity variable
$\Theta(\eta)$	Nondimensional temperature function defined in Equation (25)
$\theta(\zeta)$	Transformed nondimensional temperature function defined in Equation (34)
κ	Thermal conductivity of fluid
μ	Viscosity of fluid
ν	Fluid kinematic viscosity
ρ	Fluid density
τ_w	Wall shear stress
$\overline{\tau}$	Modified wall shear stress
$\overline{\tau}_0$	Modified wall shear stress for the $k = 0$ case
Ψ	Stream function for inviscid flow
Ω	External vorticity
$\zeta = \ln(1 + K\eta)/K$	Transformed similarity variable

Call for Papers

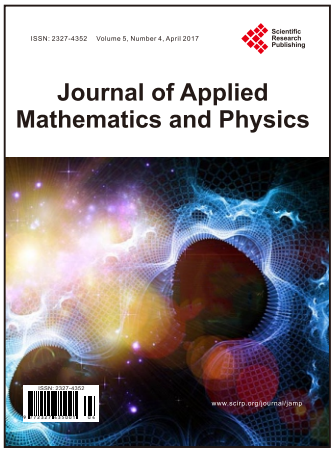

Journal of Applied Mathematics and Physics

ISSN Print: 2327-4352 ISSN Online: 2327-4379
http://www.scirp.org/journal/jamp

Journal of Applied Mathematics and Physics is an international journal dedicated to the latest advancement of applied mathematics and physics. The goal of this journal is to provide a platform for researchers and scientists all over the world to promote, share, and discuss various new issues and developments in different areas of applied mathematics and physics. We aim to publish high quality research articles in terms of originality, depth and relevance of content, and particularly welcome contributions of interdisciplinary research on applied mathematics, physics and engineering.

Subject Coverage

The journal publishes original papers including but not limited to the following fields:

- Applications of Systems
- Applied Mathematics
- Applied Non-Linear Physics
- Applied Optics
- Applied Solid State Physics
- Biophysics
- Computational Physics
- Condensed Matter Physics
- Control Theory
- Cryptography
- Differentiable Dynamical Systems
- Engineering and Industrial Physics
- Experimental Mathematics
- Fluid Mechanics
- Fuzzy Optimization
- Geophysics
- Integrable Systems
- Laser Physics
- Methodological Advances
- Multi-Objective Optimization
- Nanoscale Physics
- Nonlinear Partial Differential Equations
- Non-Linear Physics
- Nuclear Physics
- Numerical Computation
- Optical Physics
- Portfolio Selection
- Riemannian Manifolds
- Scientific Computing
- Set-Valued Analysis
- Soliton Theory
- Space Physics
- Symbolic Computation
- Topological Dynamic Systems
- Variational Inequality
- Vector Optimization

We are also interested in: 1) Short reports—2-5 page papers where an author can either present an idea with theoretical background but has not yet completed the research needed for a complete paper or preliminary data; 2) Book reviews—Comments and critiques.

Notes for Intending Authors

The journal publishes the highest quality original full articles, communications, notes, reviews, special issues and books, covering both the experimental and theoretical aspects including but not limited to the above materials, techniques and studies. Papers are acceptable provided they report important findings, novel insights or useful techniques within the scope of the journal. All manuscript must be prepared in English, and are subjected to a rigorous and fair peer-review process. Accepted papers will immediately appear online followed by prints in hard copy.

Website and E-Mail

http://www.scirp.org/journal/jamp E-mail: jamp@scirp.org

What is SCIRP?

Scientific Research Publishing (SCIRP) is one of the largest Open Access journal publishers. It is currently publishing more than 200 open access, online, peer-reviewed journals covering a wide range of academic disciplines. SCIRP serves the worldwide academic communities and contributes to the progress and application of science with its publication.

What is Open Access?

All original research papers published by SCIRP are made freely and permanently accessible online immediately upon publication. To be able to provide open access journals, SCIRP defrays operation costs from authors and subscription charges only for its printed version. Open access publishing allows an immediate, worldwide, barrier-free, open access to the full text of research papers, which is in the best interests of the scientific community.

- High visibility for maximum global exposure with open access publishing model
- Rigorous peer review of research papers
- Prompt faster publication with less cost
- Guaranteed targeted, multidisciplinary audience

Scientific Research Publishing

Website: http://www.scirp.org

Subscription: sub@scirp.org

Advertisement: service@scirp.org